

Development of a Dynamic Model of a Ducted Fan VTOL UAV

**A thesis submitted in fulfillment of the requirements for the degree of
Master of Engineering**

Hui Wen Zhao

B.Eng.

School of Aerospace, Mechanical and Manufacturing Engineering

College of Science, Engineering and Health

RMIT University

August 2009

Declaration

I certify that except where due acknowledgement has been made, the work is that of the author alone; the work has not been submitted previously, in whole or in part, to qualify for any other academic award; the content of the thesis is the result of work which has been carried out since the official commencement date of the approved research program; any editorial work, paid or unpaid, carried out by a third party is acknowledged; and, ethics procedures and guidelines have been followed.

赵荟文

Hui Wen Zhao

Date: 30/08/2009

Abstract

The technology of UAV (Unmanned Aerial Vehicle) has been developing since its conception many years ago. UAV has its own advantages such as, computerizing and autonomous without an on-board pilot by using digital and electronic system which manned aircraft don't have. Therefore, there is no risk of loss of life and it is easier to be maintained than manned aircraft. With the development of technology and requirements, UAV is widespread and used in industry, military and civil work as it can be controlled remotely or can autonomously complete missions. Examples of this are reconnaissance for firefighting and natural disasters, suspect monitoring and strategy attacks.

The School of Aerospace, Mechanical and Manufacturing Engineering in RMIT (SAMME) have been developing a new conceptual Ducted Fan VTOL UAV of which the progress is monitored by more and more aircraft researchers and designers. Because the use of ducted fans as the propulsion system of unmanned air vehicles is worthy of discovery in achieving vertical take-off, landing and hovering. Furthermore, the ducted fan UAV has been improved by the assembly of two wings on its external duct. It is hoped that this additional innovation can play an expectable role for longitudinal flight transition from a vertical climb to a horizontal flight.

The aerodynamic analysis, preliminary and detailed design, of this ducted-fan VTOL UAV, is the first and most important step. To optimize the aerodynamic characteristic of UAV, evaluating aerodynamic coefficients and analyzing the flow patterns around the vehicle at different speeds and angles of attack are necessary. Nowadays, Computational Fluid Dynamics (CFD) is one of the most popular numerical approaches for predicting the external flow around different kinds of vehicles and analyzing the internal flow through many types of tube or duct. In this project, CFD plays an important role in predicting the longitudinal and lateral stability and control characteristics of a full-scale model of ducted fan VTOL UAV at both vertical and horizontal flight without any prior knowledge of existing wind tunnel or flight test data.

Once the numerical results are calculated by the CFD code, further work in wind tunnel test can be performed and compared with CFD data. In addition, after running the full-scale model of UAV in CFD the aerodynamic performances and properties are able to be optimized by the use of CAD codes. Thus, repeating this cycle between CAD and CFD can optimize design, save time and costs.

Prior to carrying out experiments in wind tunnel, the manufacture of ducted fan VTOL UAV is focused on. Particular attention is paid to the propulsion system as the key point. As it plays a critical role in achieving flying of UAV. Meanwhile, the structure design and material option must also be considered carefully. The full-scale model of UAV is produced by Rapid Prototype Machine at SAMME to ensure its perfect aerodynamic shape by testing in the wind tunnel.

The experiment of full-scale UAV model with engines is conducted in RMIT's Industrial Wind Tunnel where its aerodynamic characteristics and its properties of counter-rotating propulsion system were tested. The investigation of wind tunnel testing provides large quantities of data for estimating derivatives of stability and control. Not only were the six components of force and moment obtained,

but also some flight parameters were measured for stability and control by deflecting control surfaces. In addition, by analyzing the correlation between experimental data and CFD results, the dynamic model of ducted fan VTOL UAV was able to be improved with more accuracy.

Flight dynamics is concerned with the motion of an airplane due to internally or externally generated disturbances. As a result ducted fan VTOL UAV stability and control abilities are attracting further research and development.. To describe the rigid-body motion of this UAV the comprehensive equations of motion with six degrees of freedom need to be considered and analyzed. A strategy to simulate a dynamic model of a vertical takeoff and landing (VTOL) unmanned aerial vehicle (UAV) in hovering, vertical climb and horizontal flight is clarified. This will require accurate estimates of the aerodynamic forces and moments acting on the airplane. Based on unique aerodynamic characteristics from the theoretical method, CFD calculation and wind tunnel test, the flight dynamics of ducted fan UAV is able to be modeled and simulated accurately.

The linear coupled dynamic model is achieved by linearizing the equations of motion and dynamic equations based on small disturbance theory and aerodynamic derivatives estimated by CFD and experiment. Furthermore, the non-linear six degree of freedom dynamic model is also considered due to the analysis of aerodynamic forces and moments combined with equations of motion and dynamic equations for the ducted fan VTOL UAV. The computer tools will be applied to simulate both non-linear model and linear state space equations for evaluating the flight performance of this UAV in different cases.

MATLAB as a special mathematical language is widely used for quantity of technical domains, such as numerical computing, engineering simulation and modeling, data analysis, graphic visualization and so on. Of course, it has been playing a critical role in modeling and optimizing aircraft flight performance and very often applied by aerospace engineers and designers not only due to its strong ability to deal complicated and sophisticated mathematical problem, but to also provide high quality visualized environment of model building which is easy to use and plays a satisfactory performance in many projects.

Real-time flight simulation and modeling is achieved when using a linear model linked with MIMO control laws during UAV hovering or low-speed cruise flight depended on unique aerodynamic characteristics from CFD calculation, wind tunnel testing and theoretical method during the flight. By designing of MIMO linear control laws for UAV hovering and low-speed slide flight, the real-time simulation and modeling in MATLAB combined with Flight-simulator displays several animations and trajectories of UAV missions with or without crosswind effect during flight. Although the MIMO nonlinear control laws are still not able to be achieved so far, it is conceivable that the nonlinear control laws will be fulfilled in the future by researchers' efforts.

List of Publications

1. Zhao, H. W. and Bil, C. "Aerodynamic Design and Analysis of a VTOL Ducted-Fan UAV," 26th AIAA Applied Aerodynamics Conference, 18 - 21 August 2008, Honolulu, Hawaii.
2. Zhao, H. W., Bil, C. and Bok, H. Y., "Aerodynamic Analysis of a Ducted Fan VTOL UAV for Transition Maneuver." KSAS-JSASS Joint International Symposium. December, 2008, Korea.
3. Zhao, H. W., Bil, C. and Bok, H. Y., "Computational Fluid Dynamics Calculations on Preproduction Ducted Fan VTOL UAV for Stability and Control," 3rd Australasian Unmanned Air Vehicles Conference, 9 - 12 March, 2009, Melbourne, Australia.
4. Zhao, H. W., Bil, C. and Bok, H. Y., "Control and Simulation of a Ducted Fan VTOL UAV," Paper accepted for SAE 2009 AeroTech Congress & Exhibition, November 10-12, 2009, Washington, USA.
5. Zhao, H. W., Bil, C. and Bok, H. Y., "Ducted Fan VTOL UAV Simulation in Preliminary Design," Paper accepted for 9th AIAA Aviation Technology, Integration, and Operations Conference (ATIO), Sep 21~24, 2009, South Carolina, USA.

Acknowledgments

Throughout my master's degree at School of Aerospace, Mechanical, and Manufacturing Engineering in RMIT, I have had the opportunity and honor of researching with A/Professor Cees Bil as my supervisor. For his guidance, support, supervision and concern throughout this project and my thesis, I cannot express enough appreciation to him.

I would like to express my appreciation to Professor Bok-Hyun Yoon for his guidance with learning CFD technology which played an important role in completing my project.

I would like to give my sincere appreciation to all of the technical staff in the SAMME workshop. Especially, I would like to thank Mr. Gill Atkins who gave me lots of support and suggestions in model manufacturing and wind tunnel experiment.

I also would like to thank RMIT for providing me essential facilities materials and support throughout my project.

I would like to thank Dr Mike Burton for his support on building the model using Rapid Prototype Machine at SAMME. Meanwhile, I also would like to give my appreciation to Rod King who is a shopkeeper of Hobby & Model shop. He offered his support in assembling the propulsion system of the model.

I would like to offer my appreciation, to all of the postgraduate students who are working in the same School as me, for their help and concern throughout my project.

Thanks to the Victorian Partnership in Advanced Computing (VPAC) for access to their facility and for the many hours of computer time that was necessary to complete this computational analysis.

Finally, I have to give my special appreciation to my parents for their continuous encouragement and support throughout my life and study.

Hui-Wen Zhao

CONTENTS

CHAPTER 1.....	1
1 Introduction.....	1
1.1 UAV's family	1
1.2 Technical Features	2
1.2.1 Counter-rotating Propeller.....	4
1.2.2 Duct	4
1.2.3 Stators/Duct Supports	4
1.2.4 Control Surfaces	4
1.2.5 Wings.....	5
1.3 Literature Review	5
1.3.1 Requirements of Design	6
1.3.2 Challenge of Aerodynamic Model.....	7
CHAPTER 2.....	9
2 Aerodynamic Theory of Ducted Fan	9
2.1 Background.....	9
2.1.1 Slipstream Theory of Ducted Fan.....	9
2.1.2 Element Theory of Rotor Blades	11
2.1.3 Propeller Slipstream Effect.....	13
2.1.4 Crosswind Effect on Ducted Fan.....	16
CHAPTER 3.....	18
3 Computational Fluid Dynamics (CFD) Analysis	18
3.1 Introduction.....	19
3.2 The Governing Equations of CFD	19
3.2.1 Navier-Stokes Equations for Viscous Flow	19
3.2.2 Euler Equations for Inviscid Flow	19
3.3 Discretization.....	20
3.4 Technology of Grid Generation	20
3.4.1 Structured Grid Scheme.....	21
3.4.2 Unstructured Grid Scheme	21
3.5 Aerodynamic Analysis of Ducted Fan.....	23
3.5.1 Aerodynamic Characteristics of Duct without Fans	23
3.5.2 Analysis of Flow around Duct with Fuselage.....	28
3.6 Modeling of Full-Scale UAV in CFD.....	29
3.6.1 Mesh Generation of Full-Scale Model.....	29
3.6.2 Properties of Mesh Generation	32
3.6.3 Governing Equations	32
3.6.4 Turbulent Model.....	33

3.6.5	Model Solving	37
3.6.6	Computer Requirements	43
3.6.7	Propeller Slipstream Interaction with Tail	43
3.6.8	Results and Discussion	50
3.7	Summary	56

CHAPTER 4.....58

4	Wind Tunnel Testing	58
4.1	Equipments and Devices.....	58
4.1.1	Propulsion System of UAV	58
4.1.2	Thrust Testing	62
4.1.3	Manufacturing of Full-scale UAV Wind Tunnel Model	64
4.1.4	UAV Model.....	65
4.1.5	Flow Pattern Testing	66
4.1.6	Industrial Wind Tunnel	67
4.1.7	Test Setting	68
4.2	Measurement of Aerodynamic Characteristics	69
4.2.1	Counter-rotating Test	69
4.2.2	Test without Wings	70
4.2.3	Test with Wings	76
4.2.4	Deflection of Control Surfaces	81
4.2.5	Crosswind Effect on UAV	87
4.3	Correlation between CFD Results and Experimental Data.....	90
4.3.1	Calibration of Wind Tunnel Testing.....	90
4.3.2	Results and Discussion	90
4.4	Summary	91

CHAPTER 5.....92

5	Flight Dynamics.....	92
5.1	General Introduction	92
5.1.1	Model of Slipstream Angle	92
5.1.2	The Forces and Moments.....	96
5.1.3	Summary of Forces and Moments	102
5.2	Dynamic Model of UAV	102
5.2.1	Nonlinear Dynamic Equations of Forces and Moments	102
5.2.2	Coordinate Systems	103
5.2.3	Equations of Motion and Dynamic Equations	107
5.3	Linearization of Dynamic Model	111
5.3.1	The Small-Disturbance Theory	111
5.3.2	Linear Methodology	111
5.3.3	Linear Forces and Moments	112
5.3.4	Linear Equations.....	113

5.3.5	Linear Model of 6DoF	114
5.4	State Space Method	116
5.4.1	The Equations of Motion in State Space Form	116
5.4.2	Aerodynamic Derivatives	118
5.4.3	Definition of Special Derivatives	120
5.5	Summary.....	121
CHAPTER 6	122	
6	Flight Simulation and Modeling in MATLAB/Simulink	122
6.1	Introduction.....	122
6.2	Linear Simulation and Control.....	122
6.2.1	Linear Model of UAV in Hovering and Low Speed Cruise Flight	123
6.2.2	High-Order System in Hovering Mode	124
6.2.3	Response Transfer Function Matrix of UAV	125
6.2.4	Application of Feedback Control.....	126
6.2.5	MIMO Control Laws of UAV	128
6.2.6	Simulation Results of MIMO Control Laws.....	131
6.2.7	Real-time Flight Simulation and Modeling	135
6.2.8	Real-time simulation of UAV Hovering in Crosswind	143
6.3	Nonlinear Simulation.....	152
6.3.1	Six Degree-of-Freedom Dynamic Model in Simulink.....	152
6.3.2	Six Degree-of-Freedom Quaternion Model	154
6.3.3	Flight Environmental Model.....	155
6.3.4	Longitudinal Nonlinear Simulation	158
6.4	Summary.....	162
CHAPTER 7	163	
7	Conclusion	163
7.1	Discussion of Results.....	163
7.2	Recommended Further work.....	164
APPENDIX-A	165	
A	Final Design of UAV	165
A.1	Three Views of UAV	165
A.2	Geometry Parameters of UAV	166
APPENDIX-B	167	
B	Mass Properties of UAV	167
B.1	Dimension Measured by Solid-work	167
B.2	Aerodynamic Parameters	168

APPENDIX-C.....	169
C Flow Visualization in CFD.....	169
C.1 Flow Patterns at Different Angle of Attack.....	169
C.2 Crosswind Effect on UAV.....	170
APPENDIX-D.....	171
D Stability and Control Derivatives.....	171
D.1 Case I : Hovering	171
D.2 Case II : Low-speed Vertical Climb and Slide Flight	172
D.3 Case III: Horizontal Cruise Flight.....	173
APPENDIX-E.....	174
E Dynamic Model Edited in M-file.....	174
REFERENCES.....	177

List of Figures

Figure1. 1 Different Prototypes of UAV	2
Figure1. 2 Ducted Fan VTOL UAV	3
Figure1. 3 Configuration View of UAV	4
Figure1. 4 Schematic Diagram of Deflected Slipstream VTOL Principle.....	5
Figure1. 5 Flow Chart of UAV Design	6
Figure1. 6 Definition of Lift and Pitching Moment	7
Figure2. 1 Flow in a Duct.....	9
Figure2. 2 Flow Through the Counter-Rotating Fans Inner of a Duct	10
Figure2. 3 Aerodynamic Analysis of Blade Element.....	12
Figure2. 4 Velocity Vectors Composition and Definition of α_{ps}	14
Figure2. 5 Sketch of Duct Ram Drag Forces Acting at UAV Center of Gravity	16
Figure3. 1 Basic Flow Chart of CFD Methodology	18
Figure3. 2 Discrete Grid Points	20
Figure3. 3 An Example of C-type Body-fitted Mesh around An Aerofoil.....	21
Figure3. 4 An Example of O-type Body-fitted Mesh around An Aerofoil.....	21
Figure3. 5 Unstructured Grids around a Three-element Aerofoil.....	22
Figure3. 6 Unstructured Grids around an Entire Configuration of Airplane.....	22
Figure3. 7 3D Duct Geometry Definition and Aerofoil of Duct	23
Figure3. 8 Hybrid-Mesh around Duct	24
Figure3. 9 Unstructured Grids Surrounding Far Flied and Structured Grids (Boundary Layer) around Aerofoil of Duct	25
Figure3. 10 Unstructured Volume Grids Surrounding Far Flied of Duct.....	25
Figure3. 11 3D Contour of Pressure Coefficient	26
Figure3. 12 (a) Lift Coefficient Versus Angle of Attack ; (b) Drag Coefficient Versus Angle of Attack ; (c) Pitching Moment Coefficient Versus Angle of Attack	27
Figure3. 13 Simplified Duct and Fuselage	28
Figure3. 14 Pathlines Show Cruise Flight , Vertical Climb, Hovering.....	29
Figure3. 15 Mesh Scheme of Volume	30
Figure3. 16 Mesh Scheme on Symmetrical Plane	30
Figure3. 17 Mesh generation of full-scale model.....	31
Figure3. 18 Problem Solving Steps.....	37
Figure3. 19 (a) Simulation on UAV with Rotational Propeller; (b) Flow Patterns around UAV; (c) Contour of Turbulent Intensity of UAV.....	45
Figure3. 20 Profile of Dynamic Pressure of Wing and Horizontal Tail in Chordwise Coordinate at Different Angle of Attack.....	46
Figure3. 21(a) High Pressure Difference Zone; (b) Profile of Dynamic Pressure of Tail in Chordwise Coordinate	47
Figure3. 22(a) Profile of Dynamic Pressure of Trail Part of Tail in Spanwise Coordinate;(b) Profile of Dynamic Pressure of Control Surface in Spanwise Coordinate	48

Figure3. 23 Dynamic Pressure on Surfaces of UAV Components (wings, tails, duct and fuselage) at Different Angles of Attack	49
Figure3. 24 Lift, Drag and Pitching Moment Coefficients versus Angle of Attack From 0 to 20 Degree at $\beta=0$ and $\delta e=0$ at Mach 0.12; Side Force Coefficients versus Sideslip Angle of Attack from 0 to 20 Degree at $\alpha=0$ and $\delta r=0$ at Mach 0.12.....	51
Figure3. 25 Longitudinal and Lateral Stability and Control Predictions	52
Figure3. 26 Flow Pass through UAV at Large Angle of Attack from 20 to 50 Degree.	53
Figure3. 27 Lift, Drag and Pitching Moment Coefficients versus Angle of Attack From 20 to 90 Degree at $\beta=0$ and $\delta e=0$ at Mach 0.12.....	55
Figure3. 28 Crosswind Act on UAV at 90 Degree Angle of Attack	56
Figure4. 1 6x4 3-Blade Series Propeller.....	58
Figure4. 2 Himark Out-runner Brushless Motor	59
Figure4. 3 EK2-0907 Servo Tester/Adjuster.....	60
Figure4. 4 Speed Controller.....	61
Figure4. 5 Description of Flowchart of Propulsion System.....	62
Figure4. 6 Using Load Cell to Test Thrust.....	63
Figure4. 7 Data of Thrust in Different Voltage	63
Figure4. 8 Rapid Prototype Machine (RPM)	64
Figure4. 9 Principle of RPM Working	65
Figure4. 10 UAV Model Assembled with Propulsion System.....	66
Figure4. 11 Flow Patterns	66
Figure4. 12 Layout of RMIT Industrial Wind Tunnel.....	67
Figure4. 13 Building up UAV Model in Test Section	68
Figure4. 14 JR-3 Six Components Load Cell	68
Figure4. 15 Propeller Torque Test in Counter-rotating	70
Figure4. 16 UAV Test without Wings	71
Figure4. 17 Forces and Moments on UAV in Wind Tunnel.....	71
Figure4. 18 Aerodynamic Coefficients versus AOA of UAV with different thrusts at 10km/h	73
Figure4. 19 Aerodynamic Coefficients versus AOA of UAV with different thrusts at 35km/h	74
Figure4. 20 Aerodynamic Coefficients versus AOA of UAV with different thrusts at 70km/h	75
Figure4. 21 UAV Test with Wings.....	76
Figure4. 22 Aerodynamic Coefficients versus AOA of UAV with wings and different thrusts at 10km/h.....	78
Figure4. 23 Aerodynamic Coefficients versus AOA of UAV with wings and different thrusts at 35km/h.....	79
Figure4. 24 Aerodynamic Coefficients versus AOA of UAV with wings and different thrusts at 70km/h.....	80
Figure4. 25 Aerodynamic Coefficients relate to Deflection of Control Surfaces	81
Figure4. 26 Lift versus Deflection of Elevator	82
Figure4. 27 Pitching Moment versus Deflection of Elevator	83
Figure4. 28 Side force versus Deflection of Rudder.....	85
Figure4. 29 Yawing Moment versus Deflection of Rudder.....	86
Figure4. 30 Rolling Moment versus Deflection of Control Surface.....	87
Figure4. 31 Crosswind Effect Testing in Wind Tunnel	88

Figure4. 32 Ram Drag and Moment versus Thrust at different velocities of Crosswind	89
Figure4. 33 CFD Results and Wind Tunnel Data.....	91
Figure5. 1 Slipstream and Angular Velocities on UAV	93
Figure5. 2 p, q and r are acting on Four Control Surfaces	93
Figure5. 3 Slipstream Angles of Four Tails.....	96
Figure5. 4 Longitudinal Forces and Moments on UAV	97
Figure5. 5 Lateral Forces and Moments on UAV	99
Figure5. 6 Rolling Moment on UAV.....	100
Figure5. 7 Relationships between Earth-Axes and Body-Axes Coordinate System.....	104
Figure5. 8 Relationships between Earth-Axes and Wind-Axes Coordinate System	105
Figure5. 9 Relationships between Wind-Axes and Body-Axes Coordinate System	107
Figure5. 10 Body-Fixed Frame and Earth-Inertial Space.....	108
Figure6. 1 Feedback Closed-loop of a Control System.....	127
Figure6. 2 MIMO Control Systems.....	128
Figure6. 3 Attitude Control Outputs Response to Inputs.....	133
Figure6. 4 Thrust Control Outputs Response to Inputs.....	135
Figure6. 5 MIMO Control Laws Linked with Flight-simulator in MATLAB.....	136
Figure6. 6 Description of UAV Mission.....	136
Figure6. 7 Trajectory of UAV Mission	137
Figure6. 8 Signal Input of UAV Mission	139
Figure6. 9 Signal Output of UAV Mission	143
Figure6. 10 Description of UAV Hovering in Crosswind.....	145
Figure6. 11 Trajectory of UAV Hovering in Crosswind.....	146
Figure6. 12 Signal Input of UAV Hovering in Crosswind	147
Figure6. 13 Signal Output of UAV Hovering in Crosswind	151
Figure6. 14 Coupled Nonlinear 6 DoF Dynamic Model of Ducted Fan UAV	152
Figure6. 15 Longitudinal Forces and Moments	153
Figure6. 16 Lateral Forces and Moments.....	154
Figure6. 17 From Quaternion to Euler Angles.....	155
Figure6. 18 Flight Environment of Ducted Fan UAV	156
Figure6. 19 UAV Model in V-Realm Builder Environment.....	157
Figure6. 20 Combine V-Realm Builder and MATLAB by Virtual Reality Toolbox	157
Figure6. 21 Description of Longitudinal Flight Maneuver	158
Figure6. 22 Trajectory of Longitudinal Flight Maneuver.....	159
Figure6. 23 Position Tracks of UAV during Flight.....	160
Figure6. 24 Attitude Variation along Trajectory	161
Figure6. 25 Pitch Rate and Angle of Attack in Real-Time Response to Elevator Input δ_e deflection of 1 deg.....	162

List of Tables

Table. 1 Principal design characteristics	7
Table. 2 Mesh Type and Data	31
Table. 3 Properties of Grids and Boundaries	32
Table. 4 Values of Constants in standard $k - \varepsilon$ model.....	34
Table. 5 Values of Constants in realizable $k - \varepsilon$ model	36
Table. 6 Physical Model.....	37
Table. 7 Solver Formulation	38
Table. 8 Fluid Properties.....	38
Table. 9 Wall Boundary Conditions	39
Table. 10 Velocity Inlet Boundary Condition	39
Table. 11 Pressure Outlet Boundary Conditions.....	40
Table. 12 Fan Boundary Conditions	40
Table. 13 Set of Solution Controls	41
Table. 14 Forces and Moments Monitors	41
Table. 15 List of Values.....	42
Table. 16 Residual Monitor.....	42
Table. 17 Initialization of Solution	43
Table. 18 Aerodynamic Derivatives of Ducted Fan VTOL UAV.....	119
Table. 19 Dimensional Derivatives in Hovering and Low-speed Cruise Flight of UAV.....	124

Nomenclature

V_i	= Induce velocity
V_e	= Exit velocity of duct fan (slipstream velocity)
ρ	= Density of air
A_d	= Area of fan disk
A_e	= Area of duct exit
\dot{m}	= Flow rate of mass
λ	= Inflow ration
σ	= Rotor solidity ratio
C_T	= Thrust coefficient
V_∞	= Free flow
j	= Ratio of V_∞ and V_e , equal to V_∞ / V_e
α_{ps}	= Slipstream angle of attack
D_{ram}	= Ram drag
M_{ram}	= Ram pitching moment
S_d	= Span area of duct
AR_d	= Aspect ratio of duct
R_e	= Renolds number
μ	= Viscous coefficient
Γ	= Stress tensor
F	= Body force

τ	= Shear stress
k	= Kinetic
ε	= Dissipation
ϑ	= Velocity scale
ℓ	= Length scale
$\sigma_k, \sigma_\varepsilon$	= Prandtl numbers
μ_t	= Eddy viscosity
G_k	= Generation of kinetic energy
G_b	= Generation of turbulence kinetic energy
$\alpha_{s,p}, \beta_{s,p}$	= Slipstream angle
L	= Lift
D	= Drag
M	= Pitching moment
Y	= Side force
l	= Rolling moment
N	= Yawing moment
J	= Rotating inertia
Ω	= Rotating speed of motor
$C_{Dow}, C_{Dot}, C_{Dod}$	= Non-lift drag (wing, tail and duct) coefficients
$C_{L\alpha w}, C_{D\alpha t}, C_{D\alpha d}$	= Lift coefficients (wing, tail and duct) of derivative α
$C_{Y\beta t}, C_{Y\beta d}$	= Side force coefficients (tail and duct) of derivative β
$C_{L\delta a}, C_{D\delta a}$	= Force coefficients of derivative δa

$C_{L\delta e}, C_{D\delta e}$	= Force coefficients of derivative δe
$C_{Y\delta r}, C_{D\delta r}$	= Force coefficients of derivative δr
δa	= Deflection of aileron
δe	= Deflection of elevator
δr	= Deflection of rudder
ϕ, θ, ψ	= Euler angles (rolling, pitching, and yawing angle)
μ, γ, χ	= Speed rolling angle, climbing angle and tracking angle
α	= Angle of attack
β	= Sideslip angle
e_0, e_1, e_2, e_3	= Elements of quaternion
T_{\circlearrowleft}	= Thrust derivatives relate to ()
L_{\circlearrowleft}	= Lift derivatives relate to ()
D_{\circlearrowleft}	= Drag derivatives relate to ()
Y_{\circlearrowleft}	= Side force derivatives relate to ()
I_{\circlearrowleft}	= Rolling moment derivatives relate to ()
M_{\circlearrowleft}	= Pitching moment derivatives relate to ()
N_{\circlearrowleft}	= Yawing moment derivatives relate to ()
I_{xx}, I_{yy}, I_{zz}	= Moment of inertia
$X_{c,g}$	= Center of gravity
$X_{a.c}, Y_{a.c}, Z_{a.c}$	= Aerodynamic center (in coordinates of body-axes)

Chapter 1

1 Introduction

UAV is the abbreviation of Unmanned Aerial Vehicle which has been in existance since tens of years ago. Compared with manned aircraft UAV has the same ability as robotic aircraft that are computerized and autonomous without an on-board pilot by using a digital and electronic system, thus there is no risk of loss of life and is easier to maintain than manned aircraft. With the development of technology and requirements of industry, UAVs have matured enough for widespread use as they can be remote controlled or autonomously complete missions, not only in civil roles, but also in military operations such as reconnaissance for firefighting and natural disaster, suspect monitoring and strategy attack.

1.1 UAV's family

There are a huge number of UAV that are currently existing and used in different fields including fixed-wing and rotary-wing unmanned aircraft. The main advantage for an unmanned helicopter Fig.1.1(a) is the Vertical Take-off and Landing capability with no need for runways, whereas the unmanned aerial fixed-wing aircraft has high efficiency on longitudinal flight with a long distance mission displayed in Fig.1.1(e). In addition, the hybrid UAV has its own unique potential to be explored in the future such as bionic, flying-wing, and flapping-wing air vehicles as shown in Fig.1.1 (b) and (d).

However, in this paper the focus is Ducted Fan VTOL UAV which can not only vertically take off and land , but can also hover and be controlled due to the two counter rotors and four control surfaces (vanes) submerged in the slipstream flow from ducted fans in figure1.1(c).



(a) Unmanned Aerial Helicopter



(b) Unmanned Bionic Vehicle



(c) Ducted Fan UAV



(d) Flying-wing UAV



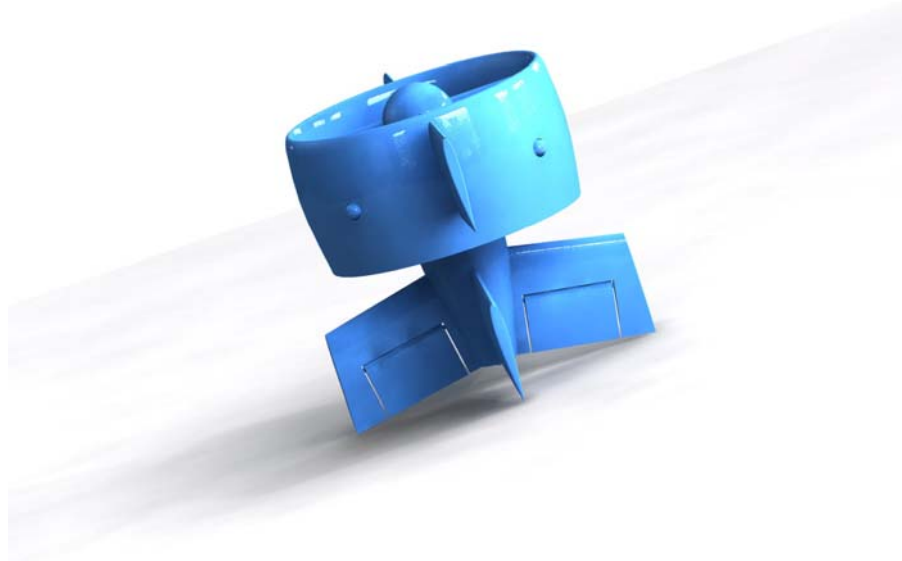
(e) Unmanned Fighter Vehicle

Figure1. 1 Different Prototypes of UAV

1.2 Technical Features

The School of Aerospace, Mechanical and Manufacturing Engineering at RMIT has been developing a new conceptual Ducted Fan VTOL UAV as shown in figure1.2 (a). The coaxial counter rotors

combined with fixed-wing as hybrid is an innovation of a ducted fan unmanned aerial vehicle (UAV) which is not only designed to take-off and land vertically, but can also hover as a helicopter.



(a) RMIT Ducted Fan VTOL UAV



(b) Honeywell Ducted Fan UAV



(c) Fantail UAV

Figure1. 2 Ducted Fan VTOL UAV

Moreover, in contrast to other Ducted Fan UAVs in figure 1.2 (b) and (c), the maneuver transition from vertical climb to horizontal flight is the unique technique of this Ducted Fan VTOL UAV in figure 1.2 (a). Making control surfaces fully submerged in the propeller slipstream from ducted fan is critical technology to successfully achieve longitudinal transition. The conventional aircraft can not achieve this transition because when they are climbing vertically at low speed, without big enough free flow over their elevators which control pitching attitude, naturally the longitudinal transition is not able to be fulfilled in conventional aircraft as well as the VTOL UAV. For this reason, the prediction of the propeller slipstream effects is critical to the successful simulating of the full-scale UAV aerodynamic characteristics.

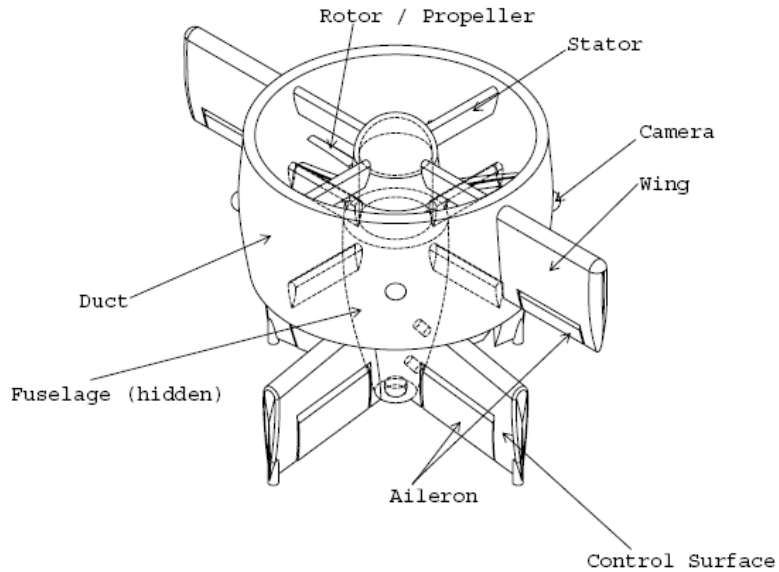


Figure1. 3 Configuration View of UAV (Ref. [56])

1.2.1 Counter-rotating Propeller

A twin counter-rotating propeller configuration is used to ensure this UAV hovering in the air without spinning torque like coaxial helicopter. The advantage is the wide angular range of the 360 degree view.

1.2.2 Duct

A duct known as a ring-wing or an annular wing of which the geometry is generated by revolving an airfoil cross section on an offset centre-line. It is not only the main lifting surface on a ducted fan aircraft but also the device of preventing propellers from damage.

1.2.3 Stators/Duct Supports

The horizontal and vertical Stators are not only used to connect ducted-fan with fuselage, but also used to rectify the turbulent flow as much as reducing the swirl velocity in order to ensure the control surfaces immersed in the exit flow (propeller slipstream) from duct.

1.2.4 Control Surfaces

Both rudders and elevators belong to control surfaces which are submerged in the propeller slipstream

are sufficient to enable attitude control even in low-speed flight and hovering. Compared with rotor-wing aircraft no complicated control devices such as cyclic pitch control systems for rotors are required for attitude control in low-speed vertical climb or horizontal flight.

1.2.5 Wings

Two wings with aileron attached to duct are the guarantees for achieving stable balance during the horizontal flight of this UAV, although the duct is able to supply lift, since it is not sure whether this is sufficient.

1.3 Literature Review

With the appearance of wing flaps in new types of configuration, the technique of the deflected-slipstream V/STOL is developed and optimized for turning the slipstream of propellers downward, so as to ensure the high speed slipstream flowing through flaps with sufficient magnitude lift created. See Figure 1.4 below.

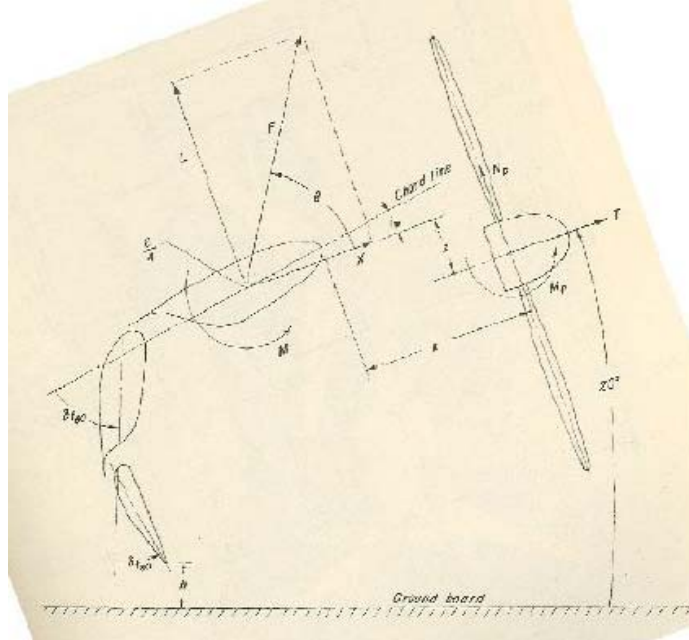


Figure1. 4 Schematic Diagram of Deflected Slipstream VTOL Principle (Ref. [8])

Most approaches to VTOL technology were innovated during NACA's golden years. The deflected propeller slipstream approach is one of the best ways to achieve VTOL (see Ref. [8]). For this purpose, government support and provide funding for technology, meanwhile many technical researchers and scientists have been concentrating on it with increased effort. However, only several prototype aircraft are achieved for use of the technology of vertical taking-off and landing. The history of deflected slipstream VTOL is the story of the invention of high-lift wing/propeller systems.

In this UAV project, the slipstream approach is still applied as the innovation, but it is no longer only

for generating sufficient lift on tails, it is also for fulfilling the transition from vertical climb or hovering to horizontal flight. Therefore, this technology is improved and applied in the Ducted Fan VTOL UAV.

1.3.1 Requirements of Design

In the preliminary design, some basic requirement guidelines for this UAV are shown in flow chart (figure.1.5).

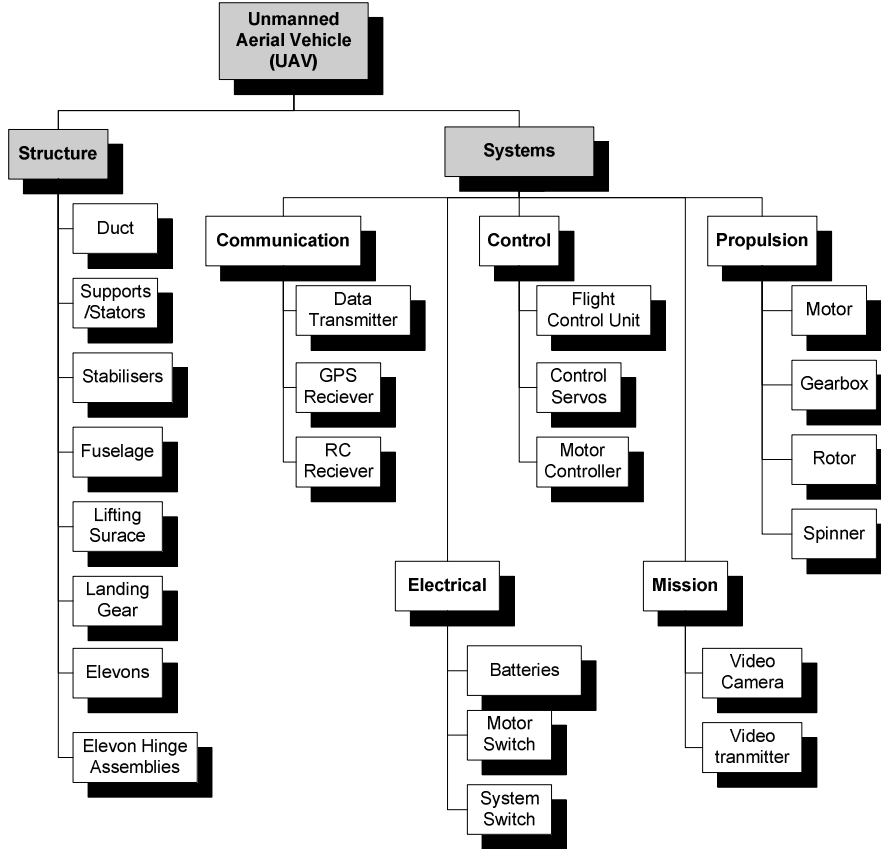


Figure1. 5 Flow Chart of UAV Design (Ref. [18])

The aerodynamic characteristics of the UAV in Ref. [56], are shown in Tab.1. To satisfy the portability aspect of the mission, the UAV should have two fans which diameter no more than 0.3m. For transport and performance reasons, the maximum weight of the UAV is 0.3kg. The total weight of all equipment needed to operate the system in the field shouldn't exceed 0.4kg.

Table. 1 Principal design characteristics

Characteristic	Value
Diameter of duct, m	0.168
Weight of UAV, kg	0.4
Cruise speed, m/s	20
Minimum climb speed, m/s	2
Maximum Thrust, N	4.6
Density of air, kg/m ³	1.225
Viscous coefficient, kg/ms	1.7894x10 ⁻⁵
Ambient pressure, kPa	101.3

More attention should be paid to the flight performance, after all it determines the value of use and how the UAV is able to be operated. As shown in figure 1.6, the total lift consists of four parts: lift from wing, ducted fan, body and tail respectively. Because the lift of the body is very small, it is ignored here. The main contributions of lift are from the wing, ducted fan and tail. According to Classical Thin Airfoil Theory, the lift of the wing and tail can easily be calculated. However, the lift and induced drag of the duct are unknown. The lift of the duct generates a pitching moment as a result, the characteristics of the ducted fan become an important part of the longitudinal aerodynamic parameters. The lift of the tail generates further contribution to the pitching moment.

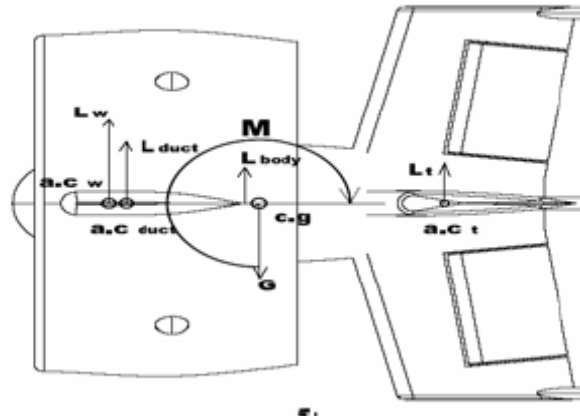


Figure1. 6 Definition of Lift and Pitching Moment (Ref. [56])

1.3.2 Challenge of Aerodynamic Model

Traditionally, wind tunnels have been used to analyse the aerodynamic characteristics of aircraft in various flow regimes. However, sometimes wind tunnel test is difficult to accurately predict the aerodynamic characteristic of some special aircraft. Thus, the CFD method is also used to predict aerodynamic characteristics which can be compared with wind tunnel results and modify the model.

Take the UAV for an example, when the free stream flows over the UAV, it is separated into two parts flow. One part is external flow around the entire body of the UAV, the other part is internal flow which pass through the ducted fan and flow transition from laminar to turbulent is created ,due to the rotating fans, with pressure jump and swirl velocity. Obviously, the tails and control surfaces are totally submerged in the slipstream (turbulent flow). Relying on extra pitching moment generated by slipstream velocity we can achieve the maneuvre transition from vertical climb to horizontal flight, which is the key innovation of the new concept UAV. So, how to get all of essential aerodynamic coefficients for building up a dynamic model is the most difficult point in this project. Both the CFD method and wind tunnel tests have to be used to resolve the challenge.

Chapter 2

2 Aerodynamic Theory of Ducted Fan

In recent years, more and more aircraft researchers and designers are interested in the use of ducted fans for propulsion of some special air vehicles which can achieve vertical taking-off and landing. Compared with open propellers, ducted fan has its own advantages in several technical fields. Such as: fewer design compromises are required; the effective range of the ducted fan is larger than its physical range; most of the noise is absorbed because of enclosing the propeller in a duct. Therefore the technology of ducted fan as propulsion system is widespread in use of low speed VTOL aircraft and air-cushion vehicles.

2.1 Background

Bernoulli's equation is a statement of Newton's law for an inviscid incompressible flow with no body force, which was not only derived from the momentum equation, but also derived from a general equation. Hence, an application of the Bernoulli's equation is in considering how the energy is changed with flow through a duct, such as that sketched in Fig.2.1.

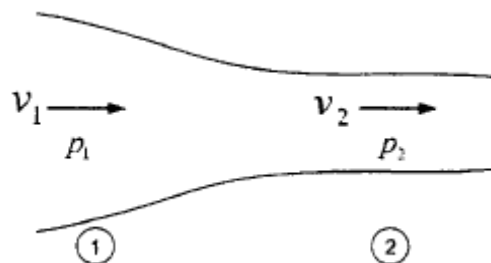


Figure2. 1 Flow in a Duct (Ref. [39])

$$p_1 + \frac{1}{2} \rho V_1^2 = p_2 + \frac{1}{2} \rho V_2^2 \quad (2.1)$$

Equation (2.1) is the Bernoulli's equation (see Refer. [4]), which describes the conservation of energy.

p_1 and $\frac{1}{2} \rho V_1^2$ is static pressure and dynamic pressure in the point 1, respectively. p_2 and $\frac{1}{2} \rho V_2^2$

represent point 2's static and dynamic pressure. It means that static pressure plus dynamic pressure of every point is equal to constant value in the case of inviscid and incompressible flow pass through a duct or a tube.

2.1.1 Slipstream Theory of Ducted Fan

To analyze the slipstream through the ducted fan of this UAV, the simplified model is shown as figure2.2. Based on Bernoulli's equation the slipstream theory can be expressed as below (see Refer. [39]): The spinning range of two fans in the duct are seen as the two disks area, the thrust produced

can be obtained as the product of the pressure distribution over the disk area. Bernoulli's equation is able to be applied for region 0 to 1, 2 to 3, and 4 to 5 in figure.2.2. but can not be applied for region 1 to 2, and 3 to 4 due to

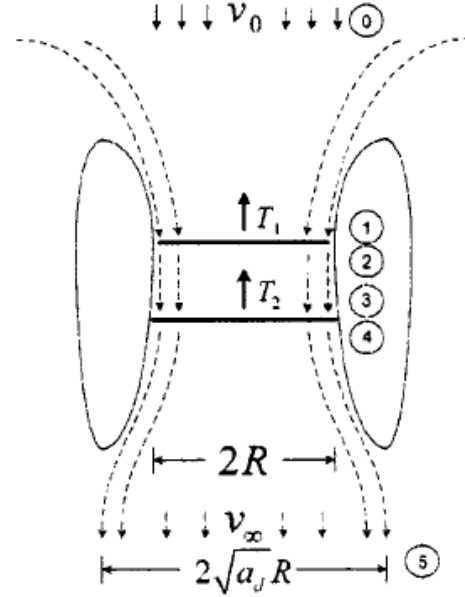


Figure2. 2 Flow through the Counter-Rotating Fans Inner of a Duct (Ref. [39])

the propeller adding some energy to the slipstream, as a result the total energy is no longer conserved as well as before, however the density of air is constant because of incompressible flow. Therefore, region 0 to 1, 2 to 3, and 4 to 5 can be analyzed using Bernoulli's equation that has led to

$$p_0 + \frac{1}{2} \rho V_0^2 = p_1 + \frac{1}{2} \rho V_1^2 \quad (2.2)$$

$$p_2 + \frac{1}{2} \rho V_2^2 = p_3 + \frac{1}{2} \rho V_3^2 \quad (2.3)$$

$$p_4 + \frac{1}{2} \rho V_4^2 = p_5 + \frac{1}{2} \rho V_5^2 \quad (2.4)$$

Although between region 1 and 2, 3 and 4 the Bernoulli's equation is not available, the mass conservation is still available with no mass lost as the flow through the two disks. Meanwhile, care should be taken on whether the velocity is changed, increased or decreased.

An expression of mass flow rate in region 1 and 2 is given by

$$\dot{m}_1 = \rho V_1 A_1 \quad (2.5)$$

$$\dot{m}_2 = \rho V_2 A_2 \quad (2.6)$$

Since both A_1 and A_2 are equal to area of disk1, and $\dot{m}_1 = \dot{m}_2$ in terms of the thin disk theory [31]. Then we get,

$$\rho V_1 A_1 = \rho V_2 A_2 \quad (2.7)$$

$$V_1 = V_2 = V_0 + V_i \quad (2.8)$$

The same as Eq (2.8),

$$V_3 = V_4 = V_0 + V_i \quad (2.9)$$

Thus, from region 1 to 4, the velocities are the same as V_i called induced velocity of propeller. We also

find $V_5 = V_0 + V_e$ which is the exit velocity of the ducted fan. And region 5 is in open zone, thus $p_5 = p_0$. Then, substituting Eq. (2.8) into Eq. (2.2), (2.3) and (2.4), we obtain,

$$p_0 + \frac{1}{2} \rho V_0^2 = p_1 + \frac{1}{2} \rho (V_0 + V_i)^2 \quad (2.10)$$

$$p_2 + \frac{1}{2} \rho (V_0 + V_i)^2 = p_3 + \frac{1}{2} \rho (V_0 + V_i)^2 \quad (2.11)$$

$$p_4 + \frac{1}{2} \rho (V_0 + V_i)^2 = p_0 + \frac{1}{2} \rho (V_0 + V_e)^2 \quad (2.12)$$

T_1 and T_2 are the thrust of rotor1 and rotor2, respectively. They are generated from pressure differences between region 1 and 2, 3 and 4.

$$T_1 = (p_2 - p_1)A_d \quad (2.13)$$

$$T_2 = (p_4 - p_3)A_d \quad (2.14)$$

From Eq(2.11), because the velocity of airflow between two rotors is the same, there is no pressure jump up or down between p_2 and p_3 . The total thrust of two rotors is calculate by combining Eq.(2.10), (2.11), (2.12), (2.13) and (2.14).

$$T_{rotor} = T_1 + T_2 = (p_2 - p_1 + p_4 - p_3)A_d = \frac{1}{2} \rho V_e (V_e + 2V_0)A_d \quad (2.15)$$

Using the quadratic formula to solve Eq.(2.15), the exit velocity is given by,

$$V_e = -V_0 + \sqrt{V_0^2 + \frac{2T_{rotor}}{\rho A_d}} \quad (2.16)$$

If in the case of hovering, the $V_0=0$, Eq.(2.16) is simplified as,

$$V_e = \sqrt{\frac{2T_{rotor}}{\rho A_d}} \quad (2.17)$$

It should also be pointed out that it can instruct the designer to optimize the diameter of ducted fans. According to expression of mass flow rate, we can obtain,

$$\dot{m} = \rho (V_0 + V_i)A_d = \rho (V_0 + V_e)A_e \quad (2.18)$$

Since in hovering state $V_0=0$, V_e and A_d are known, we get,

$$\frac{A_e}{A_d} = \frac{V_i}{V_e} \quad (2.19)$$

By analysis of Eq.(2.19), it is easy for us to find the relationship between V_i and A_e , as long as one of them is known, the other one certainly can be obtained. This method is applied to optimize the size and quality of ducted fan, especially in hovering of UAV.

2.1.2 Element Theory of Rotor Blades

The element theory of rotor blades (in Ref. [31]) is defined as the blade divided into an infinite micro-blade, analyzing aerodynamic force and moment of each micro-blade and discovering the relationship among geometry speciality, motion and aerodynamic characteristics. Then, by integrating every blade and entire rotor, the total thrust and power can be calculated.

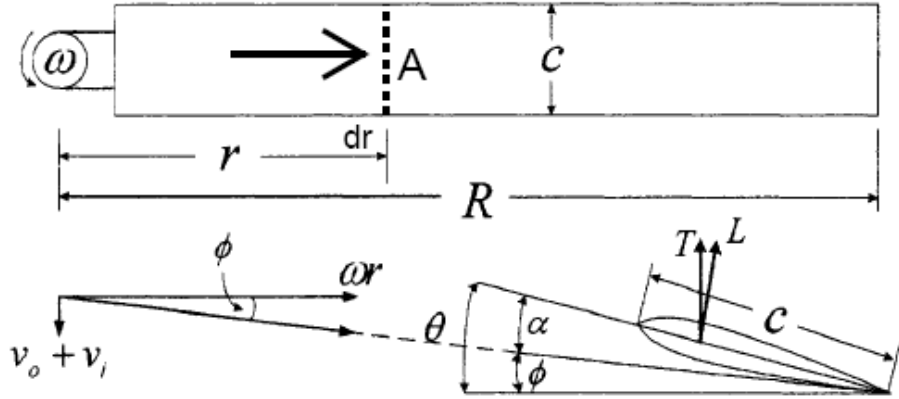


Figure2. 3 Aerodynamic Analysis of Blade Element (Ref. [39])

The figure 2.3 shows that a airfoil A of blade at radius r is viewed from left side. It has a blade pitch θ and chord c . From left below of this figure, the illustration shows the airflow across blade consists of two components. One is the local blade velocity ωr , the other one is downwash velocity which is perpendicular to blade includes induce velocity V_i and velocity of free-flow V_0 .

Here assumption is made as $V_0 + V_i \gg \omega r$, then we can get the expression of downwash angle ϕ ,

$$\tan \phi = \frac{V_0 + V_i}{\omega r} \approx \phi \quad (2.20)$$

Hence, the angle of attack α is able to be obtained,

$$\alpha = \theta - \phi \quad (2.21)$$

A dimensionless quantity is called inflow ratio given by,

$$\lambda = \frac{V_0 + V_i}{\omega R} \quad (2.22)$$

Using another formula describe inflow ratio like this,

$$\lambda = \frac{V_0 + V_i}{\omega r} \frac{r}{R} = \phi x \quad (2.23)$$

X is the ratio of local radius r to total radius R .

Before extrapolating the thrust created by one blade, the lift of micro-blade has to be listed. dr is the width of micro-blade, then the its area is given by,

$$ds = cdr \quad (2.24)$$

And lift of micro-blade is expressed,

$$dL = \frac{1}{2} \rho (\omega r)^2 Cl ds = \frac{1}{2} \rho (\omega r)^2 Cl c dr \quad (2.25)$$

By Eq.(2.25), a dimensionless coefficient is obtained,

$$dC_T = \frac{dL}{\frac{1}{2} \rho A_d (\omega R)^2} = Cl \frac{cR}{A_d} \frac{r^2}{R^2} \frac{1}{R} dr \quad (2.26)$$

The rotor solidity ratio σ is the ratio of the area of one blade to the rotor disk area,

$$\sigma = \frac{cR}{A_d} \quad (2.27)$$

Substituting Eq.(2.27) into Eq.(2.26), and use x to replace $\frac{r}{R}$, dx replaces $\frac{dr}{R}$, we get,

$$dC_T = \sigma Cl x^2 dx \quad (2.28)$$

The total thrust of one blade is equal to the airfoil lift integrated along with blade span, and airfoil lift is dependant on the its own angle of attack which depends on the local blade pitch θ , and inflow ratio λ . In this ducted fan UAV, the twisted blades are applied, so the local blade pitch is described using a linear approximation equation (Ref. [31]),

$$\theta = \theta_{75} + (x - 0.75)\theta_r \quad (2.29)$$

θ_r is the constant rate of twist per unit rotor length, whereas θ_{75} is the value of the blade pitch at 75 percent of the rotor radius R. A symmetric airfoil is used in this rotor blade, the airfoil lift coefficient is shown by,

$$Cl = a(\theta - \phi) = a[\theta_{75} + (x - 0.75)\theta_r - \frac{\lambda}{x}] \quad (2.30)$$

Combining Eq.(2.30) and Eq.(2.28), we obtain,

$$dC_T = \sigma a[\theta_{75} + (x - 0.75)\theta_r - \frac{\lambda}{x}]x^2 dx \quad (2.31)$$

$$C_T = \int_0^1 dC_T = \int_0^1 \sigma a[\theta_{75} + (x - 0.75)\theta_r - \frac{\lambda}{x}]x^2 dx = \sigma a(\frac{\theta_{75}}{3} - \frac{V_0 + V_i}{2\omega R}) \quad (2.32)$$

According to Eq.(2.32) and definition of thrust, the thrust one blade is obtained,

$$T = \frac{1}{2} C_T \rho (\omega R)^2 A_d = \frac{1}{2} \sigma a(\frac{\theta_{75}}{3} - \frac{V_0 + V_i}{2\omega R}) \rho (\omega R)^2 A_d \quad (2.34)$$

Once thrust of one blade is calculated, the total thrust of rotors also can be obtained in the way of sum of all blades. And if the thrust is decided, the fans or rotors are able to be designed by optimizing the right parameters of Eq.(2.34).

2.1.3 Propeller Slipstream Effect

Take this UAV for example, a view of section from the ducted fan as show in Fig.2.4. As the control surfaces are fully submerged in the propeller slipstream, the local flow conditions behind the ducted fan are very different from the external flow and become a function of the power setting [39].

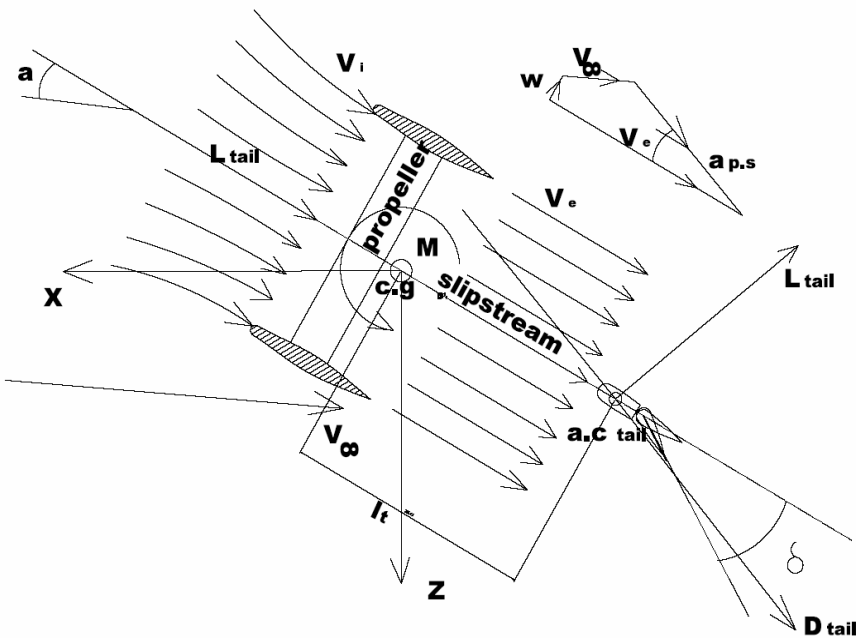


Figure2. 4 Velocity Vectors Composition and Definition of α_{ps}

In the following analysis some assumptions have been made [56]:

- 1) The control surfaces are fully submerged in the propeller exhaust flow.
- 2) V_e is the exit induced velocity of duct (slipstream velocity) and V_e vector is parallel with symmetrical axis of UAV body as shown in figure.2.4, w is the normal velocity which is perpendicular with V_e , and $V_e \gg w$.
- 3) The flow at the control surfaces is smooth and uniform.

Analyzing the case of vertical climb, the exit induced velocity of the duct V_e can be obtained from Eq.(2.16).Hence,

$$V_e = -V_0 + \sqrt{V_0^2 + \frac{2T_{rotor}}{\rho A_d}} \quad (2.35)$$

T_{rotor} is the thrust force from engine, and A_d is the area of the fans disk. From the Fig.2.4, we know that the forces acting on the tail consist of the lift, drag and pitching moment. Thus the lift is perpendicular to the total vector velocity V_{total} which is the function of other velocity vectors, such as, V_e , V_∞ and w . So the slipstream angle of attack α_{ps} is generated as following function:

$$\alpha_{ps} = f(V_e, V_\infty, w) \quad (2.36)$$

To analyze Eq.(2.36), we should get the description of w which is equivalent to,

$$w = q(x_{a.c-tail} - x_{c.g}) \quad (2.37)$$

According to vectors composed in figure.2.4 we extrapolate,

$$\tan \alpha_{p.s} = \frac{q(x_{a.c-tail} - x_{c.g}) + V_\infty \sin \alpha}{V_e + V_\infty \cos \alpha} \quad (2.38)$$

$x_{a.c-tail}$ is aerodynamic centre of tail, $x_{c.g}$ is the centre of gravity, q is velocity of pitch rotating.

$\tan \alpha_{p.s} \approx \alpha_{p.s}$ because of $V_e \gg w$, and we make $V_\infty / V_e = j$ which is the velocity parameters, then we can get,

$$\alpha_{p.s} = \frac{\frac{q}{V_e}(x_{a.c-tail} - x_{c.g}) + j \sin \alpha}{1 + j \cos \alpha} \quad (2.39)$$

Because $V_e \gg w$, q/V_e is approximately equal to zero, thus

$$\alpha_{p.s} = \frac{\sin \alpha}{\frac{1}{j} + \cos \alpha} \quad (2.40)$$

For small angles of attack, the lift and moment forces of the tail will be proportion to the slipstream angle of attack $\alpha_{p.s}$ and the deflection of control surface δ_e :

$$C_{L.t} = C_{L_{\alpha.t}} \alpha_{p.s} + C_{L_{\delta_e}} \delta_e \quad (2.41)$$

$$C_{m.t} = C_{m_{\alpha.t}} \alpha_{p.s} + C_{m_{\delta_e}} \delta_e \quad (2.42)$$

At present, we temporarily don't consider the lift contribution of deflection of control surface, just making $\delta_e = 0$, substituting Eq.(2.40) into Eq.(2.41) and Eq.(2.42), then we can simplify the final

equations of C_L and C_m of tail as below:

$$C_{L.t} = C_{L_{\alpha.t}} \alpha_{p.s} = C_{L_{\alpha.t}} \frac{\sin \alpha}{\frac{1}{j} + \cos \alpha} \quad (2.43)$$

$$C_{m.t} = C_{m_{\alpha.t}} \alpha_{p.s} = C_{m_{\alpha.t}} \frac{\sin \alpha}{\frac{1}{j} + \cos \alpha} \quad (2.44)$$

The Eq.(2.40) explain why $\alpha_{p.s}$ is smaller α . Therefore, we can get an important conclusion:

although α arrives at a high value even at stall angle of attack, the $\alpha_{p,s}$ still doesn't arrive at the value of stall angle.

2.1.4 Crosswind Effect on Ducted Fan

The longitudinal coordinate systems of duct, forces and moments acting on duct are shown in Fig.2.5. Normally, when a ducted fan UAV is hovering in unsteady crosswind, the state of hovering is difficult to maintain without extra control (see Ref. [17] and [32]). If it is desirable that transition from hovering to horizontal flight will be achieved, the counter pitch moment caused by ram drag has to be overcome.

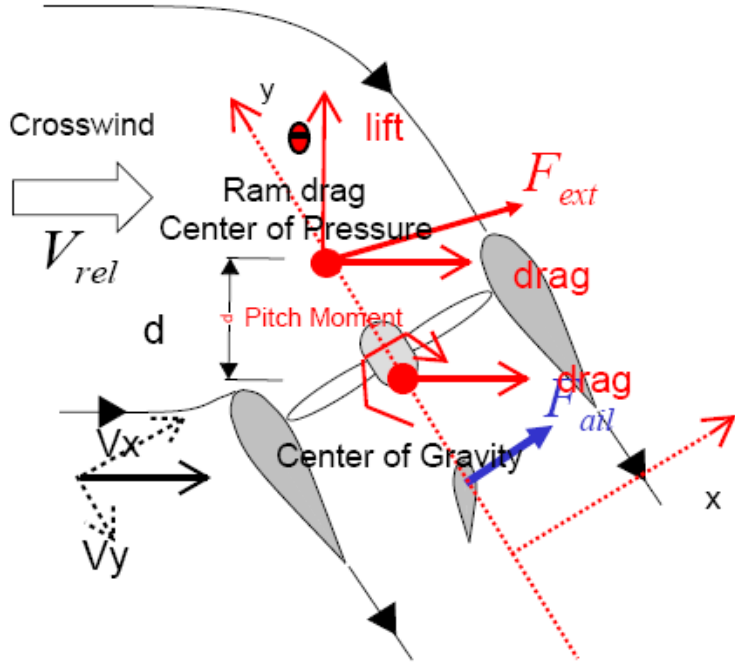


Figure2. 5 Sketch of Duct Ram Drag Forces Acting at UAV Center of Gravity

The total lift generated by a ducted fan can be divided into two components, one component of lift is due to the thrust of fans, the other one is due to the lift of duct. However, in the case of hovering, θ is zero. So the total lift is equal to the momentum flux through the duct given by,

$$L = -F_y = \rho A_e V_e^2 \quad (2.45)$$

In Eq.(2.45), the exit flow from duct is assumed as uniform flow. Because of the large contribution from crosswind momentum, a ram drag is also generated. The expression of ram drag is given by,

$$D_{ram} = F_x = \dot{m}_{duct} V_x \quad (2.46)$$

\dot{m}_{duct} is the momentum flux, in terms of mass flow through duct, it yields,

$$\dot{m}_{duct} = \rho A_e V_e \quad (2.47)$$

Substituting Eq.(2.47) into Eq.(2.46), the ram drag is,

$$D_{ram} = \rho A_e V_e V_x \quad (2.48)$$

In order to counteract this big ram drag, a big enough tilt angle of attack are required to generate the counter drag, meanwhile the stability of UAV becomes a function of pitching rate. To generate the required tilt angle, a force in the same direction as the ram drag should be created on the control surface and tails. With the ram drag generated, a nose-up duct pitch moment is created due to the ram drag center of pressure being outside of the duct and away from center of gravity of the ducted fan. The distance between center of pressure and center of gravity is d (shown in Fig.2.6) of which position is difficult to be measured and depends on several gradients, such as velocity of crosswind, induce velocity of ducted fan, dynamic pressure of flow and so on.

The ram drag pitch moment is given by,

$$M_{ram} = d \times D_{ram} \quad (2.49)$$

Hence, the nose-up pitch moment of duct is also called ram drag pitch moment which has led to two negative capabilities to ducted fan UAV. The first one is difficulty maintaining a stable position in turbulent crosswind or gust wind, because the ram drag pitch moment will tend to tilt the UAV in a random direction. The second one is difficulty in achieving pitching control, in particular to fulfill transition from vertical climb to horizontal flight due to the counter ram drag pitch moment.

Chapter 3

3 Computational Fluid Dynamics (CFD) Analysis

Computational Fluid Dynamics (CFD) is one of the most popular numerical approaches for predicting the external flow around different kinds of vehicles and analyzing the internal flow through many types of tube or duct. For instance, in aerospace engineering the use of CFD is quite frequent as a wind tunnel simulation tool during the preliminary design of aircraft and following analysis of aerodynamic coefficients. Once the numerical results are calculated by the CFD code, further work in wind tunnel test can be performed and compared with CFD data. Normally, CAD software is essential to build up a 3D solid model in preliminary design, it is also easy to be imported into CFD tool. After running simulation in CFD codes the 3D model is able to be modified back to CAD software. Thus repeating this cycle between CAD and CFD can not only optimize design but also save time and costs.

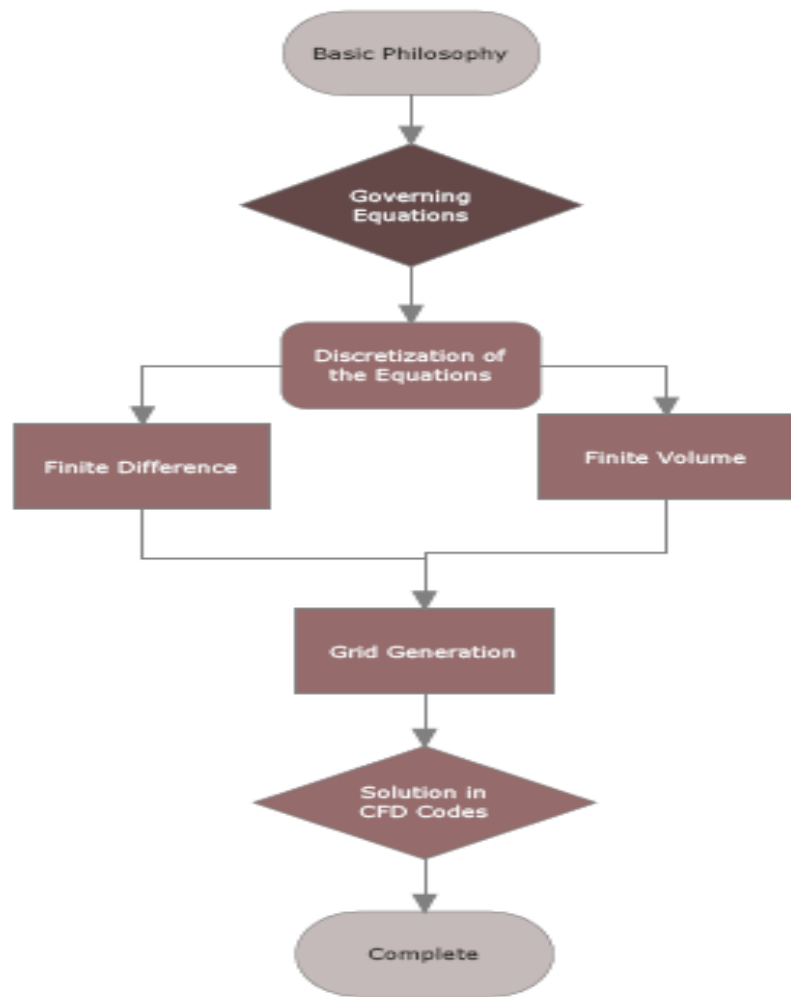


Figure3. 1 Basic Flow Chart of CFD Methodology

3.1 Introduction

As the first and most important step of this project, the aerodynamic design and analysis of a VTOL ducted-fan UAV is detailed in this chapter. Computational fluid dynamics was used to evaluate the aerodynamic coefficients and to analyze the flow patterns around the vehicle at different speeds and angles of attack. The interaction between the fan flow and duct causes complex flow structures depending on the flight condition. To evaluate the aerodynamic characteristics of the duct, two analytical models were used: a 2D model to access the flow patterns surrounding the duct in climb, cruise and hover respectively, whereas the 3D model calculates the aerodynamic coefficients of duct. The full-scale model of UAV with ducted fan rotating is also simulated using computational fluid dynamics approach. By simulating tails and control surfaces totally submerged in the propeller slipstream, the aerodynamic characteristic of tails and control surfaces are to be revealed. Computational fluid dynamics was also used to predict the longitudinal and lateral stability and control characteristics of a full-scale model of ducted fan VTOL UAV at both vertical and horizontal flight without any prior knowledge of existing wind tunnel or flight test data. The longitudinal stability and control characteristics of the UAV were evaluated using different horizontal tail deflections and different velocity of slipstream which exits from ducted fan and passes through horizontal tails (control surface). The lateral stability and control characteristics of the UAV were evaluated using several different sideslip angles at low Mach numbers.

3.2 The Governing Equations of CFD

All of the CFD methods are based on the fundamental governing equations of fluid dynamics, such as the continuity, momentum, and energy equations which are the mathematical statements of three physical principles: Law of Mass Conservation, Newton's Second Law, and Law of Energy Conservation. The governing equations are able to be obtained in different formats. There is little difference between these equations for aerodynamic theory, but for some given algorithm in CFD, the selection of the governing equations is very important due to use of different equations which lead to different results. Some of these may be accurate results, some are incorrect results and even instability or divergence. Therefore, care should be taken to ensure the right governing equation is used to solve the practical problem during the CFD process. .

3.2.1 Navier-Stokes Equations for Viscous Flow

Viscous flow includes the transportation phenomena of friction, thermal conduction or mass diffusion. Usually, the momentum equations for a viscous flow were identified as the Navier-Stokes equation due to historical experience. Therefore, in the CFD literature, a “Novier-Stokes solution” simply means a solution of a viscous flow problem using the full governing equations.

3.2.2 Euler Equations for Inviscid Flow

Compared with viscous flow, inviscid flow has totally different characteristics. In inviscid flow the

transport phenomena of viscosity, mass diffusion, and thermal conductivity are ignored. The momentum equations for inviscid flow were identified as the Euler equation. Historically, Euler derived the continuity and momentum equations in 1753; but he didn't consider how to derive the energy equation. Thus, only the continuity and momentum equations could be defined as the Euler equation which is used to resolve an inviscid flow problem.

3.3 Discretization

The word “discretization” is difficult to be found in the most popular dictionaries of today due it being unique to the literature of numerical analysis and first being introduced on partial equations in a classic book related to CFD. In essence, it is the process of solving a differential or integral equation which is assumed as including an infinite continuum of values throughout some domain. By discretization the partial differential equations can be replaced by some algebraic equations that are resolved for the value of the flow-field variables at the discrete grid points (see figure 3.1), then the partial differential equations have been discretized. This method of discretization is called the method of finite differences which is widely applied in CFD domain. .

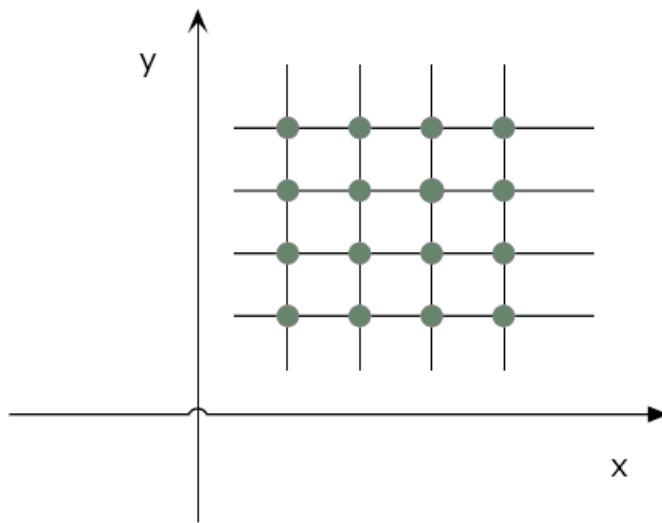


Figure3. 2 Discrete Grid Points

3.4 Technology of Grid Generation

The finite-difference approach discussed in discretization requires calculations that are solved in some discrete grid points. The flow-field is divided into lots of small space by discrete points throughout them, the small spaces are named grids. The proper grids for the flow-field over a given geometry shape is very important for the numerical results of CFD solution. The process of grid determining is called grid generation or mesh generation.

CFD methods for complex geometry shapes or solids are divided into two groups: (1) Structured grid arrangements; (2) Unstructured grid arrangements. The selection of grid arrangement is based on the specific problem which is a simple or complex shape.

3.4.1 Structured Grid Scheme

To analyze the flow field through an aerofoil, the structured body-fitted grids are always applied, in particular to deal with curved boundary flows around aerofoil. Two main structured grid scheme are shown as below.

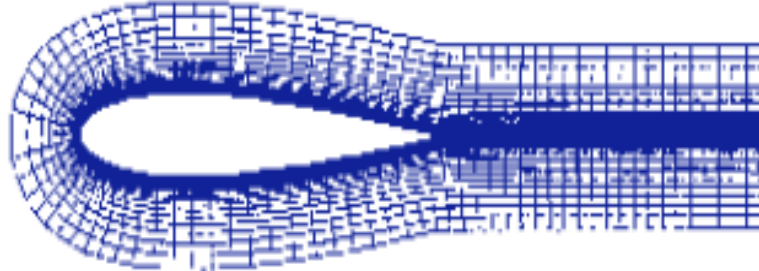


Figure3. 3 An Example of C-type Body-fitted Mesh around an Aerofoil (Ref. [36])

This type of configuration is often called a C-type because of the shape of grids' profile viewed as the letter 'C'.

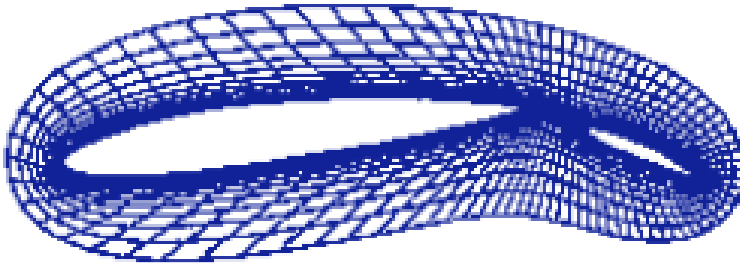


Figure3. 4 An Example of O-type Body-fitted Mesh around an Aerofoil (Ref. [36])

Compared with C-type grids scheme, the O-type can be used to surround multi-aerofoil as the curved boundary layer mesh.

3.4.2 Unstructured Grid Scheme

The advantage of an unstructured grid scheme is that only explicit structure of coordinate lines is formed by the grids, hence the mesh can be easily concentrated and generated around a complex geometry shape as Fig 3.5 shown. Moreover, for 3D geometry there are no restrictions on the number

of adjacent cells using an unstructured mesh scheme.

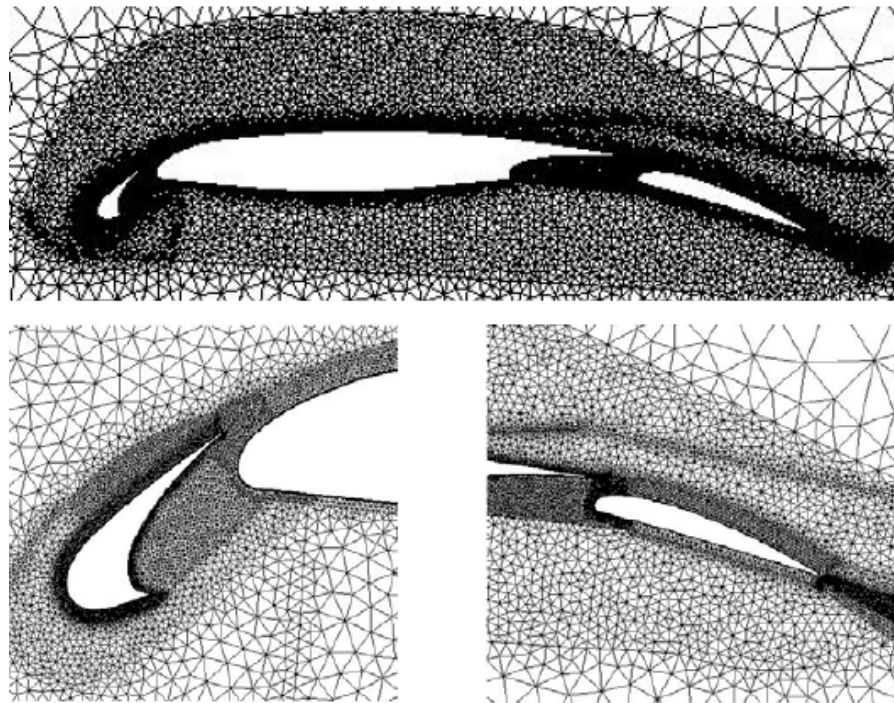


Figure3. 5 Unstructured Grids around a Three-element Aerofoil (Ref. [3])

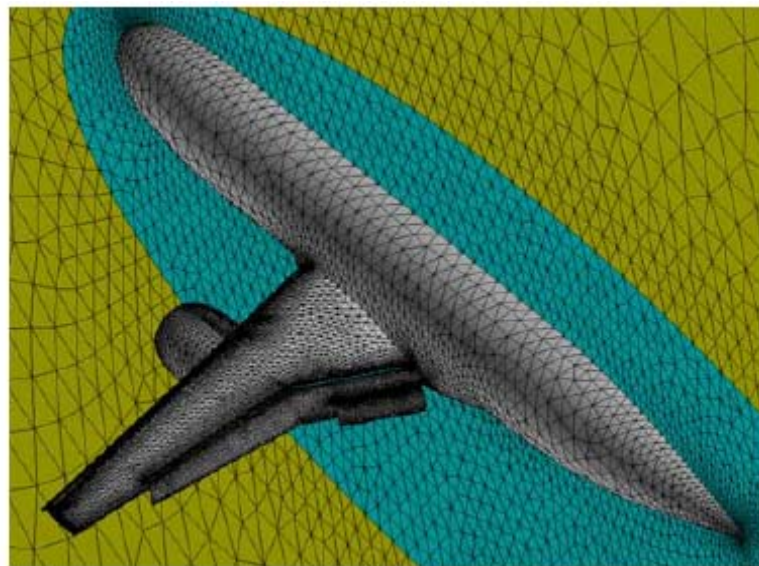


Figure3. 6 Unstructured Grids around an Entire Configuration of Airplane (Ref. [36])

In practical application of CFD, triangles or quadrilaterals are often used for 2D mesh generation, whereas the tetrahedral or hexahedral elements are applied in 3D problems, such as flow field around automotive, airplane or other vehicles in which the shape is extremely complicated. (see figure 3.6)

3.5 Aerodynamic Analysis of Ducted Fan

It is previously mentioned that the aerodynamic design and analysis of the duct is the main focus of this project. However, the theoretical methods for calculation of aerodynamic parameters for a duct are limited, hence CFD was used to analyze the duct. During CFD simulation, several critical factors have to be considered. These factors contain geometry simplification, mesh generation and quality, flow solver, convergence criteria, model options and so on. The 2D model is used to analyze the flow patterns around duct, the aerodynamic coefficients are calculated using 3D model and full scale model of UAV.

3.5.1 Aerodynamic Characteristics of Duct without Fans

GAMBIT was applied as the tool of mesh builder for FLUENT analysis in this chapter. It is a kind of software designed to help analysts and builders for FLUENT analysis and for computational fluid dynamics (CFD) or other scientific applications. GAMBIT receives user input by means of its graphical user interface (GUI) which makes the basic steps of building, meshing, and assigning zone types to a model simple and intuitive, yet it is versatile enough to accommodate a wide range of modeling applications.

As shown in Figure 3.6, S_d is defined as the area of the shadow plane in the middle of duct, and AR_d is the aspect ratio of duct. So,

$$S_d = 2rc(y_0) \quad (3.1)$$

$$AR_d = \frac{2r}{c(y_0)} \quad (3.2)$$

$$Re = \frac{\rho V_\infty c(y_0)}{\mu} \quad (3.3)$$

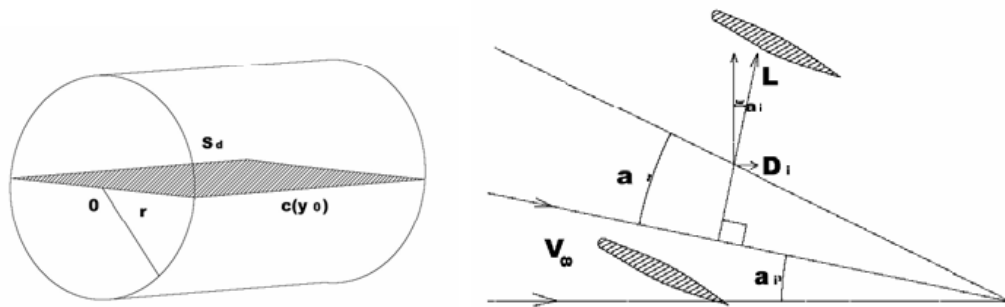


Figure3. 7 3D Duct Geometry Definition and Aerofoil of Duct

The lift and induced drag of the duct as shown in figure 3.7, are unfortunately difficult to calculate

accurately because the internal airflow of the duct is very complex (see Ref. [13]). The internal airflow approach bottom surface and top surface of duct will interfere with each other so that the internal airflow is not as smooth as the external airflow and the flow through the duct becomes completely three-dimensional. Therefore getting more accurate results requires a numerical solution. In modern aerodynamic applications, three-dimensional flow is usually calculated by means of numerical panel techniques. Computational Fluid Dynamics (CFD) was used to estimate the aerodynamic coefficient of the duct at different angles of attack.

The duct geometry is more complex than a finite-wing, and the aerofoil of the duct consists of two symmetry airfoils. As we discussed, in technology of grids generation, for single aerofoil we can use the structured mesh scheme to generate the boundary layer mesh around it, but for dual aerofoil like the duct both unstructured mesh and structured mesh have to be relied on.

During the mesh generation in GAMBIT, the application of size function is the best way to control the size of mesh intervals between edges or elements of grid for both faces and volumes. Especially, size function is always used in optimizing the mesh patterns of boundary layer and controlling the size of element of the grid within the patterns so as to get a suitable value of $Y+$ for boundary mesh. The “Great Size Function” command is applied to customize the size function dependent on the specific issue in GAMBIT. It has several properties which could be customised to include fixed-type size function, curvature-type size function, and proximity-size function. These properties determine the maximum edge lengths of element of grid, angles between two adjacent elements, and number of elements created in the gap between two entities, respectively. Therefore, by using size function not only the number of mesh could be controlled within a range, but also the qualification of grid required is able to be guaranteed.

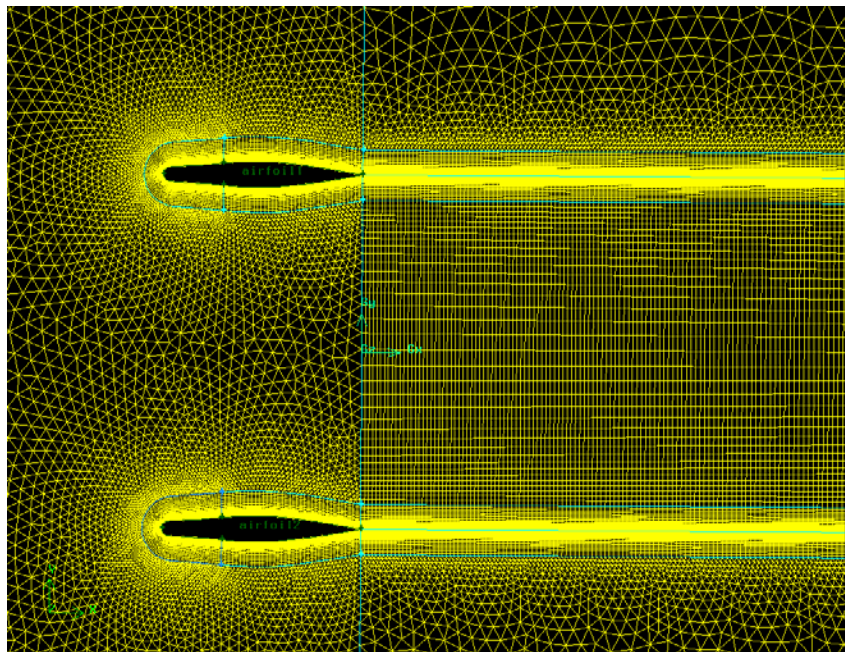


Figure3. 8 Hybrid-Mesh around Duct

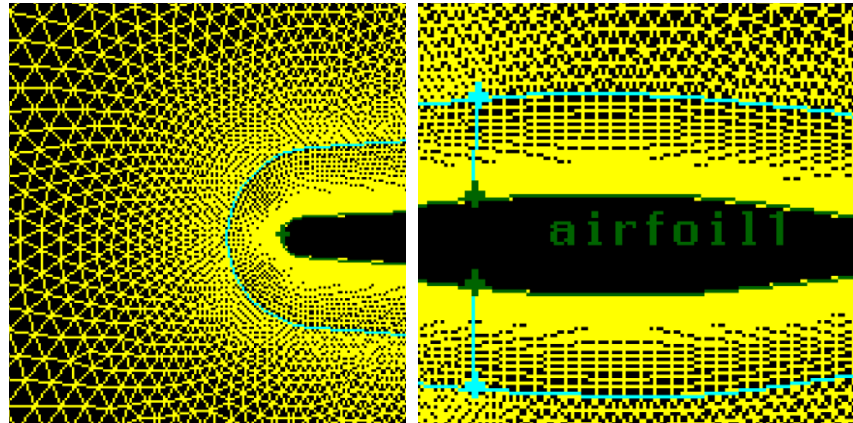


Figure3. 9 Unstructured Grids Surrounding Far Field and Structured Grids (Boundary Layer) around Aerofoil of Duct

The figure 3.8 shows the Hybrid-Mesh scheme around dual aerofoil of duct. The requirement of high quality grids and satisfied $Y+$ is the reason why both unstructured and structured grids are combined and used for mesh generation. Structured grids as the body-fitted mesh are surrounding the aerofoil, and created using size function and are available for the boundary layer. Unstructured grids are applied for far flow field, because the number of element of grid is easily controlled for customization of size function and most times there is no need to optimize the quality of grids.

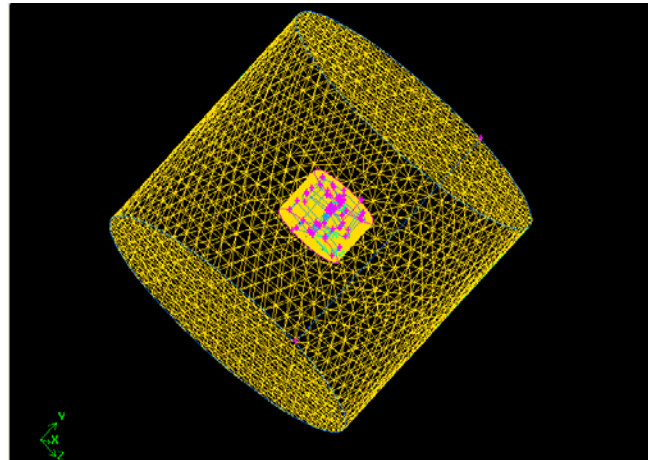


Figure3. 10 Unstructured Volume Grids Surrounding Far Field of Duct

Once the grids generation is completed in 2D symmetry aerofoil of duct, the 3D volume mesh can be easily created around the 3D geometry duct by setting up the size function in GAMBIT in figure 3.10. The next step is importing mesh file into FLUENT solver from GAMBIT and setting up various kinds of parameters in FLUENT before running simulation. FLUENT is one of the most popular software packages developed to simulate fluid flow in a wide range of CFD applications. FLUENT supplies simulation and modeling tools for both compressible and incompressible flow. Laminar and turbulent flow are also able to be solved. Not only that, various kinds of mathematical models, such as chemical reactions, heat transfer, and thermodynamics, can be analyzed by modeling in FLUENT.

Following are some properties of the CFD model for flow over the duct..

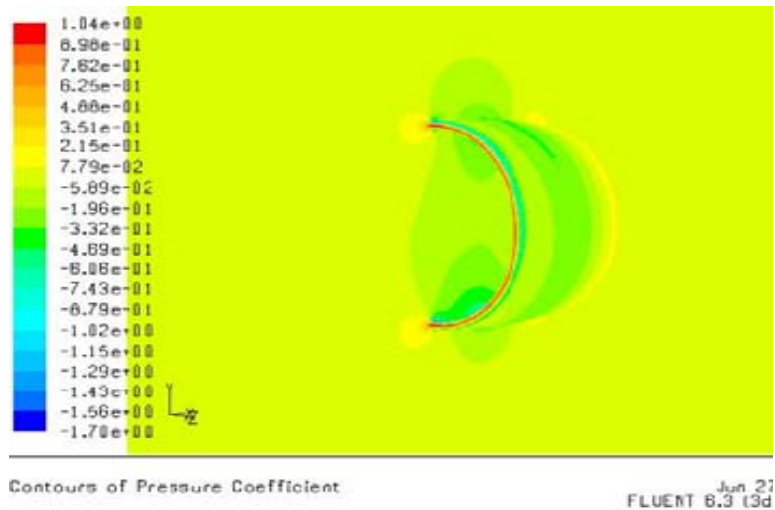


Figure3. 11 3D Contour of Pressure Coefficient

- Control volume: cylinder $\varnothing 3000\text{mm} \times H10000\text{mm}$
- Mesh generation: approximate 360,000 tetrahedral elements(see Fig.3.10)
- Quality of the skewness: 0.8% elements > 0.8 , but no element > 0.95 .
- Aspect ratio: less than 1% has no more than 1.87
- Boundaries: a velocity inlet, a pressure outlet, a symmetry for the middle surface, walls for the duct.
- Boundary conditions: the value of velocity inlet as a function of angle of attack, pressure outlet with gauge pressure is zero.
- Computational model: second order;
- Physical model: k-epsilon (with the default settings)
- Convergence criteria: velocity in X, Y or Z direction and turbulent kinematics are all set up for 0.0001 precision.
- Iterate: 600 iterations until convergence.

The lift coefficient versus angle of attack curve can be obtained by an iterated algorithm of 3D CFD results. In Fig .3.12 these results are plotted by using curves and figures

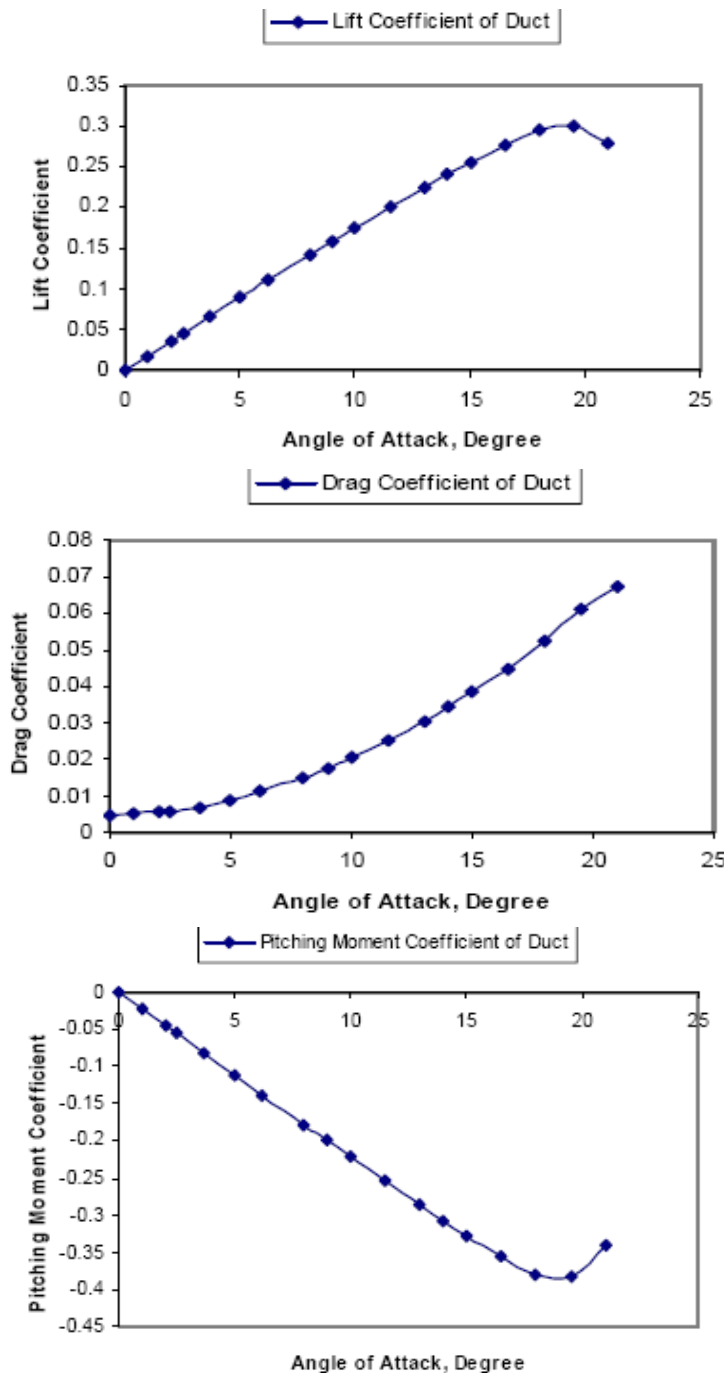


Figure3. 12 (a) Lift Coefficient Versus Angle of Attack ; (b) Drag Coefficient Versus Angle of Attack ; (c) Pitching Moment Coefficient Versus Angle of Attack

Both lift and drag coefficient are plotted as a function of angle of attack at 20 m/s for $0 < \alpha < 21$ degree (see Figure 3.11). The lift coefficient increases with angle of attack before dropping at 19 degree which is the stall angle. However, the drag coefficient keeps increasing with angle of attack changing from 0 degree to 21 degree, and the zero-lift drag coefficient can easily be obtained from figure 3.11(b). Depending on the stall angle, zero-lift drag and the slope of the two curves, the airfoil of duct can be optimized in detail. The trend of the pitching moment changed with angle of attack is plotted as curves in figure 3.11(c). The absolute values of pitching moment decrease (nose down) as a function of angle of attack and increase after stall.

3.5.2 Analysis of Flow around Duct with Fuselage

After optimizing the aerofoil of duct, a simplified duct and fuselage, without fans, was shown in Fig3.12.

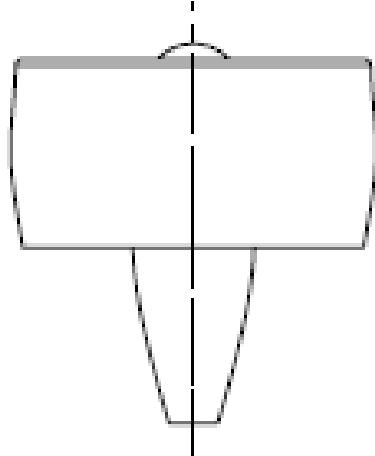
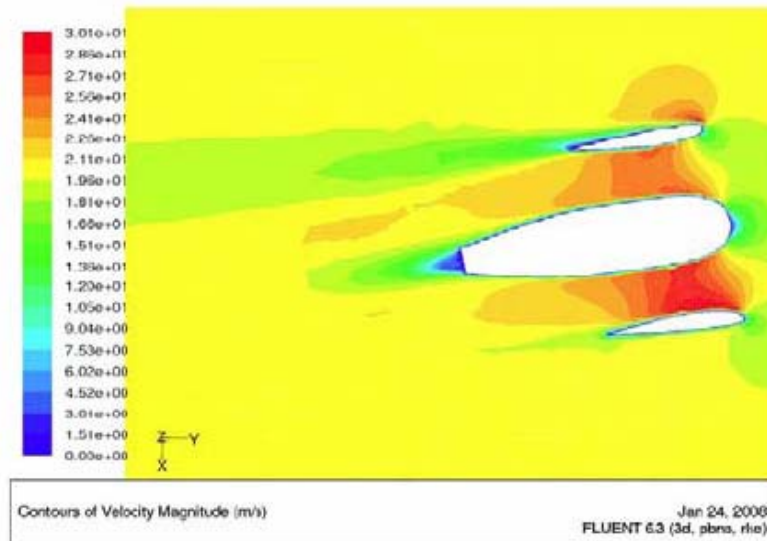


Figure3. 13 Simplified Duct and Fuselage

There are three conditions for which a duct can be optimized: horizontal flight (cruise conditions), vertical climbing and hovering (static condition). In order to analyze the flow pattern around duct with fuselage, a 2D model is built in CFD codes as well as analyzing 3D duct, and then running the model in FLUENT there are three kinds of flow patterns displayed in Fig 3.14.



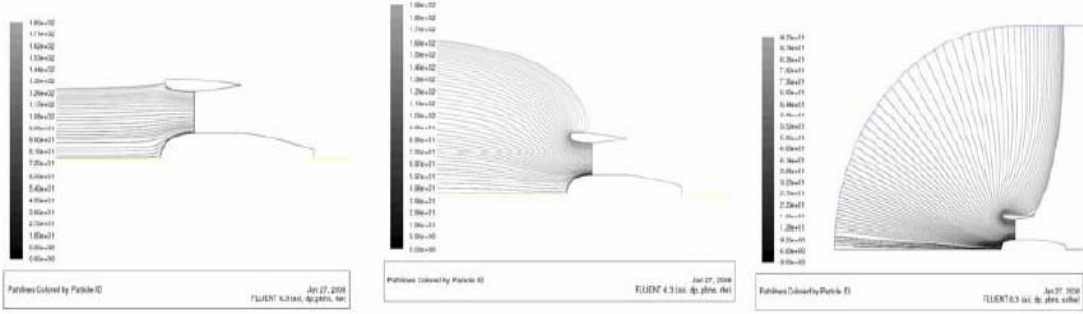


Figure3. 14 Pathlines Show Cruise Flight , Vertical Climb, Hovering

Figure 3.14 shows the different flow patterns under these three conditions. For cruise conditions everything seems to be fairly well in agreement with theory. Thrust is a little bit higher, whereas the drag is a little bit lower. For vertical climb there is an extra negative pressure drag.

3.6 Modeling of Full-Scale UAV in CFD

When the free flow over the UAV, it is separated into two parts flow. One part is external flow around the entire body of the UAV, the other part is internal flow which pass through the ducted fan and flow transition from laminar to turbulent occurs due to the rotating fans with pressure jump and swirl velocity. Obviously, the tails and control surfaces are totally submerged in the slipstream (turbulent flow). Relying on extra pitching moment generated by slipstream velocity we can realize the maneuver transition from vertical climb to horizontal flight, which is the key innovation of the new concept UAV. This part represents an investigation into the use of CFD for estimating the aerodynamic characteristic of the UAV.

3.6.1 Mesh Generation of Full-Scale Model

The geometry of the UAV is quite complex (see Fig 1.3), it consists of several components. How to simplify the geometry and not change the structure of the UAV is the main challenge in mesh generation. Controlling the mesh distribution on the surface of the entire UAV is the key point of generating high quality mesh around the full-scale model. Unstructured mesh approaches for complex geometry configuration (in Ref. [6]) is more efficient and less time consuming in figure 3.15 and figure 3.16. The density of the grid near the surface of the UAV is much higher than far field to simulate the boundary layer accurately and obtain a realistic value for the viscous drag coefficient.

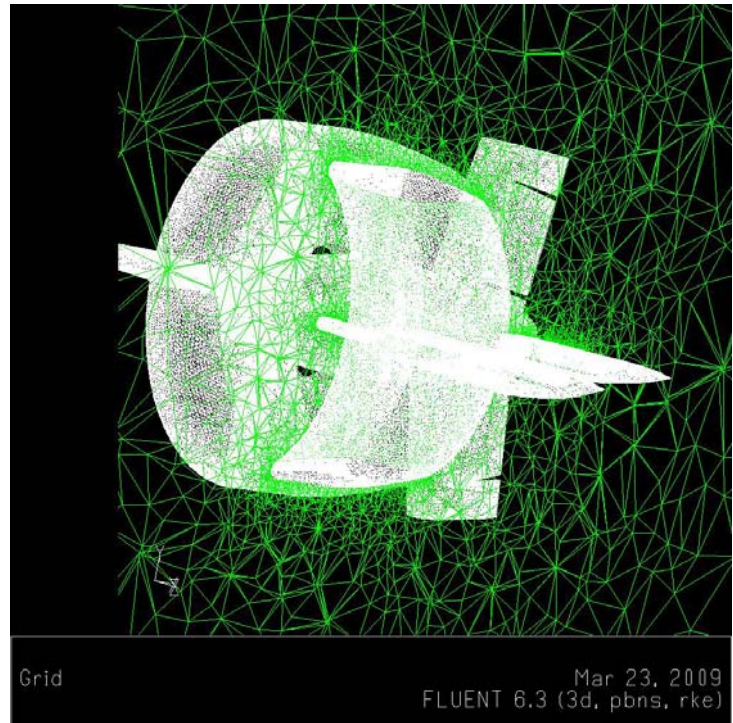


Figure3. 15 Mesh Scheme of Volume

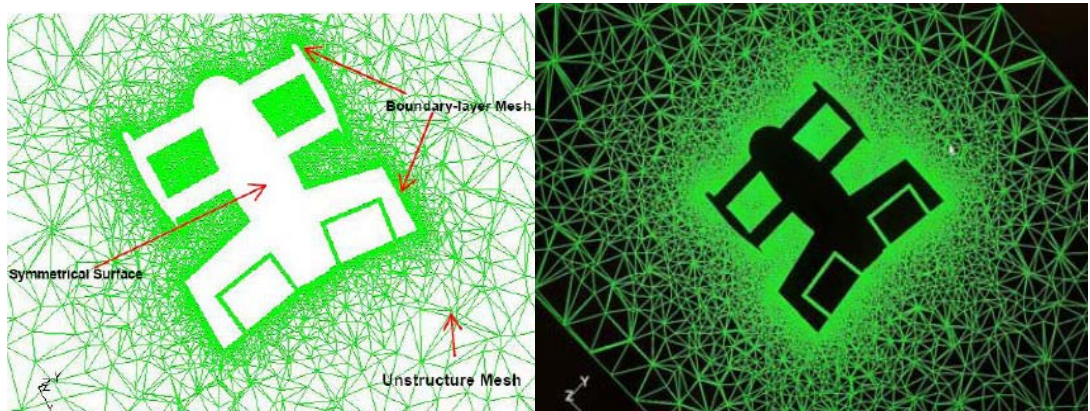


Figure3. 16 Mesh Scheme on Symmetrical Plane

Table.1 shows how to mesh different parts of full-scale model. Combining table.2 data and figure 3.17, we can see that the surfaces' mesh of cube (1.8 length, 1.2width and 1.2 high), including inlet, outlet and surrounding surfaces, are much less than surfaces' mesh of UAV. Getting accurate aerodynamic coefficients of UAV is the main purpose.

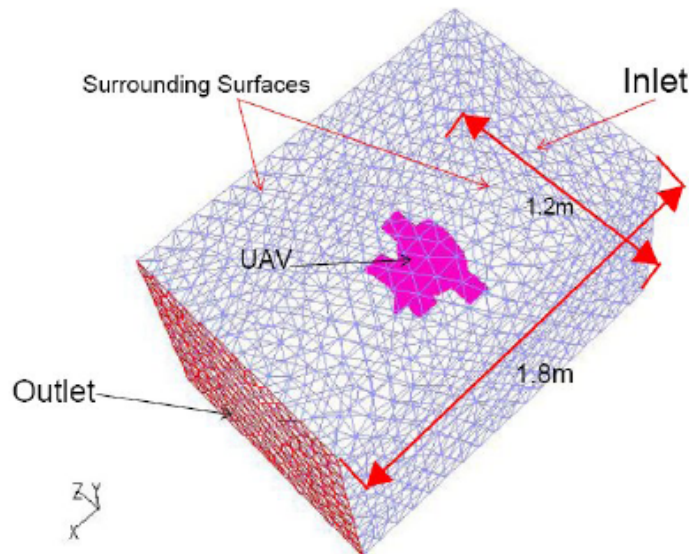
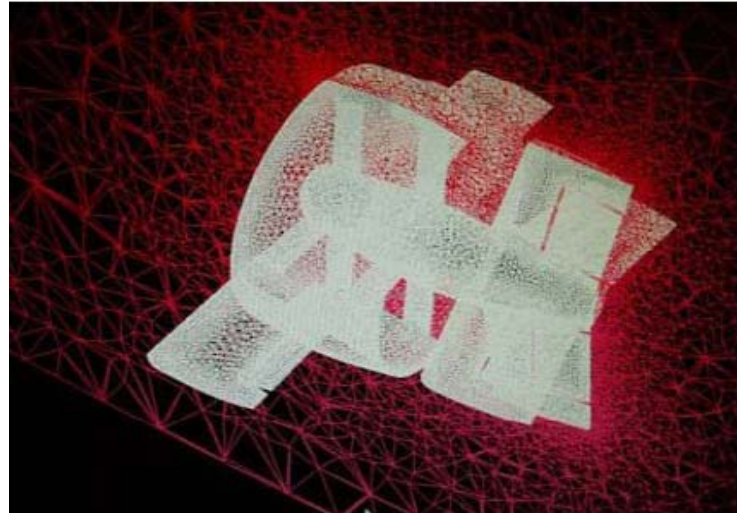


Figure3. 17 Mesh generation of full-scale model

High density mesh around UAV surfaces is to ensure high quality boundary layer. It also guarantees an accurate result. Thus how to generate the surfaces' mesh UAV requires more attention. Two types of mesh scheme are chosen for creating grid, triangle mesh is applied in surfaces' mesh, whereas tetrahedral mesh is used to generate volume mesh. Both triangle and tetrahedral mesh are called unstructured mesh which is often used for complicated mesh generation.

Table. 2 Mesh Type and Data

	Inlet	Outlet	Fan-surfaces	Fan-volume	Wings	Duct & Body	Tails	UAV-volume	Field
Mesh-type	Trig	Trig	Trig	Tetra	Trig	Trig	Trig	Tetra	Tetra-Hedral
Number	134	136	23068	101857	19562	97064	46348	1186461	2279356

3.6.2 Properties of Mesh Generation

Figure 3.17 shows the control-volume-cube whose size is depended on volume of UAV. If it is not big enough, the results of calculation will not be accurate because of the effects of cube boundary. Whereas if the size is too big, it means that the number of volume grids is very huge, which has led to time consuming calculations. Thus an appropriate size of cube has to be planned before generating grids. The range of skewness of mesh is another key point that should be considered during mesh generation. In addition, once the grids generation is done, the boundary definition has to be set up in terms of the practical physical model which is shown in table.3.

Table. 3 Properties of Grids and Boundaries

Size of Control Volume Cube	Length 1800mm Width 1200mm Height 1200mm
Number of Volume Mesh	Approximate 2,280,000 tetrahedral elements (see table 2)
Quality of the Skewness of Mesh	0.8%elements > 0.8 No element > 0.95
Aspect Ratio of Grids	Less than 1% < 1.87 Wings : wall Duct and Body : wall Horizontal and Vertical tails : wall
UAV Boundaries	Ailerons and Flaps : wall Intake fan : fan Exhaust fan : fan
Cube Boundaries	Inlet face : Velocity inlet Surrounding faces : Velocity inlet Outlet face : Pressure outlet Cube volume : Fluid (air)

3.6.3 Governing Equations

The continuity and moment equations (the Navier-Stokes Equations in Ref. [52] and Ref. [16]) are widely used in FLUENT to solve mass and momentum conservation equations. Furthermore, the energy conservation equations and transport equations can be solved as the flow transition occurs from laminar to turbulent.

The continuity equation can be written in the form of mass conservation as below,

$$\frac{\partial \rho}{\partial t} + \nabla \cdot (\rho \vec{V}) = 0 \quad (3.4)$$

In Equation 3.4, the ρ , V and t represent the density of fluid, velocity and time, respectively.

The momentum equation can be written in the form of conservation as below,

$$\frac{\partial(\rho \vec{V})}{\partial t} + \nabla \cdot (\rho \vec{V} \vec{V}) = -\nabla p + \nabla \cdot (\vec{\Gamma}) + \vec{F} \quad (3.5)$$

P is the static pressure in a specific point of flow, $\vec{\Gamma}$ and \vec{F} are the stress tensor and body force, respectively.

The energy equation [52] is written in the form of conservation as below,

$$\begin{aligned} \frac{\partial}{\partial t} [\rho(e + \frac{V^2}{2})] + \nabla \cdot [\rho(e + \frac{V^2}{2}) \vec{V}] = \\ \rho \dot{q} + \frac{\partial}{\partial x} (k \frac{\partial T}{\partial x}) + \frac{\partial}{\partial y} (k \frac{\partial T}{\partial y}) + \frac{\partial}{\partial z} (k \frac{\partial T}{\partial z}) - \frac{\partial (up)}{\partial x} \\ - \frac{\partial (vp)}{\partial x} - \frac{\partial (wp)}{\partial x} + \frac{\partial (u\tau_{xx})}{\partial x} + \frac{\partial (u\tau_{yx})}{\partial y} + \frac{\partial (u\tau_{zx})}{\partial z} + \frac{\partial (v\tau_{xy})}{\partial x} + \frac{\partial (v\tau_{yy})}{\partial x} + \frac{\partial (v\tau_{zy})}{\partial x} \\ + \frac{\partial (w\tau_{xz})}{\partial x} + \frac{\partial (w\tau_{yz})}{\partial x} + \frac{\partial (w\tau_{zz})}{\partial x} + \rho \vec{f} \cdot \vec{V} \end{aligned} \quad (3.6)$$

e is the internal energy for per unit mass due to random molecular motion. $\frac{V^2}{2}$ is the kinetic energy for

per unit mass based on translational motion of the fluid element. The heat flux \dot{q} is transferred in x,y

and z direction in a small control volume, they are defined as \dot{q}_x, \dot{q}_y and \dot{q}_z , respectively. And the

heat flux due to thermal conduction is proportional to the local temperature gradient as following:

$$\dot{q}_x = -k \frac{\partial T}{\partial x} \quad (3.7)$$

$$\dot{q}_y = -k \frac{\partial T}{\partial y} \quad (3.8)$$

$$\dot{q}_z = -k \frac{\partial T}{\partial z} \quad (3.9)$$

k is the thermal conductivity. Another variable pointed out is vector of shear stress τ which includes nine contributions are described by subtitle xx, yx, zx, xy, yy, zy, xz, yz and zz, respectively.

3.6.4 Turbulent Model

The standard $k - \varepsilon$ model consists of two model equations. One is kinetic k equation, the other one is dissipation ε equation. The k and ε are applied to define velocity scale ϑ and length scale ℓ which are the large-scale turbulence as follows:

$$\vartheta = k^{1/2} \quad (3.10)$$

$$\ell = \frac{k^{3/2}}{\varepsilon} \quad (3.11)$$

According to the above two scale variables, the eddy viscosity can be computed in the form of following:

$$\mu_t = C_\mu \rho \vartheta \ell = \rho C_\mu \frac{k^2}{\varepsilon} \quad (3.12)$$

Where C_μ is a dimensionless constant.

The standard $k - \varepsilon$ model [52] uses the following transport equations for k and ε :

$$\begin{aligned} \frac{\partial(\rho k)}{\partial t} + \nabla \cdot (\rho k \vec{V}) &= \\ \frac{\partial}{\partial x} \left[\left(\mu + \frac{\mu_t}{\sigma_k} \right) \frac{\partial k}{\partial x} \right] + \frac{\partial}{\partial y} \left[\left(\mu + \frac{\mu_t}{\sigma_k} \right) \frac{\partial k}{\partial y} \right] + \frac{\partial}{\partial z} \left[\left(\mu + \frac{\mu_t}{\sigma_k} \right) \frac{\partial k}{\partial z} \right] &+ G_k + S_k - \rho \varepsilon \end{aligned} \quad (3.13)$$

$$\begin{aligned} \frac{\partial(\rho \varepsilon)}{\partial t} + \nabla \cdot (\rho \varepsilon \vec{V}) &= \\ \frac{\partial}{\partial x} \left[\left(\mu + \frac{\mu_t}{\sigma_\varepsilon} \right) \frac{\partial \varepsilon}{\partial x} \right] + \frac{\partial}{\partial y} \left[\left(\mu + \frac{\mu_t}{\sigma_\varepsilon} \right) \frac{\partial \varepsilon}{\partial y} \right] + \frac{\partial}{\partial z} \left[\left(\mu + \frac{\mu_t}{\sigma_\varepsilon} \right) \frac{\partial \varepsilon}{\partial z} \right] &+ G_{1\varepsilon} G_k \frac{\varepsilon}{k} + S_\varepsilon - C_{2\varepsilon} \rho \frac{\varepsilon^2}{k} \end{aligned} \quad (3.14)$$

These two equations contain five adjustable constants: C_μ , $C_{1\varepsilon}$, $C_{2\varepsilon}$, σ_k and σ_ε . Constants

$C_{1\varepsilon}$ and $C_{2\varepsilon}$ affect the correct proportionality between the terms in the k and ε equations.

σ_k and σ_ε are called Prandtl numbers which connect k and ε to the eddy viscosity μ_t . The standard $k - \varepsilon$ model employs a group of specific values to fit for a range of turbulent flows in different conditions.

Table. 4 Values of Constants in standard $k - \varepsilon$ model

Constant	Value
C_μ	0.09
$C_{1\varepsilon}$	1.44
$C_{2\varepsilon}$	1.92

σ_k	1.00
σ_ε	1.30

G_k represents the generation of kinetic energy k because of the mean velocity gradient. S_k and S_ε are defined by users in terms of practical problem.

To solve the standard $k - \varepsilon$ model the boundary conditions have to be based on:

- Inlet : k and ε must be given
- Outlet and Symmetry Axis : $\frac{\partial k}{\partial x} = 0$ and $\frac{\partial \varepsilon}{\partial x} = 0$
- Free Flow : k and ε must be given or $\frac{\partial k}{\partial x} = 0$ and $\frac{\partial \varepsilon}{\partial x} = 0$
- Solid Walls : Approach depends on Reynolds number

Compared with the standard $k - \varepsilon$ model which has good performance in higher Reynolds number turbulent flow, the realizable $k - \varepsilon$ model is suitable for low Reynolds number and it has shown substantial improvements over the standard $k - \varepsilon$ model where the flow features include strong streamline curvature, vortices, and rotation.

The realizable $k - \varepsilon$ model (in Ref. [52] and [16]) uses the following transport equations for k and ε :

$$\begin{aligned} \frac{\partial(\rho k)}{\partial t} + \nabla \cdot (\rho k \vec{V}) = & \\ \frac{\partial}{\partial x} \left[\left(\mu + \frac{\mu_t}{\sigma_k} \right) \frac{\partial k}{\partial x} \right] + \frac{\partial}{\partial y} \left[\left(\mu + \frac{\mu_t}{\sigma_k} \right) \frac{\partial k}{\partial y} \right] + \frac{\partial}{\partial z} \left[\left(\mu + \frac{\mu_t}{\sigma_k} \right) \frac{\partial k}{\partial z} \right] & (3.15) \\ + G_k + G_b + S_k - \rho \varepsilon & \end{aligned}$$

$$\begin{aligned} \frac{\partial(\rho \varepsilon)}{\partial t} + \nabla \cdot (\rho \varepsilon \vec{V}) = & \\ \frac{\partial}{\partial x} \left[\left(\mu + \frac{\mu_t}{\sigma_\varepsilon} \right) \frac{\partial \varepsilon}{\partial x} \right] + \frac{\partial}{\partial y} \left[\left(\mu + \frac{\mu_t}{\sigma_\varepsilon} \right) \frac{\partial \varepsilon}{\partial y} \right] + \frac{\partial}{\partial z} \left[\left(\mu + \frac{\mu_t}{\sigma_\varepsilon} \right) \frac{\partial \varepsilon}{\partial z} \right] & (3.16) \\ + G_{1\varepsilon} G_b C_{3\varepsilon} \frac{\varepsilon}{k} + S_\varepsilon + \rho C_1 S_\varepsilon - C_2 \rho \frac{\varepsilon^2}{k + \sqrt{\mu \varepsilon}} & \end{aligned}$$

Where

$$C_1 = \max[0.43 \cdot \frac{\eta}{\eta + 5}] \quad (3.17)$$

$$\eta = S \frac{k}{\varepsilon} \quad (3.18)$$

In contrast to standard $k - \varepsilon$ model, the additional variable G_b represents generation of turbulence kinetic energy due to buoyancy. In the realizable $k - \varepsilon$ model other constants and G_k are the same as constants in the standard $k - \varepsilon$ model.

The validation of realizable $k - \varepsilon$ model has been extended for widespread flows patterns, including rotating shear flows, jets and mixing layers in free flows, and separated flows. Dealing with these cases, the realizable $k - \varepsilon$ model has much better performance than that of the standard $k - \varepsilon$ model. But in realizable $k - \varepsilon$ model the eddy viscosity is no longer a constant, it is calculated by,

$$C_\mu = \frac{1}{A_s \frac{kU}{\varepsilon} + A_0} \quad (3.19)$$

In equation 3.19 A_0 and A_s are the model constants given by,

$$A_0 = 1.44 \quad (3.20)$$

$$A_s = \sqrt{6 \cos \phi} \quad (3.21)$$

However,

$$U = \sqrt{S_{ij}S_{ji} + \Omega_{ij}\Omega_{ji}} \quad (3.22)$$

The S_{ij} and S_{ji} are the strain variables, Ω_{ij} and Ω_{ji} are the rate of rotation. Therefore, the C_μ is the function of strain and rotation.

By analyzing the flow patterns in this UAV project, as the free flow over the UAV, it is separated into two parts flow. One part is external flow around the entire body of the UAV, the other part is internal flow which pass through the ducted fan and flow transition from laminar to turbulent is happened due to the rotating fans with pressure jump and swirl velocity. In addition the low Reynolds number is calculated by Equation 3.3. Thus the realizable $k - \varepsilon$ model is selected to solve the CFD model in FLUENT. In order to ensure the performance of realizable $k - \varepsilon$ model good for predicting the flow transition happened in ducted fan of this UAV, some constants should be listed in below table.

Table. 5 Values of Constants in realizable $k - \varepsilon$ model

Constant	Value
C_2	1.9
$C_{1\varepsilon}$	1.44
$C_{2\varepsilon}$	1.92

σ_k	1.00
σ_ε	1.20

Before running the model in CFD codes, above constants have to be set up in FLUENT.

3.6.5 Model Solving

Some important features of the problem have to be determined before the model is simulated in FLUENT [16]. So the basic procedural steps shown below should be followed.

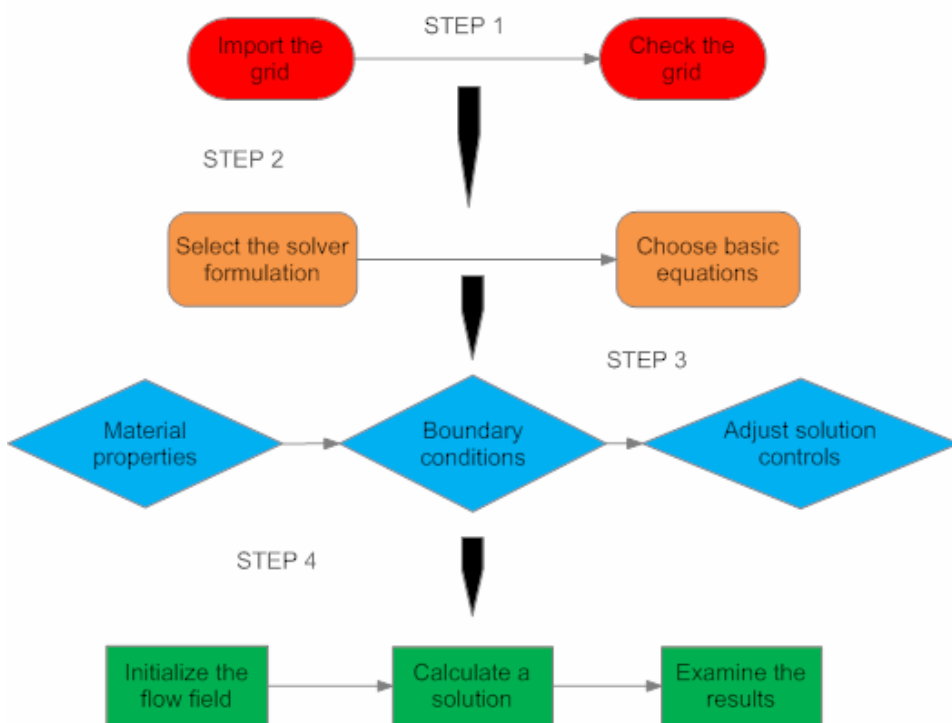


Figure3. 18 Problem Solving Steps

3.6.5.1 Defining Physical Models

The fully implicit method is recommended for general-purpose of CFD, in particular to computations of unstructured mesh. Pressure base is selected in this solver model because of the subsonic flow through the entire flow-field. Further more the Green-Gauss Node Based is chosen in gradient option

Table. 6 Physical Model

Model Defined	Option

Solver	Pressure Based
Space	3D
Formulation	Implicit
Time	Steady
Velocity Formulation	Absolutely
Gradient Option	Green-Gauss Node Based
Porous Formulation	Superficial Velocity

3.6.5.2 Selecting the Solver Formulation

Depending on the low Reynolds number of this flow model, the k-epsilon model was applied.

Table. 7 Solver Formulation

Viscous Model	Option						
Model	k-epsilon						
k-epsilon	Realizable						
Near-Wall Treatment	Standard Wall						
Model Constants	<table border="1"> <tr> <td>C₂-epsilon</td> <td>C₂-epsilon</td> </tr> <tr> <td>TKE-Prandtl Number</td> <td>TKE-Prandtl Number</td> </tr> <tr> <td>TDR-Prandtl Number</td> <td>TDR-Prandtl Number</td> </tr> </table>	C ₂ -epsilon	C ₂ -epsilon	TKE-Prandtl Number	TKE-Prandtl Number	TDR-Prandtl Number	TDR-Prandtl Number
C ₂ -epsilon	C ₂ -epsilon						
TKE-Prandtl Number	TKE-Prandtl Number						
TDR-Prandtl Number	TDR-Prandtl Number						

3.6.5.3 Specifying Fluid Properties

In FLUENT, physical properties of fluids and solids are associated with named materials, and a mixture material consists of several kinds of species included in specific problem.

Table. 8 Fluid Properties

Materials	Option	
Material Type	Fluid	
FLUENT Fluid Material	air	
Density (kg/m ³)	Constant	Density (kg/m ³)
Viscosity (kg/m-s)	Constant	Viscosity (kg/m-s)

The properties of air for this model are specified as ambient temperature. The viscosity is 1.7894e-05 kg/m-s at sea level and density is 1.225 kg/m³, for this model including energy calculations which are assumed as constants due to the high flow velocity through all the system and limited range in temperature, and buoyancy effect is too small to be considered here.

3.6.5.4 Specifying Boundary Conditions

The entire UAV model is defined as the wall boundary involved wings, duct and fuselage, horizontal tails and vertical tails. In viscous flows, the no-slip boundary condition is enforced at walls by default. The same is used for the current research on both external and internal flow through the UAV. High quality meshes around the model are used to ensure the viscous drag computed accurately.

Table. 9 Wall Boundary Conditions

Wall	Setting
Wall Motion	Stationary Wall
Shear Condition	No slip
Wall Roughness	Height(m) 0
	Constant 0.5

Velocity-inlet boundary conditions are used to define the flow property. In 3D model the velocity vector is composed by three vectors in X, Y, and Z direction, respectively. The magnitudes of these three vectors are based on the angle of attack or sideslip angle which should be analyzed for aerodynamic model of this UAV. Once the angle of attack or sideslip angle is determined these three directional vectors of velocity are able to be calculated and set up in FLUENT. In addition, the turbulent model has been chosen, so the turbulent kinetic energy and turbulent dissipation rate have to be set up in velocity boundary conditions dependant on realization k-epsilon model which has been discussed in the previous chapter.

The parameters of velocity inlet boundary conditions set up in FLUENT are given in the following table.

Table. 10 Velocity Inlet Boundary Condition

Velocity Inlet	Setting
Velocity Specification Method	Components
Reference Frame	Absolute
Coordinate System	Cartesian (X,Y,Z)
X Velocity (m/s)	Constant
Y Velocity (m/s)	Constant
Z Velocity (m/s)	Constant
Turbulent Specification Method	k-epsilon
Turbulent Kinetic Energy (m^2/s^2)	1.0
Turbulent Dissipation Rate (m^2/s^3)	1.0

During setting up the velocity-inlet boundary conditions, it should be noted that the inlet-face can not be too close to the UAV model as this causes the flow inlet to not be uniform as well as the far-field flow. Errors to results can be created due to this. the results error will be created due to this

Pressure outlet boundary conditions require the specification of a gauge pressure at the outlet boundary.

The value of gauge pressure is applied only as the flow subsonic. If the flow becomes totally supersonic, the specified pressure is no longer used. And backflow conditions set is specified and applied in the condition of the flow reversing direction at the pressure outlet boundary.

Table. 11 Pressure Outlet Boundary Conditions

Pressure Outlet	Setting
Gauge Pressure (Pa)	0
Backflow Direction Specification Method	Normal to Boundary
Turbulent Specification Method	k-epsilon
Backflow Turbulent Kinetic Energy (m^2/s^2)	1.0
Backflow Turbulent Dissipation Rate (m^2/s^3)	1.0

The fan boundary type permit you to input an empirical fan curve which governs the relationship between head and flow velocity through a fan which is able to be used in connection with other flow sources in a simulation. In this UAV model two fans must be specified, one is the intake fan that rotates in a clockwise direction,, whereas the other one is exhaust fan which rotates counter-clockwise and is opposite to the intakefan(see table). The purpose of counter-rotating is that the torque generated by each of the fans can be counteracted with each other, resulting in steady control of rolling.

Table. 12 Fan Boundary Conditions

Fan Boundary Condition			
Pressure Jump Specification		Swirl Velocity Specification	
Intake Fan Direction		Intake Fan Axis (Clockwise Rotating)	
X Coordinate	-1	X Coordinate	1
Y Coordinate	0	Y Coordinate	0
Z Coordinate	0	Z Coordinate	0
Pressure Jump (Pa)	Polynomial	Fan Hub Radius (m)	0.12
Polynomial Velocity Range		Tangential Velocity	Polynomial
Min Magnitude (m/s)	0	Radial Velocity	Polynomial
Max Magnitude (m/s)	1e+10		
Exhaust Fan Direction		Intake Fan Axis (Counter-Clockwise Rotating)	
X Coordinate	1	X Coordinate	-1
Y Coordinate	0	Y Coordinate	0
Z Coordinate	0	Z Coordinate	0
Pressure Jump (Pa)	Polynomial	Fan Hub Radius (m)	0.12
Polynomial Velocity Range		Tangential Velocity	Polynomial
Min Magnitude (m/s)	0	Radial Velocity	Polynomial
Max Magnitude (m/s)	1e+10		

To define the pressure jump, a polynomial function of velocity should be used. Meanwhile the minimum and maximum velocity magnitudes are also applied as the limited range of the pressure jump to ensure the correct calculation. Both radial and tangential velocity need to be set up as the

components of swirl velocity of the fan. And the fan hub radius is also a necessary parameter to be specified, the value of radius depends on the blade shape and the size of propeller which is used in a specific project.

3.6.5.5 Adjusting Solution Control

In this step (see table.13), the default settings for the under-relaxation factors and flow solver parameters can be defined, Quantities at cell faces are computed using a multidimensional linear reconstruction approach. In this approach, higher-order accuracy is achieved at cell faces through a CFD analysis, second-order upwind scheme is selected due to the need for high precision results.

Table. 13 Set of Solution Controls

Solution Controls	
Equations	Flow Turbulence
Pressure Velocity Coupling	SIMPLE
Under Relaxation Factors	
Pressure	0.3
Density	1
Body Forces	1
Momentum	0.7
Discretization	
Pressure	Presto
Momentum	Second Order Upwind
Turbulent Kinetic Energy	Second Order Upwind
Turbulent Dissipation Rate	Second Order Upwind

The longitudinal coefficients of forces and moments play an important role in building up a dynamic model for this UAV, so calculating the longitudinal aerodynamic coefficients should have more attention paid to it. Since the contribution of the drag or lift in X, Y and Z directions are determined by the angle of attack and sideslip angle in different cases, and the forces and moments are composed by four parts of UAV including wings, duct and body, horizontal tails and vertical tails shown in table.14. When we set up the force vector, the angle of attack and sideslip angle have to be dependable.

Table. 14 Forces and Moments Monitors

Force Monitors			
Wall Zone	Coefficient	Force Vector	
Horizontal Tails	Drag	X	Constant
		Y	Constant
	Lift	Z	Constant
		X	Constant
Vertical Tails			
Duct and Body	Lift	Y	Constant
Wings		Z	Constant

Moment (Reference Point)	X (m) Y (m) Z (m)	Constant Constant Constant
-----------------------------	-------------------------	----------------------------------

The reference values are listed below as the default parameters of this model simulated in FLUENT. It is the “compute from” which has to be taken care before running the model. With the angle of attack changed the velocity of flow inlet is also converted.

Table. 15 List of Values

Reference Values		
Area (m ²)	1	
Density (kg/m ³)	1.225	
Enthalpy (j/kg)	0	
Length (m)	1	
Pressure (Pa)	0	
Temperature (k)	288.16	
Velocity (m/s)	Constant	
Viscosity (kg/m-s)	1.7894e-05	
Ratio of Specific Heats	1.4	
Compute From	Inlet Face	
Reference Zone	Cube Volume	

3.6.5.6 Solving the Problem

The residual convergence value used in this problem is 10^{-4} as shown in table.16. Smaller residual value does not mean that the results will be more accurate but require much more time to compute.

Table. 16 Residual Monitor

Residual Monitors		
Storage Iterations	1000	
Normalization	Scale	
Convergence Criterion (Absolute)		
Residual	Absolute Criteria	
Continuity	0.0001	
X Velocity	0.0001	
Y Velocity	0.0001	
Z Velocity	0.0001	
k	0.0001	
Number of Iterations	Constant	

The flow field should be initialized for the solution before iterating. The Gauge Pressure is normally set

as default of 0, but the vector of velocity is according to the inlet face which is specified in “Computer From”.

Table. 17 Initialization of Solution

Solution Initialization	
Compute From	Inlet Face
Reference Frame	Relative to Cell Zone
Gauge Pressure (Pa)	0
X Velocity (m/s)	Constant
Y Velocity (m/s)	Constant
Z Velocity (m/s)	Constant

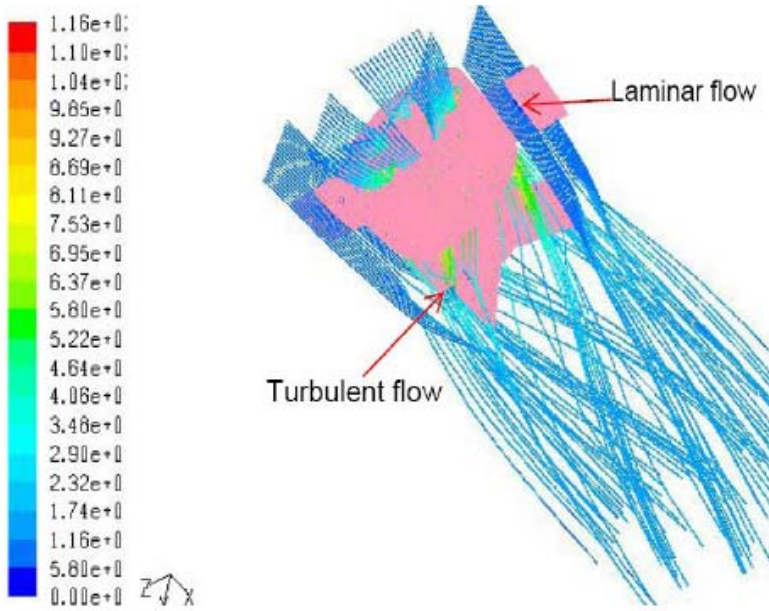
3.6.6 Computer Requirements

About 2.5 million cells and 4 million meshes were created. The calculations were performed on the high computing facility operated by the Victorian Partnership for Advanced Computing represents one of the most powerful installations in Australia. EDDA is an IBM Open estimates Edda's performance to be benchmarked at around 1 Teraflop. The technical details are as follows:

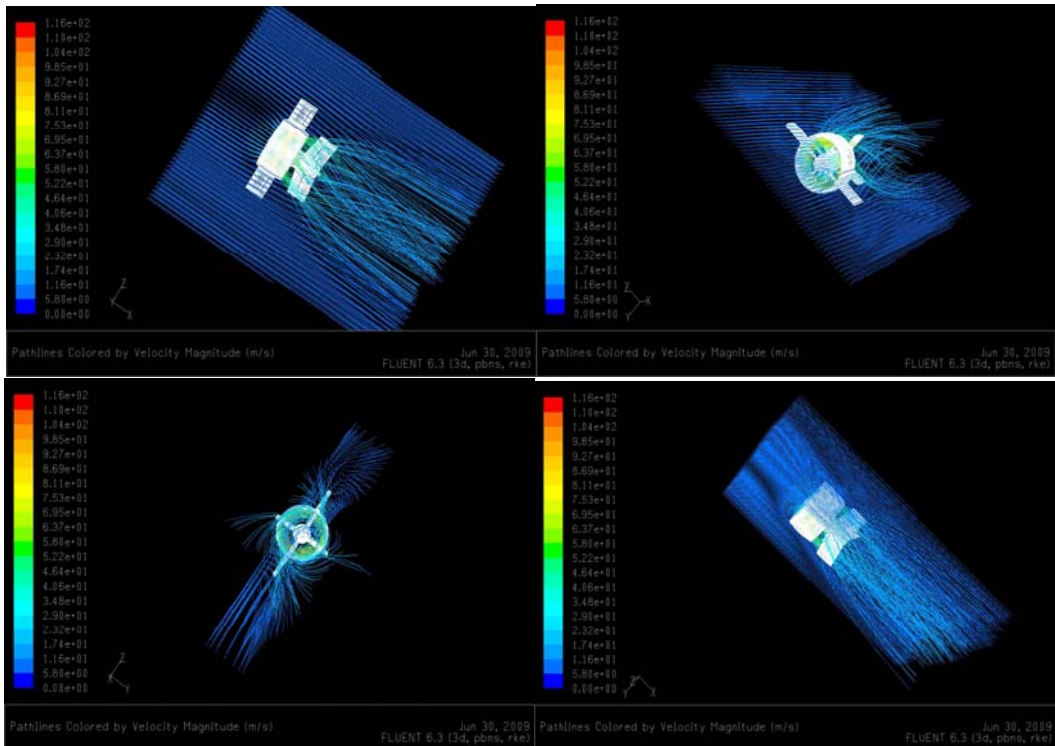
- 1) 190 1.67GHz Power5 CPUs
- 2) 474 way Compute nodes, 12 way compute node
- 3) 24 nodes with 16G ram
- 4) 24 nodes with 8G ram
- 5) SLES 9 linux from SUSE

3.6.7 Propeller Slipstream Interaction with Tail

In Fig 3.19(a) the full scale model of UAV with ducted fan rotation is simulated in Fluent to analyze the process of flow transition. We can clearly see that the free flow via wings is still laminar flow at low Mach number, whereas the uniform free flow passes through the rotors, and gradually becomes turbulent flow which is irregular and unstable.



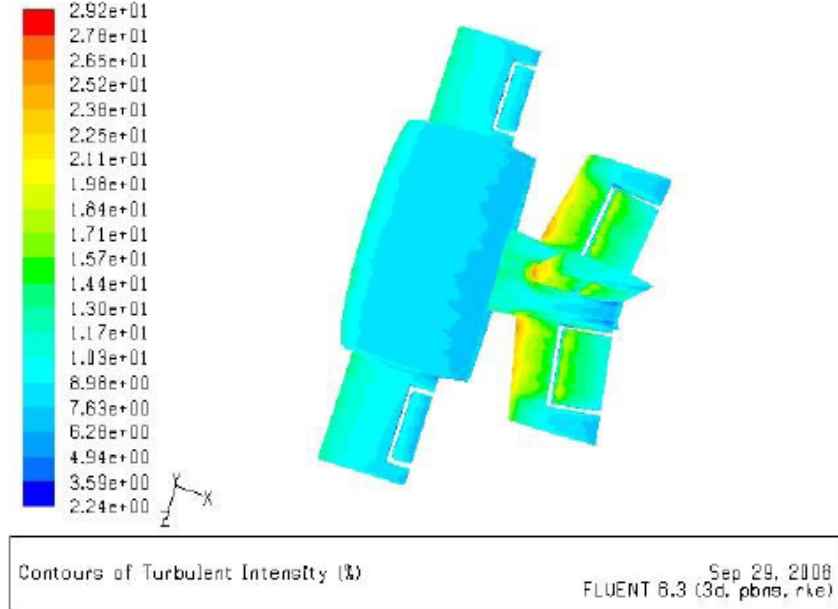
(a) Simulation on UAV with Rotational Propeller



(b) Flow Patterns around UAV

The Fig 3.19(c) shows that most of the turbulent flow passes along the control surface of the tail, because the yellow parts of tail reflect the high value of turbulent intensity. Thus once the high speed turbulent flow is over the control surface, the static and dynamic pressures are converted into a big pressure force which generates a pressure moment on the tail. This is then used to control the vehicle in pitch and to achieve transition from vertical climb to horizontal flight at very low airspeed or even zero velocity of free flow (hovering state). In contrast to tails, obviously, there is no high speed flow passing

through wings, so no big pressure force is created on wings. In order to explain the pressure-difference on tails and on wings as being different from each other, much more statements and figures are shown.



(c) Contour of Turbulent Intensity of UAV

Figure3. 19 (a) Simulation on UAV with Rotational Propeller; (b) Flow Patterns around UAV; (c) Contour of Turbulent Intensity of UAV

Before we are going to explain how the slipstream generates an effective pressure force on tails, an important assumption must be emphasized. The assumption is the flow in which the tails and control surfaces are totally submerged is inviscid and incompressible, though the flow is turbulent. Based on this condition the Bernoulli's equation is able to be used explaining why the UAV can achieve transition from vertical climb to horizontal flight even at very low speed. The Bernoulli's equation from Ref. [4] is described as below:

$$p + \frac{1}{2} \rho V^2 = \text{const} \quad (3.23)$$

The definition of P is static pressure, whereas $\frac{1}{2} \rho V^2$ is dynamic pressure. So above equation means

that the total energy is equal to static energy plus dynamic energy in terms of the law of energy conservation, Eq(3.23).

$$p_1 + \frac{1}{2} \rho V_1^2 = p_2 + \frac{1}{2} \rho V_2^2 \quad (3.24)$$

Now we separate the tail's surface into upper surface and lower surface respectively, P_1 is static pressure of upper surface, and P_2 is static pressure of lower surface. In the same way, we define $\frac{1}{2} \rho V_1^2$ and $\frac{1}{2} \rho V_2^2$ as the dynamic pressure of upper and lower surfaces. From Eq(3.24) we obtain

$$p_1 - p_2 = \frac{1}{2} \rho V_2^2 - \frac{1}{2} \rho V_1^2 \quad (3.25)$$

Then we also define $p_1 - p_2 = \Delta p$ and $\frac{1}{2} \rho V_2^2 - \frac{1}{2} \rho V_1^2 = \Delta p_{dynamic}$, which are static pressure

difference and dynamic pressure difference between upper and lower surface of tail. Both Δp and $\Delta p_{dynamic}$ are the main factors for effective tail lift generated by slipstream effects.

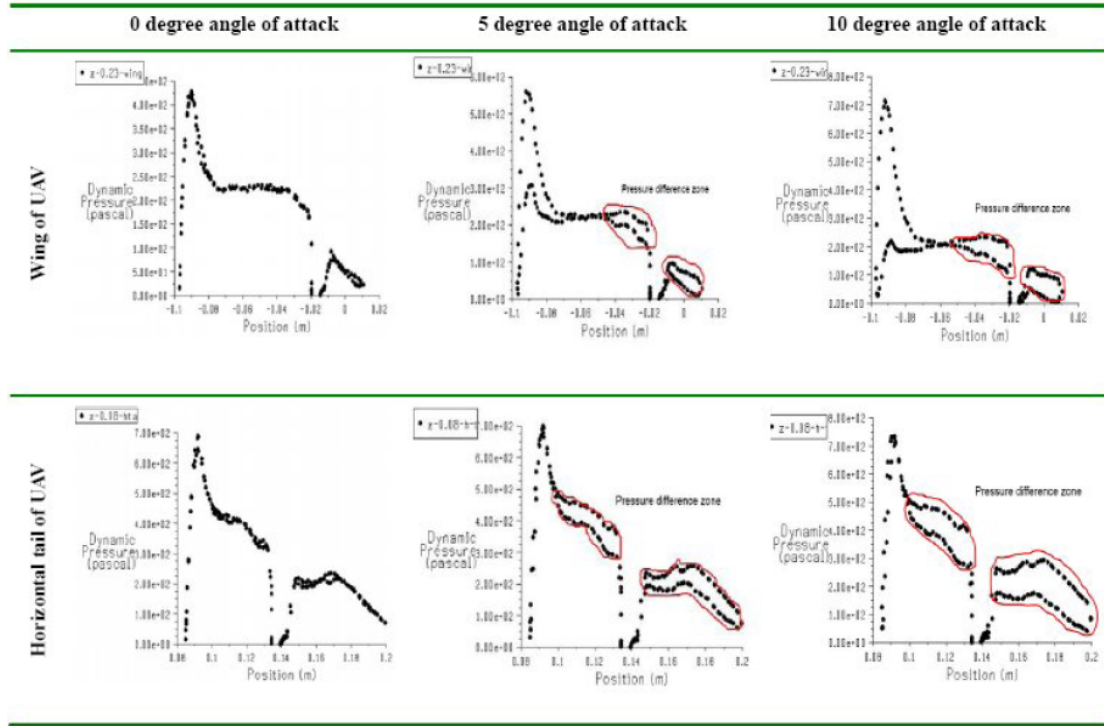


Figure3. 20 Profile of Dynamic Pressure of Wing and Horizontal Tail in Chordwise Coordinate at Different Angle of Attack

The figure3.20 shows dynamic pressure on both wing and tail are changed with the variation of angle of attack of UAV. At zero angle of attack there is no apparent pressure difference between upper and lower surface on wing or tail. However, from the marked red zone we can see that the pressure difference rises with the increase of angle of attack. Furthermore, compared with the wing's pressure difference increasing the tail's variation is more obvious, not only the range of chordwise increasing, but also the value of pressure difference between upper and lower surface. It means that the $P_{dynamic}$ of tail is further bigger than $p_{dynamic}$ of wing due to the high speed turbulent flow generated by propeller slipstream. Therefore it has led to the effective force and moment on the tails. And this is what we expect in aerodynamic design of the VTOL UAV.

Previously, we explain the $P_{dynamic}$ how it impacts on force generation of tail as an important factor, in this part another key factor which determines the efficiency of lift generation should also be considered. It is called pressure difference zone marked by the red color profile in figure.3.21. How to evaluate the range of pressure difference zone is to be expatiated as following.

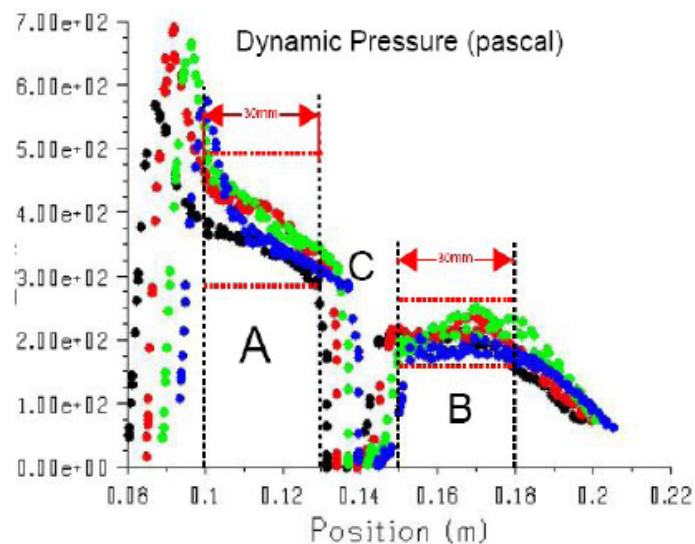
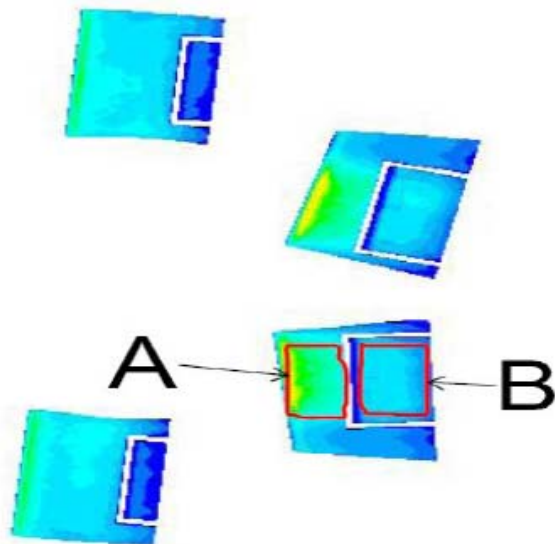


Figure 3. 21(a) High Pressure Difference Zone; (b) Profile of Dynamic Pressure of Tail in Chordwise Coordinate

In figure 3.21(b), there are four groups of particles that stand for the value of profile of dynamic pressure at four different positions in spanwise coordinate of tail. Black colour is the profile of 0.06m in spanwise coordinate, red colour is 0.08m, green is 0.1m and blue is 0.12m. These spanwise coordinates' value are observed from figure 3.22. Combining figure 3.22(a) and figure 3.22 (b), we can find zone A is leading part of the tail, zone B is the part of the control surface, and zone C is the gap between A and B. So the value of dynamic pressure in zone C suddenly decreases, whereas the values of dynamic pressure in zone A and B are almost stable. In zone A these values change between $3.00e+02$ Pa and $5.00e+02$ Pa (marked by red dash). In zone B these values fluctuate between $2.00e+02$ Pa and $2.50e+02$ Pa (marked by red dash). Dating back to previous figure 3.21, we can see zone A and zone B locating at high pressure difference zone. Now let's look at figure 3.22 which displays nine groups of colourful particles so as to show the value of profile of dynamic pressure at nine different positions in chordwise coordinate of the tail. In figure 3.22 (a) Black colour is the profile of 0.1m in chordwise coordinate, red colour is 0.11m, green is 0.12m, blue is 0.13m and light blue is

0.14. And in figure. 3.22(b) Black colour is the profile of 0.15m in chordwise coordinate, red colour is 0.16m, green is 0.17m and blue is 0.18m. These chordwise coordinates' values are obtained from previous figure.3.20. The value of dynamic pressure between two red dash lines in zone A and B shown in figure.3.22 are the same as shown in figure.3.21.

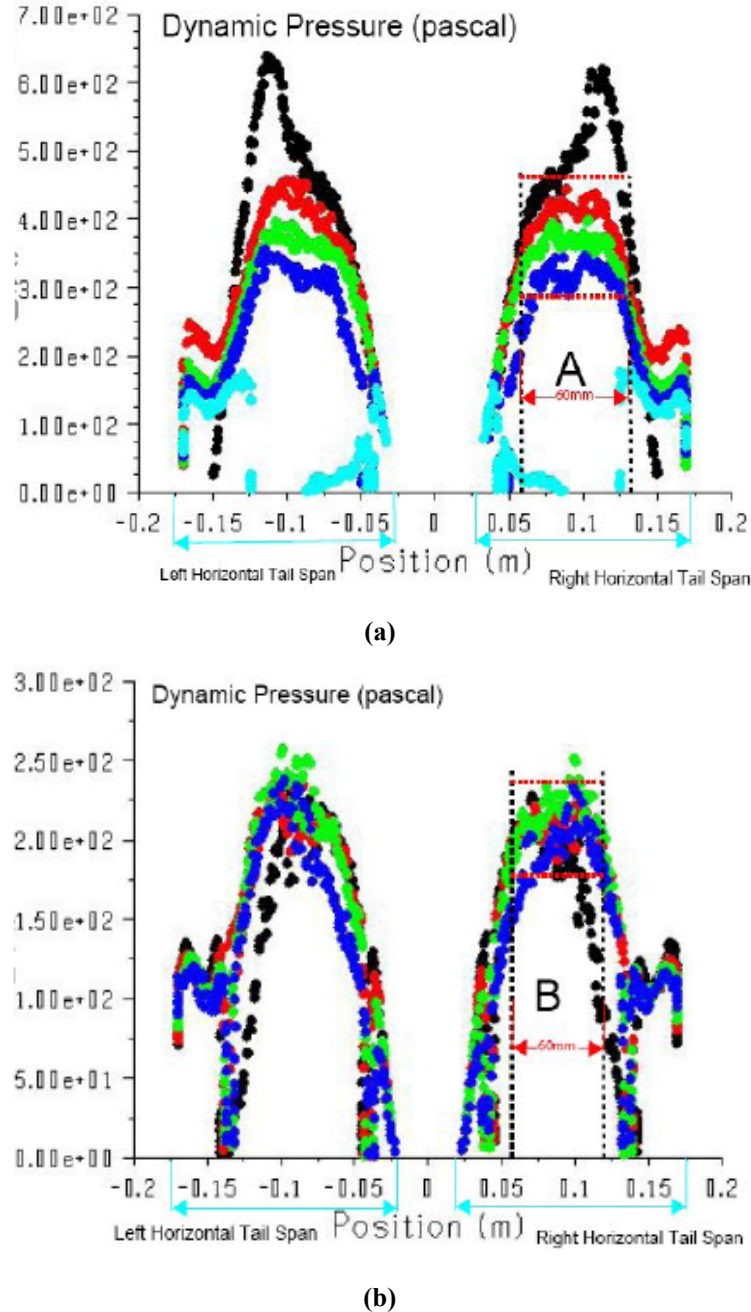


Figure3. 22(a) Profile of Dynamic Pressure of Trail Part of Tail in Spanwise Coordinate;(b) Profile of Dynamic Pressure of Control Surface in Spanwise Coordinate

Then we can evaluate the range of pressure difference zone both in spanwise coordinate and chordwise coordinate based on comparison between Fig.3.21 and Fig.3.22. To get the spanwise range of pressure difference zone, we should observe spanwise coordinate in figure 3.22 . It is approximately (0.06~0.12)m marked by the dimensional arrow in zone A and B. In the same way we also can get the

chordwise range of pressure difference zone which is around (0.1~0.13)m and (0.15~0.18)m by observing zone A and B in figure3.21. Finally, we point out the range of high pressure difference zone on tail in figure3.21 (a).

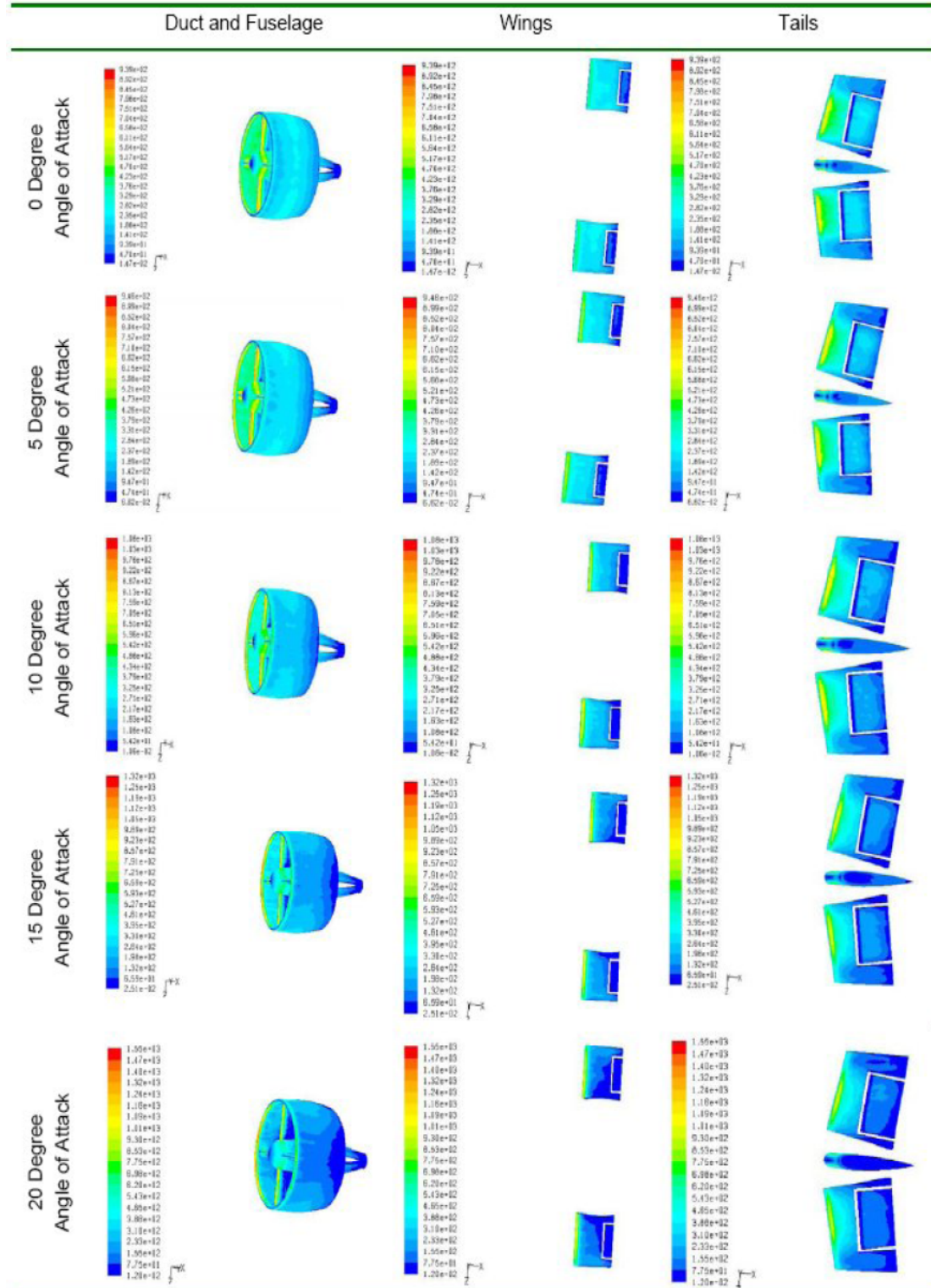
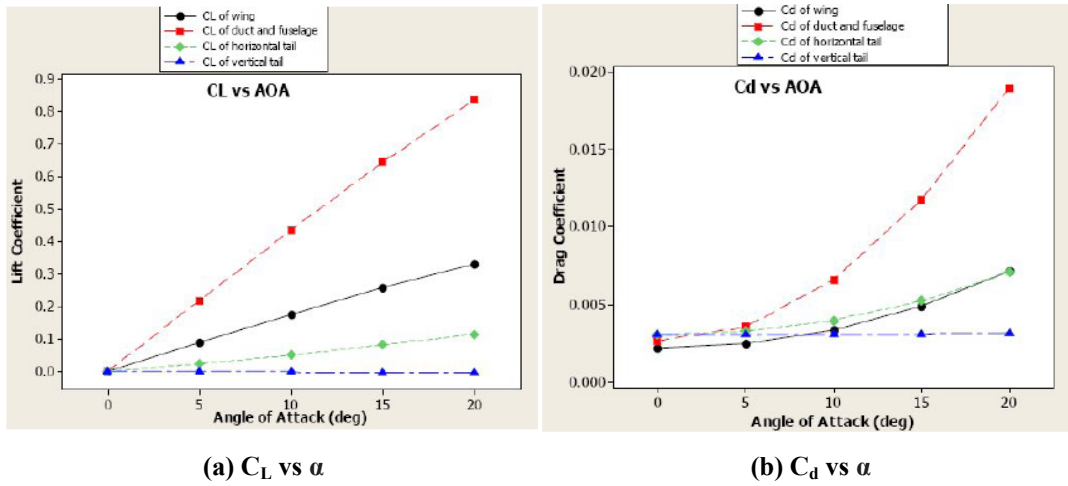


Figure3. 23 Dynamic Pressure on Surfaces of UAV Components (wings, tails, duct and fuselage) at Different Angles of Attack

This figure displays that the dynamic pressure profile on different parts of UAV are changed with an increase of angle of attack [58]. The variation of color is from light to deep, which means the dynamic pressure is decreasing. However, by comparison among three components of UAV, we can see that the dynamic pressure decreasing on tails' surface is much slower than wings and ducts. In particularly, the zone which belongs to pressure difference zone A and B shown in figure.3.21 decreases the slowest due to slipstream angle of attack $\alpha_{p.s}$ in these zones increasing slower than α angle of attack. The Eq.(10) also explains why $\alpha_{p.s}$ is smaller than α . Therefore, we can reach an important conclusion: although α arrives at a high value even at stall angle of attack, the $\alpha_{p.s}$ is still at a small value.

3.6.8 Results and Discussion

In Fig.3.24 from (a) to (d), the CFD results represent the aerodynamic parameters of different part of UAV (in Ref. [56] and [58]). The reference areas for wings, tails and duct are different. The black circle symbols represent the results of wing, the red square symbols is the results of duct and fuselage, the results of horizontal tail and vertical tail are displayed by green diamond and blue triangular symbols, respectively. Fig.3.24 (a), (b) and (c) shows the lift, drag and pitching moment coefficients, respectively, which are plotted as the function of angle of attack of entire UAV belonging to longitudinal aerodynamic parameters. We can see that the aerodynamic data of vertical tail in these three figures are all almost keeping stable without any obvious fluctuation or variation. Whereas the results of wing, duct and horizontal tail are all arise with angle of attack increasing, in addition, from the slope trend of curves we are clear that the value of duct is increasing more dramatically than the wing's and tail's due to the high pressure jumping which occurred in the inner part of duct with fan rotating which has resulted in high value of lift [2]. Compared with duct and wing, the value of horizontal tail increases slowly and gradually, which identifies that the angle of attack of horizontal tail is changing slower than the α of UAV. the correlation between $\alpha_{p.s}$ and α which is described in Eq.(2.40).



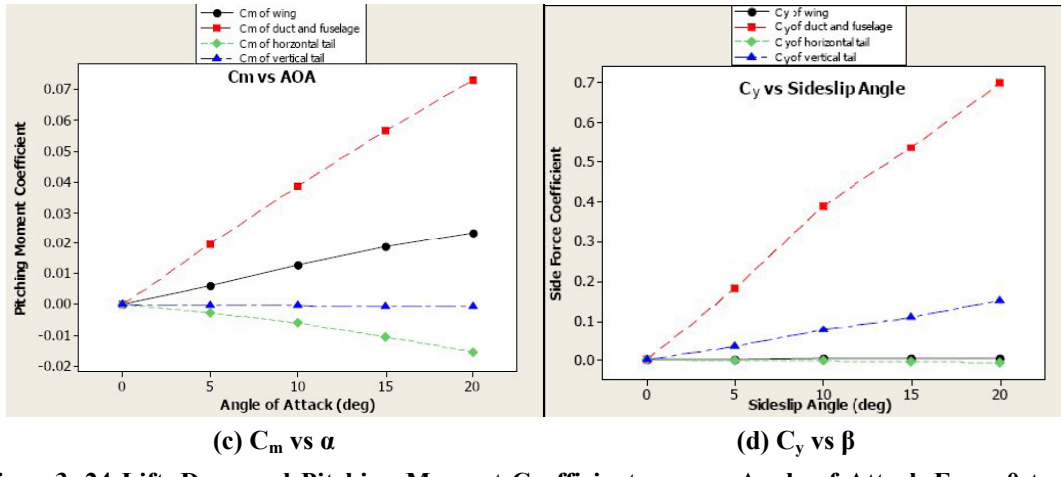


Figure3. 24 Lift, Drag and Pitching Moment Coefficients versus Angle of Attack From 0 to 20 Degree at $\beta=0$ and $\delta e=0$ at Mach 0.12; Side Force Coefficients versus Sideslip Angle from 0 to 20 Degree at $\alpha=0$ and $\delta r=0$ at Mach 0.12.

According to Eq.(2.43) in chapter 2, we know that,

$$C_{L_t} = C_{L_{\alpha,t}} \alpha_{p.s} = C_{L_{\alpha,t}} \frac{\sin \alpha}{\frac{1}{j} + \cos \alpha} \quad (3.26)$$

By CFD simulation from above figures, we also can get,

$$C_{L_{t-CFD}} = C_{L_{\alpha,t-CFD}} \times \alpha \quad (3.27)$$

If we assume that the theory result is equal to CFD results, the following conclusion is obtained by combining the Eq.(3.26) and Eq.(3.27) ,

$$C_{L_{t-CFD}} = C_{L_t} \quad (3.28)$$

$$C_{L_{\alpha,t}} \frac{\sin \alpha}{\frac{1}{j} + \cos \alpha} = C_{L_{\alpha,t-CFD}} \times \alpha \quad (3.29)$$

In chapter 2 we have assumed that if the α is very small, $\sin \alpha \approx \alpha$ and $\cos \alpha \approx 1$,then the simplified equation is like,

$$C_{L_{\alpha,t}} = C_{L_{\alpha,t-CFD}} \times \frac{1+j}{j} \quad (3.30)$$

The equation (3.30) will be used to calculate the aerodynamic coefficient of UAV through CFD results. In Fig.3.24 (d), the side force coefficients are plotted as the function of side angle. The main contribution of side force lift is from duct and vertical tail and the slope of duct curve is bigger than vertical tail, whereas the contribution of wing and horizontal tail is almost zero because of 0 degree angle of attack. The pitching moment, drag and lift coefficients of horizontal tail for Mach 0.12, α is equal to -5, 0 and 5 degree respectively, are plotted as a function of deflection of elevator from -13 to 13 degree on the left side of figure.3.25. The yawing moment, drag and side force coefficients of vertical tail for Mach 0.12, β is equal to -5, 0 and 5 degree respectively, are plotted as a function of deflection of rudder from -8 to 8 degree in right hand of figure.3.25.The circle symbols present the results at 0 degree of α or β , square and diamond symbols represent 5 and -5 degree of α or β , respectively. From longitudinal aerodynamic characteristic in Fig.3.25 we can see that the CL and Cm

are increasing not only based on α , but also δe which is the deflection of elevator. According to this, we can predict the value of $C_{L\delta e}$ and $C_{m\delta e}$ for longitudinal stability and control. In the same way, we also can evaluate $C_{y\delta r}$ and $C_{n\delta r}$ from lateral aerodynamic characteristic in Fig.3.25 for lateral stability and control. And because the value of drag coefficient are very small in comparison with lift, pitching moment, side force and yawing moment coefficient, we can neglect the effects of $C_{D\delta e}$ and $C_{D\delta r}$ for stability and control. As might be expected, the trend of curves either in figure.3.24 or in figure.3.25 looks approximately linear. But more work is required. Especially, by conducting experiments in Wind Tunnel more data should be obtained, then we will compare the results between CFD and Wind Tunnel experiments so as to identify whether the CFD data are accurate enough to be used in prediction of UAV stability and control.

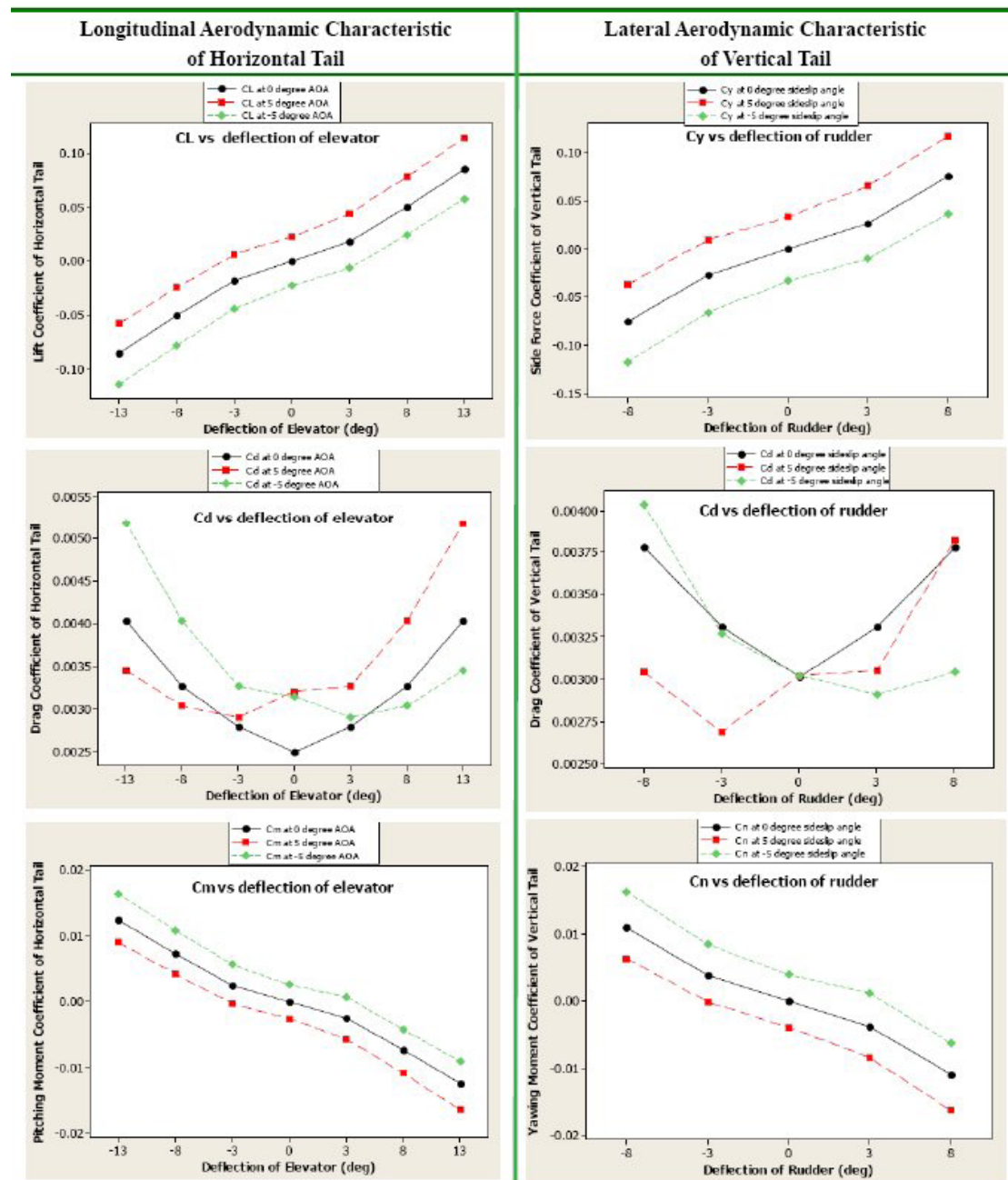


Figure3. 25 Longitudinal and Lateral Stability and Control Predictions

From figure 3.26 we can see that the mass of high speed turbulent flow through the ducted fan gradually decreases with the angle of attack increasing from 20 to 50 degree. The reason this occurs is the mass flux in X direction decreasing in terms of the relationship between X mass flux and angle of attack mentioned in chapter 2. Meanwhile the flow separation becomes more serious due to the gradient of negative pressure raise, this can actually be observed in figure 3.25(c) and (d). The dark blue area is extended, and then the zone of negative pressure is expanded as well.

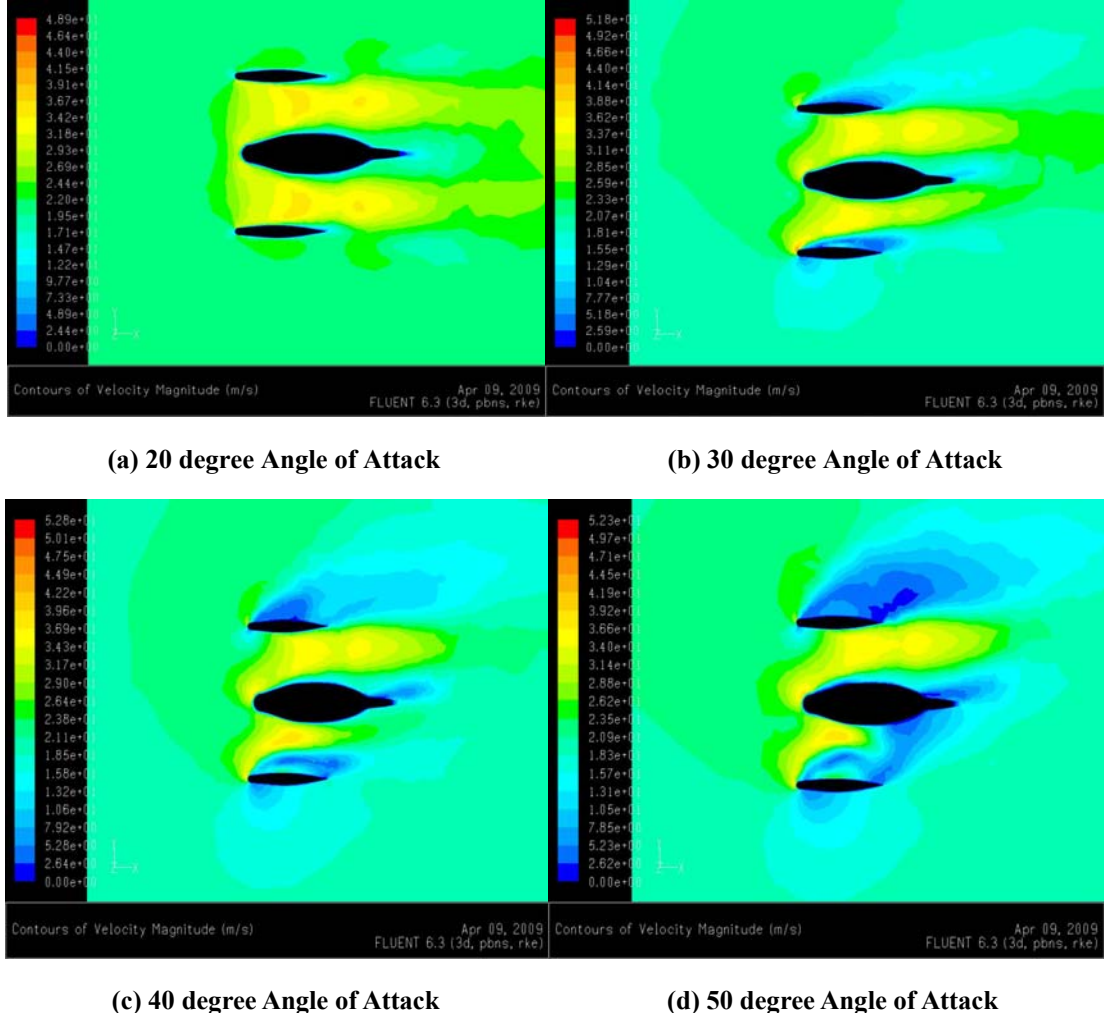
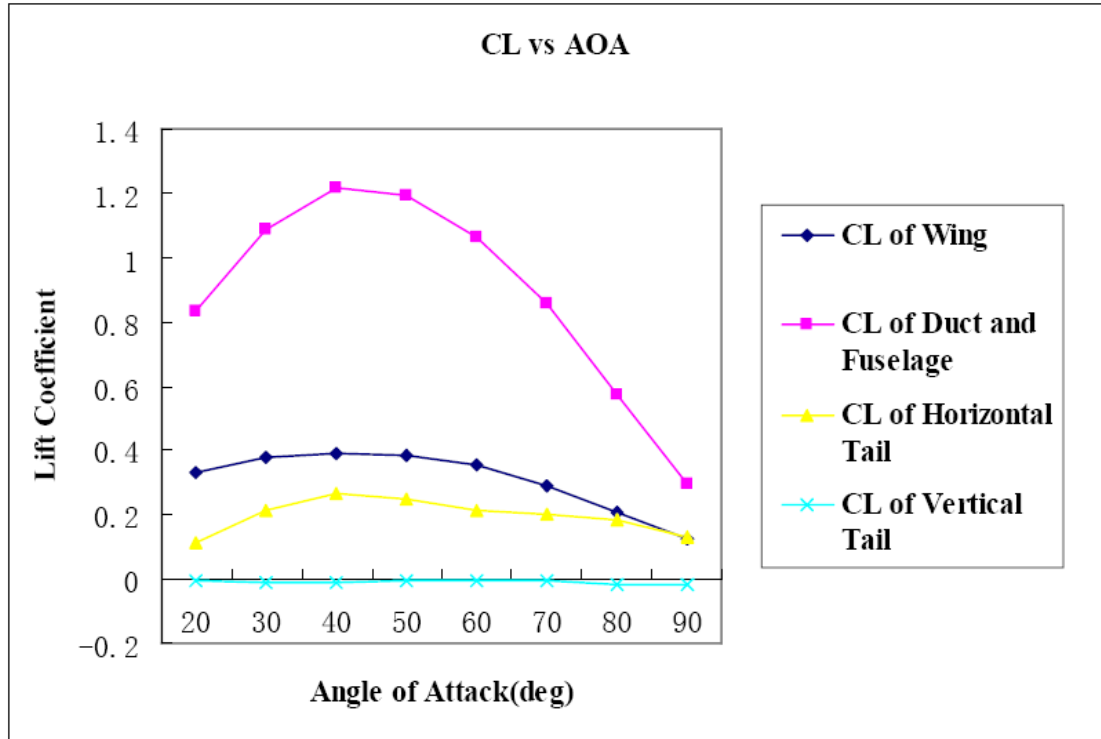


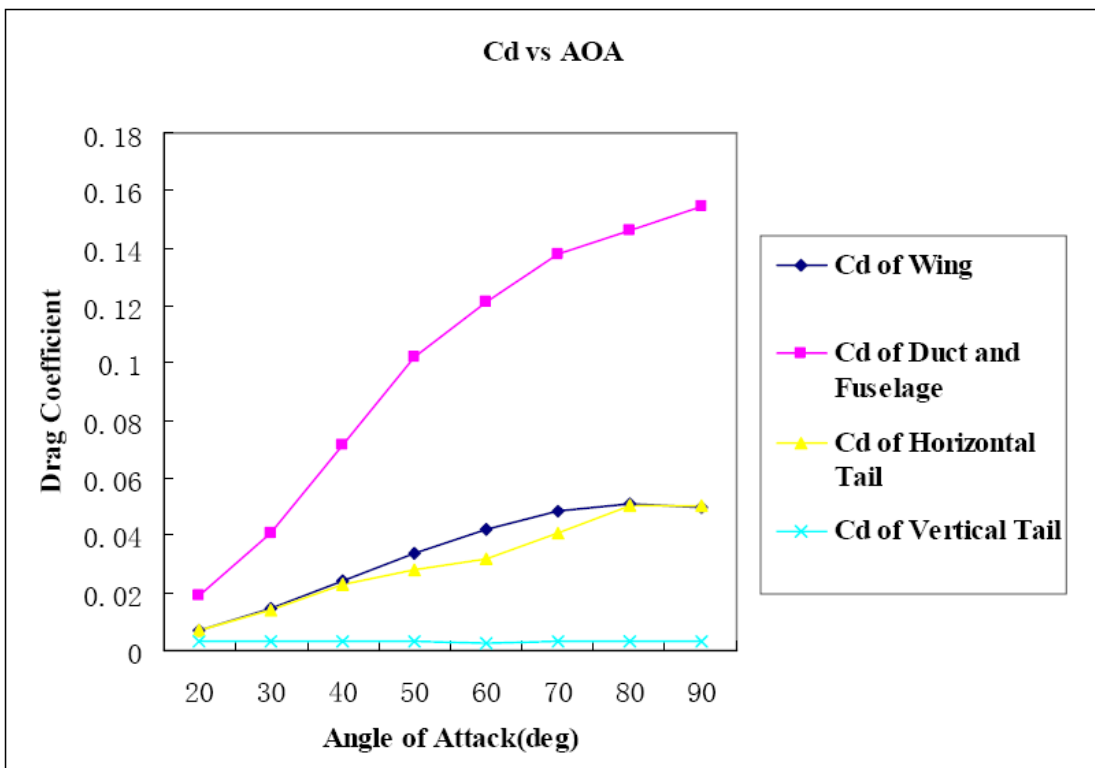
Figure3. 26 Flow Pass through UAV at Large Angle of Attack from 20 to 50 Degree.

From figure 3.24 the trend of C_L vs α , C_d vs α and C_m vs α are plotted as a function of angle of attack from 0 to 20 degree. They are all nearly linear at a low value of α . However, in the case of large angle of attack the trend of curves are converted because of the mass flux through ducted fan reducing and the zone of negative pressure increasing. The figure 3.27 shows the tendency of lift, drag and pitching moment changed with risen of angle of attack. The square curve of (a) describes that the lift of duct and fuselage keeps increasing and arrives at top value of 1.2 at 40 degree which is the stall angle of duct with fuselage. Then it decreases sharply and gets the bottom value at 90 degree angle of attack. Compared with lift of duct and fuselage, the wing and horizontal tails' lift coefficient rise gradually. From 40 to 55 degree lift, coefficient of wing keep stable and don't decrease until 55. This means that the stall angles of wing are delayed. In contrast to wing, the lift coefficient of horizontal tail nearly remains at approximate 0.2 from 30 to 80 degree with a little bit fluctuation, which explains that the

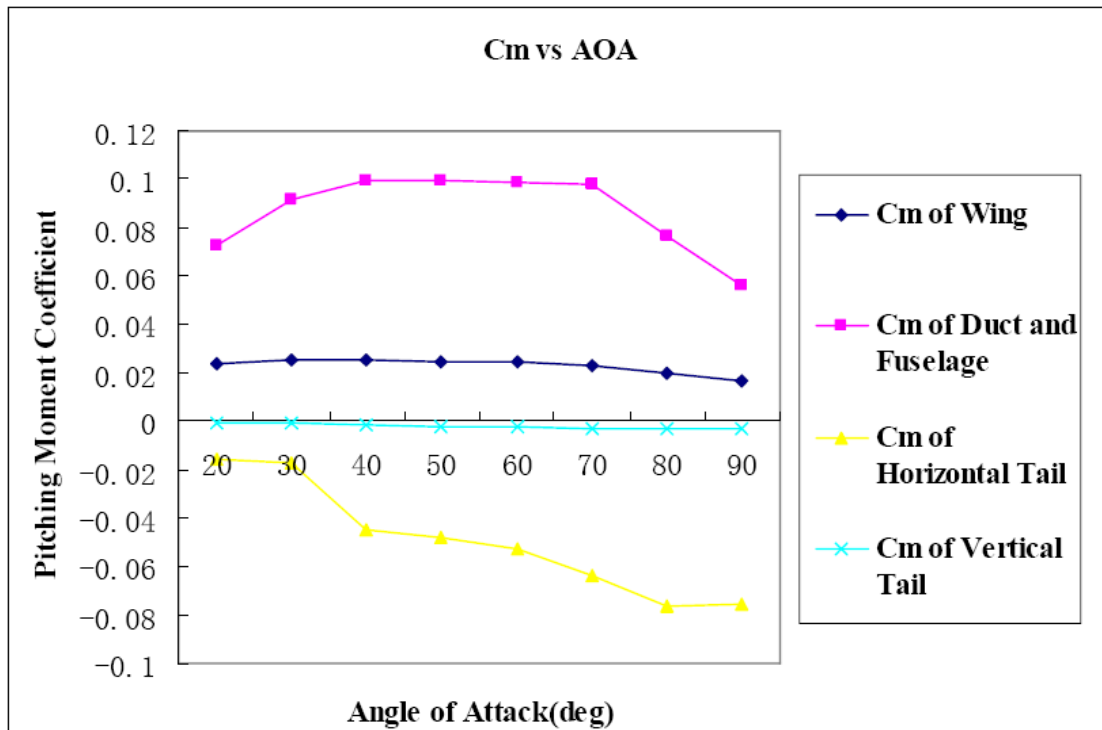
stall phenomena which happens on horizontal tail is not obvious. From curve of (a) in 3.27 we know that the extrapolation of Eq.2.40 in chapter 2 is matched well with CFD results. This confirms the conclusion: although α of wing, duct with fuselage arrive at stall angle of attack, the $\alpha_{p,s}$ still doesn't arrive at the value of stall angle. Based on this correlation between angle of attack α and slipstream angle $\alpha_{p,s}$ this UAV is able to realize special flight performances, such as, slide flying at large angle of attack or sideslip angle (70~80)degree.



(a) Lift Coefficient VS Angle of Attack



(b) Drag Coefficient VS Angle of Attack



(c) Pitching Moment Coefficient VS Angle of Attack

Figure3. 27 Lift, Drag and Pitching Moment Coefficients versus Angle of Attack From 20 to 90 Degree at $\beta=0$ and $\delta_e=0$ at Mach 0.12

In figure 3.27(b) the drag coefficient of wing, duct with fuselage and horizontal tail keeping rising with the increase of angle of attack. C_d of duct with fuselage climbs up dramatically, whereas the wing's and horizontal tail's is going up gradually relative to duct with fuselage. Let's look at the figure 3.27(c), the positive value means that the pitching moment is nose-up moment, naturally, the negative value is nose-down moment. Wing and duct with fuselage provide the nose-up moment from 0 to 90 degree. C_m of wing is stable at a low value from 30 to 70 before going down. The values of C_m of duct with fuselage from 40 to 70 degree remain at a high number of 0.1 before decreasing to 0.06 at 90 degree. Obviously, the contribution of nose-up moment coefficient is supplied by duct and fuselage.

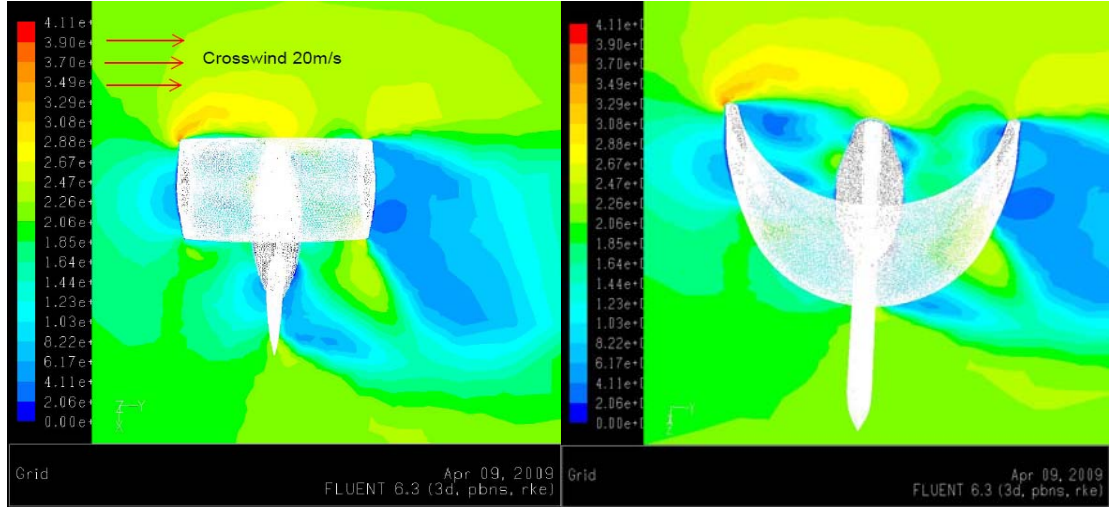


Figure3. 28 Crosswind Act on UAV at 90 Degree Angle of Attack

C_m of horizontal tail is sharply increasing from 30 degree although it generates nose-down moment. This is what we want to use to achieve the longitudinal control as the innovation of this project. Among the components of UAV the vertical tail's contribution is the smallest in longitudinal aerodynamic coefficients regardless of C_L , C_d or C_m , thus it can be ignored during analyzing the longitudinal dynamic model.

Figure 3.28 displays the UAV hovering at 90 degree with crosswind at 20m/s (see also Appendix C). We can see that the low pressure region generated on the windward lip of the duct in a strong crosswind, and the high pressure region created on the other side of the duct with fuselage. This tends to increase the windward lip's local angle of attack of duct. Then the duct lip suction becomes asymmetric, creating a counter-torque that has an opposite direction in contrast to the desired pitching motion which is required to counteract the crosswind nose-up moment because of the ram drag mentioned in Eq.(2.49). Therefore, the high efficiency of control relied on horizontal tail is the key point of longitudinal control in the use of conquering this crosswind nose-up moment.

3.7 Summary

In this chapter the main achievement is use of an existing CFD code (FLUENT) to predict the complicated longitudinal and lateral characteristics of the preproduction ducted fan VTOL UAV at low Mach number. By using CFD methodology to simulate UAV tails and control surfaces totally

submerged in the propeller slipstream, the innovation of using propeller slipstream effects on control surfaces to achieve attitude control of UAV is available in conditions of low speed or hovering. Because the correlation of CFD with Wind Tunnel data is still unknown, much more work is required to be done, in particularly, how to design a proper experiment in Wind Tunnel to measure some essential aerodynamic parameters for this VTOL UAV stability and control is necessary. This will be detailed in the following chapter. Only using experimental data to compare with CFD result and support them, and dependent on much more data in different Reynolds and Mach numbers, a more convincing conclusion is able to be obtained. Based on both computational fluid dynamic results and wind tunnel data, the dynamic model of UAV is able to be built up.

Chapter 4

4 Wind Tunnel Testing

In this chapter, the materials of UAV model with propulsion system are listed and the investigation of aerodynamic coefficients and flight parameters of ducted fan VTOL UAV in wind tunnel are detailed. The full-scale UAV model with engine is placed in RMIT Industrial Wind Tunnel for testing its aerodynamic characteristics and its properties of counter-rotating propulsion system. The detailed data will be shown after the description of wind tunnel testing process.

4.1 Equipments and Devices

The experiment is composed by two main steps including test of UAV model with fan rotating and wind tunnel testing. Therefore, several devices and equipment used in this experiment will be introduced.

4.1.1 Propulsion System of UAV

The propulsion system of UAV includes four components which are a couple of propellers, two motors, two speed controllers and servo adjustors.

- **Propeller**



Figure4. 1 6x4 3-Blade Series Propeller (Ref. website)

In figure 4.1 the 3-blades propeller is shown. It includes following features:

- 6x4 inches-15x10cm
- NACA airfoils
- True pitch
- Accurately balanced.
- Greater thrust at lower RPM
- Two types: clockwise (normal) and counter-clockwise (pusher)

- **Motor**



Figure4. 2 Himark Out-runner Brushless Motor (Ref. website)

Above figure shows the motor with washer and some screws. In table 4.1 the specification of motor is given.

Table 4.1 Specification of Brushless Motor

1/ C2808-20 Himark Outrunner BL Motor	
Kv(rpm/V)	1720
Maximum Power (rpm)	24080
Shaft Diameter (mm)	3.17mm
Cells NO	2~3(Li-poly)
Current A	8~12A
MAX current A	13.4A
Diameter(mm)	28mm
Length(mm)	25mm
Weight	44g

- **Servo Adjuster**



Figure4. 3 EK2-0907 Servo Tester/Adjuster (Ref. website)

This E-sky servo adjuster allows the user to connect 1 or 2 servos for testing without the use of receiver and transmitter. Process: connect any 4-5 receiver packs for power, plug in servos, rotating the knob to test the travel then return the knob to the middle to centre servos

Table 4.2 Specification of Servo Adjuster

EK2-0907 Servo Tester Specification	
Consumption	<=15mA(Current 5.0V)
Static current	<=3mA (5.0V), ta=25 C output
Signal	1.5ms~.5ms
Size	42.5*24.0*23.5mm
Weight	8g
Pulse generator for servo testing Pulse width adjust	: MANUAL Also can read the transmitter pulse width via receiver output terminal

● **Speed Controller**

HOBBYWING

SWORD-18A



www.icantoy.com

Figure 4.4 Speed Controller (Ref. website)

Following points are copied directly from manual on website.

- 3 start modes: Normal / Soft / Super-Soft, compatible with fixed-wing aircraft and helicopters.
- Throttle range can be configured and is fully compatible with all transmitters currently available on the market.
- Smooth, linear and precise throttle response.
- Separate voltage regulator IC for microprocessor, providing good anti-jamming capability.
- Supported motor speed (Maximum): 210000 RPM (2 poles), 70000 RPM (6 poles), 35000 RPM (12 poles).

Table 4.3 Specification of Speed Controller

SWORD-18A	
Output	Continuous 18A, Burst 20A up to 10 Seconds
Input Voltage	2-4 cells lithium battery or 5-12 cells NiCd/NIMh battery
BEC	: 2A / 5V (Linear mode).
Max Speed	210,000rpm for 2 Poles BLM, 70,000rpm for 6 poles BLM, 35,000rpm for 12 poles BLM. (BLM: Brushless Motor)
Size	45mm (L) * 24mm (W) * 11mm (H)
Weight	22g

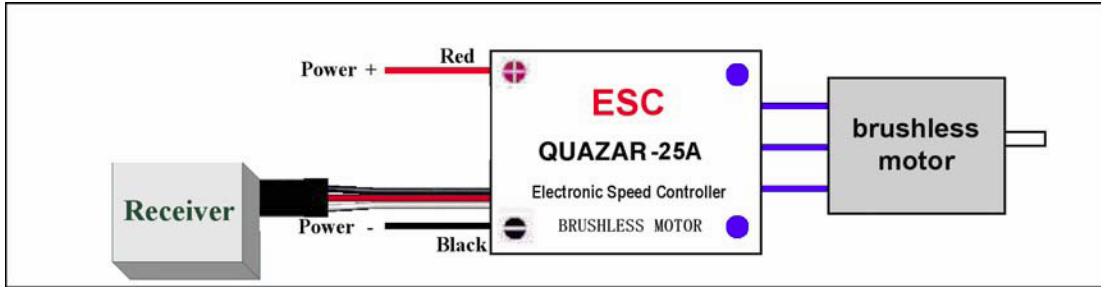


Figure4. 5 Description of Flowchart of Propulsion System (Ref. website)

Following three points are copied directly from manual on website.

1. Move the throttle stick to the bottom position and then switch on the transmitter.
2. Connect the battery pack to the ESC, the ESC begins the self-test process, a special tone “123” is emitted, which means the voltage of the battery pack is in normal range, and then N “beep” tones will be emitted, means the number of lithium battery cells. Finally a long “beep-----” tone will be emitted, which means self-test is OK, the aircraft/helicopter is ready to go flying.
 - If nothing happens, please check the battery pack and all the connections;
 - If a special tone “ ” is emitted after 2 beep tones (“beep-beep-”), means the ESC has entered the program mode, it is because the throttle channel of your transmitter is reversed, please set it correctly;
 - If the very rapid “beep-beep-, beep-beep-” tone is emitted, means the input voltage is too low or too high, please check your battery’s voltage.
3. Because transmitters have different throttle ranges, the operator use the “Throttle Range Setting Function” to calibrate throttle range is strongly suggested.

4.1.2 Thrust Testing

According to flowchart of propulsion system in Fig 4.5, we can connect the propeller and motor with speed controller, and mount the propulsion system to load cell using screws as shown in Fig 4.6. Then the thrust generated is able to be recorded by digital equipment which collects the data from load cell through cables.

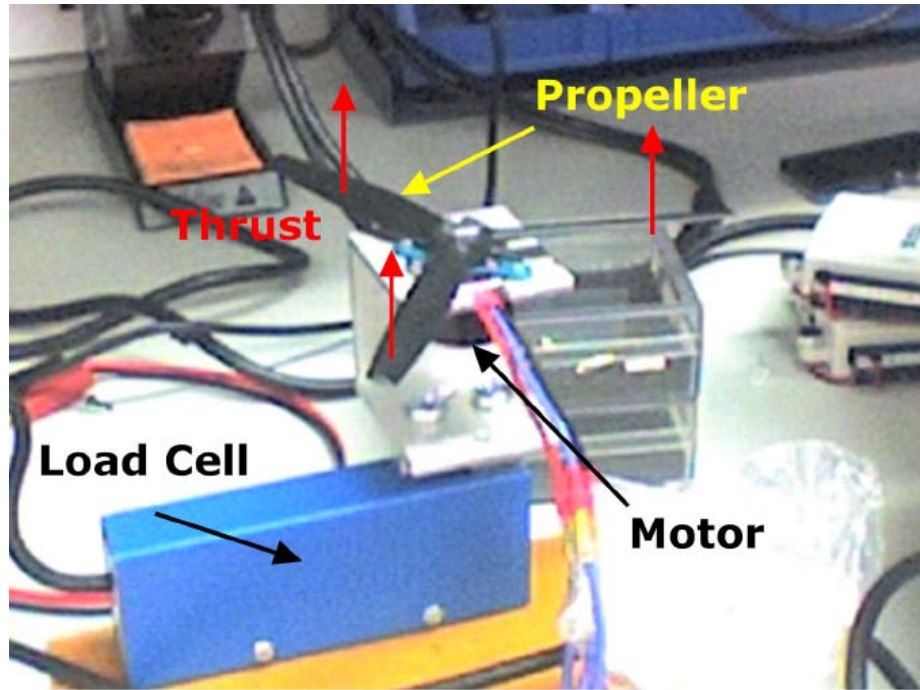


Figure4. 6 Using Load Cell to Test Thrust

The results in figure 4.7 are thrust generated by one motor and one propeller in different voltage. It means that the thrust is increasing with the increase of voltage adding to motor. This figure gives two kinds of units for value of thrust. One is given by μ strain, the other one is gram which is also equal to 10^{-2} Newton. To get from μ strain to gram, we can use 1.9 to divide μ strain. From the results we then know that each motor with propeller supplies maximum thrust about 2.3 Newton. So, two propellers with motors can provide approximate 4.6 Newton for thrust of UAV.

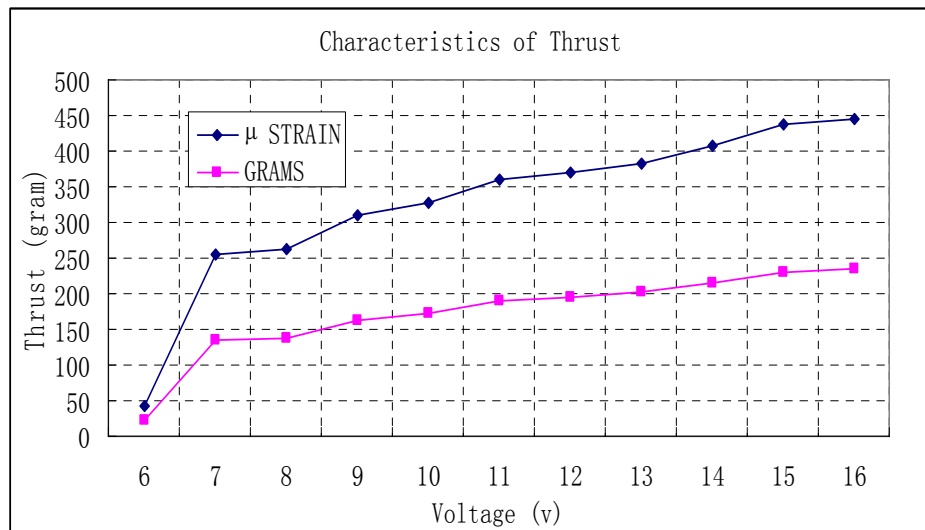


Figure4. 7 Data of Thrust in Different Voltage (per motor)

4.1.3 Manufacturing of Full-scale UAV Wind Tunnel Model

The School of Aerospace, Mechanical and Manufacturing Engineering (SAMME) has various kinds of machines to manufacture different types of model, such as road vehicles, UAV and robots. Rapid Prototype Machine (RPM) is one of the popular manufacturing devices for producing and building small size models of which structures are usually too complicated to make by hand. In this case, the RPM plays a significant role in manufacturing, compared with human-work, not only saving time, but also improving the quality of products.



Figure4. 8 Rapid Prototype Machine (RPM)

Figure 4.8 displays the RPM (brand is called Dimension FDM) located at School of Aerospace, Mechanical and Manufacturing Engineering of RMIT. It is this RPM that we used to build up the UAV model. It consists of workshop, control panel, material entrance and computer input.

- Computer Input: Transfer the 3D model file from any format (CATIA, Solid-work, or Pro-Engineer) into STL format. Then sent the command of work into RPM through a digital cable.
- Material Entrance: Put the material in the machine from entrance. Two kinds of material are applied. (Support material and Structure material ABS which is a common thermoplastic used to make light, rigid, molded products such as piping, for example plastic pressure pipe systems, musical instruments).
- Control Panel: Include start, pause, time record and stop to control the RPM in need of working.
- Workshop: It is also called working area in which the models are built by small automatic mechanical robots (mechanical arms and automatic material supplied)

In figure 4.9 we can see how the RPM is working. The UAV model is gradually built layer by one layer relying on the robot. When the first layer is done on the support disk, the robot builds the second

layer overlapping the first layer. Each layer is supported by Support Material and is formed by Structure Material. The process of model building doesn't stop working until it is all finished in the workshop.

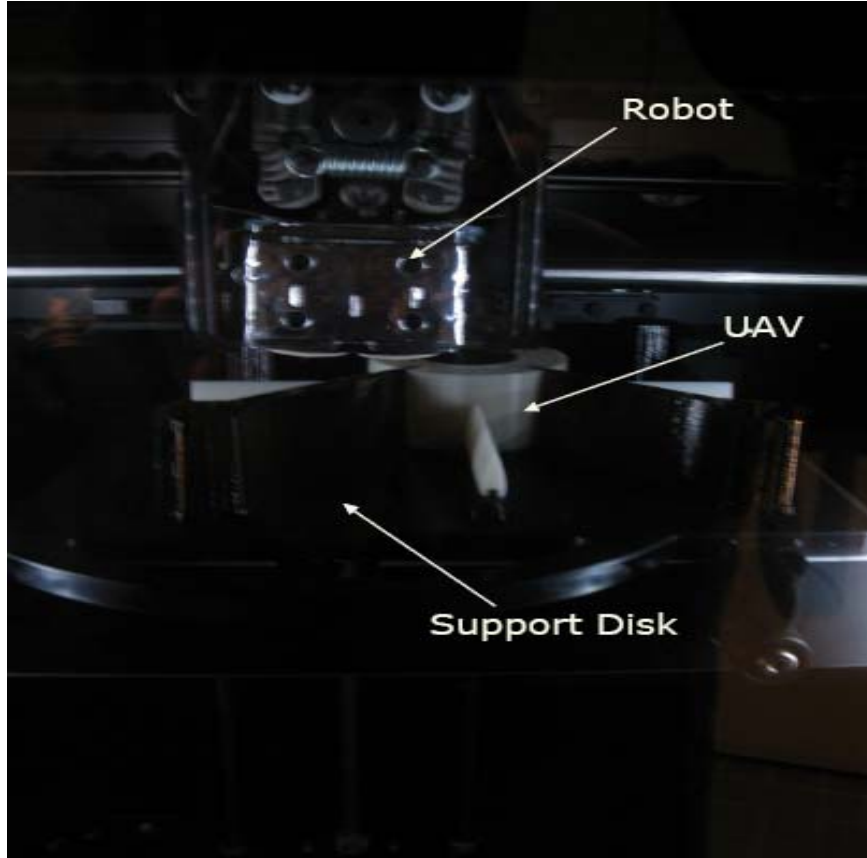


Figure4. 9 Principle of RPM Working

4.1.4 UAV Model

The components of UAV model are made by Rapid Prototype Machine one by one, then assembling all of them using screws and pins in the student workshop at SAMME. The propulsion system is also mounted in the hollow of hub and fuselage of UAV with the conjunction of washer and adapter in Fig 4.10. The three holes in the front of the hub are used to cool down the temperature of the motor, which is rotating at high speed within long periods, to avoid burning up.

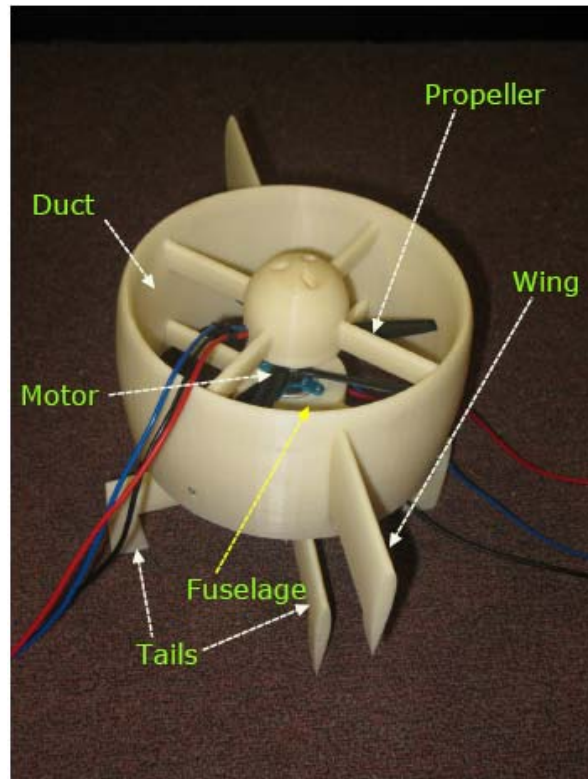


Figure4. 10 UAV Model Assembled with Propulsion System

4.1.5 Flow Pattern Testing

To make sure the counter-rotating of two propellers is working well and to observe propeller slipstream flowing over the four control surfaces (tails), simple testing can be done for capturing the flow patterns.



Figure4. 11 Flow Patterns

First of all, using transparent tapes attach some red color woolen strings on trailing edge of tails as shown in Fig 4.11, but turning off the power to make sure the propeller slipstream is null. The photo on left hand shows the appearance of strings without slipstream. All of them are going down. Then switching on power, it is obvious that the red strings are almost horizontal like flow streamline in water

tunnel. Finally, from this figure we can conclude that the four tails are totally submerged within the propeller slipstream. The phenomena are what we expect.

4.1.6 Industrial Wind Tunnel

The engineering wind tunnel at RMIT is low-speed and closed-jet type (see Ref. [37]), which has a test section of 2 meters' height, 3 meters' width and 9 meters' length. The flow generator is a turbo fan which can provide a maximum speed of around 50m/s (180km/h). It is big enough to fulfill different types of industrial test, such as automotive experiment, aerodynamic and aerospace testing.

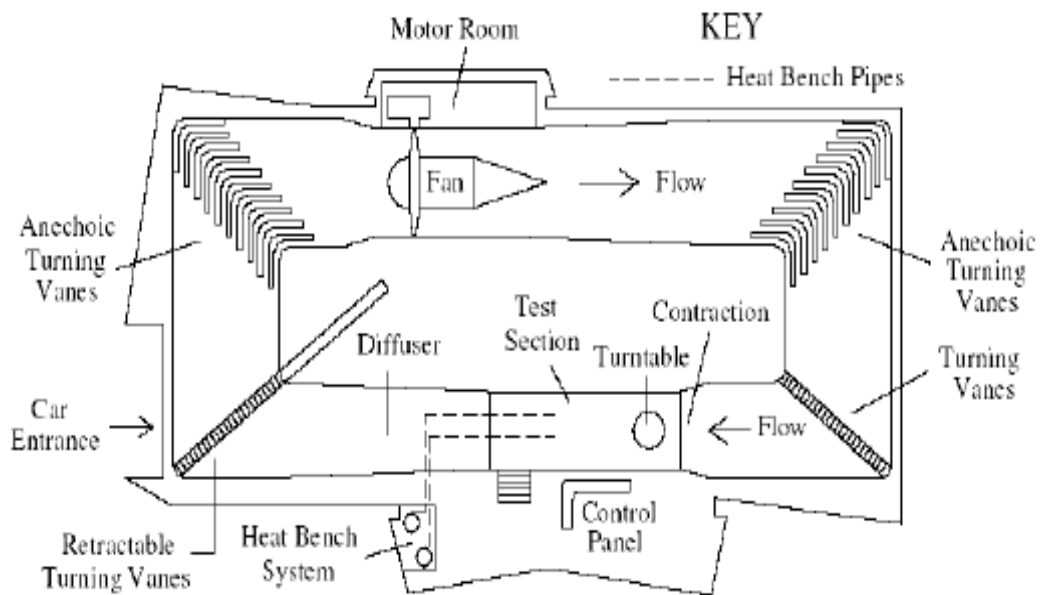


Figure4. 12 Layout of RMIT Industrial Wind Tunnel (Ref. [37])

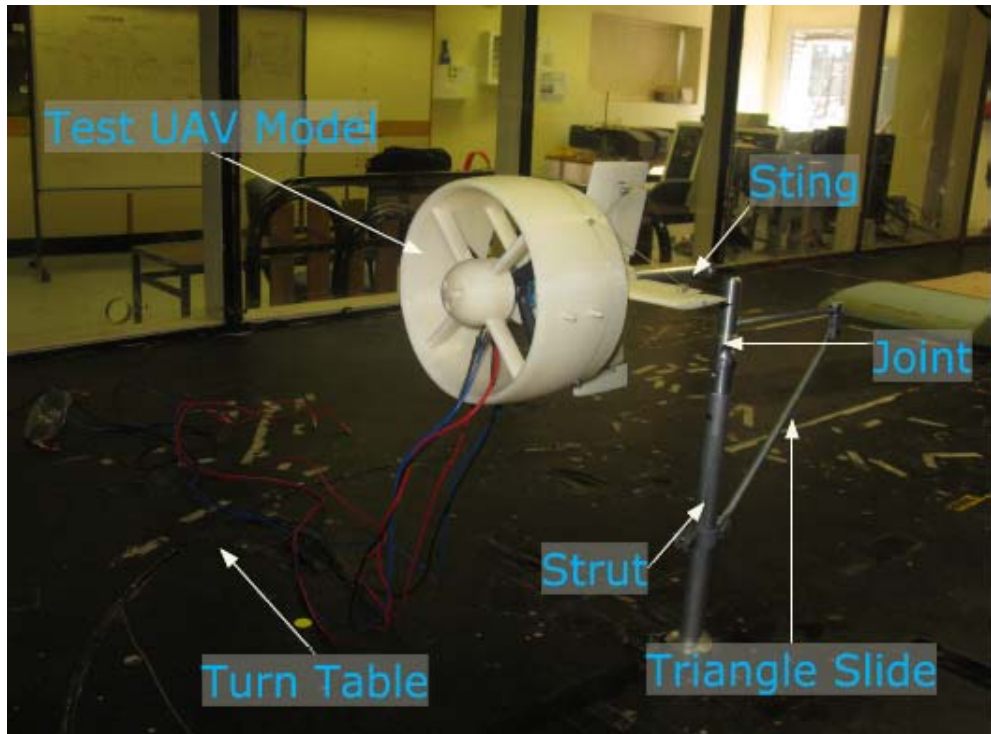


Figure4. 13 Building up UAV Model in Test Section

4.1.7 Test Setting

Figure 4.13 displays the layout of test setting in wind tunnel. At the beginning, the UAV is mounted with sting which is plugging into backside of fuselage. Secondly, using strut support joint connected with sting to assure the UAV model keeps the fixed position and attitude along the central line of test section of wind tunnel. Meanwhile, the strut is fixed to turntable and goes down to the underneath where the six components force balance and JR-3 six components load cell [37] are combined to measure the three forces (X, Y and Z) and three moments (M_x , M_y and M_z) of UAV as the flow pass through. Finally, the test results are able to be collected from the computer outside the tunnel near the control panel.



Figure4. 14 JR-3 Six Components Load Cell (Ref. [37])

Based on CFD results and theoretical calculation, we can the measure range of six components of forces and moments. The JR-3 load cell is chosen in terms of measure range as shown in table 4.4. The reason why the load cell is selected is the sensitivity which is suitable for the case of UAV model. To choose a good sensitivity load cell for testing is the key point which determines the quality of final results.

Table 4.4 Measure Range of Six Components

Six Components of Forces and Moments	Measure Range
F_Z (Lift)	± 100 N
F_X (Drag)	± 50 N
M_Y (Pitching Moment)	± 10 N/m
F_Y (Side-force)	± 100 N
M_X (Rolling Moment)	± 10 N/m
M_Z (Yawing Moment)	± 10 N/m

4.2 Measurement of Aerodynamic Characteristics

Two schemes are going to be applied during the wind tunnel testing. First scheme is measuring the aerodynamic coefficients of UAV without two wings. In this case, the geometry of UAV model is total symmetry about central axis of itself. So longitudinal tests and lateral tests are the same as each other. However, the second scheme is assembling two wings to the model. Then the aerodynamic testing has to be done not only in the longitudinal position, but also in the lateral position. Also the lift and pitching moment will be different from the model without wings.

4.2.1 Counter-rotating Test

As we all know that counter-rotating always happens in the case of coaxial propellers used in helicopters. In this project, this methodology is also applied to reduce the torque generated by two directional rotating propellers or fans. Even in some special conditions two of the torques can counteract with each other. The case is called zero counter torque.

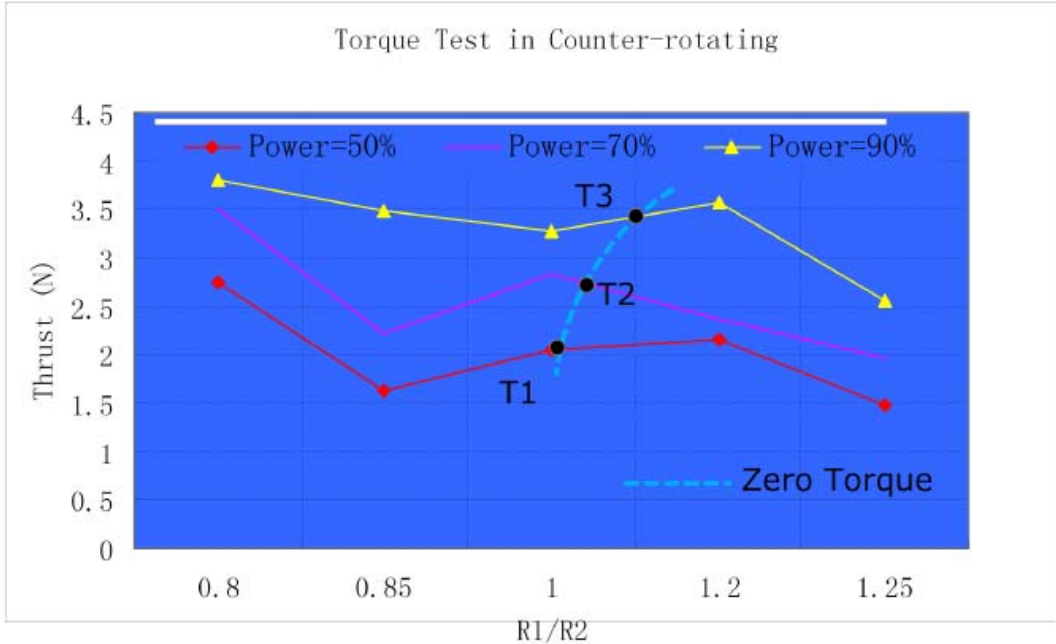


Figure4. 15 Propeller Torque Test in Counter-rotating

Figure 4.15 highlights three important points marked by black dots. The diamond symbol, none symbol and triangle symbol curve represent thrust versus the ratio of R1 and R2 within 50%, 70% and 90% of maximum power, respectively. R1 and R2 mean the RPM of front propeller and back propeller. The dash line is the zero counter torque line which presents the zero torque versus R1/R2 within any power. This dash is crossing with three thrust curves at point T1, T2 and T3 where the zero torque occurs. From the trend of the dash line, we can conclude that for the counter torque to be zero, the ratio of R1 and R2 should be increasing with the rise of power. And at least the R1>R2 means that rotating speed of front engine is higher than back one.

4.2.2 Test without Wings

Now, let's focus on the aerodynamic experiment of UAV model without its wings. In Fig 4.16, it is clear that there are no wings fixed with UAV. Therefore, the aerodynamic data measured by six components force balance exclude forces and moments generated by two wings.

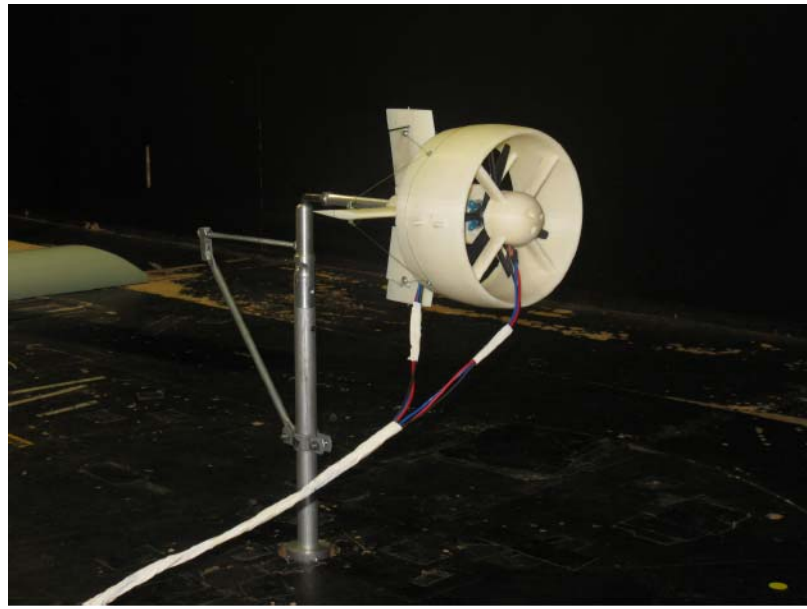


Figure4. 16 UAV Test without Wings

First of all, we change the angle of attack of UAV from 0 to 90 degrees. To achieve this, the joint plays an important role in changing the attitude of model through moving triangle slide up or down. Meanwhile, we can control the air speed from the control panel of the wind tunnel. Three schemes are tested. They are 10km/h (3m/s), 35km/h (10m/s) and 70km/h (20m/s), respectively. The thrust which we use are T1, T2 and T3 shown in figure 4.15.

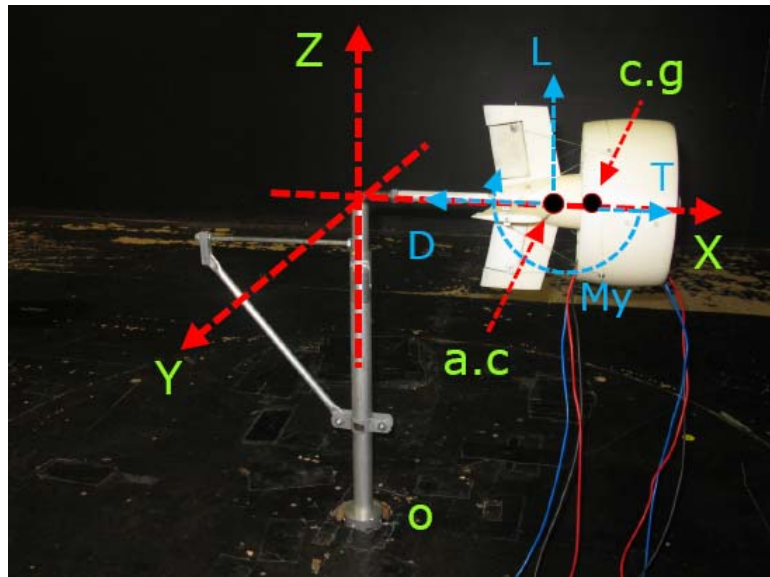
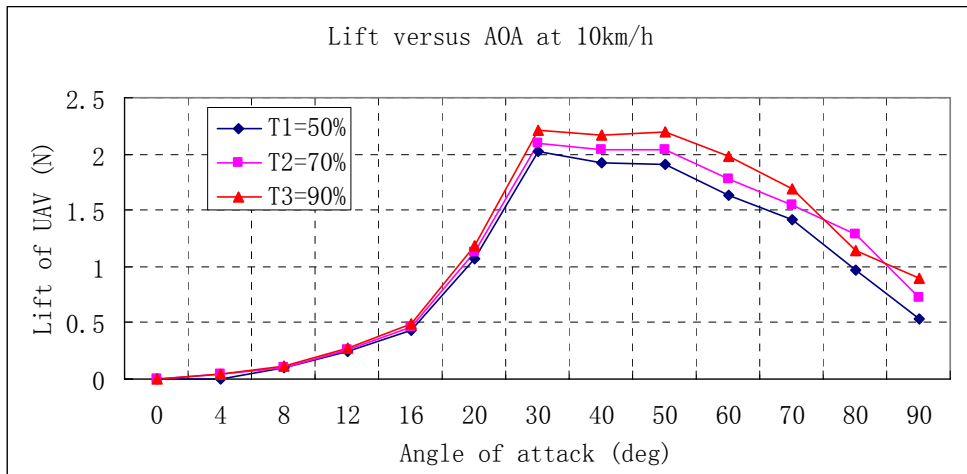
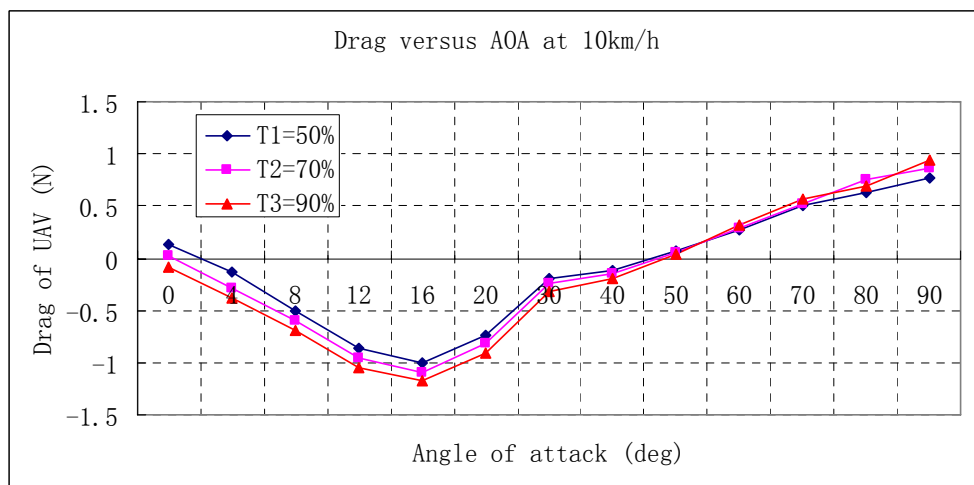


Figure4. 17 Forces and Moments on UAV in Wind Tunnel

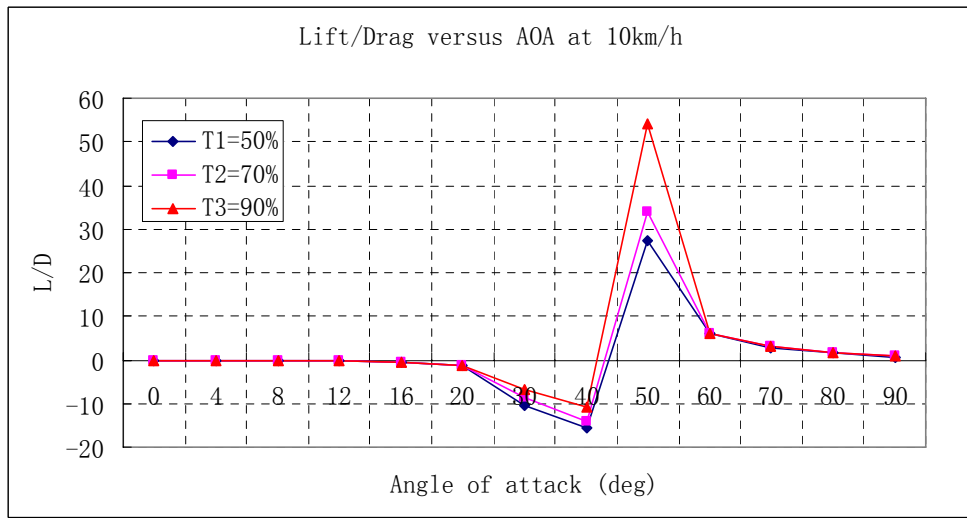
Before we collect and record the data using software in computer, one point should be taken into account. It is the initializing zero for initial value of load cell to avoid the error generated by environment, equipment or mechanical vibration due to the accuracy of results have to be guaranteed.



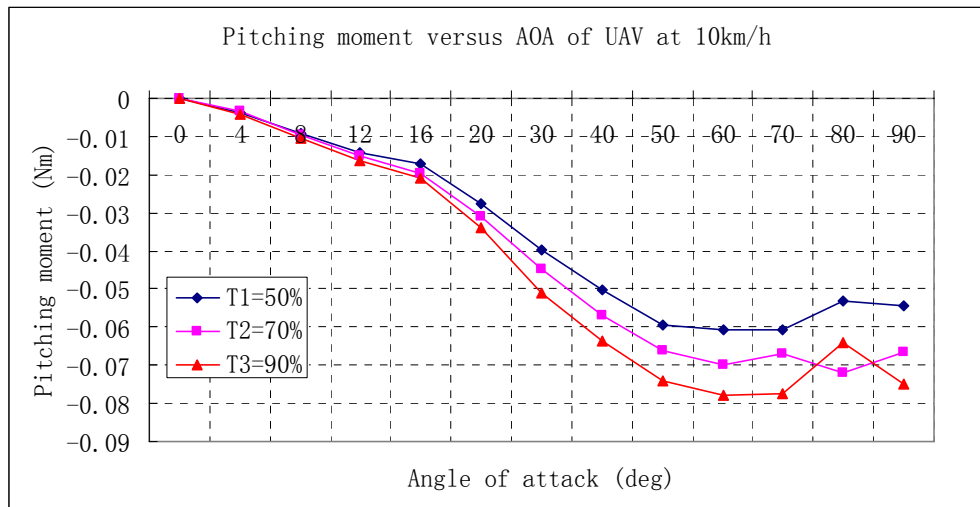
(a) Lift vs AOA



(b) Drag vs AOA

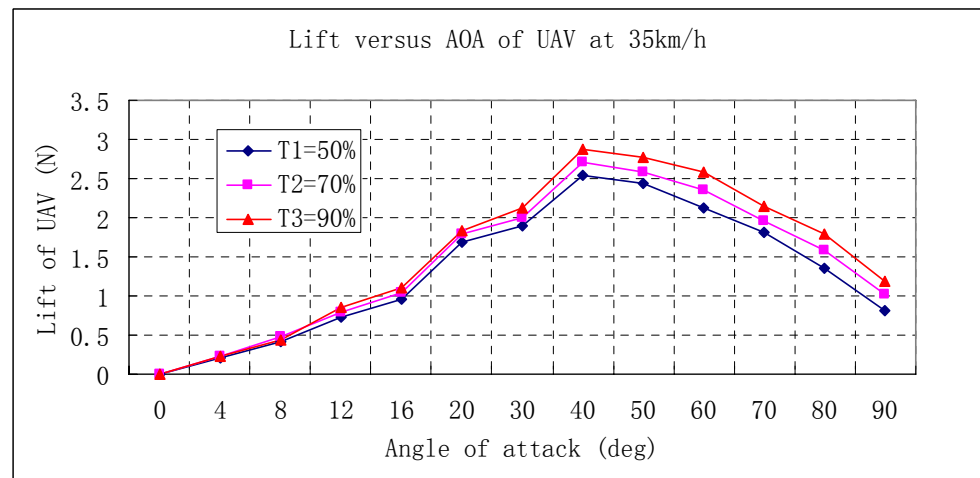


(c) L/D vs AOA

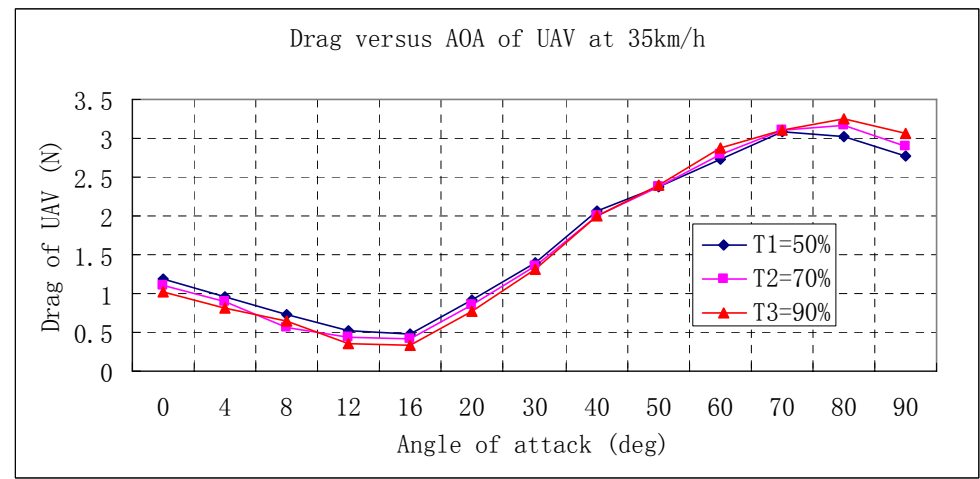


(d) Pitching moment vs AOA

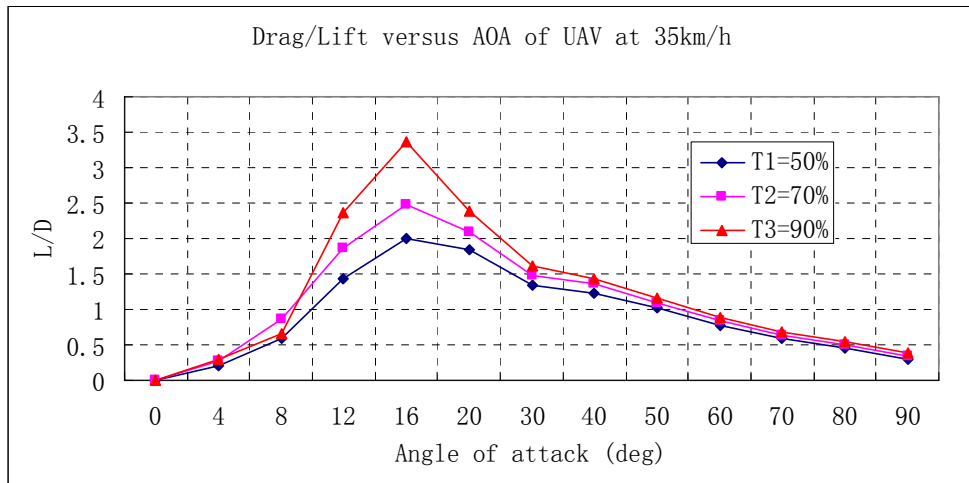
Figure4. 18 Aerodynamic Coefficients versus AOA of UAV with different thrusts at 10km/h



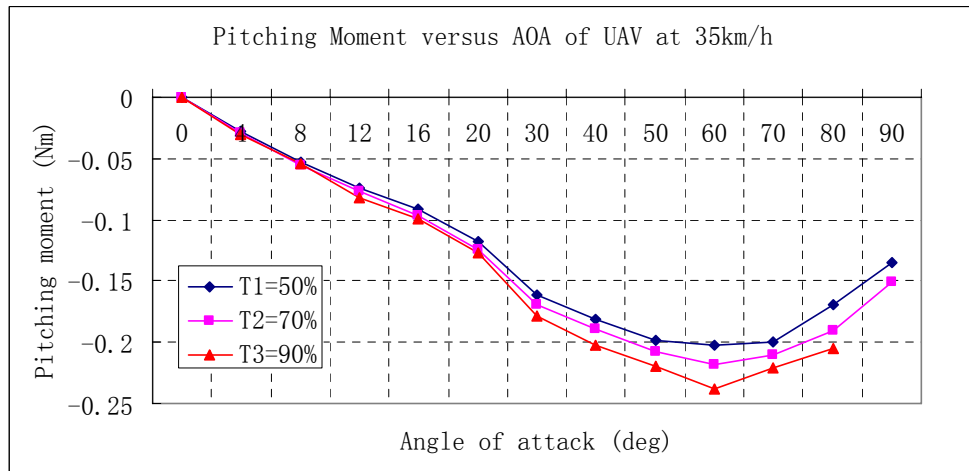
(a) Lift vs AOA



(b) Drag vs AOA

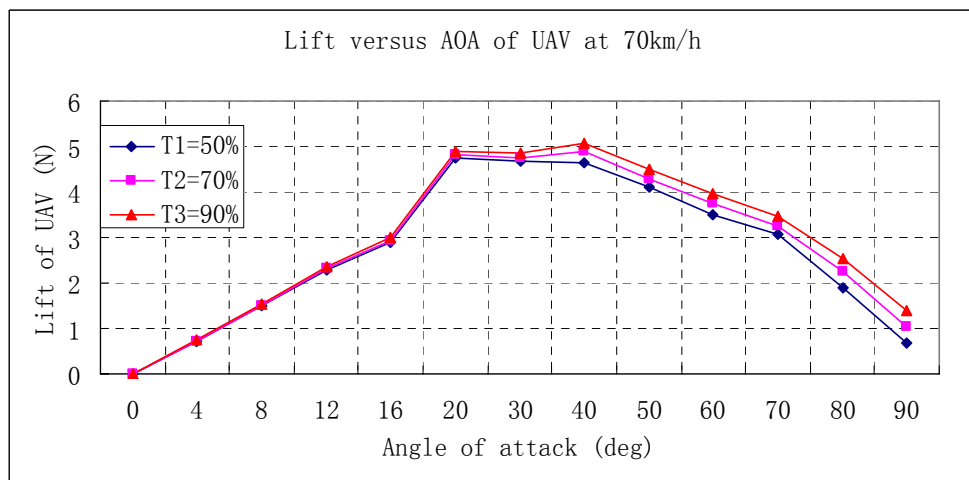


(c) L/D vs AOA

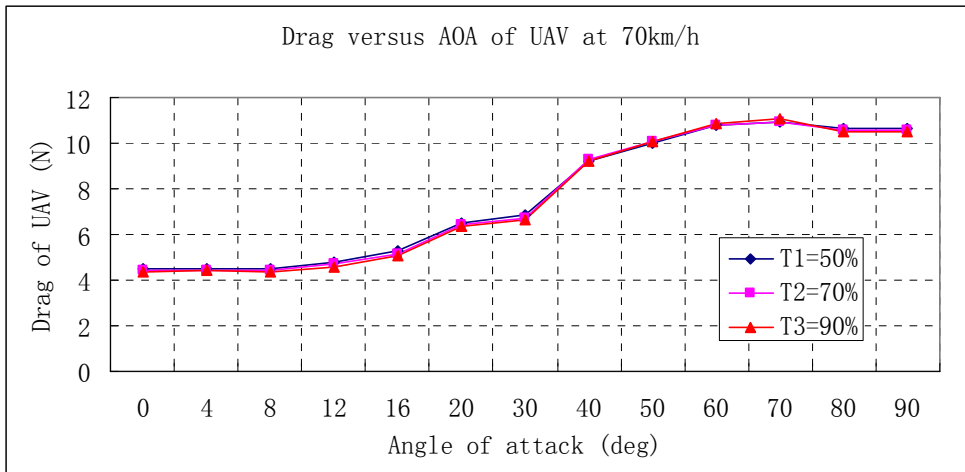


(d) Pitching moment vs AOA

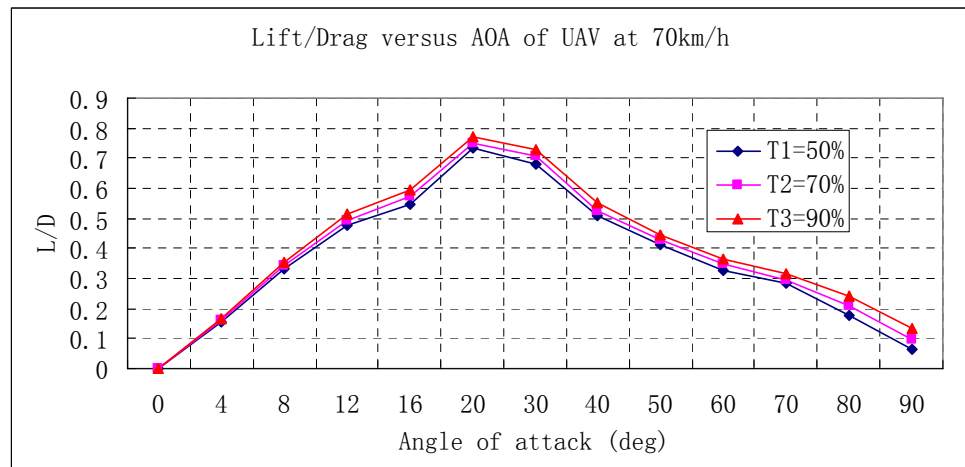
Figure4. 19 Aerodynamic Coefficients versus AOA of UAV with different thrusts at 35km/h



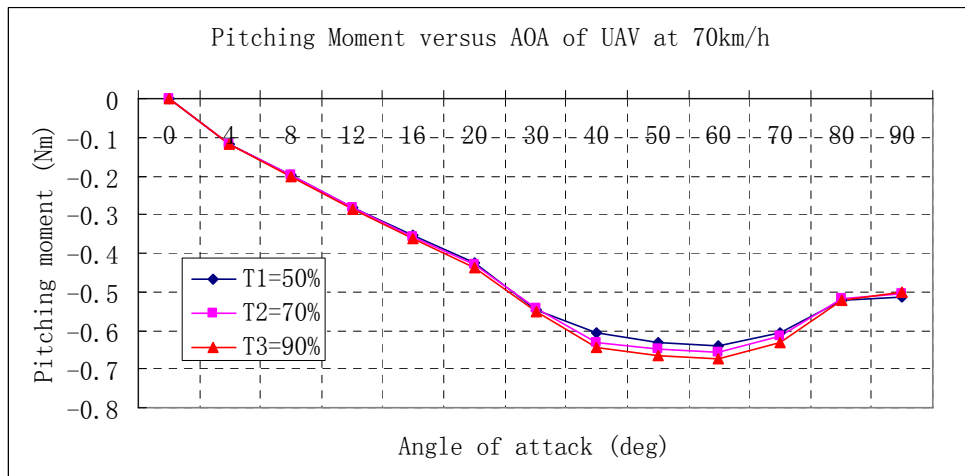
(a) Lift vs AOA



(b) Drag vs AOA



(c) L/D vs AOA



(d) Pitching moment vs AOA

Figure 4.20 Aerodynamic Coefficients versus AOA of UAV with different thrusts at 70km/h

Fig 4.18, Fig 4.19 and Fig 4.20 represent the lift, drag, ratio of lift and drag, and pitching moment of UAV without wings versus angle of attack at different velocities. These curves are plotted as the function of angle of attack with thrust which includes T1, T2 and T3 (diamond, square and triangle

symbols). From the above three groups of figures, we can get some conclusions as following. First of all, the air speed is slower, the aerodynamic forces and moments are increasing or decreasing more dramatically. Secondly, the drag is negative if the air speed is at 10km/h, which means the aerodynamic drag is smaller than thrust in the case of low speed flight. Thirdly, the best L/D happens at 35km/h. Thus at this velocity UAV has a high efficiency of flight. Moreover, the pitching moments are negative. This means that the aerodynamic center of whole UAV is behind the center of gravity. So it is dynamic stable in the view of flight dynamics. In addition, from lift curves at different velocities it is clear that the stall angle of entire UAV is delayed with the increase of air speed. Finally, these figures point out that UAV has better ratio of lift and drag between 16 to 30 degrees of angle of attack.

However, we find that it is almost impossible to achieve horizontal flight at low or high angle of attack for UAV without wings. Even if it arrives at high speed flight to generate big enough lift force whereas the drag created is also very large at the same time. Therefore, more research should be pursued on UAV with wings.

4.2.3 Test with Wings

After the test without wings is completed, we continue the research of UAV with wings. Then by comparison of two tests some important conclusions will be figured out.

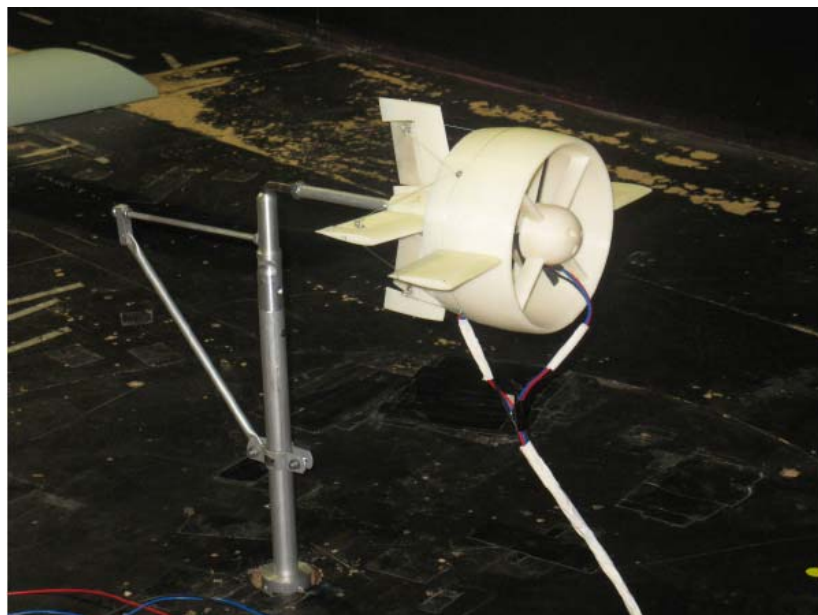
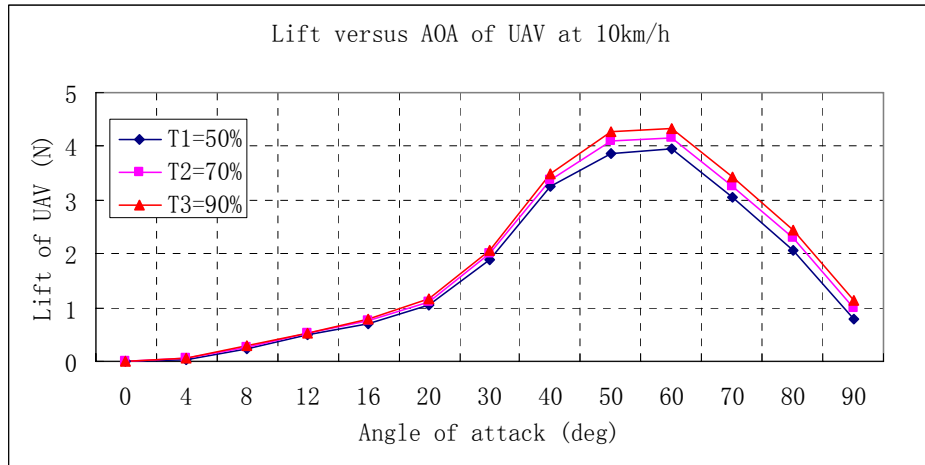
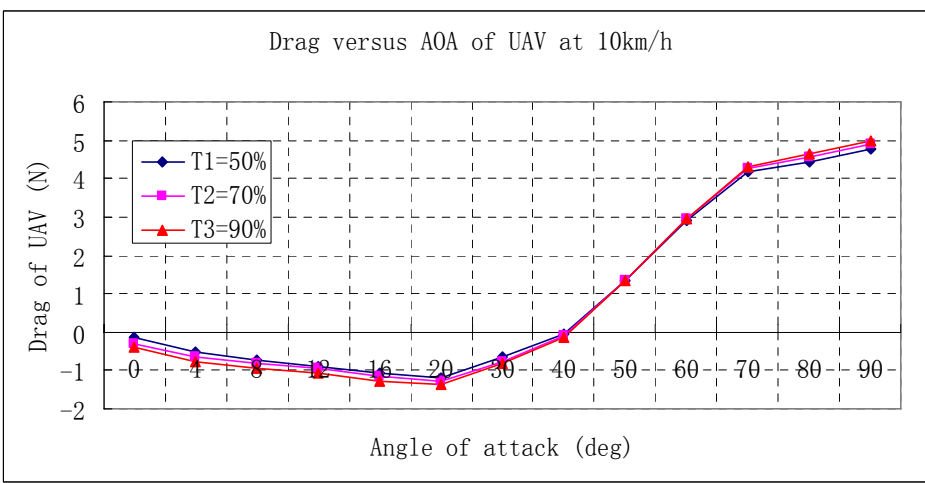


Figure4. 21 UAV Test with Wings

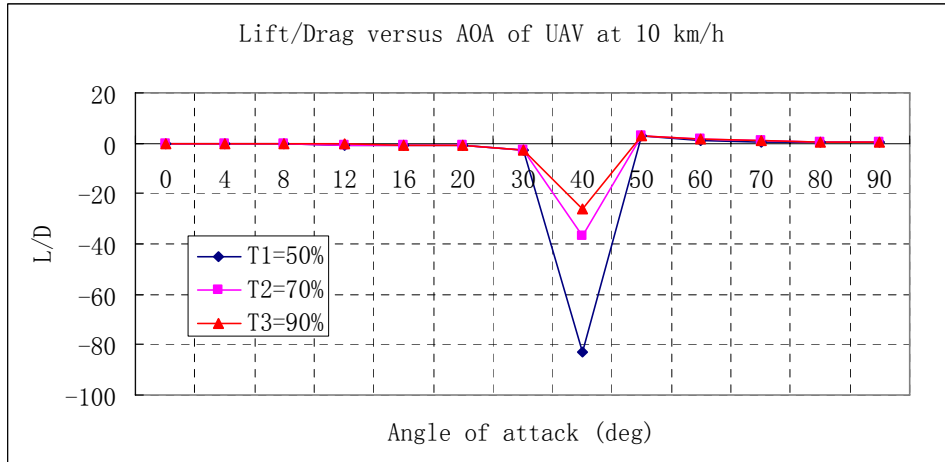
Firstly, let's get some longitudinal aerodynamic coefficients changing angle of attack at different air speed with thrust increasing as well.



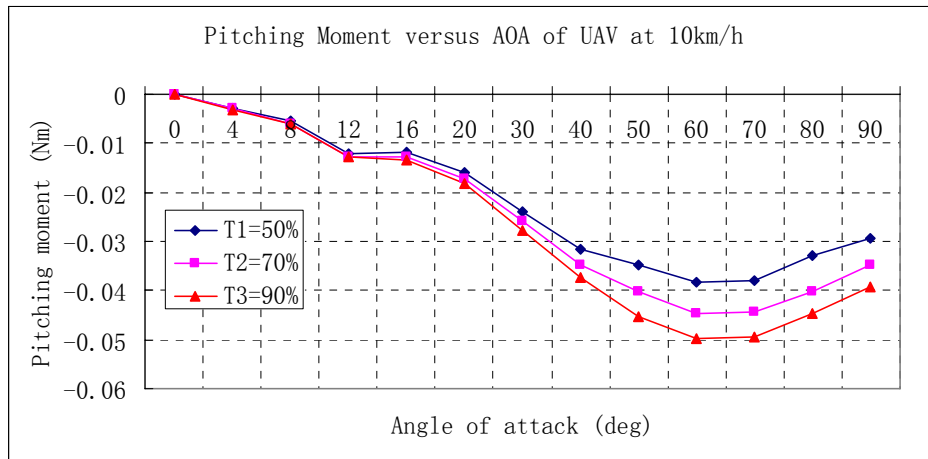
(a) Lift vs AOA



(b) Drag vs AOA

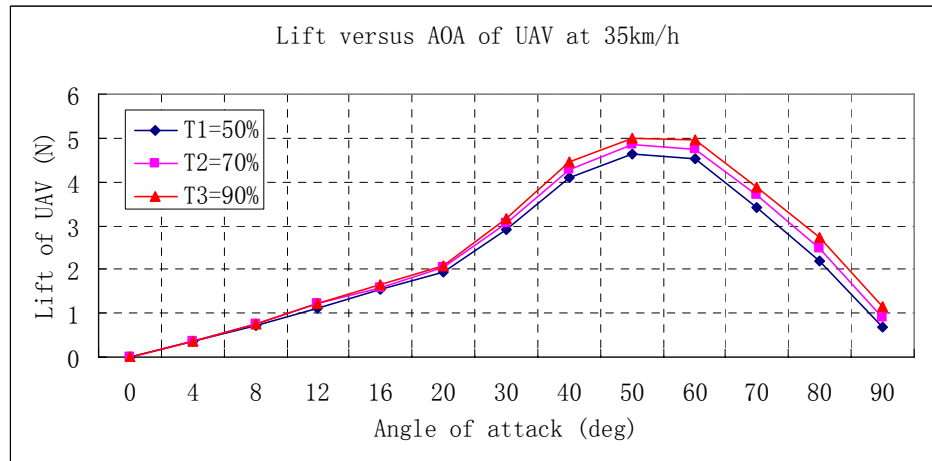


(c) L/D vs AOA

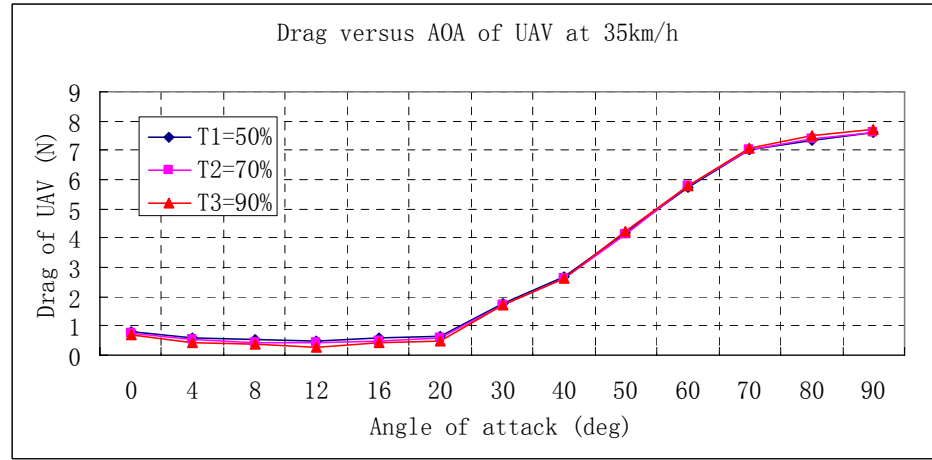


(d) Pitching moment vs AOA

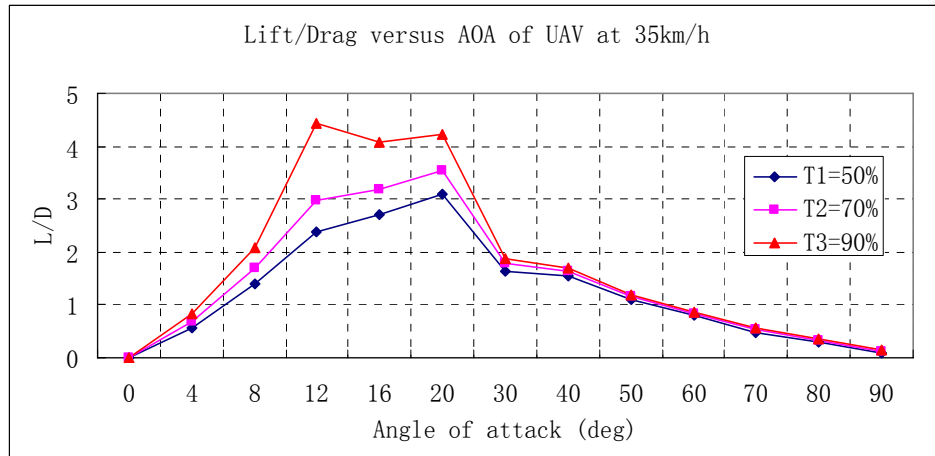
Figure4. 22 Aerodynamic Coefficients versus AOA of UAV with wings and different thrusts at 10km/h



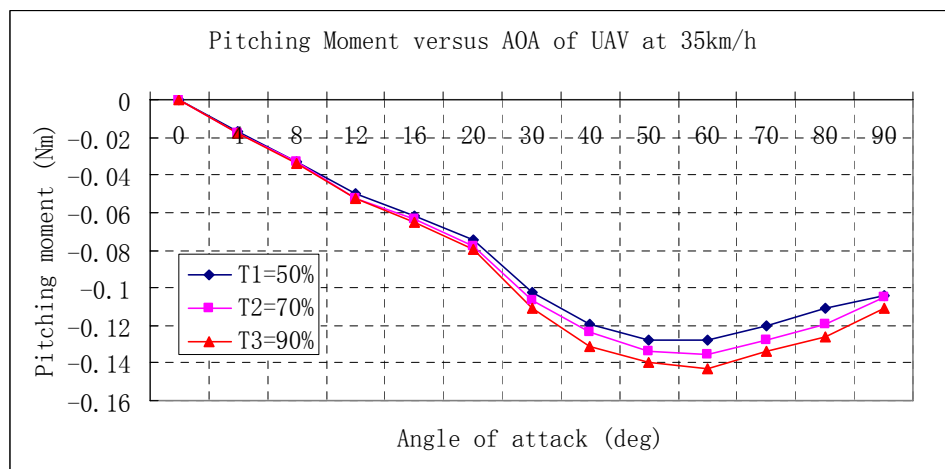
(a) Lift vs AOA



(b) Drag vs AOA

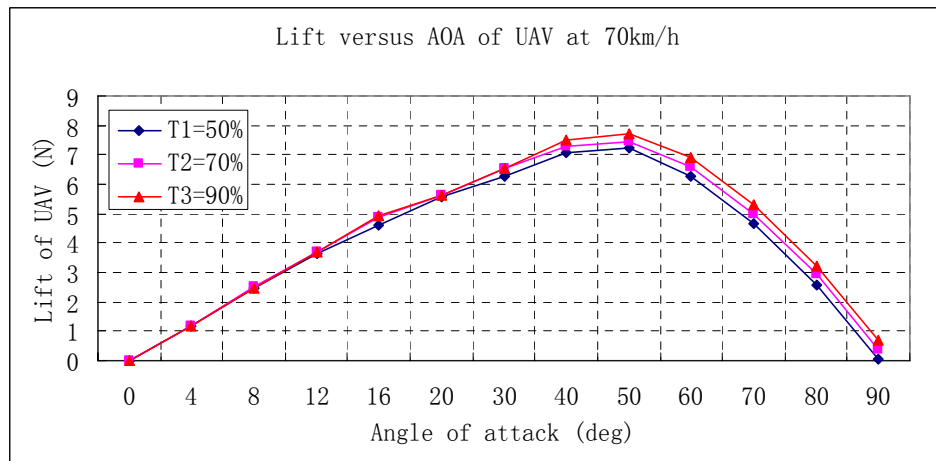


(c) L/D vs AOA

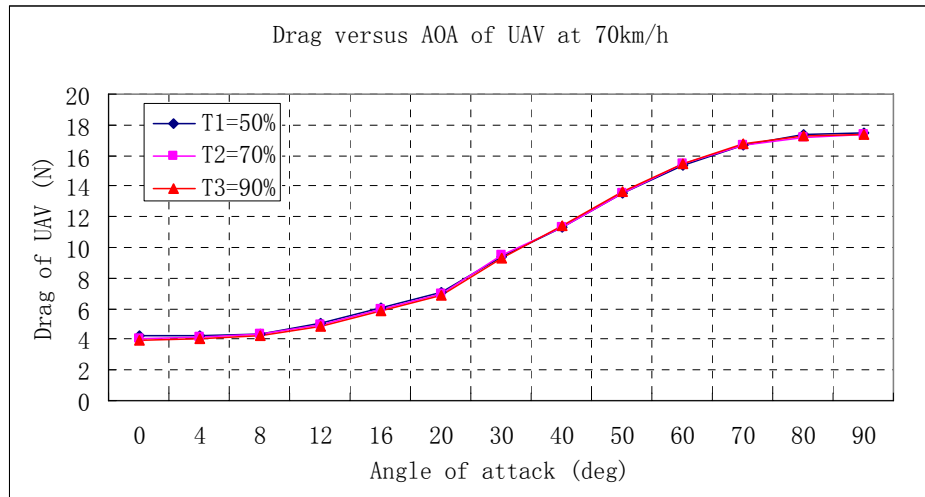


(d) Pitching moment vs AOA

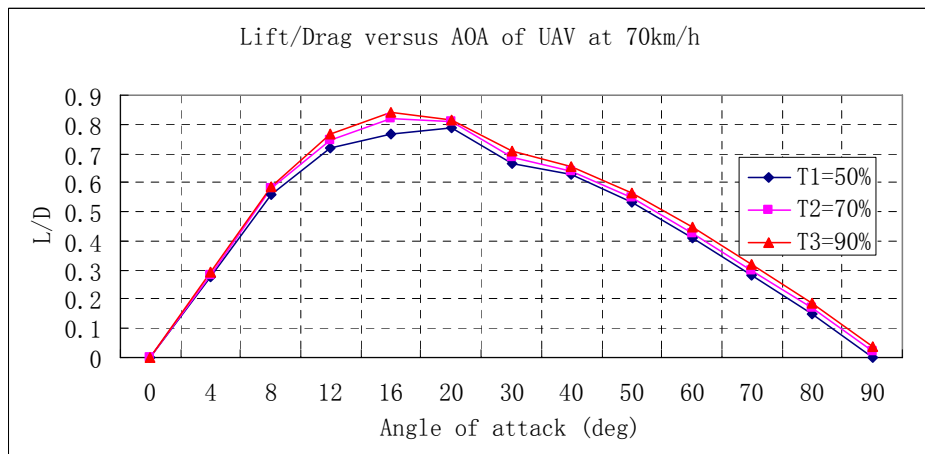
Figure4. 23 Aerodynamic Coefficients versus AOA of UAV with wings and different thrusts at 35km/h



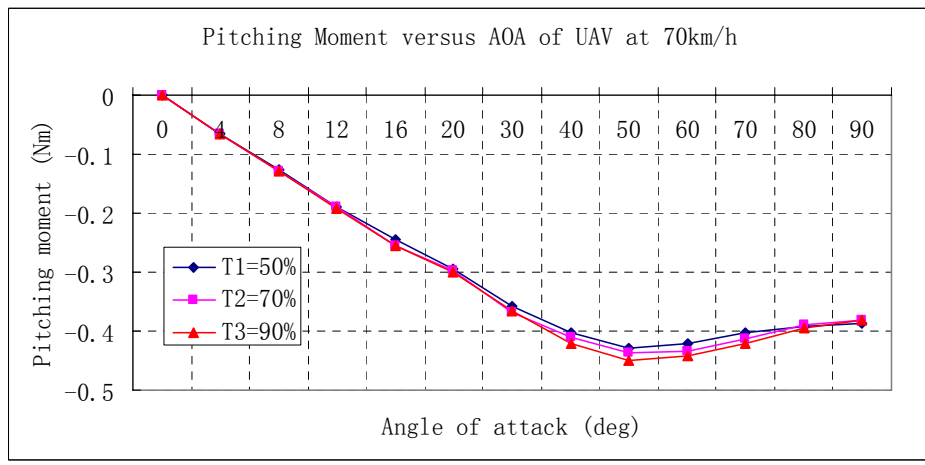
(a) Lift vs AOA



(b) Drag vs AOA



(c) L/D vs AOA



(d) Pitching moment vs AOA

Figure4. 24 Aerodynamic Coefficients versus AOA of UAV with wings and different thrusts at 70km/h

Fig 4.22, Fig 4.23 and Fig 4.24 show the lift, drag, ratio of lift and drag, and pitching moment of UAV with wings versus angle of attack at different velocities. These curves are plotted as the function of angle of attack with thrust which includes T1, T2 and T3 (diamond, square and triangle symbols). These figures point out that UAV has better ratio of lift and drag between 12 to 20 degrees of angle of attack. In contrast to the aerodynamic forces and moments of UAV without wings, obviously, the lift is rising significantly whereas the drag is increasing slightly. It states that the ratio of lift and drag is improved as the wings are mounted to UAV. Meanwhile, compared with no wings UAV, the stall angle is rising about 10 degrees. Therefore, we can conclude that the UAV with wings has a much better horizontal flight performance than no wings'. The two wings play a critical role in keeping horizontal fight. Therefore, it is essential to assemble wings with UAV for achieving flight transition from vertical climb to horizontal flight.

4.2.4 Deflection of Control Surfaces

Fig 4.25 displays the process of deflecting the control surface of UAV using strings to hold or release. By testing the results of deflection we can obtain lots of useful data to evaluate the stability and control derivatives for improving the dynamic model of UAV.

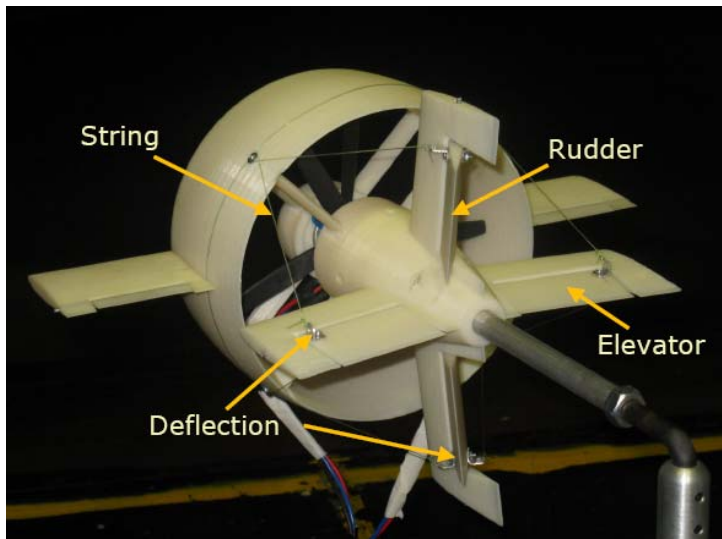


Figure4. 25 Aerodynamic Coefficients relate to Deflection of Control Surfaces

Fig 4.26 and Fig 4.27 calculate the curves on longitudinal force and moment which are plotted as the function of deflection of elevator at different angle of attack marked by various kinds of colors.

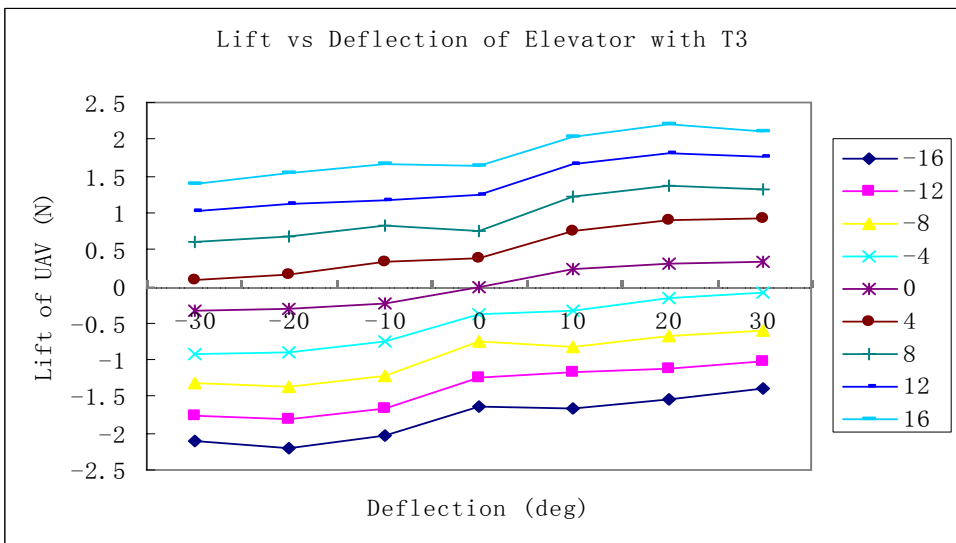
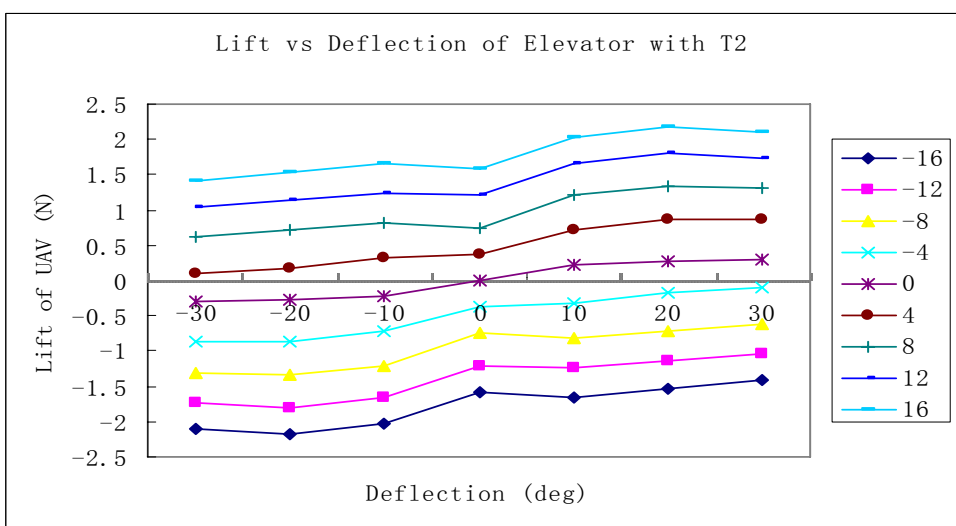
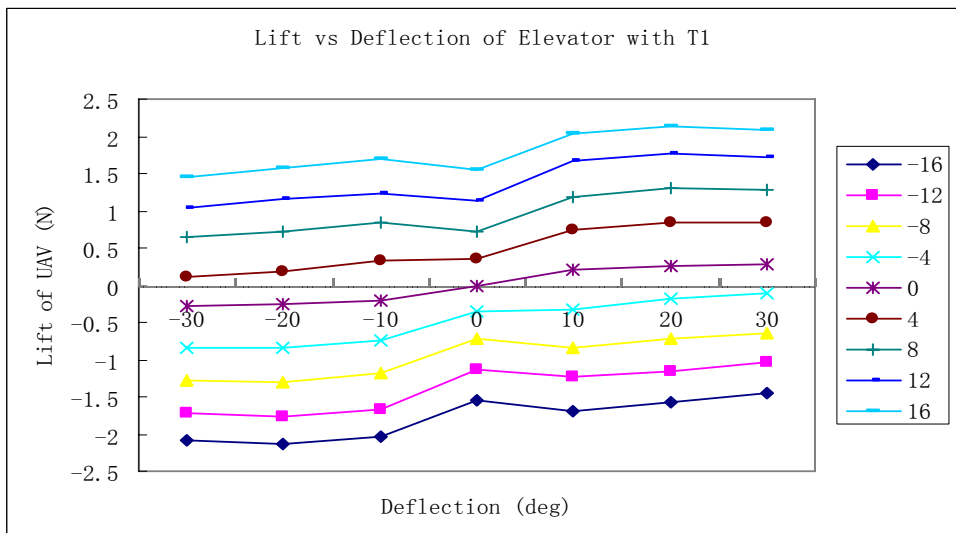


Figure4. 26 Lift versus Deflection of Elevator

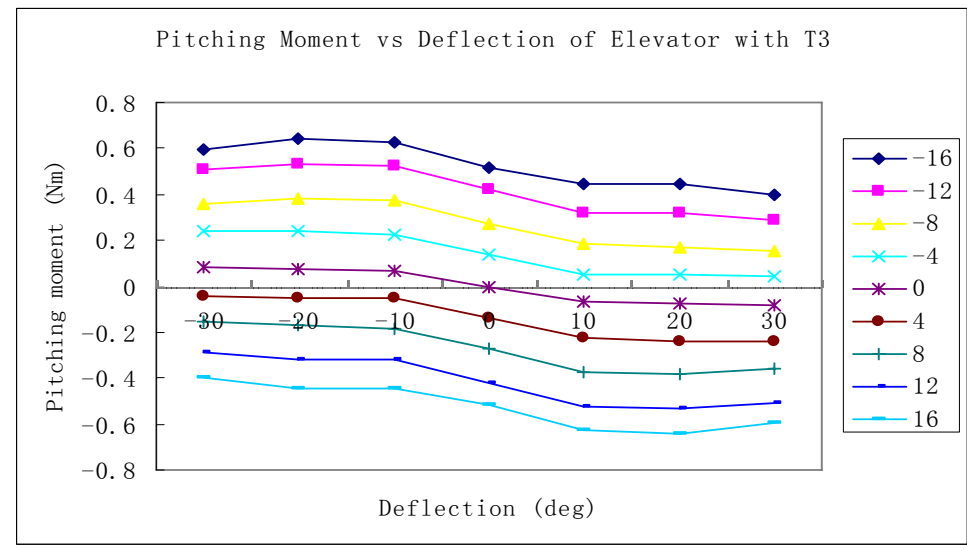
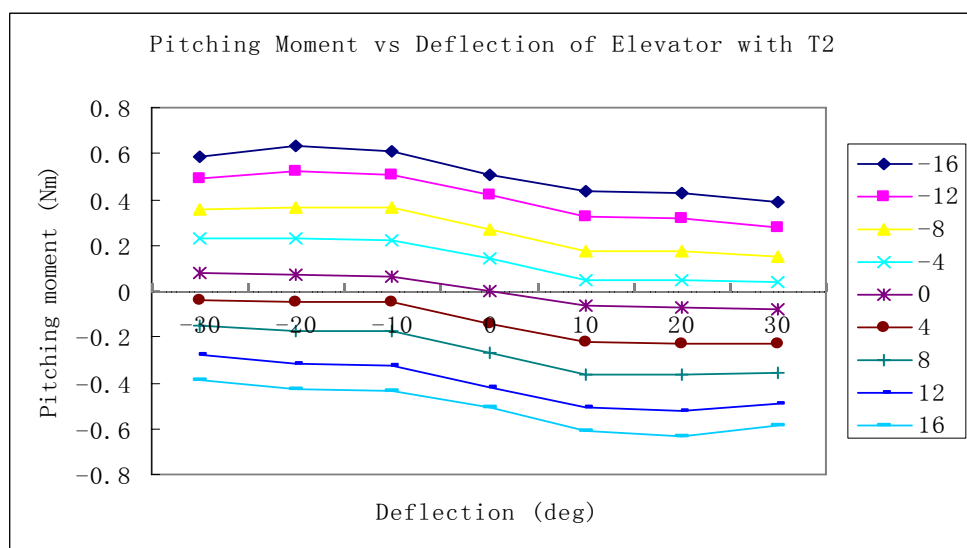
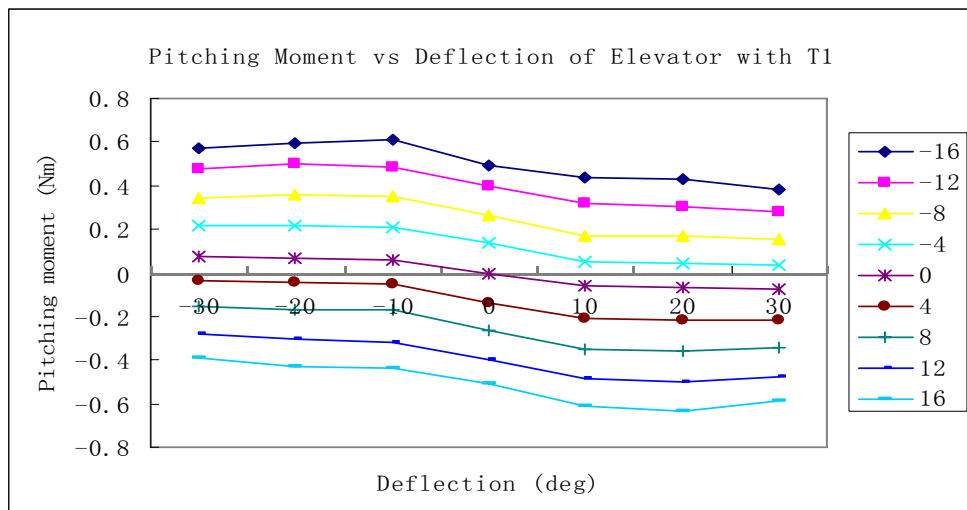
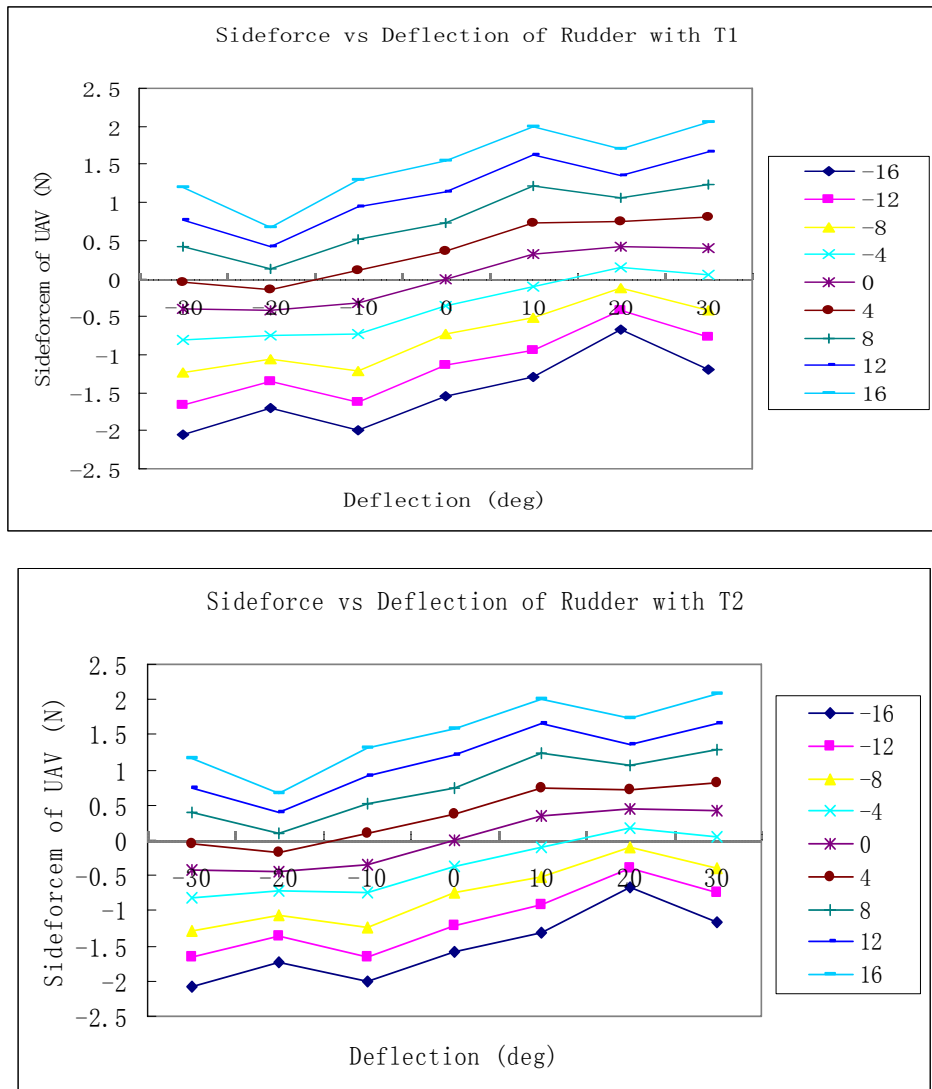


Figure4. 27 Pitching Moment versus Deflection of Elevator

From the value of above figures, we know that the variation of thrust impact on force and moment slightly although the propeller slipstream become more turbulent flow. And both lift and moment curves look almost linear with deflected angles. This is good for control design in further work.

Fig 4.28 and Fig 4.29 show the curves on lateral force and moment which are plotted as the function of deflection of elevator at different angle of attack marked by various kinds of symbols. Compared with longitudinal curves, their trend are not linear in particular to large deflected angles. But at low angle of attack the side force and yawing moment still keep linear about deflected angles and even the thrust is increasing from T1 to T3.



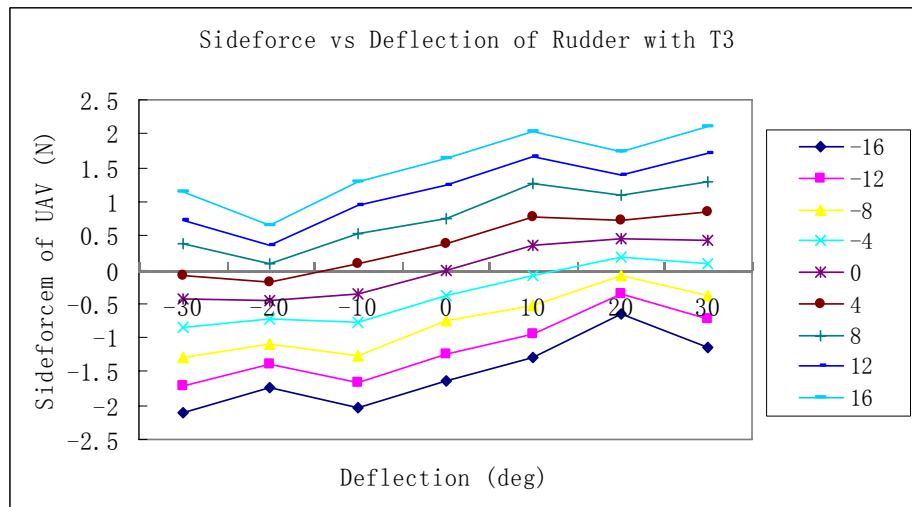
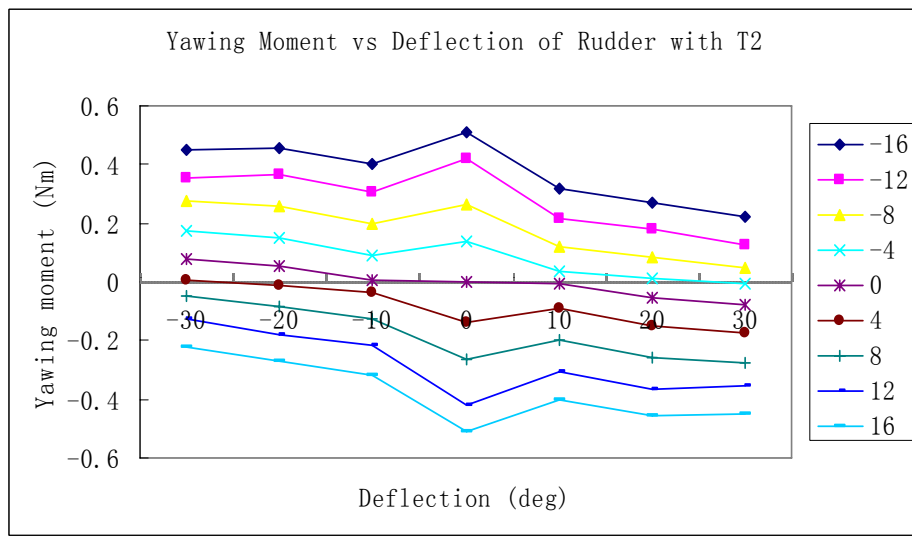
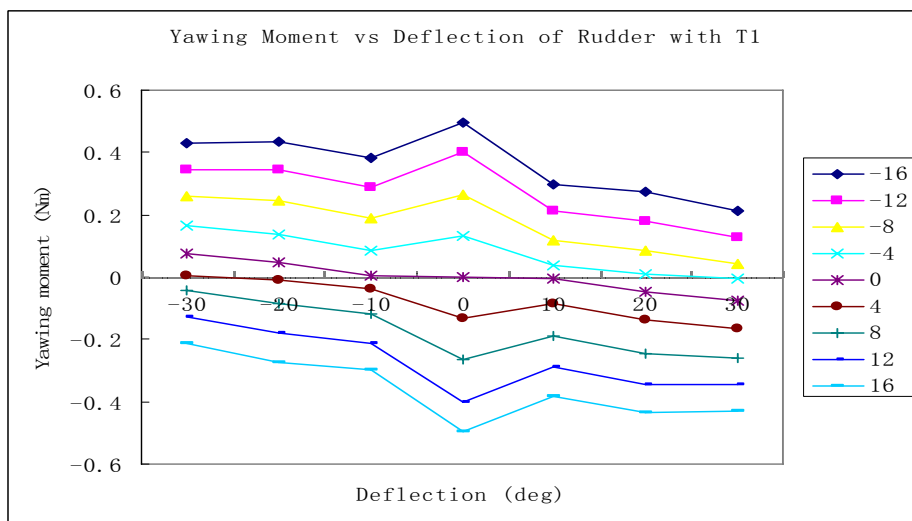


Figure4. 28 Side force versus Deflection of Rudder



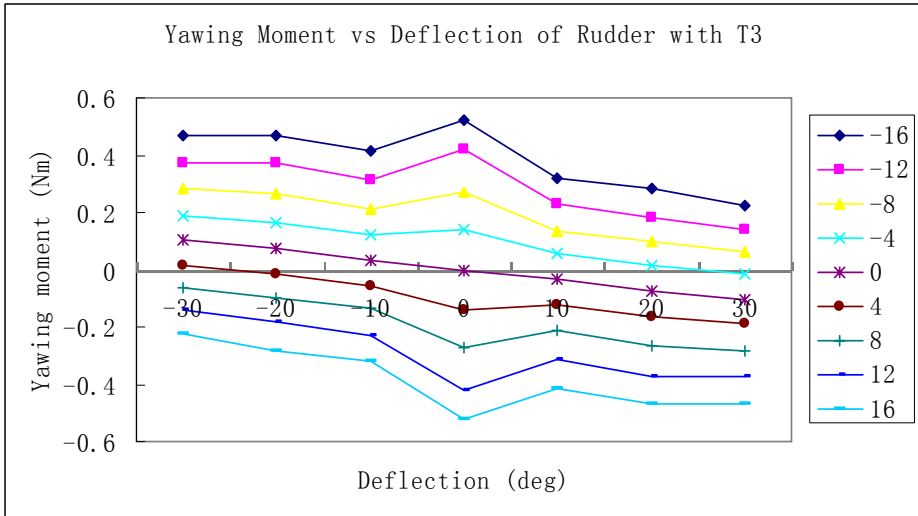
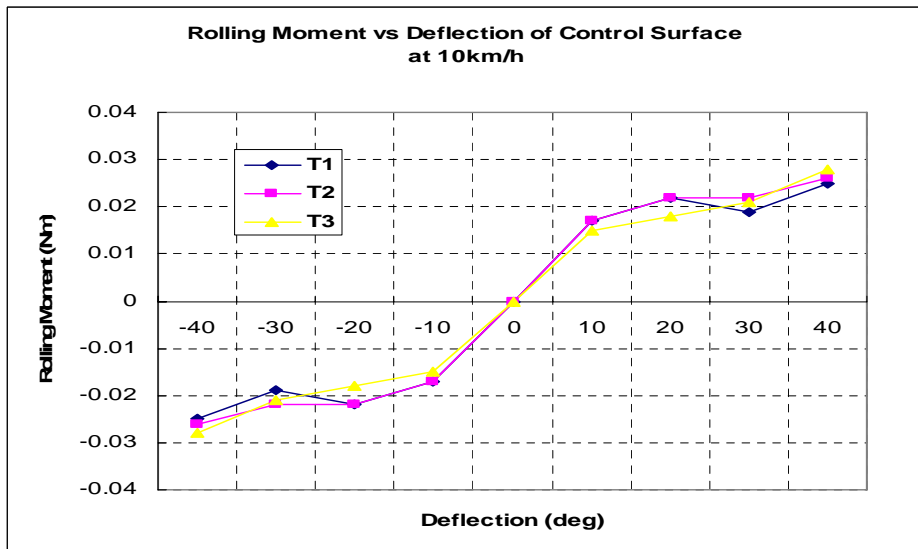


Figure4. 29 Yawing Moment versus Deflection of Rudder

The following figure is about rolling moment versus deflection of control surface. Since the four control surfaces of UAV are symmetrical with central line of itself, we can find the relationship between rolling moment and deflected angle by testing any one of four control surfaces at different air speed as shown in Fig 4.30.



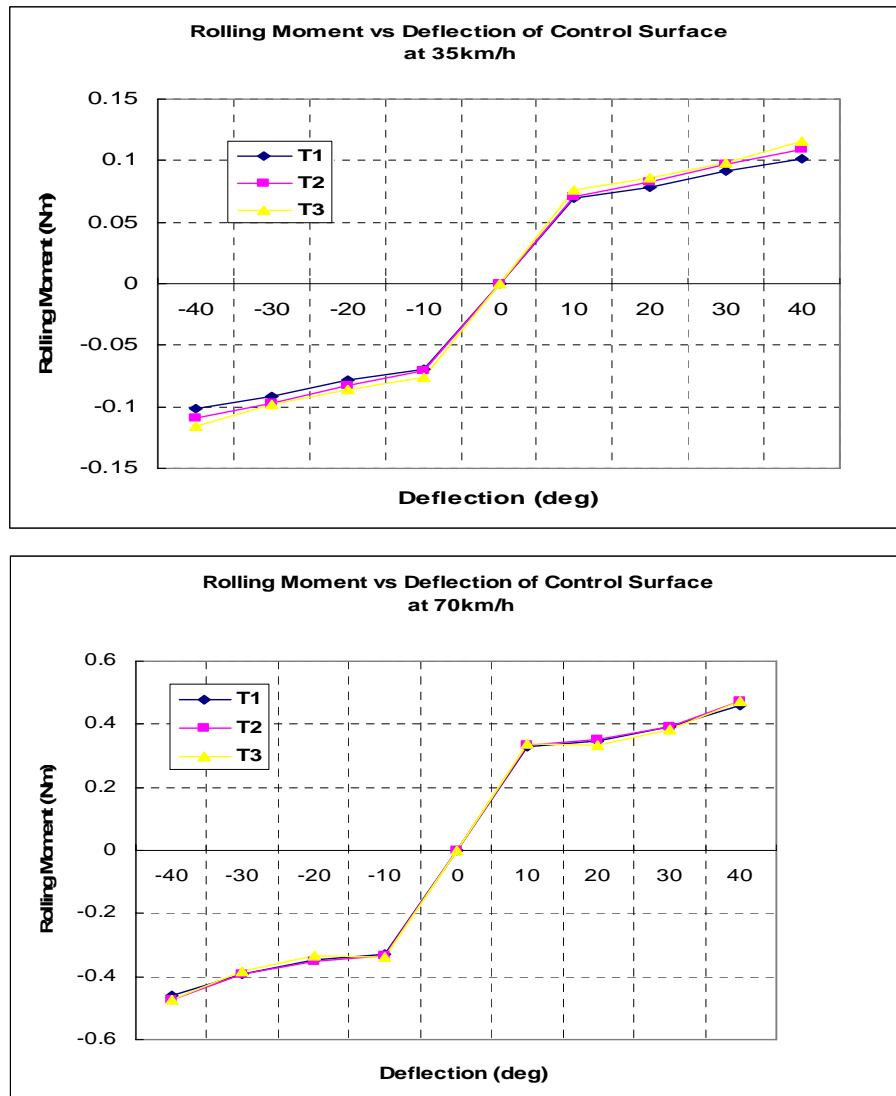


Figure4. 30 Rolling Moment versus Deflection of Control Surface

The slope of curves is bigger at low deflection (0~10 degrees) than high deflection (10~40 degrees). However, they are linear with deflected angles very well regardless of low deflection or high deflection.

4.2.5 Crosswind Effect on UAV

To confirm the existence of crosswind effect as ducted fan UAV is hovering in the air, the following test has been done.

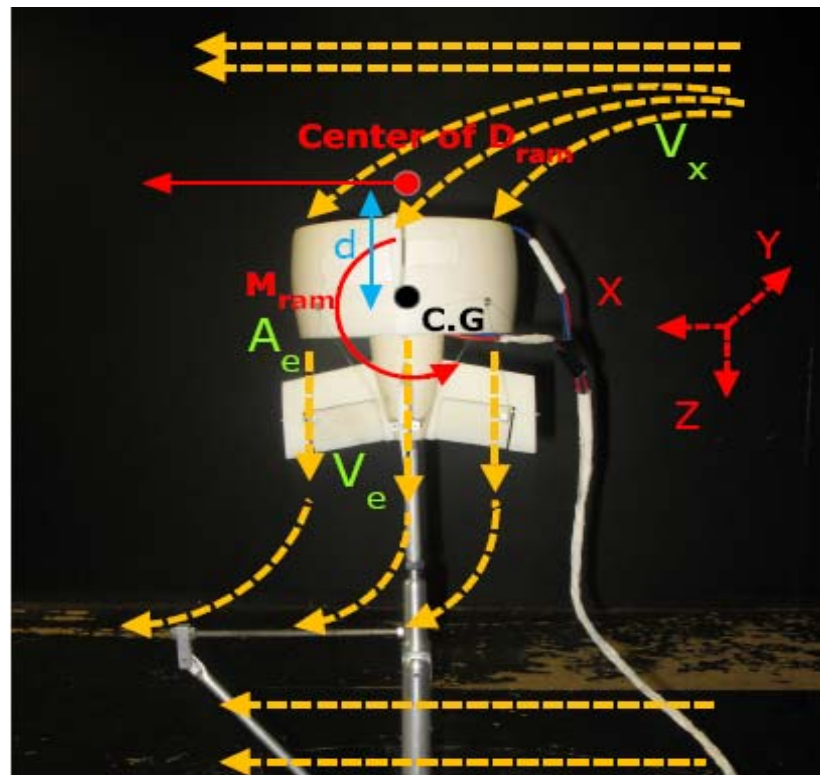
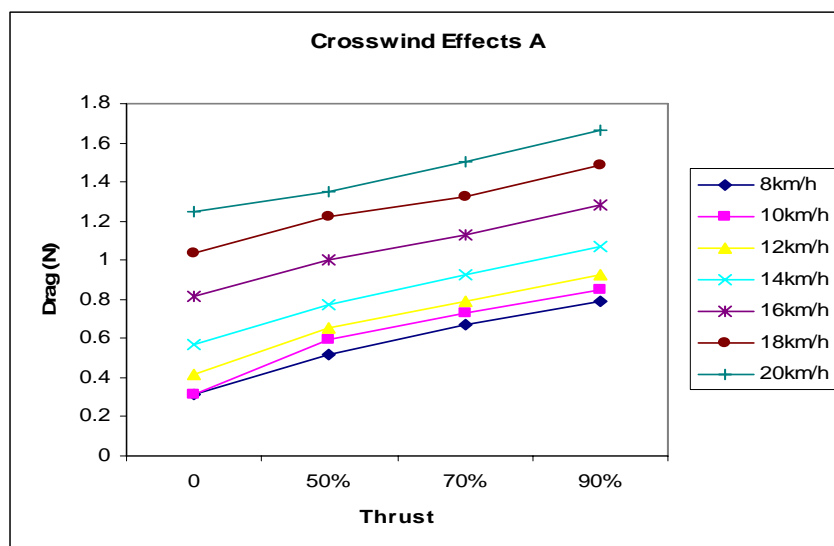
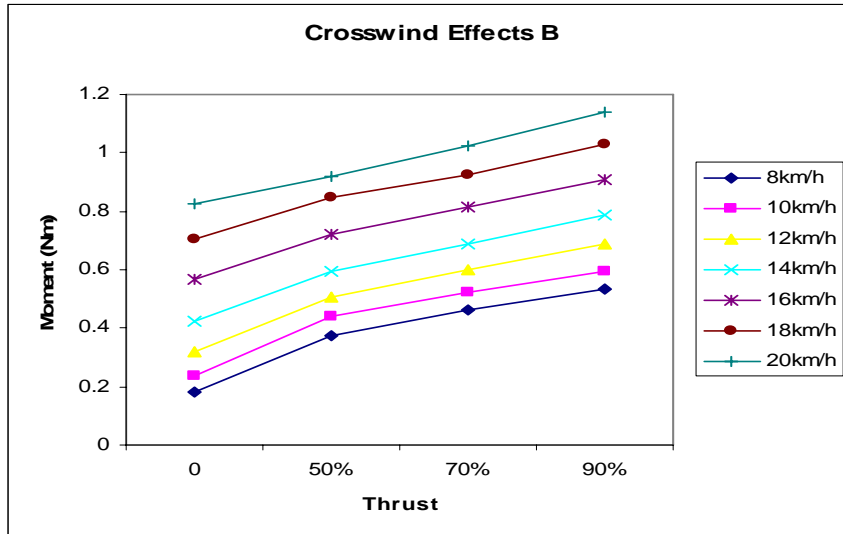


Figure 4.31 Crosswind Effect Testing in Wind Tunnel

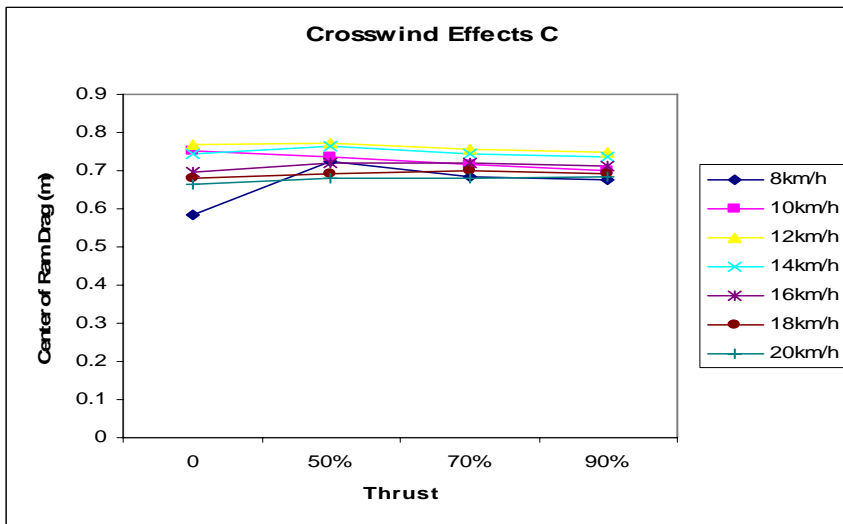
We make UAV vertical in wind tunnel to ensure it is perpendicular crossing with airflow which is constant. From figure 4.31 (combined Appendix C2) we can see the flow passing the UAV at top and bottom. However if we switch on the throttle and increase the power of engine, the flow is sucked by the ducted fan as mentioned in chapter 2 section 2.1.4. The moment flow pass through ducted fan, the ram drag is created.



(a) Drag versus Thrust



(b) Moment versus Thrust



(c) Center of Ram Drag versus Thrust

Figure4. 32 Ram Drag and Moment versus Thrust at different velocities of Crosswind

$$D_{ram} = \rho A_e V_e V_x \quad (4.1)$$

$$M_{ram} = d \times D_{ram} \quad (4.2)$$

Let's combine Fig 4.32 (a) and (b) with Eq.(4.1) and Eq.(4.2) which has been explained in section 2.14.

If the thrust is increasing, the ram drag and ram moment are rising as well. Because the V_e is going up

with the increase of thrust whereas ρ, A_e and V_x are constants, which has led to rise of D_{ram} . At the same time the d is almost keeping constant as shown in Fig 4.32 (c), so the M_{ram} is growing up. This phenomenon is called crosswind effect. It means that if UAV is hovering in the air with the crosswind, the ram drag and moment has to be counteracted by extra control. The difficulty of control is how to estimate the direction of crosswind that is possibly from anywhere. Therefore, automatic control methodology will be considered and designed for unpredictable crosswind.

4.3 Correlation between CFD Results and Experimental Data

In order to compare CFD results and Experimental data, the dimensionless aerodynamic coefficients are applied in the following figures. It is convenient for us to find out the similarities or differences between them.

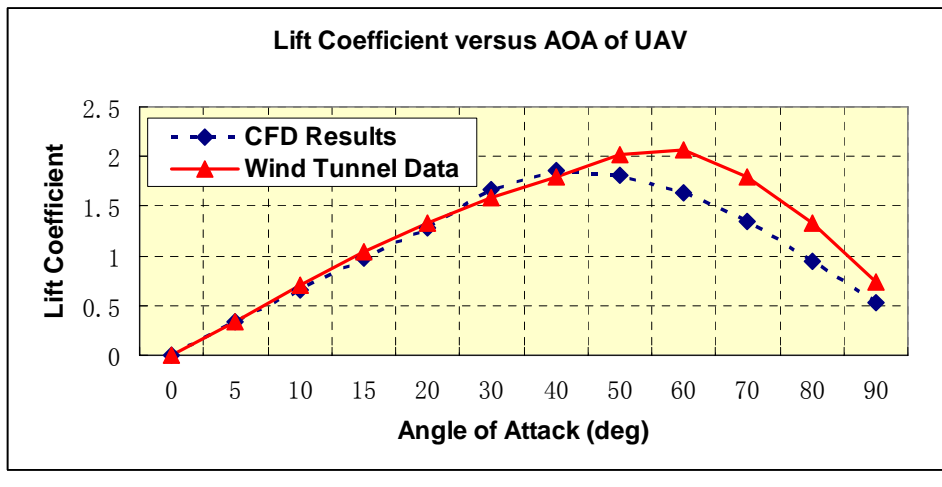
4.3.1 Calibration of Wind Tunnel Testing

During the UAV in wind tunnel testing, three errors have to be noted to calibrate the results measured by experiment. The first one is the equipment error from sting which is mounted to UAV model generates drag. The second one is that cables linked with DC power out of wind tunnel can not pass through the inside of UAV which has limited space. The third one is the error from vibration caused by flow of wind tunnel which can not supply the absolute laminar flow because the boundary layer of ambient wall around wind tunnel. The three points mentioned previously will lead to results error. Thus, we have to consider the errors firstly, then calibrate the data measured.

For decreasing the error caused by cables, the cables are fixed vertically with ground to ensure it will not push or drag model during testing. To reduce the effects from vibration, the average value should be calculated. Fortunately, the data collection is done by a special software called JR-3 collector which can collect wind tunnel data within 5~10 seconds as a group of data. Because this group of data represents one result of UAV testing, we can average these data to cancel error caused by vibration. Then using averaged data to abstract sting's drag is the final results which we need.

4.3.2 Results and Discussion

The following are the figures of comparison of CFD and experiment. The lift and drag coefficient of UAV with wings are plotted as the function of angle of attack at 20m/s. The dash curves describe CFD data in terms of chapter 3. Wind tunnel data are shown by triangle symbols.



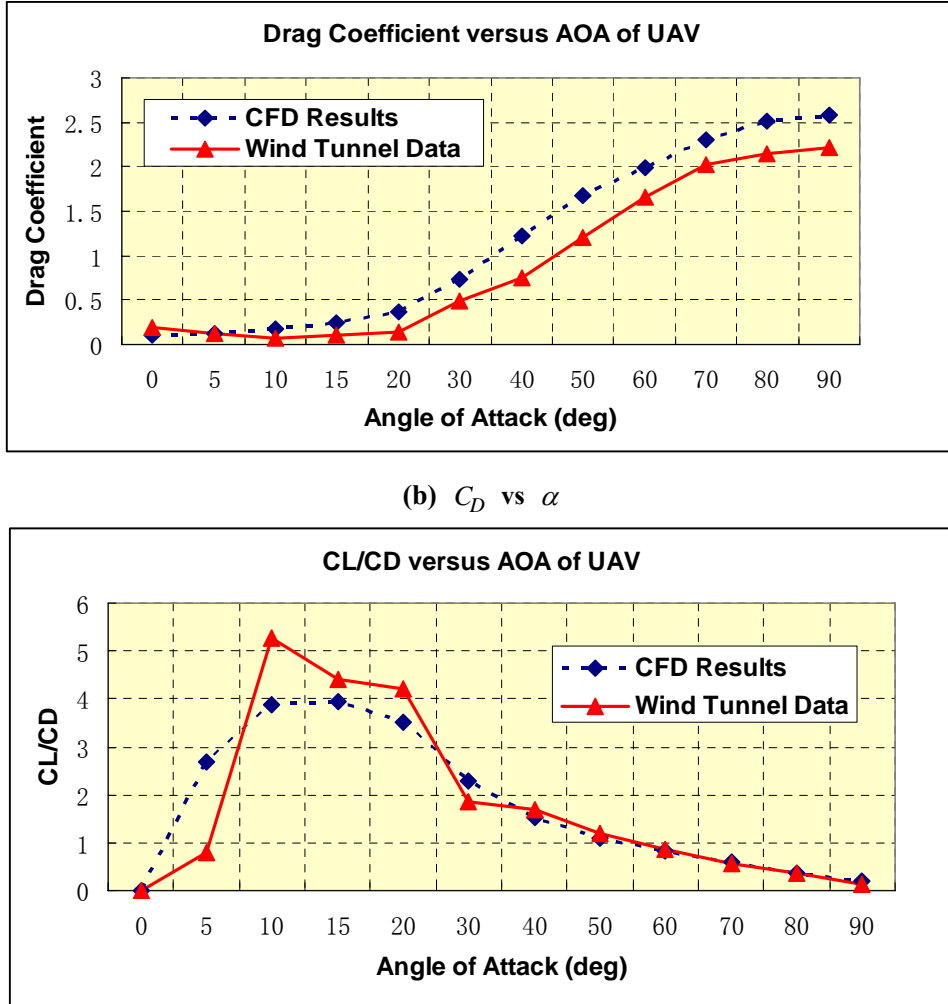


Figure 4.33 CFD Results and Wind Tunnel Data

It is clear that the lift and drag coefficient given by wind tunnel data are very similar with CFD results. Especially the trend of curve looks close to each other although some of points have slight difference. For instance the stall angle shown by CFD is smaller than experimental data, but at low angle of attack the values of CFD and experiment are matched with each other very well. By comparison CFD and Experimental data, we can conclude that the data obtained by wind tunnel testing are convincing to use for optimizing dynamic model of UAV.

4.4 Summary

The investigation of wind tunnel testing provides large quantity of data for estimating derivatives of stability and control. Not only were the six components of force and moment obtained, but also some flight parameters are measured for stability and control by deflecting control surfaces. In addition, by analyzing the correlation between experimental data and CFD results, we can sure that the data listed in this chapter is convincing. It becomes an important database for building up dynamic model in following chapters. Although some errors, which we can not avoid, affect the accuracy of final dynamic model, these data play a critical role in improving flight dynamics in further work.

Chapter 5

5 Flight Dynamics

Flight dynamics is concerned with the motion of an airplane due to internally or externally generated disturbances. For this ducted fan VTOL UAV the stability and control abilities are attractive to be researched and developed. To describe the rigid-body motion of this UAV the comprehensive equations of motion with six degrees of freedom need to be considered and analyzed. In this chapter the detailed description of a strategy to simulate a dynamic model of a vertical takeoff and landing (VTOL) unmanned aerial vehicle (UAV) in hovering, vertical climb and horizontal flight is clarified. This will require accurate estimates of the aerodynamic forces and moments acting on the airplane. Based on unique aerodynamic characteristics from a theoretical method, CFD calculation and wind tunnel test the flight dynamics of ducted fan UAV is able to be modeled and simulated accurately.

5.1 General Introduction

The motions of this UAV can be divided for convenience into two parts. One of these consists of the longitudinal motions in which the wings remain level, and the center of gravity moves in a vertical plane. The other consists of the lateral motions including rolling, yawing and sideslip, while the angle of attack, the speed, and angle of elevation of the x axis remains constant. To analyze both longitudinal and lateral motions the longitudinal and lateral forces and moments are essential elements which contain various kinds of factors, such as, thrust, lift, drag, gravity, gyro, nose-up or nose-down moments, internal torque or external torque and so on.

5.1.1 Model of Slipstream Angle

To consider the aerodynamic forces on the UAV it is essential to note that these are all associated with the flow induced by the propellers over the UAV's control surfaces as well as by the disturbance of this flow due to the motion of UAV in figure 5.1. Thus the starting point for any analysis is determination of the slipstream angle caused by propeller slipstream velocities. In the following analysis some assumptions have been made:

- Propeller Normal Forces are negligible;
- The control surfaces are fully submerged in the propeller slipstream
- V_e is the exit induced velocity of duct (slipstream velocity) and V_e vector is parallel with symmetrical axis of UAV body as shown in figure 5.1, p, q and r are the angular velocities which are perpendicular with V_e , and $V_e \gg p, q$ and r.
- The flow at the control surfaces is smooth and uniform.

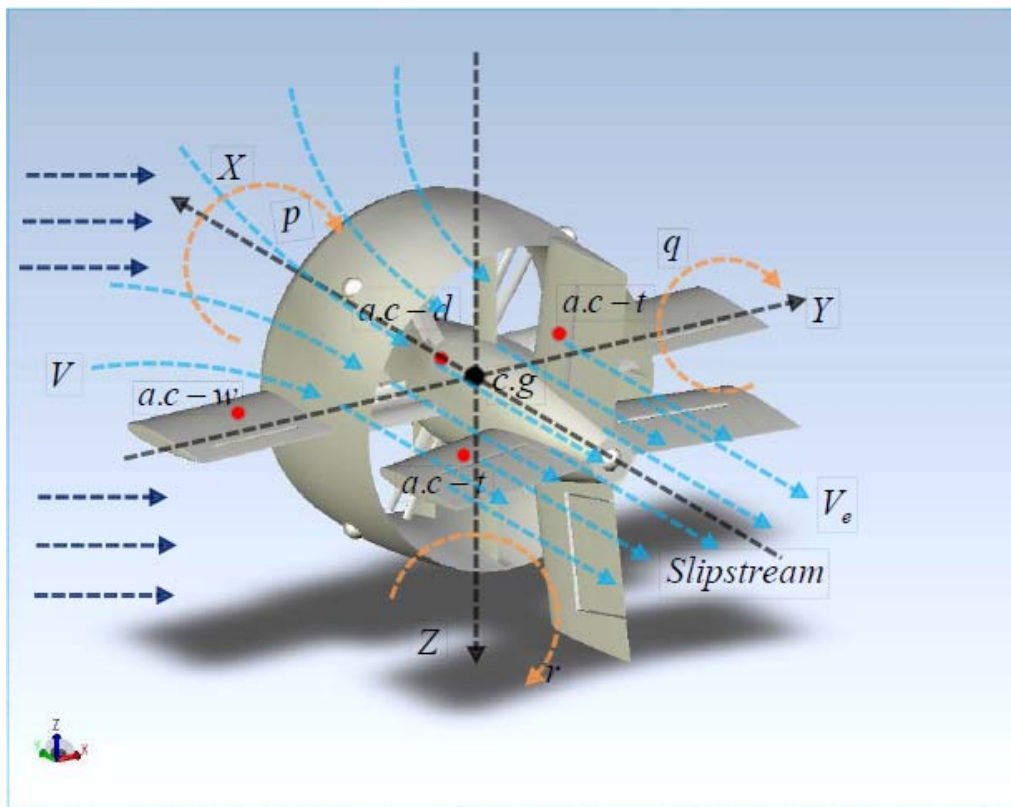


Figure5. 1 Slipstream and Angular Velocities on UAV

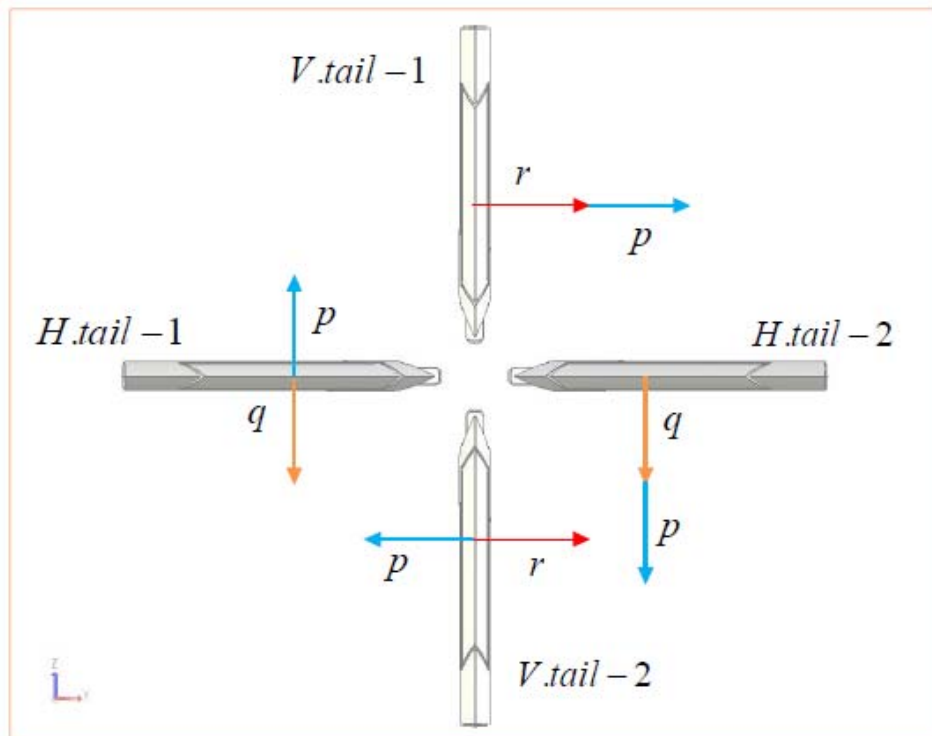
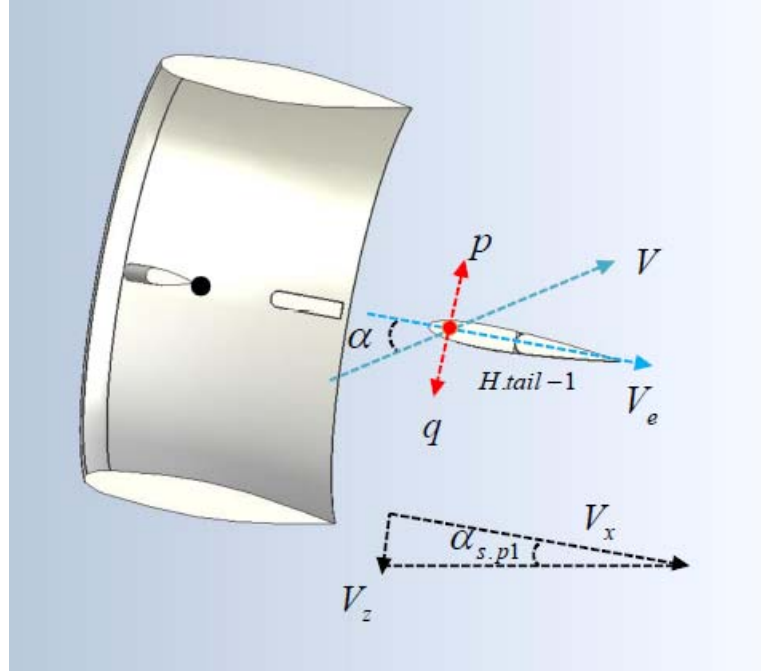


Figure5. 2 p, q and r are acting on Four Control Surfaces

From figure 5.2 we can recognize that the four control surfaces of UAV are impacted by small disturbance due to angular velocities during flying maneuver, such as pitching, yawing and rolling.

Therefore, the slipstream angles of these are totally different to each other because of the different contribution of angular velocities. The following is a group of figures which display how the four slipstream angles are generated because of the perturbation from p, q and r combined with slipstream velocity [14].



(a) Slipstream angle of H.tail-1

In XOZ plane, $\alpha_{s,p1}$ is created because of V_x and V_z which are two velocities' vector in X and Z coordinates shown in figure 5.3(a), respectively.

$$V_x = V \cos \alpha + V_e \quad (5.1)$$

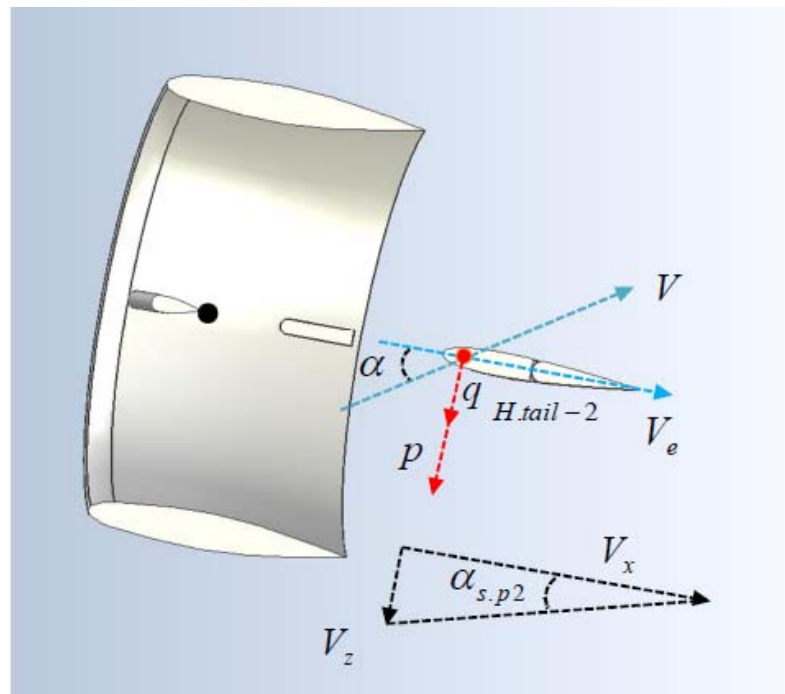
$$V_z = V \sin \alpha + p |y_{c.g} - y_{a.c-t}| - q |X_{c.g} - X_{a.c-t}| \quad (5.2)$$

Since, $V_e \gg p, q$ and r ,

$$\alpha_{s,p1} \approx \tan \alpha_{s,p1} = \frac{V_z}{V_x} \quad (5.3)$$

$$\tan \alpha_{s,p1} = \frac{V \sin \alpha + p |y_{c.g} - y_{a.c-t}| - q |X_{c.g} - X_{a.c-t}|}{V \cos \alpha + V_e} \approx \alpha_{s,p1} \quad (5.4)$$

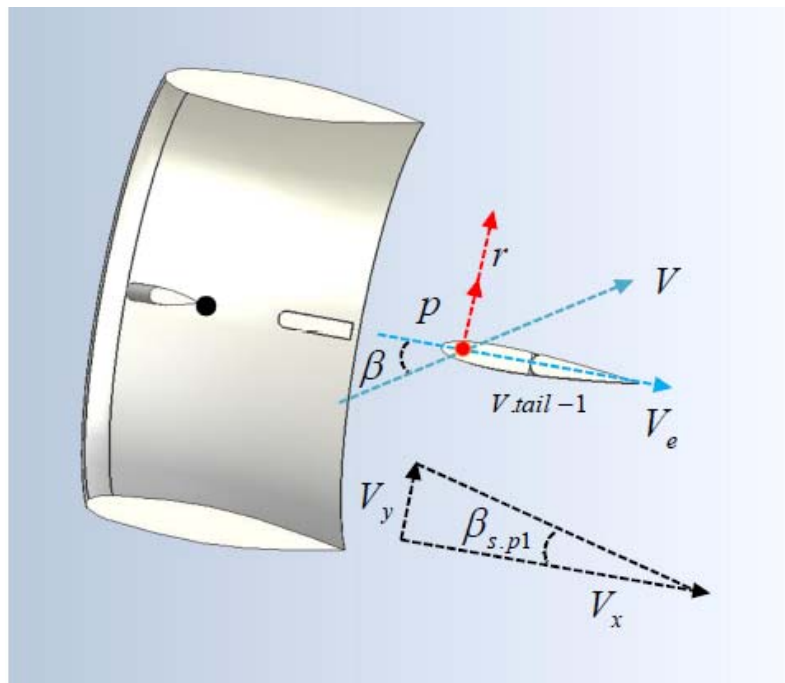
$\alpha_{s,p1}$ is the slipstream angle of attack of horizontal control surface 1;



(b) Slipstream angle of H.tail-2

The same as $\alpha_{s.p1}$, $\alpha_{s.p2}$ is the slipstream angle of attack of horizontal control surface 2 given by,

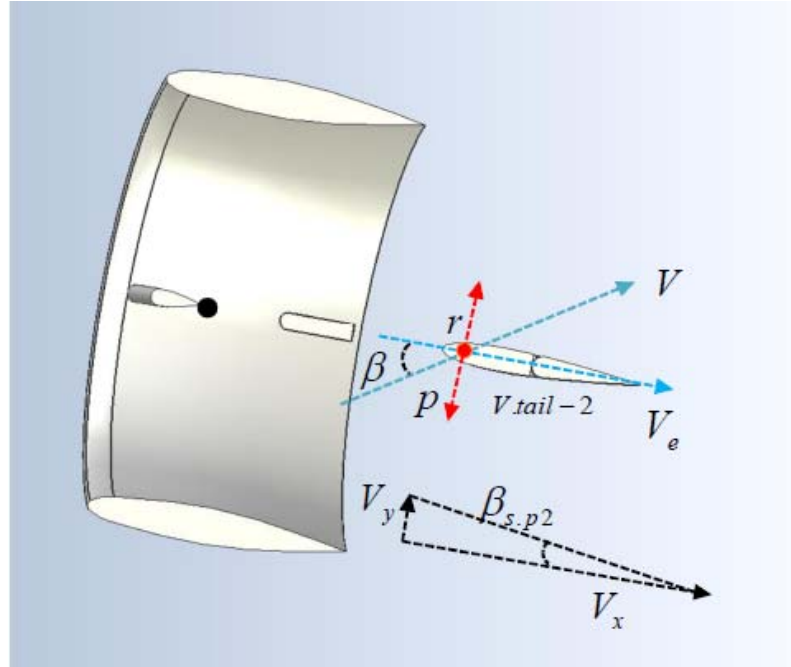
$$\tan \alpha_{s.p2} = \frac{V \sin \alpha - p|y_{c.g} - y_{a.c-t}| - q|X_{c.g} - X_{a.c-t}|}{V \cos \alpha + V_e} \approx \alpha_{s.p2} \quad (5.5)$$



(c) Slipstream angle of V.tail-1

$$\tan \beta_{s.p1} = \frac{V \sin \beta + p|z_{c.g} - z_{a.c-t}| + r|X_{c.g} - X_{a.c-t}|}{V \cos \beta + V_e} \approx \beta_{s.p1} \quad (5.6)$$

$\beta_{s,p1}$ is the slipstream sideslip angle of vertical control surface 1;



(d) Slipstream angle of V.tail-2

Figure 5. 3 Slipstream Angles of Four Tails

$$\tan \beta_{s,p2} = \frac{V \sin \beta - p |z_{c,g} - z_{a,c-t}| + r |X_{c,g} - X_{a,c-t}|}{V \cos \beta + V_e} \approx \beta_{s,p2} \quad (5.7)$$

$\beta_{s,p2}$ is the slipstream sideslip angle of vertical control surface 2.

The above four slipstream angles are very important for analyzing contribution of p, q and r in flight dynamic and control. Because they are combined with V_e , which has led to sensitive response from variation of slipstream angles

5.1.2 The Forces and Moments

Forces and moments act on this UAV including several elements, some of which are variable, called aerodynamic forces and moments, the other parts are constants, such as body force, buoyancy and so on. To build up a flight dynamic model of UAV, these forces and moments are essential to be involved in longitudinal (see figure 5.4) and lateral (see figure 5.5 and figure 5.6) analysis.

5.1.2.1 Gravity

In considering body force of UAV, there is no need to think about the variation of gravity acceleration with the different latitude. Hence g is constant, the gravity of this UAV is computed by,

$$W = mg \quad (5.8)$$

5.1.2.2 Thrust

From chapter 2 we know that thrust T is based on both characteristic of blade and rotor speed. However, only the rotor speed is a variable which is able to be controlled by us. Normally, the thrust is expressed as a function of rotor speed controlled by throttle. But here we really want to use another variable to replace throttle. Because, the value of exit velocity V_e of ducted fan can be calculated as a function of throttle, and compared with applying rotor speed to express thrust force, using V_e as a control input variable is very convenient for further analysis of the dynamic model.

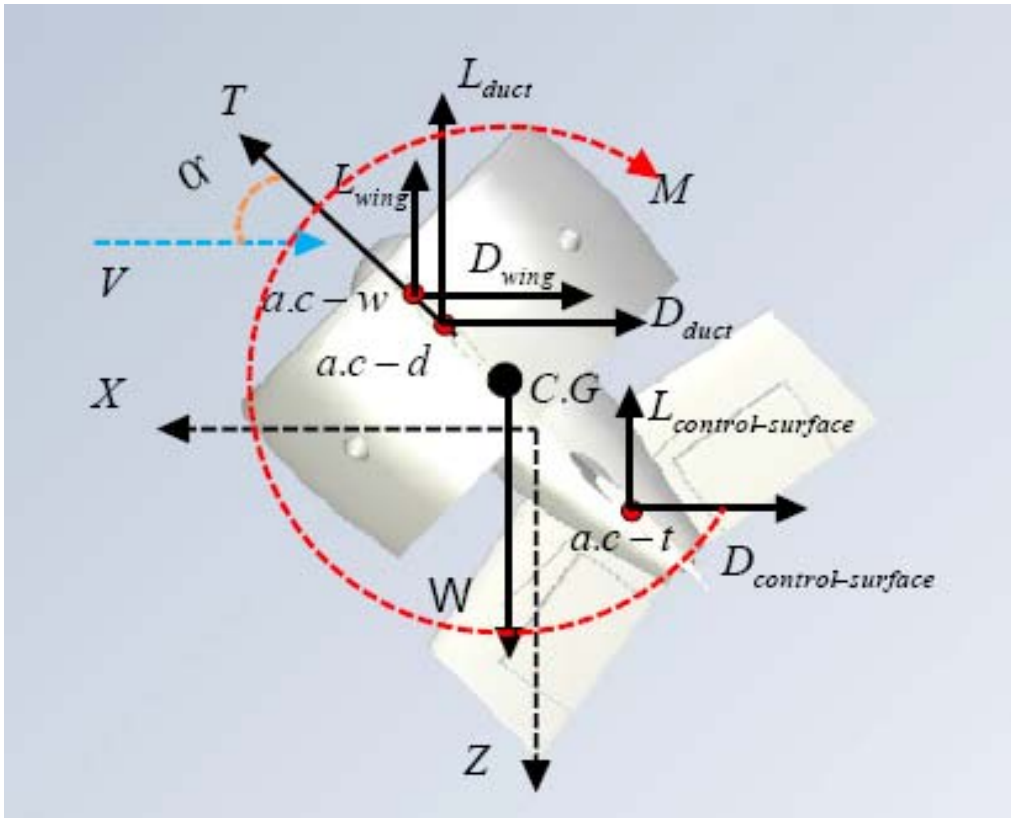


Figure5. 4 Longitudinal Forces and Moments on UAV

According to Eq.(2.18), an expression of the total thrust as a function of the mass flow rate and the overall acceleration of the airflow is given by

$$T = \dot{m}(V_e + V) - \dot{m}V = \rho A_e V_e (V + V_e) \quad (5.9)$$

By simplifying, we find the thrust force as a function of V_e to be expressed in Eq.(5.9)

5.1.2.3 Lift

The lift of an airplane usually consists of three parts' contribution including wing, body and tail. Compared with the wing and tail's contribution, the lift of body is very small. However, for this UAV the body (fuselage) is connected with duct which provides a large magnitude of lift due to the results of CFD and Wind tunnel data. So the duct with fuselage is the main part of the lift's contribution, which should be taken into account seriously to analyze not only longitudinal forces and moments, but also lateral.

The total lift of UAV is expressed as following,

$$L = L_{wing} + L_{duct} + L_{control-surface} \quad (5.10)$$

According to fundamental aerodynamics, the non-lift coefficient is equal to zero in symmetrical aerofoil which is employed in all of the components of this UAV, thus the lifts of three parts are given by,

$$L_{wing} = \frac{1}{2} \rho V^2 S_w C_{L_{\alpha^w}} \alpha \quad (5.11)$$

$$L_{duct} = \frac{1}{2} \rho V^2 S_d C_{L_{\alpha^d}} \alpha \quad (5.12)$$

$$L_{control-surface} = \frac{1}{2} \rho V_e^2 S_t (C_{L_{\alpha^t}} \alpha_{s.p} + C_{L_{\delta_e}} \delta_e) \quad (5.13)$$

An assumption has to be pointed out in Eq.(5.4). Though the duct is not a simple aerofoil like a wing, is formed by spanning NACA airfoil, indeed, the duct is created as NACA airfoil circled with shaft. The calculation of duct lift is done by using of the same principle as wing lift. Based on some tests and results this assumption is widely applied in aerodynamic analysis of duct, and it gives good performance as well as satisfactory results. 1. Another assumption should be figured out in Eq.(5.13).

Since $V_e >> V$, $V_e + V \approx V_e$, the flow passing through control surface (tail) is considered as the exit flow from ducted fan without external free flow. These two assumptions are widely used in the following content; regardless of considering other forces and moments.

5.1.2.4 Drag

In the same way the total drag consists of drag of wing, duct with fuselage and tail shown as below,

$$D = D_{wing} + D_{duct} + D_{control-surface} \quad (5.14)$$

In contrast to lift, the non-lift drag coefficient has to be considered in the contribution of drag of three components.

$$D_{wing} = \frac{1}{2} \rho V^2 S_w (C_{D_{0^w}} + C_{D_{\alpha^w}} \alpha) \quad (5.15)$$

$$D_{duct} = \frac{1}{2} \rho V^2 S_d (C_{D_{0^d}} + C_{D_{\alpha^d}} \alpha) \quad (5.16)$$

$$D_{control-surface} = \frac{1}{2} \rho V_e^2 S_t (C_{D_{0^t}} + C_{D_{\alpha^t}} \alpha_{s.p} + C_{D_{\delta_e}} \delta_e) \quad (5.17)$$

5.1.2.5 Pitching Moment

The figure 5.5 shows that the pitching moment is generated by wing's, duct with fuselage's and two horizontal tails' lift and drag. So, the expression of pitching moment is shown by,

$$\begin{aligned}
M = & (L_{wing} \cos \alpha + D_{wing} \sin \alpha)(X_{c.g} - X_{a.c-w}) + \\
& (L_{duct} \cos \alpha + D_{duct} \sin \alpha)(X_{c.g} - X_{a.c-d}) + \\
& (L_{control-ht1} \cos \alpha_{s.p1} + D_{control-ht1} \sin \alpha_{s.p1})(X_{c.g} - X_{a.c-t}) + \\
& (L_{control-ht2} \cos \alpha_{s.p2} + D_{control-ht2} \sin \alpha_{s.p2})(X_{c.g} - X_{a.c-t})
\end{aligned} \quad (5.18)$$

Since $\sin \alpha$ and $\sin \alpha_{s.p}$ are very small, the contribution of drag can be neglected.

$\cos \alpha \approx 1, \cos \alpha_{s.p} \approx 1$, pitching moment is simplified as below:

$$\begin{aligned}
M = & L_{wing}(X_{c.g} - X_{a.c-w}) + L_{duct}(X_{c.g} - X_{a.c-d}) + \\
& L_{control-ht1}(X_{c.g} - X_{a.c-t}) + L_{control-ht2}(X_{c.g} - X_{a.c-t})
\end{aligned} \quad (5.19)$$

5.1.2.6 Side Force

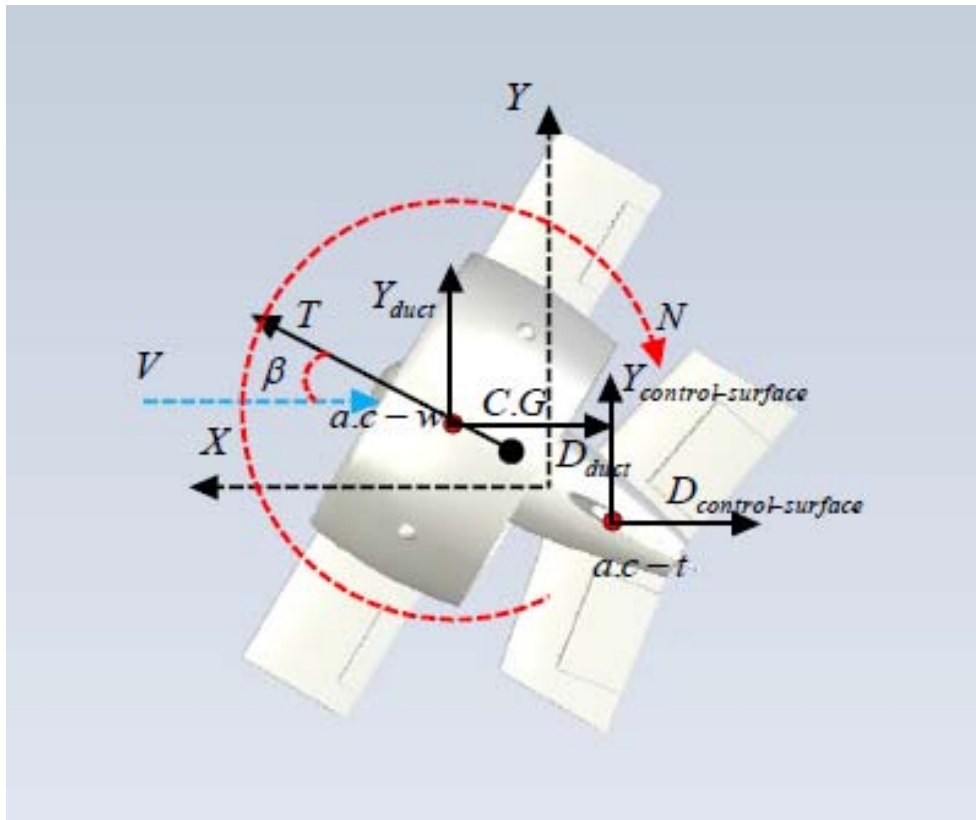


Figure 5. 5 Lateral Forces and Moments on UAV

The side force consists of two parts which are duct and vertical control surfaces excluding wing and horizontal control surface. As a result contributions of wing and horizontal tails are negligible in lateral analysis. The expression of total side force is given by.,

$$Y = Y_{duct} + Y_{control-surface} \quad (5.20)$$

$$Y_{duct} = \frac{1}{2} \rho V^2 S_d C_{Y\beta_d} \beta \quad (5.21)$$

$$Y_{control-surface} = \frac{1}{2} \rho V_e^2 S_t (C_{Y\beta_t} \beta_{s,p} + C_{L\delta_r} \delta_r) \quad (5.22)$$

5.1.2.7 Yawing Moment

The initial analysis of yawing moment is like this,

$$\begin{aligned} N &= (Y_{duct} \cos \beta + D_{duct} \sin \beta)(X_{c,g} - X_{a.c-d}) + \\ &(Y_{control-vt1} \cos \beta_{s,p1} + D_{control-vt1} \sin \beta_{s,p1})(X_{c,g} - X_{a.c-t}) + \\ &(Y_{control-vt2} \cos \beta_{s,p2} + D_{control-vt2} \sin \beta_{s,p2})(X_{c,g} - X_{a.c-t}) \end{aligned} \quad (5.23)$$

$\sin \beta$ and $\sin \beta_{s,p}$ are very small, $\cos \beta \approx 1$ and $\cos \beta_{s,p} \approx 1$, the contribution of drag can be neglected. Yawing moment is simplified as below:

$$N = Y_{duct} (X_{c,g} - X_{a.c-d}) + Y_{control-vt1} (X_{c,g} - X_{a.c-t}) + Y_{control-vt2} (X_{c,g} - X_{a.c-t}) \quad (5.24)$$

5.1.2.8 Rolling Moment

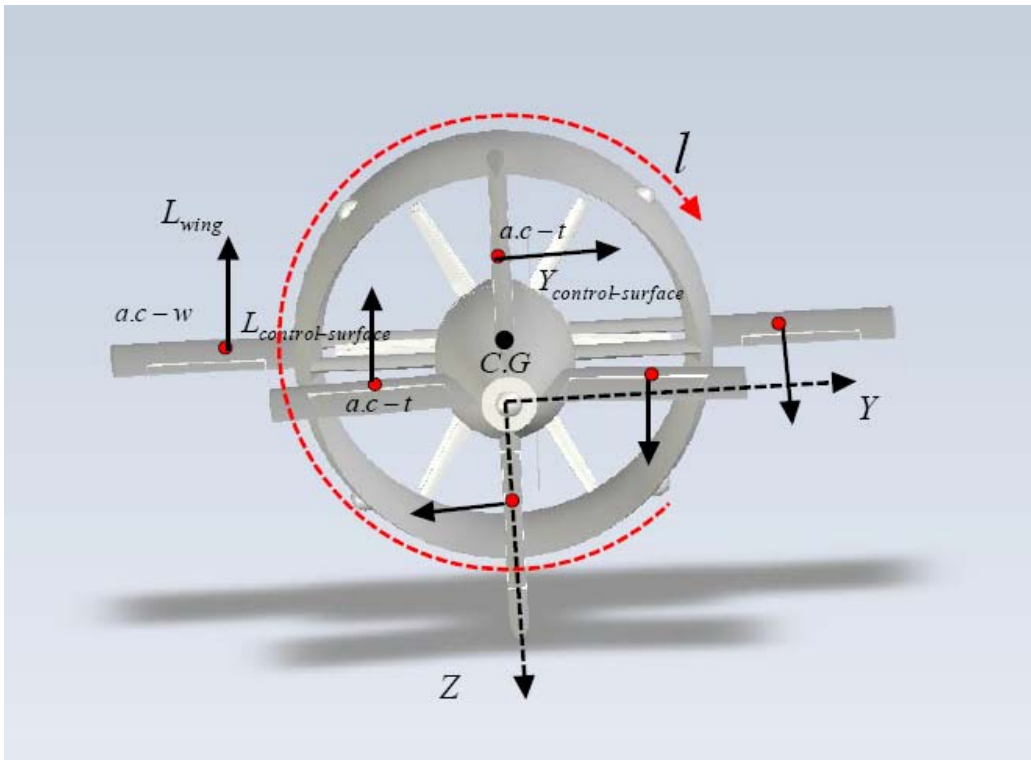


Figure 5.6 Rolling Moment on UAV

From this figure, it is clear that rolling moment is generated due to the forces act on wings and tails (control surface). Moreover, as the flaps and ailerons are controlled, the angle changes. Obviously, the rolling control is achieved. The total rolling moment is expressed as following,

$$\begin{aligned}
l = & L_{wing} (y_{c.g} - y_{a.c-w}) + \\
& L_{control ht1} (y_{c.g} - y_{a.c-t}) + L_{control ht2} (y_{c.g} - y_{a.c-t}) + \quad (5.25) \\
& Y_{control vt1} (y_{c.g} - y_{a.c-t}) + Y_{control vt2} (y_{c.g} - y_{a.c-t})
\end{aligned}$$

5.1.2.9 Rotor Torque

M_{rotor} is always generated in rotor-wing aircraft. Since the rotor is driven by motor rotating moment, another torque can not be avoided to act on the part which is used to amount the motor. In order to ensure the aircraft flies steadily, a counter-torque has to be created to counteract this torque. Like the helicopter, the tail rotor is used to generate the counter-torque to counteract the torque of the main rotor. Since the new concept coaxial helicopter came out, the best way to balance rotor-wing aircraft is using two rotors which rotate opposite to each other around the same axis. Indeed this innovation is widely used in many fields of aerospace engineering.

In this UAV, the same methodology is applied in design. There are two rotors in the internal duct. They are the same prototype, but only the pitch angles are opposite with each other so as to achieve counter-rotating. One rotor is rotating clockwise, the other one is counter-clockwise as mentioned in chapter 4. Therefore, we can get,

$$M_{rotor-1} = M_{rotor-2} \quad (5.26)$$

.Finally, the rotor torque needn't be considered in total moment when we analyze the aerodynamic characteristic of this UAV.

5.1.2.10 Gyroscopic Moment

A very important moment generated by gyroscopic effect should be taken into account. Since the rotating speed of motor Ω is very high during the UAV flight, meanwhile the UAV is flying maneuver transition, for instance, from vertical climb to horizontal, another angular velocity is ϖ generated. If there are two angular velocities acting on a rigid body, the gyroscopic moment is created as below,

$$M_{gyro} = \Omega \times J \varpi \quad (5.27)$$

J is the rotating inertia around the shaft of the motor. As there are two motors mounted in this UAV and the rotating speed of two motors are Ω_1 and Ω_2 respectively, two gyroscopic moments are created during flight.

$$M_{gyro-1} = \Omega_1 \times J_1 \varpi \quad (5.28)$$

$$M_{gyro-2} = \Omega_2 \times J_2 \varpi \quad (5.29)$$

Fortunately, the $J_1 = J_2$ and $\Omega_1 = \Omega_2$, therefore,

$$M_{gyro-1} = M_{gyro-2} \quad (5.30)$$

and the direction of two gyroscopic moments are opposite to each other, thus the gyroscopic moment will not supply the contribution on total moment of this UAV.

5.1.3 Summary of Forces and Moments

Above all, the forces and moments are summarized,

$$F_{total} = F_{thrust} + F_{drag} + F_{lift} + F_{side} + F_{gravity} + F_{cross-wind} \quad (5.31)$$

$$M_{total} = M_{rotor} + M_{drag} + M_{lift} + M_{side} + M_{cross-wind} \quad (5.32)$$

5.2 Dynamic Model of UAV

In this section the aerodynamic forces and moments will be expressed in the form of six degrees of freedom and combined with the vector equations of motion to obtain UAV models. Both the dimensional derivatives and dimensionless derivatives are listed and explained for simulation and for analytical purposes. First, the vector equations will be expanded with the translational-velocity state equation expressed in terms of velocity components in this UAV body-fixed state system. In addition, for the purpose of linearizing the equations of motion and researching the dynamic performance, it is better to use the velocity equation due to stability or wind-axes variables including airspeed and aerodynamic angles. The stability and wind-axes equations are used to build up a small perturbation model of UAV for linear analysis and design.

5.2.1 Nonlinear Dynamic Equations of Forces and Moments

The following dynamic equations are extrapolated by combining aerodynamic coefficients and forces' and moments' equations mentioned in previous section. Because the flow through wings and duct are different from the slipstream over the control surfaces, the dimensional description is used instead of dimensionless equations of aerodynamic coefficient for convenient analysis.

Thrust equation:

$$T = \rho A_e V_e (V + V_e) \quad (5.33)$$

Drag equation:

$$\begin{aligned} D = & \frac{1}{2} \rho V^2 S_w (C_{D_0 w} + C_{D_\alpha w} \alpha) + \frac{1}{2} \rho V^2 S_d (C_{D_0 d} + C_{D_\alpha d} \alpha) + \\ & \frac{1}{2} \rho V_e^2 S_t [C_{D_0 t} + C_{D_\alpha t} (\alpha_{s.p1} + \alpha_{s.p2}) + C_{D\delta_e} (\delta_{e1} + \delta_{e2}) + C_{D\delta_r} (\delta_{r1} + \delta_{r2})] \end{aligned} \quad (5.34)$$

Lift equation:

$$L = \frac{1}{2} \rho V^2 S_w C_{L_\alpha w} \alpha + \frac{1}{2} \rho V^2 S_d C_{L_\alpha d} \alpha + \frac{1}{2} \rho V_e^2 S_t [C_{L_\alpha t} (\alpha_{s,p1} + \alpha_{s,p2}) + C_{L\delta_e} (\delta_{e1} + \delta_{e2})] \quad (5.35)$$

Side force equation:

$$Y = \frac{1}{2} \rho V^2 S_d C_{Y\beta_d} \beta + \frac{1}{2} \rho V_e^2 S_t [C_{Y\beta_t} (\beta_{s,p1} + \beta_{s,p2}) + C_{Y\delta_r} (\delta_{r1} + \delta_{r2})] \quad (5.36)$$

Rolling moment equation:

$$l = \frac{1}{2} \rho V^2 S_w C_{L_{\dot{\alpha}}} \dot{\alpha} (y_{c,g} - y_{a,c-w}) + \frac{1}{2} \rho V_e^2 S_t \{ [C_{L_\alpha t} (\alpha_{s,p1} - \alpha_{s,p2}) + C_{L\delta_e} (\delta_{e1} - \delta_{e2})] + [C_{Y\beta_t} (\beta_{s,p1} - \beta_{s,p2}) + C_{Y\delta_r} (\delta_{r1} - \delta_{r2})] \} (y_{c,g} - y_{a,c-t}) \quad (5.37)$$

Pitching moment equation:

$$M = \frac{1}{2} \rho V^2 S_w C_{L_\alpha w} \alpha (X_{c,g} - X_{a,c-w}) + \frac{1}{2} \rho V^2 S_d C_{L_\alpha d} \alpha (X_{c,g} - X_{a,c-d}) + \frac{1}{2} \rho V_e^2 S_t [C_{L_\alpha t} (\alpha_{s,p1} + \alpha_{s,p2}) + C_{L\delta_e} (\delta_{e1} + \delta_{e2})] (X_{c,g} - X_{a,c-t}) \quad (5.38)$$

Yawing moment equation:

$$N = \frac{1}{2} \rho V^2 S_d C_{Y\beta_d} \beta (X_{c,g} - X_{a,c-d}) + \frac{1}{2} \rho V_e^2 S_t [C_{Y\beta_t} (\beta_{s,p1} + \beta_{s,p2}) + C_{Y\delta_r} (\delta_{r1} + \delta_{r2})] (X_{c,g} - X_{a,c-t}) \quad (5.39)$$

5.2.2 Coordinate Systems

To build up the equations of motion of aircraft to ensure the relative position, speed, acceleration and contributions of forces' vector, several axes' coordinates should be mentioned.

- Earth-Axes Coordinate System $Ox_g y_g z_g$
- Body-Axes Coordinate System $Ox_b y_b z_b$
- Wind-Axes Coordinate System $Ox_a y_a z_a$
- Track-Axes Coordinate System $Ox_k y_k z_k$

5.2.2.1 Transfer between $Ox_g y_g z_g$ and $Ox_b y_b z_b$

The position and attitude of aircraft in the body-axes coordinate relative to earth-axes coordinate are usually described by three Euler angles. They are yawing angle ψ , pitching angle θ and rolling angle ϕ , respectively.

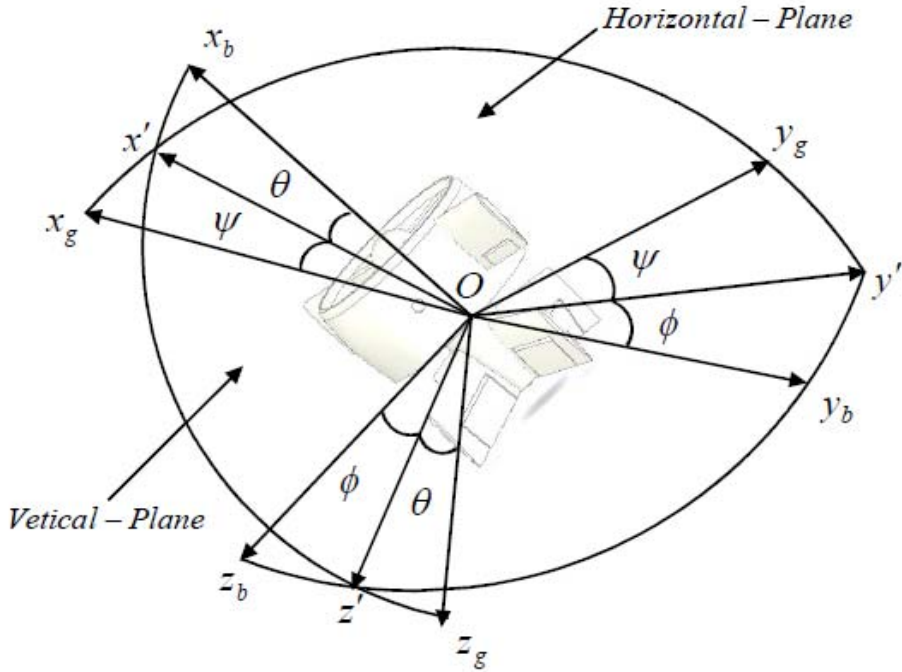


Figure5. 7 Relationships between Earth-Axes and Body-Axes Coordinate System

The figure 5.7 shows the process of coordinate transition. If the earth-axes coordinate $Ox_g y_g z_g$ rotates ψ with axis Oz_g , then spins θ around Oy' , finally it rotates ϕ degree with axis Ox_b , we can see that $Ox_g y_g z_g$ is overlapped with body-axes coordinate $Ox_b y_b z_b$. According to the principle of coordinate transfer, the transfer matrix between $Ox_g y_g z_g$ and $Ox_b y_b z_b$ is obtained,

$$R_{bg} = R_x(\phi)R_y(\theta)R_z(\psi) \quad (5.40)$$

Substituting the single axis transfer matrix into above equation, the transfer matrix is extended by,

$$R_{bg} = \begin{bmatrix} \cos\theta\cos\psi & \cos\theta\sin\psi & -\sin\theta \\ \sin\theta\sin\phi\cos\psi - \cos\phi\sin\psi & \sin\theta\sin\phi\sin\psi + \cos\phi\cos\psi & \sin\phi\cos\theta \\ \sin\theta\cos\phi\cos\psi + \sin\phi\sin\psi & \sin\theta\cos\phi\sin\psi - \sin\phi\cos\psi & \cos\phi\cos\theta \end{bmatrix} \quad (5.41)$$

5.2.2.2 Transfer between $Ox_g y_g z_g$ and $Ox_k y_k z_k$

There are only two angles between track-axes coordinate system and earth-axes coordinate system because of the Oz_k overlapped with Oz_g in the vertical plane. One is called track angle χ , the other one is climb angle γ .(see figure 5.8)

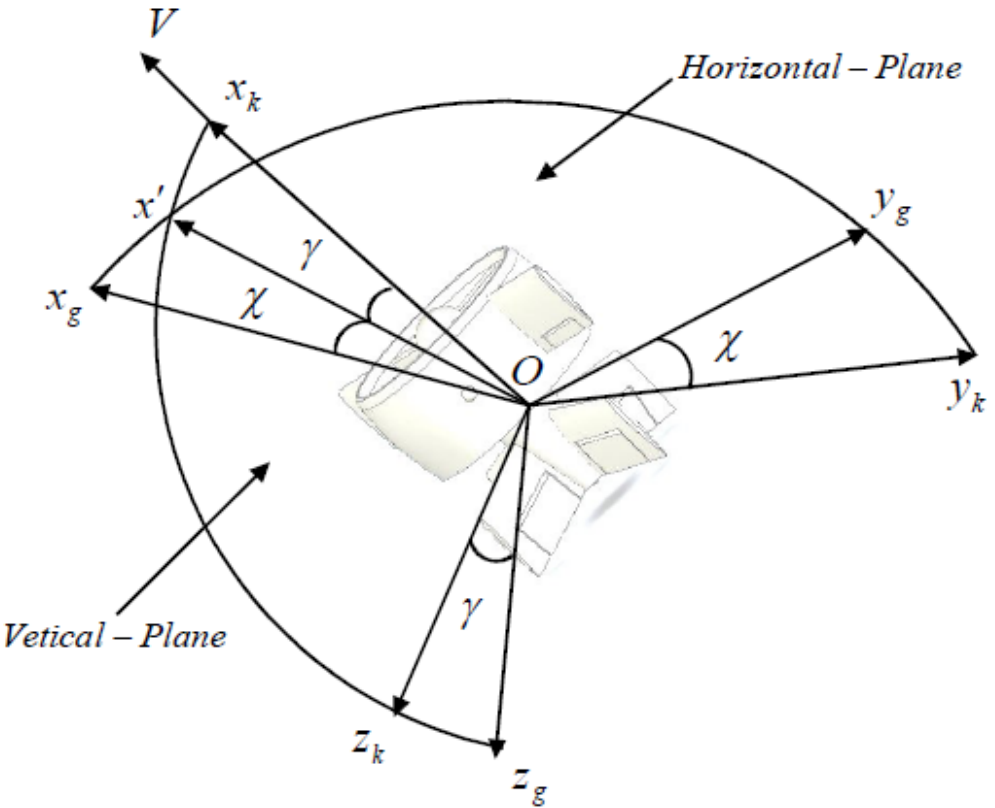


Figure5. 8 Relationships between Earth-Axes and Wind-Axes Coordinate System

The transfer matrix from $Ox_g y_g z_g$ to $Ox_k y_k z_k$ can be extrapolated based on $Ox_g y_g z_g$ rotating χ with Oz_g axis, then rotating γ around Oy_k axis.

$$R_{kg} = R_y(\gamma)R_z(\chi) \quad (5.42)$$

Substituting the single axis transfer matrix into above equation, the transfer matrix is given by,

$$R_{kg} = \begin{bmatrix} \cos \gamma \cos \chi & \cos \gamma \sin \chi & -\sin \gamma \\ -\sin \chi & \cos \chi & 0 \\ \sin \gamma \cos \chi & \sin \gamma \sin \chi & \cos \gamma \end{bmatrix} \quad (5.43)$$

5.2.2.3 Transfer between $Ox_k y_k z_k$ and $Ox_a y_a z_a$

Ox_k and Ox_a are in the same axis without wind, though they are in track-axes coordinate and wind-axes coordinate, respectively. So only one angle should be rotated between two coordinate systems, it is called speed rolling angle μ .

$$R_{ak} = R_x(\mu) \quad (5.44)$$

The transfer matrix is expressed as following,

$$R_{ak} = \begin{bmatrix} 1 & 0 & 0 \\ 0 & \cos \mu & \sin \mu \\ 0 & -\sin \mu & \cos \mu \end{bmatrix} \quad (5.45)$$

If the wind is considered, Ox_k and Ox_a are not in the same axis. Obviously, the matrix is not equal to this.

5.2.2.4 Transfer between $Ox_g y_g z_g$ and $Ox_a y_a z_a$

Apparently, the transfer matrix between earth-axes coordinate and wind-axes coordinate can be obtained through combining matrix R_{ak} and matrix R_{kg} . Therefore, there are three angles which have to be mentioned as a group of Euler angles are μ , χ and γ , respectively.

$$R_{ag} = R_{ak} R_{kg} = R_x(\mu) R_y(\chi) R_z(\gamma) \quad (5.46)$$

Substituting transfer matrix R_{ak} and R_{kg} into above equation, the transfer matrix is given by,

$$R_{ag} = \begin{bmatrix} \cos \gamma \cos \chi & \cos \gamma \sin \chi & -\sin \gamma \\ \sin \gamma \sin \mu \cos \chi - \cos \mu \sin \chi & \sin \gamma \sin \mu \sin \chi + \cos \mu \cos \chi & \sin \mu \cos \gamma \\ \sin \gamma \cos \mu \cos \chi + \sin \mu \sin \chi & \sin \gamma \cos \mu \sin \chi - \sin \mu \cos \chi & \cos \mu \cos \gamma \end{bmatrix} \quad (5.47)$$

5.2.2.5 Transfer between $Ox_a y_a z_a$ and $Ox_b y_b z_b$

Only two angles exist between wind-axes coordinate system and body-axes coordinate system because of the Oz_a overlapped with Oz_b in the vertical symmetrical plane of aircraft. One is called angle of attack α , the other one is sideslip angle β .

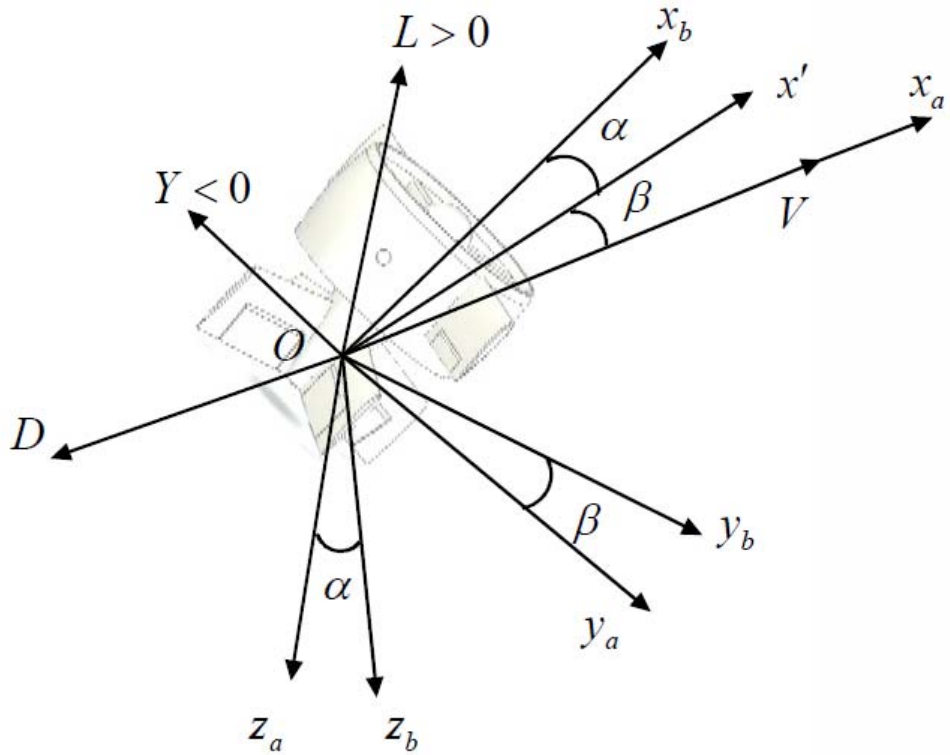


Figure5. 9 Relationships between Wind-Axes and Body-Axes Coordinate System

From this figure, we easily know that as long as $Ox_b y_b z_b$ rotates $-\alpha$ with Oy_b axis and then β with Oz_a axis. It will overlap to $Ox_a y_a z_a$. According to this, the transfer matrix is shown as below,

$$R_{ab} = R_x(\beta)R_y(-\alpha) \quad (5.48)$$

$$R_{ab} = \begin{bmatrix} \cos \alpha \cos \beta & \sin \beta & \sin \alpha \cos \beta \\ -\cos \alpha \sin \beta & \cos \beta & -\sin \alpha \sin \beta \\ -\sin \alpha & 0 & \cos \alpha \end{bmatrix} \quad (5.49)$$

5.2.3 Equations of Motion and Dynamic Equations

In this section, six dynamic equations and six equations of motion are listed so as to build up six degrees of freedom dynamic model for this UAV. The UAV is treated as a single rigid body with six degrees of freedom. This body is free to move in the atmosphere under the actions of gravity and aerodynamic forces. In addition, the earth is treated as a flat and stationary in inertial space (see figure 5.10). These assumptions simplify the model, and are available for dealing with complex problems of UAV flight.

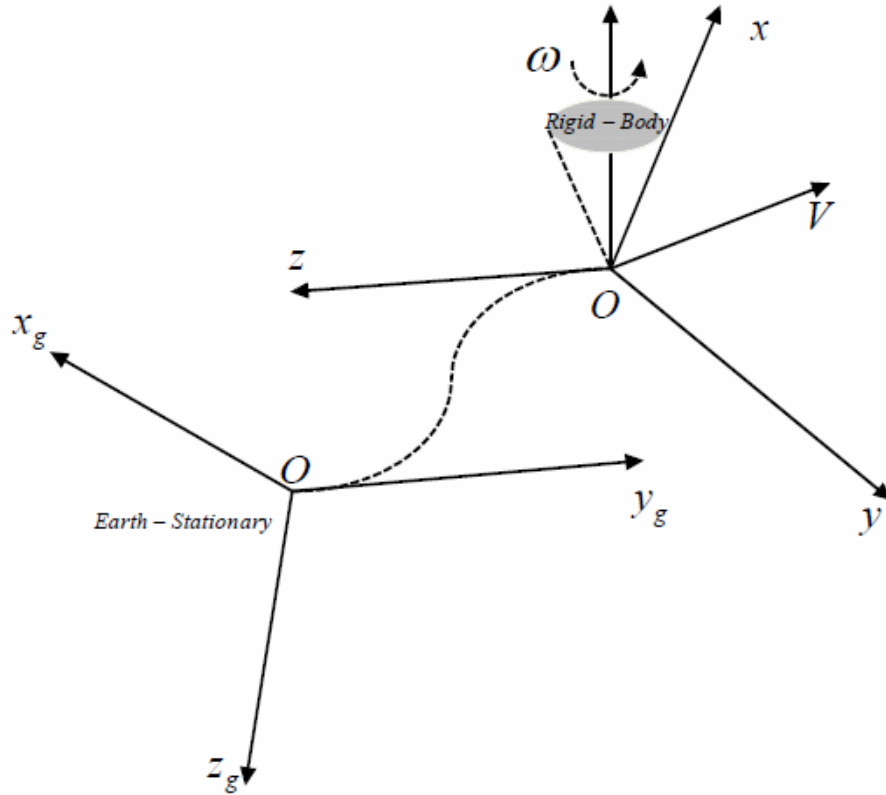


Figure5. 10 Body-Fixed Frame and Earth-Inertial Space

5.2.3.1 Dynamic Equations (centre of mass)

To research the motion of mass centre of rigid-body, scalars of force replacing vectors of forces is convenient for analyzing. Therefore, the forces which act on the mass centre of rigid-body can be expressed by three scalars in body-fixed frame in terms of momentum principle of Newton. The three dynamic equations relate to mass centre are given by,

$$m\left(\frac{du}{dt} + qw - rv\right) = F_x \quad (5.50)$$

$$m\left(\frac{dv}{dt} + ru - pw\right) = F_y \quad (5.51)$$

$$m\left(\frac{dw}{dt} + pv - qu\right) = F_z \quad (5.52)$$

5.2.3.2 Dynamic Equations (rotate around centre of mass)

The self-rotation of rigid-body is able to be treated as rotating around its own mass centre. Based on the principle of moment of momentum the dynamic equations on moments can be expressed as below,

$$I_x \frac{dp}{dt} + (I_z - I_y)qr - I_{zx}(pq - \frac{dr}{dt}) = L \quad (5.53)$$

$$I_y \frac{dq}{dt} + (I_x - I_z)rp + I_{zx}(p^2 - r^2) = M \quad (5.54)$$

$$I_z \frac{dr}{dt} + (I_y - I_x)pq + I_{zx}(qr - \frac{dp}{dt}) = N \quad (5.55)$$

Because this UAV is symmetry relate to plane Ox_bz_b in body-axes frame, the inertia moment

$I_{xy} = I_{yz} = 0$ have been substituted into dynamic equations of rotating with mass centre. Then above three simplified dynamic equations of moments are obtained

5.2.3.3 Equations of Motion (rotate around centre of mass)

In order to observe the flight path of trajectory of aircraft, the equations of motion are essential. Following are three equations of motion of aircraft rotating with its mass of centre.

$$\frac{dx_g}{dt} = V \cos \gamma \cos \chi \quad (5.56)$$

$$\frac{dy_g}{dt} = V \cos \gamma \sin \chi \quad (5.57)$$

$$\frac{dz_g}{dt} = -V \sin \gamma \quad (5.58)$$

By integrating the above three equations with time variable, the position of aircraft can be known in the form of x, y and z coordinates.

5.2.3.4 Equations of Motion (centre of mass)

Only the trajectory tracked on is not enough for analyzing the six degrees of freedom of aircraft. The attitude is important as well as position. There two options that are often used to describe the equations of motion on centre of mass.

- Euler angle

$$\frac{d\phi}{dt} = p + \tan \theta (q \sin \phi + r \cos \phi) \quad (5.59)$$

$$\frac{d\theta}{dt} = q \cos \phi - r \sin \phi \quad (5.60)$$

$$\frac{d\psi}{dt} = \frac{1}{\cos \theta} (q \sin \phi + r \cos \phi) \quad (5.61)$$

Yawing angle ψ , pitching angle θ and rolling angle ϕ are three Euler angles.

• Quaternion

$$\frac{de_0}{dt} = -\frac{1}{2}(e_1 p + e_2 q + e_3 r) \quad (5.62)$$

$$\frac{de_1}{dt} = \frac{1}{2}(e_0 p + e_2 r - e_3 q) \quad (5.63)$$

$$\frac{de_2}{dt} = \frac{1}{2}(e_0 q + e_3 p - e_1 r) \quad (5.64)$$

$$\frac{de_3}{dt} = \frac{1}{2}(e_0 r + e_1 q - e_2 p) \quad (5.65)$$

e_0, e_1, e_2, e_3 are four elements of quaternion, they also satisfy the constrain condition as

$$e_0^2 + e_1^2 + e_2^2 + e_3^2 = 1.$$

From the equation, we can see that if the aircraft achieves the maneuver transition, the pitch angle approaches 90 degree, the equation exists abnormal point which will prevent the flight simulation from calculating. In order to avoid this case to happen, the quaternion methodology is always used to describe the equation of motion.

Before explaining the relationship between Euler angle and quaternion, an important transfer matrix has to be listed,

$$R_{bg} = \begin{bmatrix} e_0^2 + e_1^2 - e_2^2 - e_3^2 & 2(e_1 e_2 + e_0 e_3) & 2(e_1 e_3 - e_0 e_2) \\ 2(e_1 e_2 - e_0 e_3) & e_0^2 - e_1^2 + e_2^2 - e_3^2 & 2(e_2 e_3 + e_0 e_1) \\ 2(e_0 e_2 + e_1 e_3) & 2(e_2 e_3 - e_0 e_1) & e_0^2 - e_1^2 - e_2^2 + e_3^2 \end{bmatrix} \quad (5.66)$$

Compared with matrix in Eq., this matrix has nine elements which are expressed in the use of quaternion instead of Euler angles. According to this, it is not difficult to find the relationship between Euler angles and quaternion. Using this relationship the Euler angles can be calculated from quaternion similar to the following equations,

$$\theta = \arcsin[-(e_1 e_3 - e_0 e_2)] \quad (5.67)$$

$$\phi = \arccos[\frac{e_0^2 - e_1^2 - e_2^2 + e_3^2}{\sqrt{1 - 4(e_1 e_3 - e_0 e_2)^2}}] \text{sgn}[2(e_2 e_3 + e_0 e_1)] \quad (5.68)$$

$$\psi = \arccos[\frac{e_0^2 + e_1^2 - e_2^2 - e_3^2}{\sqrt{1 - 4(e_1 e_3 - e_0 e_2)^2}}] \text{sgn}[2(e_1 e_2 + e_0 e_3)] \quad (5.69)$$

The function $\text{sgn}(\bullet)$'s meaning is: if the independent variable is positive, $\text{sgn}(\bullet) = 1$; otherwise the

independent variable is negative, $\text{sgn}(\bullet) = -1$. It is clear that once we use the quaternion to calculate

Euler angles, even $\theta = \frac{\pi}{2} = 90^\circ$ the abnormal point will not appear during flight simulation and modeling.

5.2.3.5 Dynamic Equations in Track-Axes Coordinate System

Combining the Eq.(5.30), Eq.(5.31) Eq.(5.32) and coordinate transfer functions, the dynamic equations in track-axes coordinate are able to be extrapolated as below,

$$m \frac{dV}{dt} = T \cos \alpha \cos \beta - D - mg \sin \gamma \quad (5.70)$$

$$mV \cos \gamma \frac{d\chi}{dt} = T(\sin \alpha \sin \mu - \cos \alpha \sin \beta \cos \mu) + C \cos \mu + L \sin \mu \quad (5.71)$$

$$-mV \frac{d\gamma}{dt} = T(-\sin \alpha \cos \mu - \cos \alpha \sin \beta \sin \mu) + C \sin \mu - L \cos \mu + mg \cos \gamma \quad (5.72)$$

These three equations are useful for linearization which will be discussed next section for linear model of UAV.

5.3 Linearization of Dynamic Model

As mentioned in Sec.5.2 these equations of motion or dynamic equations are frequently linearized for use in stability and control analysis. It is assumed that the motion of the airplane consists of small deviations from a reference condition of steady flight. The use of the small-disturbance theory in linearization has been found in practice to give good performance and results.

5.3.1 The Small-Disturbance Theory

It predicts with satisfactory precision the stability of non-accelerated flight with sufficient accuracy for engineering purposes. The reasons for the success of this include: (1) In many cases, the major aerodynamic effects are nearly linear functions of the disturbances; (2) The disturbed flight can occur with quite small values of the linear and angular velocity disturbances.

Several assumptions of small-disturbance theory are restricted to current practice. They are,

- The effects of gyroscope caused by spinning rotors are negligible.
- The wind velocity is quite small.
- The variation of aerodynamic coefficient is proportional to disturbed variable as linear.

5.3.2 Linear Methodology

Arbitrary equation can be expressed as a function,

$$f(x_1, x_2, \dots, x_n) = 0 \quad (5.73)$$

In this equation, $x_i (i = 1, 2, \dots, n)$ is independent variable. According to small-disturbance theory,

these kinds of variables can be expressed as the sum of x_{i*} and Δx_i :

$$x_i = x_{i*} + \Delta x_i \quad (5.74)$$

Then Eq.(5.73) is able to be written as,

$$f(x_{1*} + \Delta x_1, x_{2*} + \Delta x_2, \dots, x_{n*} + \Delta x_n) = 0 \quad (5.75)$$

Which is also able to extended relate to $(x_{1*}, x_{2*}, \dots, x_{n*})$ using Taylor series and high order variables are neglected in terms of small-disturbance theory as below,

$$f(x_{1*}, x_{2*}, \dots, x_{n*}) + \left(\frac{\partial f}{\partial x_{1*}}\right)\Delta x_1 + \left(\frac{\partial f}{\partial x_{2*}}\right)\Delta x_2 + \dots + \left(\frac{\partial f}{\partial x_{n*}}\right)\Delta x_n = 0 \quad (5.76)$$

Obviously,

$$f(x_{1*}, x_{2*}, \dots, x_{n*}) = 0 \quad (5.77)$$

Using Eq.(5.76) minus Eq.(5.77), we obtain,

$$\left(\frac{\partial f}{\partial x_{1*}}\right)\Delta x_1 + \left(\frac{\partial f}{\partial x_{2*}}\right)\Delta x_2 + \dots + \left(\frac{\partial f}{\partial x_{n*}}\right)\Delta x_n = 0 \quad (5.78)$$

This equation is called linear small-disturbance equation. Then we define this equation using another format,

$$\Delta f = \left(\frac{\partial f}{\partial x_{1*}}\right)\Delta x_1 + \left(\frac{\partial f}{\partial x_{2*}}\right)\Delta x_2 + \dots + \left(\frac{\partial f}{\partial x_{n*}}\right)\Delta x_n = f_{x_1}\Delta x_1 + f_{x_2}\Delta x_2 + \dots + f_{x_n}\Delta x_n \quad (5.79)$$

5.3.3 Linear Forces and Moments

Both longitudinal and lateral equations of forces and moments are listed in section 5.2, according to this; we can get the linear expression of forces and moments as following,

$$T = T(V, H, V_e) \quad (5.80)$$

$$D = D(V, H, \alpha, \beta, V_e, \delta_{e1}, \delta_{e2}, \delta_{r1}, \delta_{r2}) \quad (5.81)$$

$$L = L(V, H, \alpha, p, q, V_e, \delta_{e1}, \delta_{e2}) \quad (5.82)$$

$$Y = Y(V, H, \beta, p, r, V_e, \delta_{r1}, \delta_{r2}) \quad (5.83)$$

$$l = l(V, H, \alpha, \beta, p, q, r, V_e, \delta_a, \delta_{e1}, \delta_{e2}, \delta_{r1}, \delta_{r2}) \quad (5.84)$$

$$M = M(V, H, \alpha, p, q, V_e, \delta_{e1}, \delta_{e2}) \quad (5.85)$$

$$N = N(V, H, \beta, p, r, V_e, \delta_a, \delta_{r1}, \delta_{r2}) \quad (5.86)$$

They all can be written like $\Delta f = f_{x_1} \Delta x_1 + f_{x_2} \Delta x_2 + \dots + f_{x_n} \Delta x_n$ that is what we will use to linear equations.

5.3.4 Linear Equations

Now, using the same methodology to deal with the equation of motion and dynamic equations in sec.5.2.3, we can get a quantity of linear equations in the form of small-disturbance.

- **Force equations**

$$m \frac{d\Delta V}{dt} = \Delta T \cos \alpha_* - T_* \sin \alpha_* \Delta \alpha - \Delta D - mg \sin \gamma_* \Delta \gamma \quad (5.87)$$

$$mV_* \frac{d\Delta \gamma}{dt} = \Delta T \sin \alpha_* + T_* \cos \alpha_* \Delta \alpha + \Delta L + mg \sin \gamma_* \Delta \gamma \quad (5.88)$$

$$mV_* \frac{d\Delta \beta}{dt} + mV_* \Delta \gamma - mV_* \alpha_* \Delta p = -D_* \Delta \beta + \Delta Y + mg \Delta \phi \cos \theta_* \quad (5.89)$$

- **Moment equations**

$$I_x \frac{d\Delta p}{dt} - I_{zx} \frac{d\Delta r}{dt} = \Delta l \quad (5.90)$$

$$I_y \frac{d\Delta q}{dt} = \Delta M \quad (5.91)$$

$$I_z \frac{d\Delta r}{dt} - I_{zx} \frac{d\Delta p}{dt} = \Delta N \quad (5.92)$$

- **Position equations**

$$\frac{d\Delta x_g}{dt} = \Delta V \cos \gamma_* - V_* \sin \gamma_* \Delta \gamma \quad (5.93)$$

$$\frac{d\Delta y_g}{dt} = V_* \cos \gamma_* \Delta \chi \quad (5.94)$$

$$\frac{d\Delta z_g}{dt} = -\frac{d\Delta H}{dt} = -\Delta V \sin \gamma_* - V_* \cos \gamma_* \Delta \gamma \quad (5.95)$$

- **Euler angle equations**

$$\frac{d\Delta \phi}{dt} = \tan \theta_* \Delta r + \Delta p \quad (5.96)$$

$$\frac{d\Delta \theta}{dt} = \Delta q \quad (5.97)$$

$$\frac{d\Delta\psi}{dt} = \frac{1}{\cos\theta_*} \Delta r \quad (5.98)$$

- *Geometry angle equations*

$$\Delta\alpha = \Delta\theta - \Delta\gamma \quad (5.99)$$

$$\Delta\beta = \cos\gamma_* (\Delta\psi - \Delta\chi) + \sin\alpha_* \Delta\phi \quad (5.100)$$

$$\Delta\mu = \tan\gamma_* \Delta\beta + \frac{\cos\theta_*}{\cos\gamma_*} \Delta\phi \quad (5.101)$$

It should be noted that $\Delta(\cdot)$ represents the approximate value of (\cdot) in the case of small disturbance rather than derivatives of (\cdot) .

5.3.5 Linear Model of 6DoF

Substituting the linear forces and moments into six force and moment equations, we can obtain,

$$\begin{aligned} \frac{d\Delta V}{dt} &= \frac{(T_V \cos\alpha_* - D_V)}{m} \Delta V - \frac{(T_* \sin\alpha_* - mg \cos\gamma_* + D_\alpha)}{m} \Delta\alpha \\ &+ g \cos\gamma_* \Delta\theta + \frac{(T_H \cos\alpha_* - D_H)}{m} \Delta H - \frac{(T_{ve} \cos\alpha_* - D_{ve})}{m} \Delta V_e \\ &+ \frac{D_{\delta e}}{m} \Delta\delta e_1 + \frac{D_{\delta e}}{m} \Delta\delta e_2 + \frac{D_{\delta r}}{m} \Delta\delta r_1 + \frac{D_{\delta r}}{m} \Delta\delta r_2 \end{aligned} \quad (5.102)$$

$$\begin{aligned} \frac{d\Delta\alpha}{dt} &= -\frac{(T_V \sin\alpha_* + L_V)}{mV_*} \Delta V - \frac{(T_* \cos\alpha_* + L_\alpha - mg \sin\gamma_*)}{mV_*} \Delta\alpha \\ &+ \frac{(mV_* - L_q)}{mV_*} \Delta q - \frac{g \sin\gamma_*}{V_*} \Delta\theta - \frac{(T_H \sin\alpha_* + L_H)}{mV_*} \Delta H \\ &- \frac{L_p}{mV_*} \Delta p - \frac{(T_{ve} \sin\alpha_* + L_{ve})}{mV_*} \Delta V_e - \frac{L_{\delta e}}{mV_*} \Delta\delta e_1 - \frac{L_{\delta e}}{mV_*} \Delta\delta e_2 \end{aligned} \quad (5.103)$$

$$\begin{aligned} \frac{d\Delta q}{dt} &= \frac{M_V}{I_y} \Delta V + \frac{M_\alpha}{I_y} \Delta\alpha + \frac{M_q}{I_y} \Delta q + \frac{M_H}{I_y} \Delta H \\ &+ \frac{M_p}{I_y} \Delta p + \frac{M_{ve}}{I_y} \Delta V_e + \frac{M_{\delta e}}{I_y} \Delta\delta e_1 + \frac{M_{\delta e}}{I_y} \Delta\delta e_2 \end{aligned} \quad (5.104)$$

$$\begin{aligned}
\frac{d\beta}{dt} &= \frac{Y_V}{mV_*} \Delta V + \frac{Y_H}{mV_*} \Delta H + \frac{(Y_\beta - D_*)}{mV_*} \Delta \beta + \\
&\frac{(Y_p + mV_* \alpha_*)}{mV_*} \Delta p + \frac{(Y_r - mV_*)}{mV_*} \Delta r + \frac{mg \cos \theta_*}{mV_*} \Delta \phi \quad (5.105) \\
&+ \frac{Y_{ve}}{mV_*} \Delta V_e + \frac{Y_{\delta r}}{mV_*} \Delta \delta_{r1} + \frac{Y_{\delta r}}{mV_*} \Delta \delta_{r2}
\end{aligned}$$

$$\begin{aligned}
\frac{d\Delta p}{dt} &= \frac{I_z l_V + I_{zx} N_V}{I_x I_z - I_{zx}^2} \Delta V + \frac{I_z l_\alpha}{I_x I_z - I_{zx}^2} \Delta \alpha + \frac{I_z l_q}{I_x I_z - I_{zx}^2} \Delta q + \frac{I_z l_H + I_{zx} N_H}{I_x I_z - I_{zx}^2} \Delta H \\
&+ \frac{I_z l_\beta + I_{zx} N_\beta}{I_x I_z - I_{zx}^2} \Delta \beta + \frac{I_z l_p + I_{zx} N_p}{I_x I_z - I_{zx}^2} \Delta p + \frac{I_z l_r + I_{zx} N_r}{I_x I_z - I_{zx}^2} \Delta r + \frac{I_z l_{ve} + I_{zx} N_{ve}}{I_x I_z - I_{zx}^2} \Delta V_e \\
&+ \frac{I_z l_{\dot{\alpha}} + I_{zx} N_{\dot{\alpha}}}{I_x I_z - I_{zx}^2} \Delta \delta_a + \frac{I_z l_{\dot{\alpha}}}{I_x I_z - I_{zx}^2} \Delta \delta_{e1} + \frac{I_z l_{\dot{\alpha}}}{I_x I_z - I_{zx}^2} \Delta \delta_{e2} \\
&+ \frac{I_z l_{\dot{\sigma}} + I_{zx} N_{\dot{\sigma}}}{I_x I_z - I_{zx}^2} \Delta \delta_{r1} + \frac{I_z l_{\dot{\sigma}} + I_{zx} N_{\dot{\sigma}}}{I_x I_z - I_{zx}^2} \Delta \delta_{r2} \quad (5.106)
\end{aligned}$$

$$\begin{aligned}
\frac{d\Delta r}{dt} &= \frac{I_{zx} l_V + I_x N_V}{I_x I_z - I_{zx}^2} \Delta V + \frac{I_{zx} l_\alpha}{I_x I_z - I_{zx}^2} \Delta \alpha + \frac{I_{zx} l_q}{I_x I_z - I_{zx}^2} \Delta q + \frac{I_{zx} l_H + I_x N_H}{I_x I_z - I_{zx}^2} \Delta H \\
&+ \frac{I_{zx} l_\beta + I_x N_\beta}{I_x I_z - I_{zx}^2} \Delta \beta + \frac{I_{zx} l_p + I_x N_p}{I_x I_z - I_{zx}^2} \Delta p + \frac{I_{zx} l_r + I_x N_r}{I_x I_z - I_{zx}^2} \Delta r + \frac{I_{zx} l_{ve} + I_x N_{ve}}{I_x I_z - I_{zx}^2} \Delta V_e \\
&+ \frac{I_{zx} l_{\dot{\alpha}} + I_x N_{\dot{\alpha}}}{I_x I_z - I_{zx}^2} \Delta \delta_a + \frac{I_{zx} l_{\dot{\alpha}}}{I_x I_z - I_{zx}^2} \Delta \delta_{e1} + \frac{I_{zx} l_{\dot{\alpha}}}{I_x I_z - I_{zx}^2} \Delta \delta_{e2} \\
&+ \frac{I_{zx} l_{\dot{\sigma}} + I_x N_{\dot{\sigma}}}{I_x I_z - I_{zx}^2} \Delta \delta_{r1} + \frac{I_{zx} l_{\dot{\sigma}} + I_x N_{\dot{\sigma}}}{I_x I_z - I_{zx}^2} \Delta \delta_{r2} \quad (5.107)
\end{aligned}$$

The above six equations are composed to linear six degree of freedom (6DoF) model for this UAV. We also can combine the three position equations and three Euler angle equations, moreover, adding the three geometry angle equations, another group of linear equations of motion are obtained as following shown,

$$-\frac{d\Delta z_g}{dt} = \frac{d\Delta H}{dt} = \sin \gamma_* \Delta V - V_* \cos \gamma_* \Delta \alpha + V_* \cos \gamma_* \Delta \theta \quad (5.108)$$

$$\frac{d\Delta x_g}{dt} = \cos \gamma_* \Delta V - V_* \sin \gamma_* \Delta \gamma \quad (5.109)$$

$$\frac{d\Delta y_g}{dt} = V_* \cos \gamma_* \Delta \chi \quad (5.110)$$

$$\frac{d\Delta \phi}{dt} = \Delta p + \tan \theta_* \Delta r \quad (5.111)$$

$$\frac{d\Delta\theta}{dt} = \Delta q \quad (5.112)$$

$$\frac{d\Delta\psi}{dt} = \frac{1}{\cos\theta_*} \Delta r \quad (5.113)$$

For these 12 linear equations, 9 of them have a relationship with each other called coupled equation, another 3 are independent called decoupled equation. So, for convenient analysis, they are normally separated into two groups. One group is longitudinal equations, the other one is lateral equations. However, for this UAV, we know that it has four control surfaces which are not only used to achieve longitudinal control, but also used to fulfill lateral control. Therefore, the longitudinal control is coupled with lateral control, which is totally different from other existing UAVs or aircraft. Due to this, a coupled linear model has to be built up for coupled control.

5.4 State Space Method

The use of the state space method facilitates the solution of the small-disturbance equations of motion of aircraft. Since the computational mechanism depends on the use of matrix algebra it is most conveniently handled by a digital computer and many suitable software packages are available. Most commercial software is intended for application to problems in modern control and to ensure that the aircraft equations of motion are correctly assembled before a solution is simulated by computed tools.

5.4.1 The Equations of Motion in State Space Form

Nowadays, the solution of the equations of motion poses few problems since powerful computational tools are already available. Since computers are very good at dealing with numerical matrix calculations in use of matrix methods for solving linear dynamic system problems has become an important project in applied mathematics. For small disturbance, the aircraft is an example of a linear dynamic system which is the prelude to flight control system design and analysis. Following is a suitable format to arrange the equations of motion.

$$\dot{x} = Ax + Bu \quad (5.114)$$

$$y = Cx + Du \quad (5.115)$$

In Eq.(5.114) x is the column vector of n state variables called the state vector. u is the column vector of m state variables called the input vector. A is the $n \times n$ state matrix. B is the $n \times m$ input matrix.

In Eq.(5.115) y is the column vector of n state variables called the output vector. C is the $r \times n$ output matrix. D is the $r \times m$ direct matrix.

Combining Eq.(5.102), (5.103), (5.104), (5.105), (5.106), (5.107), (5.108), (5.111) and (5.112), the state equations can be obtained. These nine equations of motion are coupled because of the control input from four control surfaces which are not only for longitudinal control, but also for lateral control. of

motion,

$$\begin{bmatrix} \frac{d\Delta V}{dt} \\ \frac{d\Delta \alpha}{dt} \\ \frac{d\Delta q}{dt} \\ \frac{d\Delta \theta}{dt} \\ \frac{d\Delta H}{dt} \\ \frac{d\Delta \beta}{dt} \\ \frac{d\Delta p}{dt} \\ \frac{d\Delta r}{dt} \\ \frac{d\Delta \phi}{dt} \end{bmatrix} = A \begin{bmatrix} \Delta V \\ \Delta \alpha \\ \Delta q \\ \Delta \theta \\ \Delta H \\ \Delta \beta \\ \Delta p \\ \Delta r \\ \Delta \phi \end{bmatrix} + B \begin{bmatrix} \Delta V_e \\ \Delta \delta_{e1} \\ \Delta \delta_{e2} \\ \Delta \delta_a \\ \Delta \delta_{r1} \\ \Delta \delta_{r2} \end{bmatrix} \quad (5.116)$$

Using four variables describe the input vectors including $\Delta\delta_{e1}$ $\Delta\delta_{e2}$ $\Delta\delta_{r1}$ and $\Delta\delta_{r2}$. They are elevator-1 deflection, elevator-2 deflection, rudder-1 deflection and rudder-2 deflection, respectively. $\Delta\delta_a$ is the aileron deflection. ΔV_e is called variable of exit velocity of ducted fan, which controlled by throttle of motor. In addition, the state vector contains $(\Delta V, \Delta \alpha, \Delta q, \Delta \theta, \Delta H, \Delta \beta, \Delta p, \Delta r, \Delta \phi)$ and so on. \dot{x} is the derivatives of x . Then we can get the format of equations like Eq.(5.116).

The state matrix A and input matrix B are expressed,

Matrix A.

$$\begin{bmatrix} T_V \cos\alpha_* - D_V & T_* \sin\alpha_* - mg \cos\gamma_* + D_\alpha & 0 & g \cos\gamma_* & T_H \cos\alpha_* - D_H & 0 & 0 & 0 & 0 \\ \frac{m}{mV_*} & \frac{m}{mV_*} & 0 & V_* & \frac{m}{mV_*} & 0 & -\frac{L_p}{mV_*} & 0 & 0 \\ (T_V \sin\alpha_* + L_V) & (T_* \cos\alpha_* + L_\alpha - mgsin\gamma_*) & (mV_* - L_q) & g \sin\gamma_* & (T_H \sin\alpha_* + L_H) & 0 & 0 & 0 & 0 \\ \frac{M_V}{mV_*} & \frac{M_\alpha}{mV_*} & 0 & M_q & \frac{M_H}{mV_*} & 0 & \frac{M_p}{I_y} & 0 & 0 \\ \frac{M_V}{I_y} & \frac{M_\alpha}{I_y} & 0 & I_y & \frac{M_H}{I_y} & 0 & 0 & 0 & 0 \\ 0 & 0 & 1 & 0 & 0 & 0 & 0 & 0 & 0 \\ \sin\gamma_* & -V_* \cos\gamma_* & 0 & V_* \cos\gamma_* & 0 & 0 & 0 & 0 & 0 \\ \frac{Y_V}{mV_*} & 0 & 0 & 0 & \frac{Y_H}{mV_*} & \frac{Y_\beta - D_*}{mV_*} & \frac{Y_p + mV_* \alpha_*}{mV_*} & \frac{Y_r - mV_*}{mV_*} & \frac{mg \cos\theta_*}{mV_*} \\ \frac{I_z l_V + I_{zx} N_V}{I_x I_z} & \frac{l_\alpha}{I_x} & \frac{l_q}{I_x} & 0 & \frac{I_z l_H + I_{zx} N_H}{I_x I_z} & \frac{I_z l_\beta + I_{zx} N_\beta}{I_x I_z} & \frac{I_z l_p + I_{zx} N_p}{I_x I_z} & \frac{I_z l_r + I_{zx} N_r}{I_x I_z} & 0 \\ \frac{I_{zx} l_V + I_x N_V}{I_x I_z} & \frac{I_{zx} l_\alpha}{I_x I_z} & \frac{I_{zx} l_q}{I_x I_z} & 0 & \frac{I_{zx} l_H + I_x N_H}{I_x I_z} & \frac{I_{zx} l_\beta + I_x N_\beta}{I_x I_z} & \frac{I_{zx} l_p + I_x N_p}{I_x I_z} & \frac{I_{zx} l_r + I_x N_r}{I_x I_z} & 0 \\ 0 & 0 & 0 & 0 & 0 & I_x I_z & I_x I_z & I_x I_z & \tan\theta_* \\ 0 & 0 & 0 & 0 & 0 & 0 & 1 & 0 & 0 \end{bmatrix}$$

Matrix B.

$$\begin{bmatrix} -\frac{(T_{Ve} \cos \alpha_* - D_{Ve})}{m} & \frac{D_{\delta e}}{m} & \frac{D_{\delta e}}{m} & 0 & \frac{D_{\delta r}}{m} & \frac{D_{\delta r}}{m} \\ -\frac{(T_{Ve} \sin \alpha_* + L_{Ve})}{mV_*} & -\frac{L_{\delta e}}{mV_*} & -\frac{L_{\delta e}}{mV_*} & 0 & 0 & 0 \\ \frac{M_{Ve}}{I_y} & \frac{M_{\delta e}}{I_y} & \frac{M_{\delta e}}{I_y} & 0 & 0 & 0 \\ 0 & 0 & 0 & 0 & 0 & 0 \\ 0 & 0 & 0 & 0 & 0 & 0 \\ \frac{Y_{Ve}}{mV_*} & 0 & 0 & 0 & \frac{Y_{\delta r}}{mV_*} & \frac{Y_{\delta r}}{mV_*} \\ I_z l_{Ve} + I_{zx} N_{Ve} & \frac{l_{\delta e}}{I_x} & \frac{l_{\delta e}}{I_x} & \frac{I_z l_{\delta a} + I_{zx} N_{\delta a}}{I_x I_z} & \frac{I_z l_{\delta r} + I_{zx} N_{\delta r}}{I_x I_z} & \frac{I_z l_{\delta r} + I_{zx} N_{\delta r}}{I_x I_z} \\ I_x I_z & I_x & I_x & I_x I_z & I_x I_z & I_x I_z \\ I_{zx} l_{Ve} + I_x N_{Ve} & \frac{I_{zx} l_{\delta e}}{I_x I_z} & \frac{I_{zx} l_{\delta e}}{I_x I_z} & \frac{I_{zx} l_{\delta a} + I_x N_{\delta a}}{I_x I_z} & \frac{I_{zx} l_{\delta r} + I_x N_{\delta r}}{I_x I_z} & \frac{I_{zx} l_{\delta r} + I_x N_{\delta r}}{I_x I_z} \\ I_x I_z & I_x I_z \\ 0 & 0 & 0 & 0 & 0 & 0 \end{bmatrix}$$

5.4.2 Aerodynamic Derivatives

In aerodynamic analysis, normally, the stability and control derivatives are estimated by theoretical methodology, computed by CFD code or measured by experiment and flight test. Aerodynamic derivatives as the basic parameters for flight simulation and control development are taken care of so much in order to get accurate and satisfactory results for providing the essential link between aircraft dynamics and airframe aerodynamics.

Usually, the dimensionless derivatives are involved in many kinds of handbooks for building up a dynamic model of aircraft. However, during analyzing aerodynamic characteristic of this UAV, we find that the input variable V_e is used throughout analysis from Eq.(5.33) to Eq.(5.39). If these

equations divide $\frac{1}{2} \rho V^2 S$ to transfer into dimensionless equations, the variable V_e still exists in them.

Therefore, to get a convenient format to analyze flight dynamics of this UAV, the dimensional derivatives are strongly proposed as shown in table.18.

Table. 18 Aerodynamic Derivatives of Ducted Fan VTOL UAV

$T_V = \rho A_e V_e$	$T_{V_e} = 2 \rho A_e V_e$	
$D_V = \rho V [S_w(C_{D_0 w} + C_{D_\alpha w} \alpha) + S_d(C_{D_0 d} + C_{D_\alpha d} \alpha)]$	$D_\alpha = \frac{1}{2} \rho V^2 (S_w C_{D_\alpha w} + S_d C_{D_\alpha d}) + \rho V_e^2 S_t C_{D_\alpha t}$	$D_{V_e} = \rho V_e S_t C_{D_0 t}$
$D_{\hat{\alpha}} = \rho V_e^2 S_t C_{D \hat{\alpha}}$	$D_{\hat{\sigma}} = \rho V_e^2 S_t C_{D \hat{\sigma}}$	
$L_V = \rho V (S_w C_{L_\alpha w} \alpha + S_d C_{L_\alpha d} \alpha)$	$L_\alpha = \frac{1}{2} \rho V^2 (S_w C_{L_\alpha w} + S_d C_{L_\alpha d}) + \rho V_e^2 S_t C_{L_\alpha t}$	$L_q = -\rho V_e^2 S_t C_{L_\alpha t} \times \frac{ X_{c,g} - X_{a,c-t} }{V \cos \alpha + V_e}$
$L_p = 0$	$L_{V_e} = 2 \rho V_e S_t C_{L_\alpha t} \frac{V \alpha}{V + V_e}$	$L_{\hat{\alpha}} = \rho V_e^2 S_t C_{L \hat{\alpha}}$
$Y_V = \rho V S_d C_{Y_\beta d} \beta$	$Y_\beta = \frac{1}{2} \rho V^2 S_d C_{Y_\beta d} + \rho V_e^2 S_t C_{Y_\beta t}$	$Y_p = 0$
$Y_r = \rho V_e^2 S_t C_{Y_\beta t} \times \frac{ X_{c,g} - X_{a,c-t} }{V \cos \beta + V_e}$	$Y_{V_e} = 2 \rho V_e S_t C_{Y_\beta t} \frac{V \beta}{V + V_e}$	$Y_{\hat{\sigma}} = \rho V_e^2 S_t C_{Y \hat{\sigma}}$
$l_V = \rho V S_w C_{L \hat{\alpha}} \hat{\alpha} a (y_{c,g} - y_{a,c-w})$	$l_\alpha = 0$	$l_q = 0$
		$l_r = 0$
$l_p = \rho V_e^2 S_t (C_{L_\alpha t} \frac{ Y_{c,g} - Y_{a,c-t} }{V \cos \alpha + V_e} + C_{Y_\beta t} \frac{ Z_{c,g} - Z_{a,c-t} }{V \cos \beta + V_e}) (Y_{c,g} - Y_{a,c-t})$	$l_\beta = 0$	$l_{V_e} = 0$
$l_{\hat{\alpha}} = \frac{1}{2} \rho V^2 S_w C_{L \hat{\alpha}} (y_{c,g} - y_{a,c-w})$	$l_{\hat{\alpha}} = \frac{1}{2} \rho V_e^2 S_t C_{L \hat{\alpha}} (y_{c,g} - y_{a,c-t})$	$l_{\hat{\sigma}} = \frac{1}{2} \rho V_e^2 S_t C_{Y \hat{\sigma}} (y_{c,g} - y_{a,c-t})$

$M_V = \rho V S_w C_{L_\alpha w} \alpha$ $\times (X_{c,g} - X_{a.c-w})$	$M_\alpha = \frac{1}{2} \rho V^2 [S_w C_{L_\alpha w} (X_{c,g} - X_{a.c-w})$ $S_d C_{L_\alpha d} (X_{c,g} - X_{a.c-d})]$ $+ \rho V_e^2 S_t C_{L_\alpha t} (X_{c,g} - X_{a.c-t})$	$M_q = -\rho V_e^2 S_t C_{L_\alpha t}$ $\times \frac{ X_{c,g} - X_{a.c-t} }{V \cos \alpha + V_e} (X_{c,g} - X_{a.c-t})$
$M_p = 0$	$M_{V_e} = 2\rho V_e S_t C_{L_\alpha t} \frac{V \alpha}{V + V_e} (X_{c,g} - X_{a.c-t})$	$M_{\dot{\alpha}} = \rho V_e^2 S_t C_{L_\alpha t} (X_{c,g} - X_{a.c-t})$
$N_V = \rho V S_d C_{Y\beta_d} \beta$ $\times (X_{c,g} - X_{a.c-d})$	$N_\beta = \frac{1}{2} \rho V^2 S_d C_{Y\beta_d} (X_{c,g} - X_{a.c-d})$ $+ \rho V_e^2 S_t C_{Y\beta_t} (X_{c,g} - X_{a.c-t})$	$N_{V_e} = 2\rho V_e S_t G_{Y\beta_t} \frac{V \alpha}{V + V_e} (X_{c,g} - X_{a.c-t})$
$N_p = 0$ $N_{\dot{\alpha}} = 0$	$N_r = \rho V_e^2 S_t C_{Y\beta_t} \frac{ X_{c,g} - X_{a.c-t} }{V \cos \beta + V_e}$ $\times (X_{c,g} - X_{a.c-t})$	$N_{\dot{\alpha}} = \rho V_e^2 S_t C_{Y\beta_t} (X_{c,g} - X_{a.c-t})$

5.4.3 Definition of Special Derivatives

All of the aircrafts have their own airframe, but most derivatives of them are estimated in the same way in terms of handbook or experience. In some special cases, several derivatives should be calculated and estimated in the use of pacific methodology.

5.4.3.1 Derivatives Due to $\dot{\alpha}$

The derivative relate to variable $\dot{\alpha}$ which is included as an attempt to model the time dependence of the downwash at the horizontal tail. Imaging an airplane in gliding level flight where α is increasing with time. This means that the downwash angle ε at the horizontal tail is increasing with time. From table 5.1 we can see that there are no terms on $\dot{\alpha}$. Because the downwash phenomenon of this UAV is different from normal aircraft due to the propeller slipstream effects (see figure 5.1). Here we have to use slipstream angle to replace downwash angle to consider this problem, naturally, the $\dot{\alpha}$ terms are negligible. Then some derivatives relate to $\dot{\alpha}$ are ignored.

5.4.3.2 Derivatives Due to (p, q, r)

As it is mentioned in section 5.1 that the slipstream plays a important role in determining the angle of attack of the horizontal tail and vertical tail which are $\alpha_{s,p}$ and $\beta_{s,p}$. However, the contribution of (p, q, r) should be taken into account the generation of slipstream angle as well. According to Eq.(5.4), (5.5), (5.6) and (5.7), it is easy to use the relationship between (p, q, r) and $\alpha_{s,p}$ or $\beta_{s,p}$ to extrapolate the derivatives about (p, q, r) of which the results are shown in table. 18.

5.5 Summary

The non-linear six degrees of freedom dynamic model is already assembled due to the analysis of aerodynamic forces and moments combined with equations of motion and dynamic equations for the ducted fan VTOL UAV. Both CFD and experimental results are employed to the aerodynamic model of the UAV airframe. Furthermore, the linear coupled dynamic model is achieved by linearizing the equations of motion and dynamic equations based on small disturbance theory. And some theoretical analysis is used to estimate the aerodynamic derivatives which play the main role in determining the linear six degrees of freedom model. In the following chapter the computer tools will be applied to simulate both non-linear model and linear state space equations for evaluating the flight performance of this UAV in different cases.

Chapter 6

6 Flight Simulation and Modeling in MATLAB/Simulink

MATLAB as a special mathematical language is widely used for quantity of technical domains, such as numerical computing, engineering simulation and modeling, data analysis, graphic visualization and so on. Of course, it has played a critical role in development of aerospace engineering, in particular to flight simulation and modeling with the development of computer capability. In fact, an aircraft designer has to investigate the huge cost of building and testing a real aircraft without the support of high performance software and commercial codes. Therefore the importance of how to make the mathematical model of aircraft conjunct with computer simulation has been a high-tech issue since the development of aerospace engineering many years ago. So far computer technology has already been a dominant technical support for the developing aerospace industry. Obviously, MATLAB as one of the most popular software for modeling and optimizing aircraft flight performance is applied very often by aerospace engineers and designers due to not only its strong ability to deal with complicated and sophisticated mathematical problems, but also its ability to provide high quality visual environment for model building which is easy to use and plays a satisfactory performance in many real projects.

6.1 Introduction

In this chapter, real-time flight simulation and modeling is achieved in use of linear model linked with MIMO control laws during UAV hovering or low-speed cruise flight. Furthermore, it describes a strategy to simulate a vertical takeoff and landing (VTOL) unmanned aerial vehicle (UAV) in flight transition from vertical climb to horizontal flight by using a nonlinear model. Based on unique aerodynamic characteristics from CFD calculation and theoretical method, the flight dynamics of ducted fan UAV is able to be modeled and simulated accurately. MATLAB/Simulink V-Realm Builder is a design and modeling software tool for air vehicles that is capable of modeling the performance and flight dynamics during the conceptual and preliminary stage of aircraft design. To develop a control strategy, modeling and simulation of flight dynamics of ducted fan UAV is necessary, because it not only can be applied to optimize dynamic model, but also can be used to ensure the dynamic model match with control laws.

6.2 Linear Simulation and Control

It is known that the equations of motion or dynamic equations are frequently linearized for use in stability and control analysis. Based on small-disturbance theory, the motion of the airplane consists of small deviations forming a reference condition of steady flight. Such as cruise flight, vertical climb or hovering, in these cases, linearization of dynamic model of aircraft is normal in use of flight simulation and control design which has been found in practice to give good performance and results.

6.2.1 Linear Model of UAV in Hovering and Low Speed Cruise Flight

Hovering and low speed cruise flight which is one of the most expected flying modes of this ducted fan VTOL UAV is able to be seen as the case of small-disturbance of steady flight. Therefore, to analyze the performance of hovering or cruise flight and design the control law for this, the linearization of flight dynamics of UAV in this case is essential.

From section 5.4.1, we get the 6 degree-of-freedom linear model of UAV. Now, in order to obtain the hovering model, some initial state values are given. ($\alpha_* = 0, \beta_* = 0, \theta_* = \frac{\pi}{2}, \gamma_* = \frac{\pi}{2}$) according to the attitude of UAV in hovering state. Substituting the above initial values into the state matrix A and input matrix B expressed in section 5.4.1. The hovering state matrix A and input matrix B are given by,

$$A = \begin{bmatrix} \frac{T_V}{m} & -\frac{D_\alpha}{m} & 0 & 0 & 0 & 0 & 0 & 0 & 0 \\ 0 & -\frac{T_* + L_\alpha - mg}{mV_*} & \frac{(mV_* - L_q)}{mV_*} & -\frac{g}{V_*} & 0 & 0 & 0 & 0 & 0 \\ 0 & \frac{M_\alpha}{I_y} & 0 & \frac{M_q}{I_y} & 0 & 0 & 0 & 0 & 0 \\ 0 & 0 & 1 & 0 & 0 & 0 & 0 & 0 & 0 \\ 1 & 0 & 0 & 0 & 0 & 0 & 0 & 0 & 0 \\ 0 & 0 & 0 & 0 & 0 & \frac{Y_\beta - D_*}{mV_*} & 0 & \frac{Y_r - mV_*}{mV_*} & 0 \\ 0 & \frac{l_\alpha}{I_x} & 0 & 0 & 0 & \frac{l_\beta}{I_x} & \frac{l_p}{I_x} & 0 & 0 \\ 0 & 0 & 0 & 0 & 0 & \frac{N_\beta}{I_z} & 0 & \frac{N_r}{I_z} & 0 \\ 0 & 0 & 0 & 0 & 0 & 0 & 1 & \tan\theta_* & 0 \end{bmatrix}$$

$$B = \begin{bmatrix} \frac{(T_{Ve} - D_{Ve})}{m} & \frac{D_{\delta e}}{m} & \frac{D_{\delta e}}{m} & 0 & \frac{D_{\delta r}}{m} & \frac{D_{\delta r}}{m} \\ 0 & -\frac{L_{\delta e}}{mV_*} & -\frac{L_{\delta e}}{mV_*} & 0 & 0 & 0 \\ 0 & \frac{M_{\delta e}}{I_y} & \frac{M_{\delta e}}{I_y} & 0 & 0 & 0 \\ 0 & 0 & 0 & 0 & 0 & 0 \\ 0 & 0 & 0 & 0 & \frac{Y_{\delta r}}{mV_*} & \frac{Y_{\delta r}}{mV_*} \\ 0 & \frac{l_{\delta e}}{I_x} & -\frac{l_{\delta e}}{I_x} & 0 & \frac{l_{\delta r}}{I_x} & -\frac{l_{\delta r}}{I_x} \\ 0 & 0 & 0 & 0 & \frac{N_{\delta r}}{I_z} & \frac{N_{\delta r}}{I_z} \\ 0 & 0 & 0 & 0 & 0 & 0 \end{bmatrix}$$

The dimensional derivatives appearing in matrix A and matrix B are listed in Tab.19. To calculate these derivatives and matrices, the M-file (shown in Appendix E) should be used.

Table. 19 Dimensional Derivatives in Hovering and Low-speed Cruise Flight of UAV

$T_V = 0.5424$	$l_{\delta e} = -0.0030$	$l_{\delta r} = -0.0045$
$T_{Ve} = 1.0849$	$Y_\beta = 0.3519$	$M_V = 0$
$D_V = 3.1620e-005$	$Y_p = 0$	$M_\alpha = -0.0031$
$D_\alpha = 0.0127$	$Y_r = -0.0011$	$M_q = 1.0098e-005$
$D_{Ve} = 0.0040$	$Y_{Ve} = 0$	$M_p = 0$
$D_{\delta e} = 0.0026$	$Y_{\delta r} = 0.2355$	$M_{Ve} = 0$
$D_{\delta r} = 0.0026$	$l_V = -1.6405e-006$	$M_{\delta e} = -0.0102$
$L_V = 0$	$l_\alpha = 0$	$N_V = 0$
$L_\alpha = 0.0479$	$l_q = 0$	$N_\beta = -0.0229$
$L_q = -1.5511e-004$	$l_r = 0$	$N_{Ve} = 0$
$L_p = 0$	$l_p = -2.8723e-005$	$N_p = 0$
$L_{Ve} = 0$	$l_\beta = 0$	$N_{\delta a} = 0$
$L_{\delta e} = 0.1561$	$l_{Ve} = 0$	$N_r = -0.0014$
$Y_V = 0$	$l_{\delta a} = -8.2026e-008$	$N_{\delta r} = -0.0153$

6.2.2 High-Order System in Hovering Mode

As mentioned in chapter 5, the attitude control of UAV is achieved by four control surfaces of tails. For each control surface it is not only in charge of longitudinal control, but it also has to fulfill the lateral control. Actually, the four control surfaces are coupled by both longitudinal and lateral control in hovering mode. So the flight dynamics should be analyzed as the coupled model. Due to this, the High-Order System (see Ref. [7]) should be in use for linear control design. The state space is shown below,

$$\begin{bmatrix} \frac{d\Delta V}{dt} \\ \frac{d\Delta \alpha}{dt} \\ \frac{d\Delta q}{dt} \\ \frac{d\Delta \theta}{dt} \\ \frac{d\Delta H}{dt} \\ \frac{d\Delta \beta}{dt} \\ \frac{d\Delta p}{dt} \\ \frac{d\Delta r}{dt} \\ \frac{d\Delta \phi}{dt} \end{bmatrix} = A \begin{bmatrix} \Delta V \\ \Delta \alpha \\ \Delta q \\ \Delta \theta \\ \Delta H \\ \Delta \beta \\ \Delta p \\ \Delta r \\ \Delta \phi \end{bmatrix} + B \begin{bmatrix} \Delta V_e \\ \Delta \delta_{e1} \\ \Delta \delta_{e2} \\ \Delta \delta_a \\ \Delta \delta_{r1} \\ \Delta \delta_{r2} \end{bmatrix} \quad (6.1)$$

Substituting matrix A and B into this state space equation, the High-Order System is given by,

$$\frac{d\Delta V}{dt} = \frac{T_V}{m} \Delta V - \frac{D_\alpha}{m} \Delta \alpha - \frac{(T_{ve} \cos \alpha_* - D_{ve})}{m} \Delta V_e + \frac{D_{\dot{\alpha}}}{m} \Delta \dot{\alpha}_1 + \frac{D_{\dot{\alpha}}}{m} \Delta \dot{\alpha}_2 + \frac{D_{\dot{r}}}{m} \Delta \dot{r}_1 + \frac{D_{\dot{r}}}{m} \Delta \dot{r}_2$$

$$\frac{d\Delta \alpha}{dt} = -\frac{(T_* + L_\alpha - mg)}{mV_*} \Delta \alpha + \frac{(mV_* - L_q)}{mV_*} \Delta q - \frac{g}{V_*} \Delta \theta - \frac{L_{\dot{\alpha}}}{mV_*} \Delta \dot{\alpha}_1 - \frac{L_{\dot{\alpha}}}{mV_*} \Delta \dot{\alpha}_2$$

$$\frac{d\Delta q}{dt} = \frac{M_\alpha}{I_y} \Delta \alpha + \frac{M_q}{I_y} \Delta q + \frac{M_{\dot{\alpha}}}{I_y} \Delta \dot{\alpha}_1 + \frac{M_{\dot{\alpha}}}{I_y} \Delta \dot{\alpha}_2$$

$$\frac{d\Delta \theta}{dt} = \Delta q$$

$$\frac{d\Delta H}{dt} = \Delta V$$

$$\frac{d\Delta \beta}{dt} = \frac{(Y_\beta - D_*)}{mV_*} \Delta \beta + \frac{(Y_r - mV_*)}{mV_*} \Delta r + \frac{Y_{\dot{r}}}{mV_*} \Delta \dot{r}_1 + \frac{Y_{\dot{r}}}{mV_*} \Delta \dot{r}_2$$

$$\frac{d\Delta p}{dt} = \frac{l_\alpha}{I_x} \Delta \alpha + \frac{l_\beta}{I_x} \Delta \beta + \frac{l_p}{I_x} \Delta p + \frac{I_z l_{\dot{\alpha}}}{I_x I_z - I_{zx}^2} \Delta \dot{\alpha}_1 - \frac{I_z l_{\dot{\alpha}}}{I_x I_z - I_{zx}^2} \Delta \dot{\alpha}_2 + \frac{l_{\dot{\alpha}}}{I_x} \Delta \dot{r}_1 - \frac{l_{\dot{\alpha}}}{I_x} \Delta \dot{r}_2$$

$$\frac{d\Delta r}{dt} = \frac{N_\beta}{I_z} \Delta \beta + \frac{N_r}{I_z} \Delta r + \frac{N_{\dot{r}}}{I_z} \Delta \dot{r}_1 + \frac{N_{\dot{r}}}{I_z} \Delta \dot{r}_2$$

$$\frac{d\Delta \phi}{dt} = \Delta p + \tan \theta_* \Delta r$$

6.2.3 Response Transfer Function Matrix of UAV

The general state equations describing a linear dynamic system can be written as below,

$$\dot{x}(t) = Ax(t) + Bu(t) \quad (6.2)$$

$$y(t) = Cx(t) + Du(t) \quad (6.3)$$

The Laplace transform of above two equations is given by,

$$sx(s) = Ax(s) + Bu(s) \quad (6.4)$$

$$y(s) = Cx(s) + Du(s) \quad (6.5)$$

Combining the two equations, $y(s)$ is expressed by,

$$y(s) = [C(sI - A)^{-1}B + D]u(s) = G(s)u(s) \quad (6.6)$$

where $G(s)$ is called the transfer function matrix. It is also able to be simplified as,

$$G(s) = C(sI - A)^{-1}B + D \quad (6.7)$$

Meanwhile, it is usually required that $y(s)=x(s)$ and $C=I$, $D=0$. Therefore, we can get,

$$G(s) = (sI - A)^{-1}B = \frac{Adj(sI - A)B}{|sI - A|} \quad (6.8)$$

According to matrix A (9x9) and matrix B (9x6) in section 6.2.1, we know that matrix $G(s)$ is 9 rows by 6 columns as shown below,

$$G(s) = \begin{bmatrix} G_{Ve}^V(s) & G_{\dot{\delta}\epsilon 1}^V(s) & G_{\dot{\delta}\epsilon 2}^V(s) & G_{\dot{\alpha}}^V(s) & G_{\dot{\delta}\tau 1}^V(s) & G_{\dot{\delta}\tau 2}^V(s) \\ G_{Ve}^\alpha(s) & G_{\dot{\delta}\epsilon 1}^\alpha(s) & G_{\dot{\delta}\epsilon 2}^\alpha(s) & G_{\dot{\alpha}}^\alpha(s) & G_{\dot{\delta}\tau 1}^\alpha(s) & G_{\dot{\delta}\tau 2}^\alpha(s) \\ G_{Ve}^q(s) & G_{\dot{\delta}\epsilon 1}^q(s) & G_{\dot{\delta}\epsilon 2}^q(s) & G_{\dot{\alpha}}^q(s) & G_{\dot{\delta}\tau 1}^q(s) & G_{\dot{\delta}\tau 2}^q(s) \\ G_{Ve}^\theta(s) & G_{\dot{\delta}\epsilon 1}^\theta(s) & G_{\dot{\delta}\epsilon 2}^\theta(s) & G_{\dot{\alpha}}^\theta(s) & G_{\dot{\delta}\tau 1}^\theta(s) & G_{\dot{\delta}\tau 2}^\theta(s) \\ G_{Ve}^H(s) & G_{\dot{\delta}\epsilon 1}^H(s) & G_{\dot{\delta}\epsilon 2}^H(s) & G_{\dot{\alpha}}^H(s) & G_{\dot{\delta}\tau 1}^H(s) & G_{\dot{\delta}\tau 2}^H(s) \\ G_{Ve}^\beta(s) & G_{\dot{\delta}\epsilon 1}^\beta(s) & G_{\dot{\delta}\epsilon 2}^\beta(s) & G_{\dot{\alpha}}^\beta(s) & G_{\dot{\delta}\tau 1}^\beta(s) & G_{\dot{\delta}\tau 2}^\beta(s) \\ G_{Ve}^p(s) & G_{\dot{\delta}\epsilon 1}^p(s) & G_{\dot{\delta}\epsilon 2}^p(s) & G_{\dot{\alpha}}^p(s) & G_{\dot{\delta}\tau 1}^p(s) & G_{\dot{\delta}\tau 2}^p(s) \\ G_{Ve}^r(s) & G_{\dot{\delta}\epsilon 1}^r(s) & G_{\dot{\delta}\epsilon 2}^r(s) & G_{\dot{\alpha}}^r(s) & G_{\dot{\delta}\tau 1}^r(s) & G_{\dot{\delta}\tau 2}^r(s) \\ G_{Ve}^\phi(s) & G_{\dot{\delta}\epsilon 1}^\phi(s) & G_{\dot{\delta}\epsilon 2}^\phi(s) & G_{\dot{\alpha}}^\phi(s) & G_{\dot{\delta}\tau 1}^\phi(s) & G_{\dot{\delta}\tau 2}^\phi(s) \end{bmatrix} \quad (6.9)$$

In expression of $G_j^k(s)$, the k is the output variable and j represents the input variable. The meaning of

$G_j^k(s)$ is the transfer function of the k variable response to j variable. It is widely used in control law design which will be detailed in following section.

6.2.4 Application of Feedback Control

Feedback control as the classical control theory has been applied in many domains. It is defined based upon a input signal of a system obtained through output fed back as shown in figure 6.1.

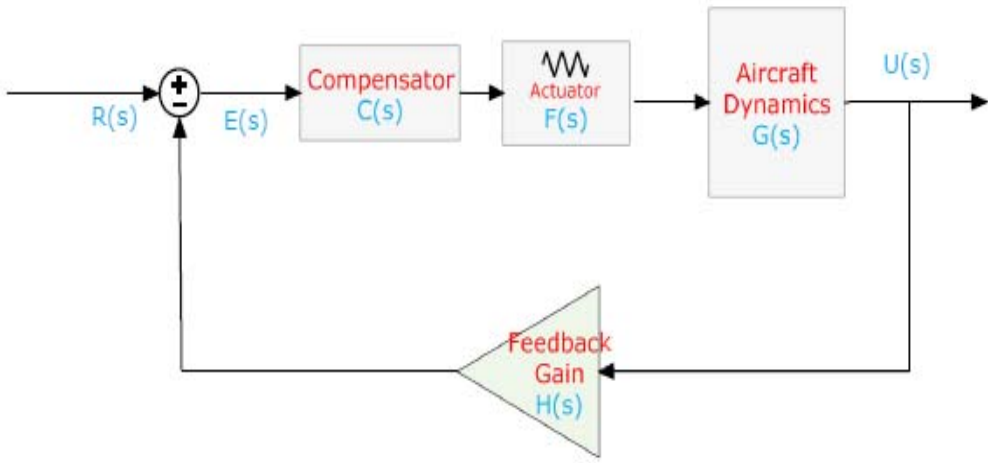


Figure6. 1 Feedback Closed-loop of a Control System

The Feedback Closed-loop include a compensator $C(S)$, a actuator $F(s)$, aircraft dynamics or plant $G(s)$ and feedback gain $H(s)$ which are four basic components of system function. $R(s)$ is signal input, whereas $U(s)$ is output variable. The control error is defined by,

$$E(s) = R(s) - U(s)H(s) \quad (6.10)$$

The output is expressed by,

$$U(s) = E(s)C(s)F(s)G(s) \quad (6.11)$$

Combining Eq.(6.10) and Eq.(6.11), we get,

$$U(s) = \frac{C(s)F(s)G(s)}{1 + H(s)C(s)F(s)G(s)} R(s) \quad (6.12)$$

We define the Closed-loop transfer function $G_{CL}(s)$ is,

$$G_{CL}(s) = \frac{C(s)F(s)G(s)}{1 + H(s)C(s)F(s)G(s)} \quad (6.13)$$

Therefore,

$$U(s) = G_{CL}(s)R(s) \quad (6.14)$$

There is single input variable and single output variable in this feedback closed-loop, so it is also named SISO system. To design a control law for complicated system (MIMO), the SISO system is necessary to be analyzed in initial step of control design. Usually, $G_{CL}(s)$ is optimized via modifying $C(s)$ and $H(s)$ to achieve stable output using frequency domain, root locus or robust methodology.

6.2.5 MIMO Control Laws of UAV

In order to fulfill the control of UAV in hovering and low speed cruise flight, the attitude and thrust (speed) have to be held during flying. There are five input variables ($V_i, \theta_{i1}, \theta_{i2}, \psi_{i1}, \psi_{i2}$) and four output variables ($V_o, \theta_o, \psi_o, \phi_o$) which should be taken into account in design of control laws (see Fig.6.2). Multiple inputs and multiple outputs (MIMO) are considered in this system (see Ref. [7]).

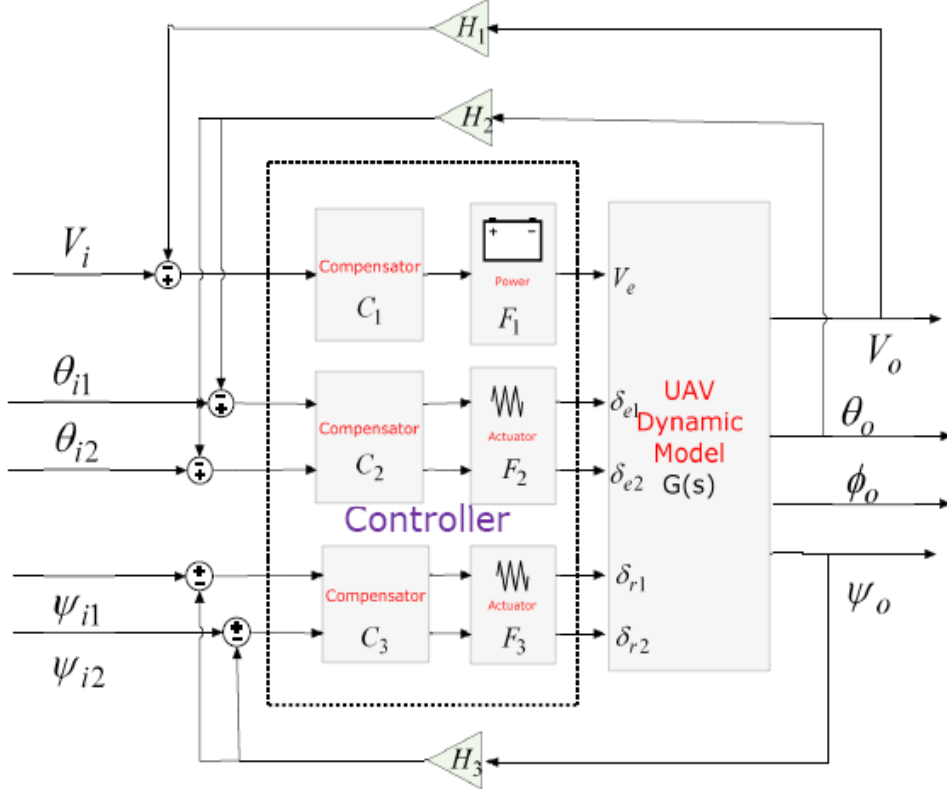


Figure6. 2 MIMO Control Systems

6.2.5.1 Attitude Holding Control Law (AHCL)

The attitude of UAV is composed by three Euler angles. They are pitch angle θ , yaw angle ψ and roll angle ϕ , respectively. To achieve the attitude control, the AHCL is designed in terms of feedback closed-loop control theory.

- Control law of pitch angle

From the second closed-loop, we can obtain,

$$\theta_o = G_{\delta e 1}^\theta \delta_{e1} + G_{\delta e 2}^\theta \delta_{e2} \quad (6.15)$$

$$\delta_{e1} = (\theta_{i1} - \theta_o H_2) C_2 F_2 \quad (6.16)$$

$$\delta_{e2} = (\theta_{i2} - \theta_o H_2) C_2 F_2 \quad (6.17)$$

Substituting Eq.(6.16) and Eq.(6.17) into Eq.(6.15), the control law of pitch angle is,

$$\theta_o = \frac{C_2 F_2 G_{\dot{\alpha}e1}^\theta}{1 + H_2 C_2 F_2 G_{\dot{\alpha}e1}^\theta} \theta_{i1} + \frac{C_2 F_2 G_{\dot{\alpha}e2}^\theta}{1 + H_2 C_2 F_2 G_{\dot{\alpha}e1}^\theta} \theta_{i2} \quad (6.18)$$

Since $G_{\dot{\alpha}e1}^\theta = G_{\dot{\alpha}e2}^\theta = G_{\dot{\alpha}e}^\theta$, we get,

$$\theta_o = \frac{C_2 F_2 G_{\dot{\alpha}e}^\theta}{1 + H_2 C_2 F_2 G_{\dot{\alpha}e}^\theta} (\theta_{i1} + \theta_{i2}) \quad (6.19)$$

$$(\delta_{e1} + \delta_{e2}) = \frac{C_2 F_2}{1 + H_2 C_2 F_2 G_{\dot{\alpha}e}^\theta} (\theta_{i1} + \theta_{i2}) \quad (6.20)$$

- Control law of yaw angle

From the third closed-loop, we can obtain,

$$\psi_o = G_{\dot{\alpha}r1}^\psi \delta_{r1} + G_{\dot{\alpha}r2}^\psi \delta_{r2} \quad (6.21)$$

$$\delta_{r1} = (\psi_{i1} - \psi_o H_3) C_3 F_3 \quad (6.22)$$

$$\delta_{r2} = (\psi_{i2} - \psi_o H_3) C_3 F_3 \quad (6.23)$$

Substituting Eq.(6.23) and Eq.(6.22) into Eq.(6.21), the control law of yaw angle is,

$$\psi_o = \frac{C_3 F_3 G_{\dot{\alpha}r1}^\psi}{1 + H_3 C_3 F_3 G_{\dot{\alpha}r1}^\psi} \psi_{i1} + \frac{C_3 F_3 G_{\dot{\alpha}r2}^\psi}{1 + H_3 C_3 F_3 G_{\dot{\alpha}r2}^\psi} \psi_{i2} \quad (6.24)$$

Since $G_{\dot{\alpha}r1}^\psi = G_{\dot{\alpha}r2}^\psi = G_{\dot{\alpha}r}^\psi$, we get,

$$\psi_o = \frac{C_3 F_3 G_{\dot{\alpha}r}^\psi}{1 + H_3 C_3 F_3 G_{\dot{\alpha}r}^\psi} (\psi_{i1} + \psi_{i2}) \quad (6.25)$$

$$(\delta_{r1} + \delta_{r2}) = \frac{C_3 F_3}{1 + H_3 C_3 F_3 G_{\dot{\alpha}r}^\psi} (\psi_{i1} + \psi_{i2}) \quad (6.26)$$

- Control law of roll angle

From the open-loop, we get,

$$\phi_o = G_{\dot{\alpha}e1}^\phi \delta_{e1} + G_{\dot{\alpha}e2}^\phi \delta_{e2} + G_{\dot{\alpha}r1}^\phi \delta_{r1} + G_{\dot{\alpha}r2}^\phi \delta_{r2} \quad (6.27)$$

Because $G_{\dot{\alpha}e1}^\phi = -G_{\dot{\alpha}e2}^\phi$ and $|G_{\dot{\alpha}e1}^\phi| = |G_{\dot{\alpha}e2}^\phi| = G_{\dot{\alpha}e}^\phi$; $G_{\dot{\alpha}r1}^\phi = -G_{\dot{\alpha}r2}^\phi$ and $|G_{\dot{\alpha}r1}^\phi| = |G_{\dot{\alpha}r2}^\phi| = G_{\dot{\alpha}r}^\phi$,

ϕ output is given by,

$$\phi_o = G_{\dot{\alpha}}^\phi (\delta_{e1} - \delta_{e2}) + G_{\dot{\alpha}r}^\phi (\delta_{r1} - \delta_{r2}) \quad (6.28)$$

Substituting Eq.(6.16), Eq.(6.17) ,Eq.(6.22), Eq.(6.23)into Eq.(6.28), the control law of roll angle is,

$$\phi_o = C_2 F_2 G_{\dot{\alpha}}^\phi (\theta_{i1} - \theta_{i2}) + C_3 F_3 G_{\dot{\alpha}r}^\phi (\psi_{i1} - \psi_{i2}) \quad (6.29)$$

In the above three control laws, we can see that (C_2, C_3, H_2, H_3) are able to be modified based upon frequency domain and root locus methodology in use of control design to make sure the outputs are stable responses to inputs.

6.2.5.2 Thrust Holding Control Law (THCL)

In hovering state, the thrust is desire to be controlled in low rate variation so as to make sure the UAV flying up or down as slowly as possible. As the AHCL is completed, the THCL will be realized.

$$V_o = G_{Ve}^V V_e + G_{\dot{\alpha}1}^V \delta_{e1} + G_{\dot{\alpha}2}^V \delta_{e2} + G_{\dot{\alpha}r1}^V \delta_{r1} + G_{\dot{\alpha}r2}^V \delta_{r2} \quad (6.30)$$

$$V_e = (V_i - V_o H_1) C_1 F_1 \quad (6.31)$$

Since $G_{\dot{\alpha}1}^V = G_{\dot{\alpha}2}^V = G_{\dot{\alpha}}^V$ and $G_{\dot{\alpha}r1}^V = G_{\dot{\alpha}r2}^V = G_{\dot{\alpha}r}^V$, we get,

$$V_o = G_{Ve}^V (V_i - V_o H_1) C_1 F_1 + G_{\dot{\alpha}}^V (\delta_{e1} + \delta_{e2}) + G_{\dot{\alpha}r}^V (\delta_{r1} + \delta_{r2}) \quad (6.32)$$

Combining Eq.(6.16), Eq.(6.17) ,Eq.(6.22), Eq.(6.23) and Eq.(6.32)

$$V_o = \frac{C_1 F_1 G_{Ve}^V}{1 + H_1 C_1 F_1} V_{i1} + \frac{C_2 F_2 G_{\dot{\alpha}}^V}{(1 + H_2 C_2 F_2 G_{\dot{\alpha}}^\theta)(1 + H_1 C_1 F_1)} (\theta_{i1} + \theta_{i2}) + \frac{C_3 F_3 G_{\dot{\alpha}r}^V}{(1 + H_3 C_3 F_3 G_{\dot{\alpha}r}^\psi)(1 + H_1 C_1 F_1)} (\psi_{i1} + \psi_{i2}) \quad (6.33)$$

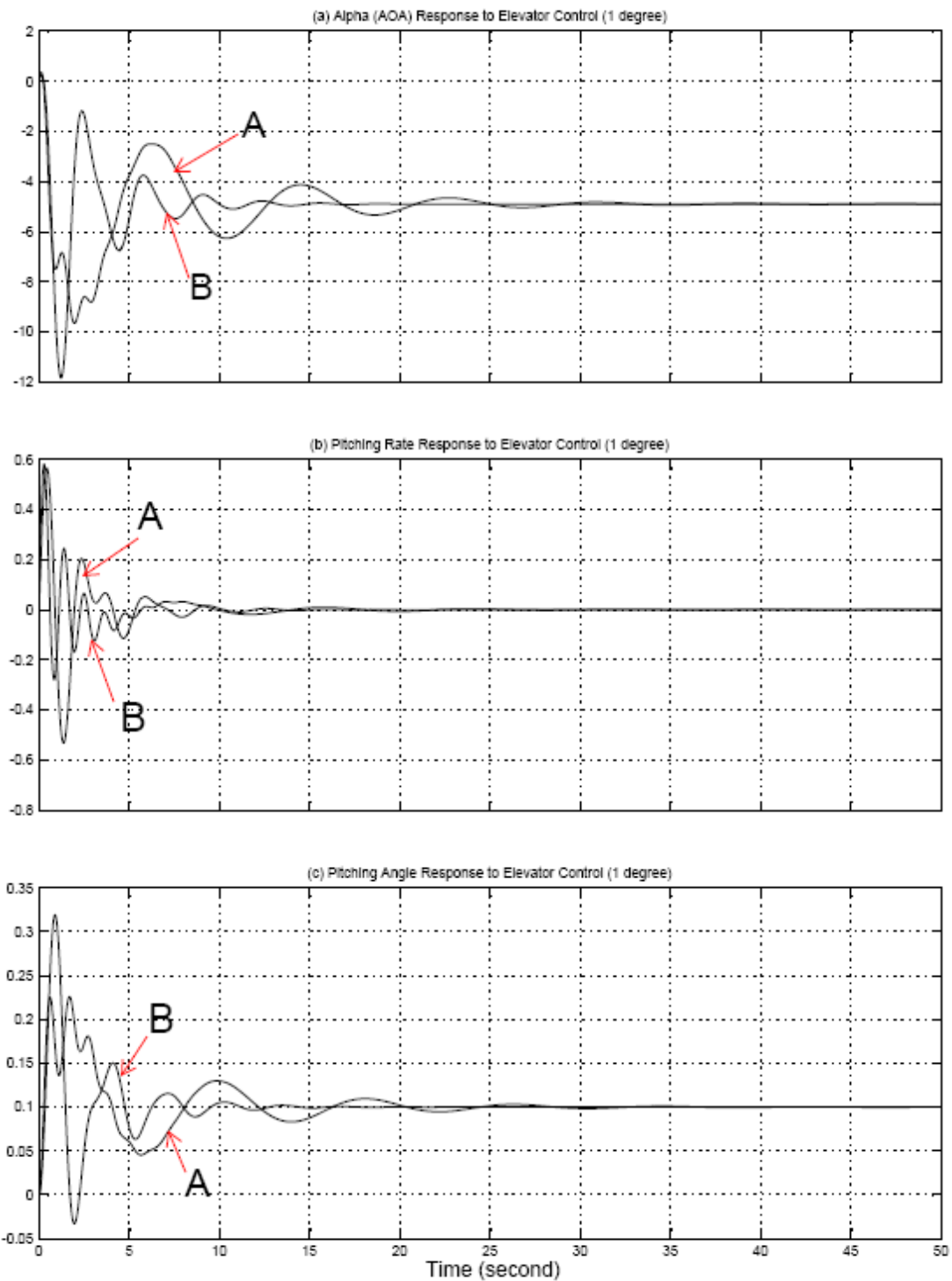
The format of matrix is,

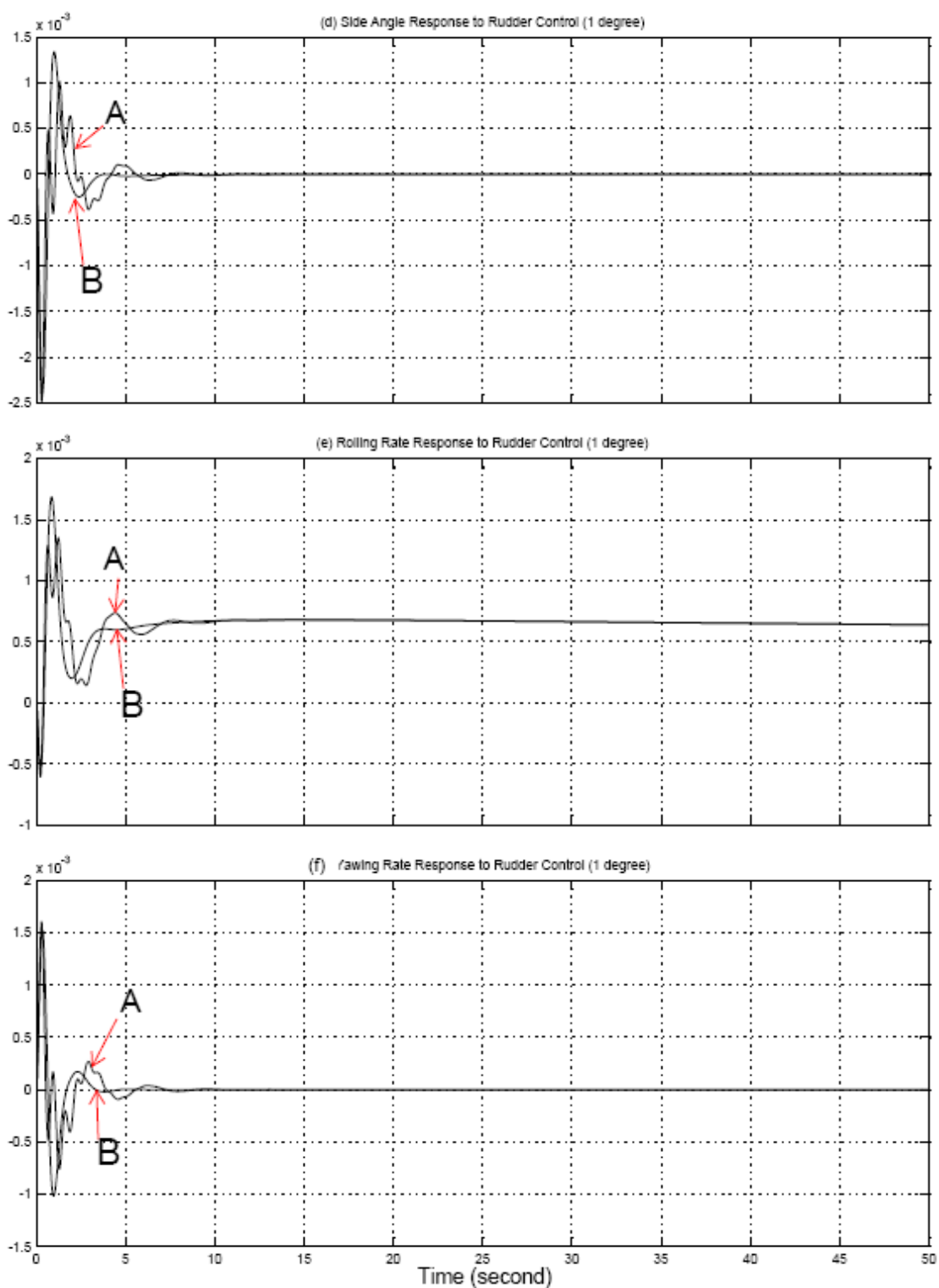
$$V_o = \begin{bmatrix} \frac{C_1 F_1 G_{Ve}^V}{1 + H_1 C_1 F_1} \\ \frac{C_2 F_2 G_{\dot{\alpha}}^V}{(1 + H_2 C_2 F_2 G_{\dot{\alpha}}^\theta)(1 + H_1 C_1 F_1)} \\ \frac{C_3 F_3 G_{\dot{\alpha}r}^V}{(1 + H_3 C_3 F_3 G_{\dot{\alpha}r}^\psi)(1 + H_1 C_1 F_1)} \end{bmatrix}^T \times \begin{bmatrix} V_{i1} \\ \theta_{i1} + \theta_{i2} \\ \psi_{i1} + \psi_{i2} \end{bmatrix} \quad (6.34)$$

From matrix (6.34) we know that as long as the $(C_1, C_2, C_3, H_1, H_2, H_3)$ are optimized to satisfy the stable output control, the thrust holding is able to be achieved.

6.2.6 Simulation Results of MIMO Control Laws

Based on MIMO control laws in the previous section, the output variables response to input variables are able to be simulated by building the mathematic model in MATLAB. In Fig.6.3 and Fig.6.4 some simulation results are listed including original system and optimizing system. The curves A represent the results of initial control system whereas the curves B display the response results after optimizing the control system.





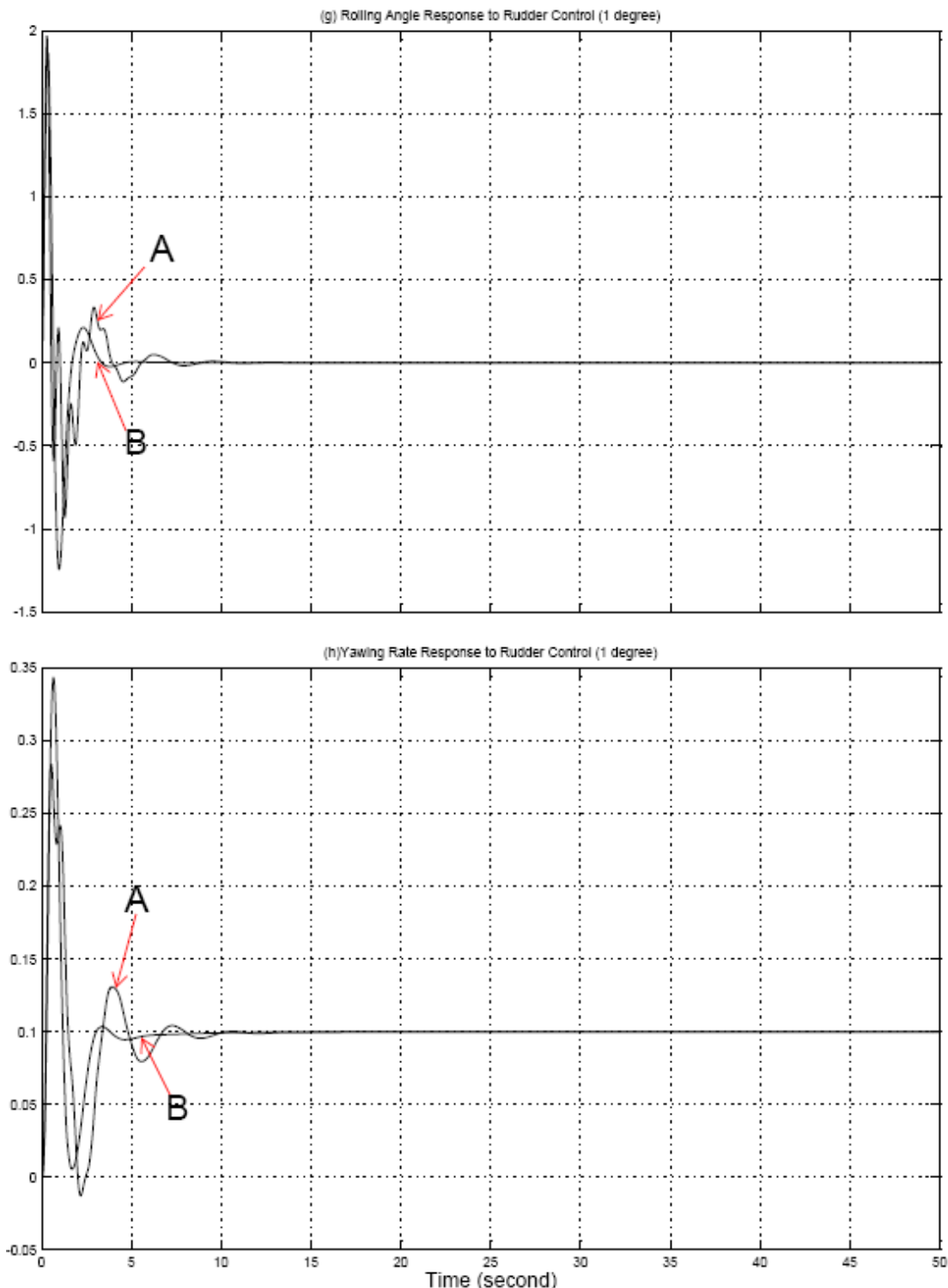
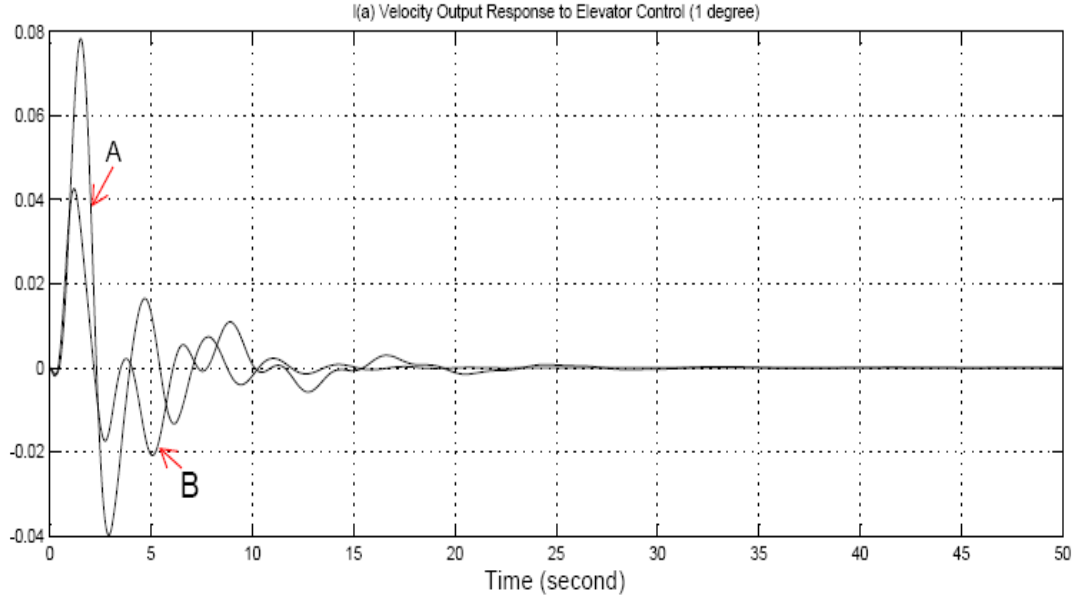


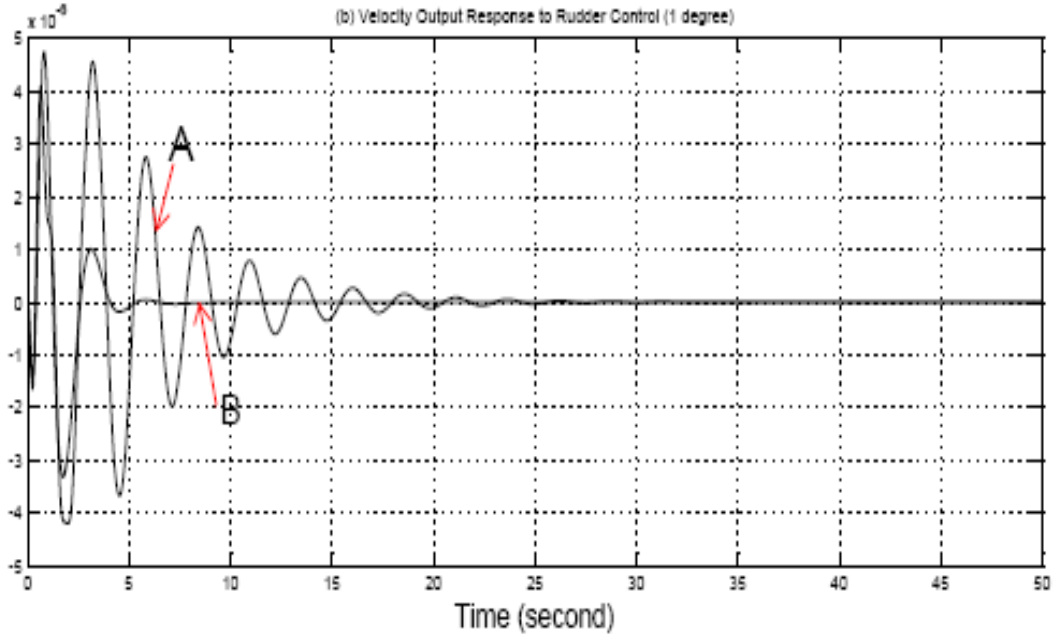
Figure 6.3 Attitude Control Outputs Response to Inputs

From Fig.6.3 (a) to (g), we can see that the attitude control law plays an expectable role in effective holding pitching angle, rolling angle and yawing angle. In particular, the optimizing system has better performance than the original system since the compensators and values of feedback gain are

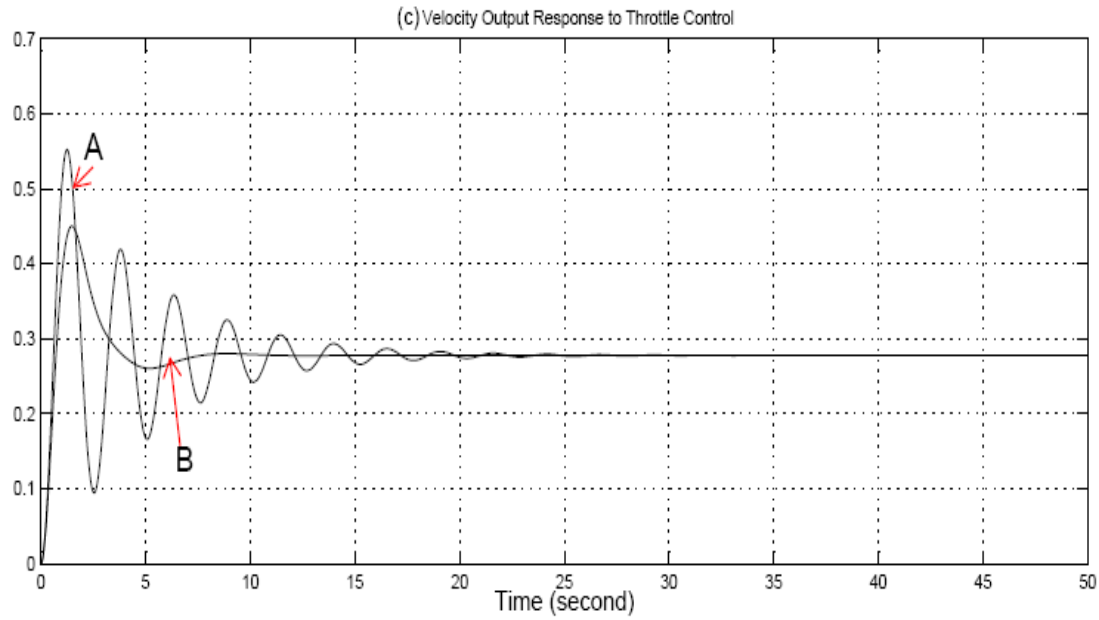
optimized due to root-locus and frequency domain methodology in use of control design. Having observed the comparison between original output curves and optimizing output curves in Fig.6.3, both short-time period and phugoid period response are improved in damping ratio and oscillation. Apparently, the damping ratio and time-range of oscillation are reduced in optimizing system to modify the control efficiency and stability.



(a) Velocity Response to Elevator Control



(b) Velocity Response to Rudder Control



(c) Velocity Response to Throttle Control

Figure 6.4 Thrust Control Outputs Response to Inputs

The optimizing system plays a good role in thrust control as well. Fig 6.4 (a),(b) and (c) show the velocity response to elevator, rudder and throttle, respectively. Obviously, by optimizing parameters of compensator and feedback to gain the control performance is much better than the original system in attitude control or thrust control.

6.2.7 Real-time Flight Simulation and Modeling

Flight-simulator is one of popular codes to output flight simulation or modeling in visual environment. Usually, it is combined with other software including program C++, Visual C and MATLAB in which the mathematical models are written as a program or built in the form of functions and blocks (see Fig 6.5). In Fig.6.6 the process of UAV fight simulation is modeled as real-time animation in Flight-simulator. To check whether the above MIMO control laws are expectable and available making a flight mission for UAV is necessary. At the beginning, the UAV is hovering at point A before it slides flight at low speed to point B at which UAV is kept in hovering mode. Then it maintains attitude and descends to the top of building which is the landing target of this mission. By reducing thrust it successfully lands at point C.

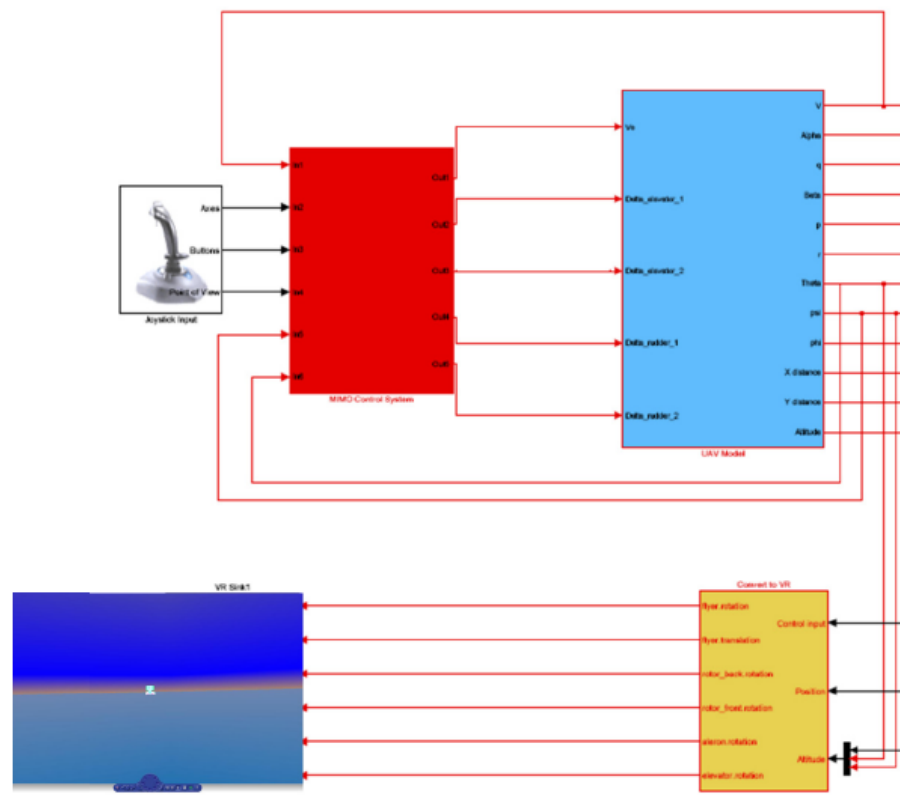


Figure6. 5 MIMO Control Laws Linked with Flight-simulator in MATLAB

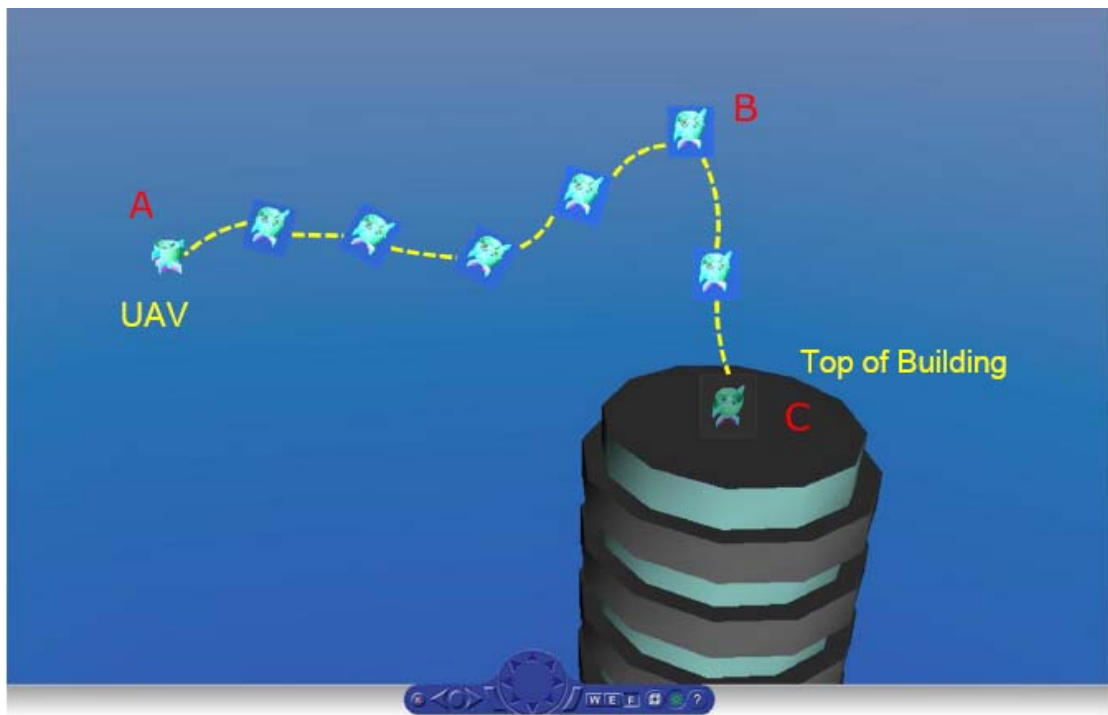


Figure6. 6 Description of UAV Mission

Fig 6.7 also shows the trajectory of UAV mission from point A to B and landing at point C. We can see

that its altitude decreases about 2 meters from A to C, meanwhile it passes 20 meters in X direction and 10 meters in Y direction, respectively as shown in 3D coordinates of Fig 6.7.

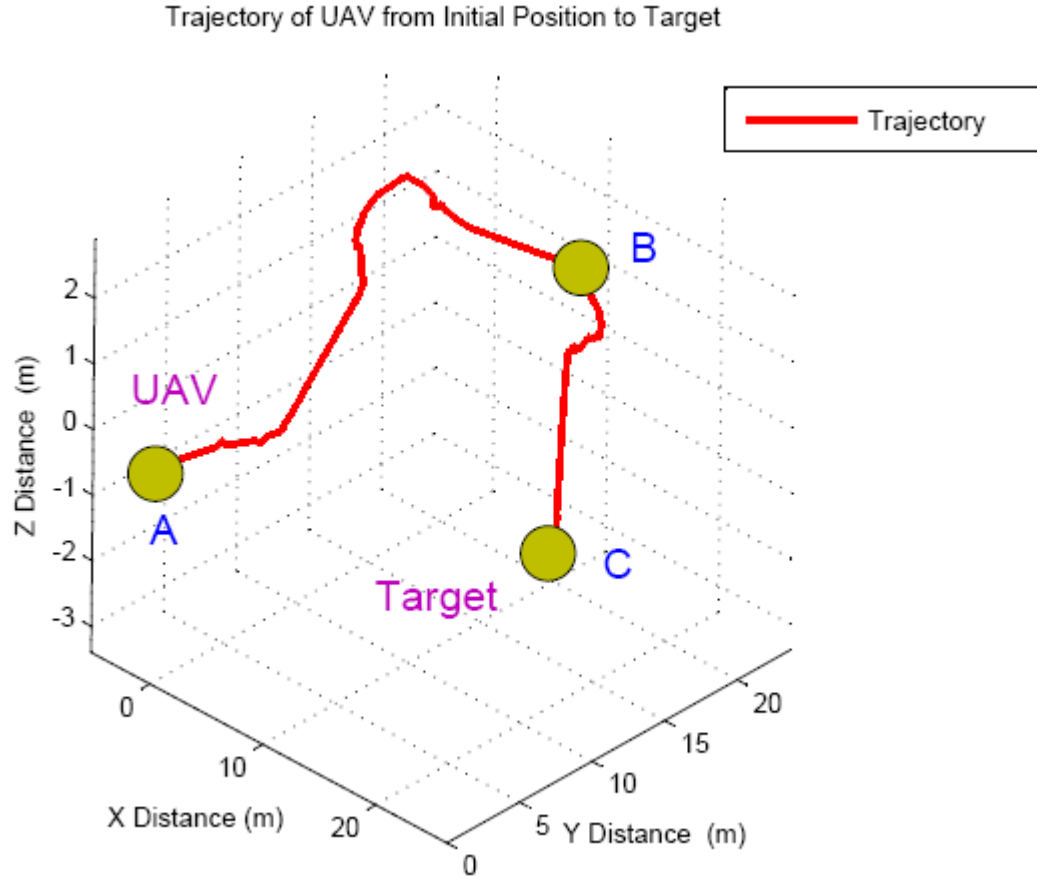
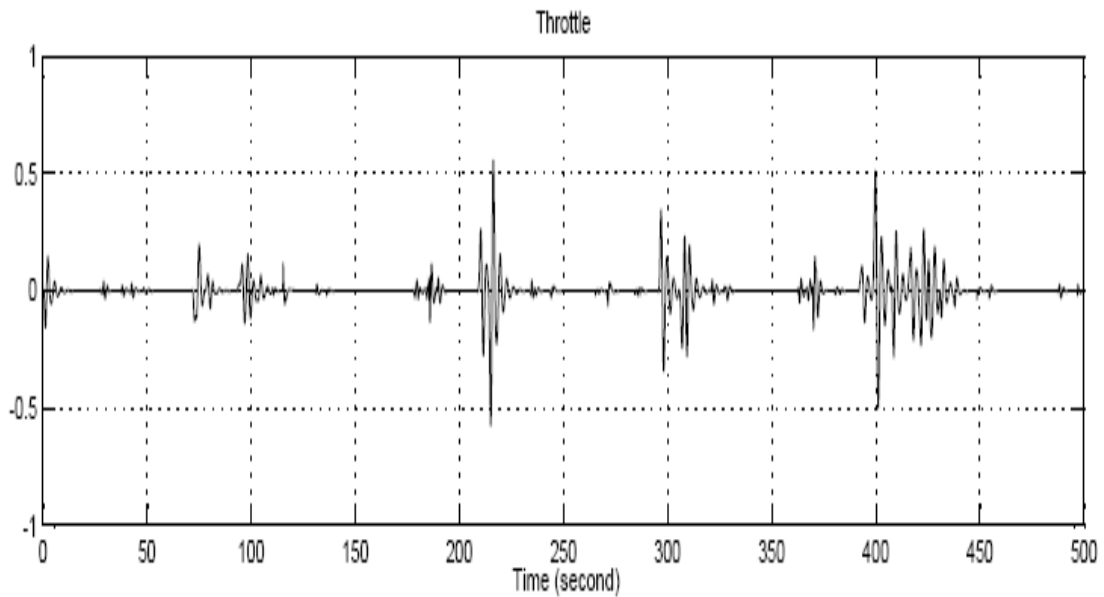
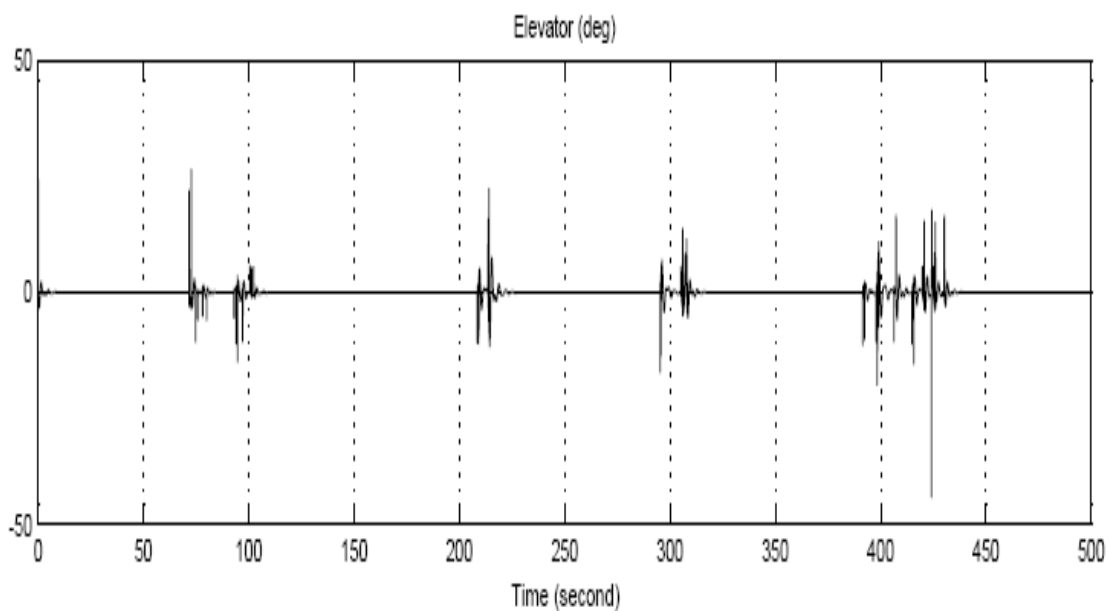


Figure6. 7 Trajectory of UAV Mission

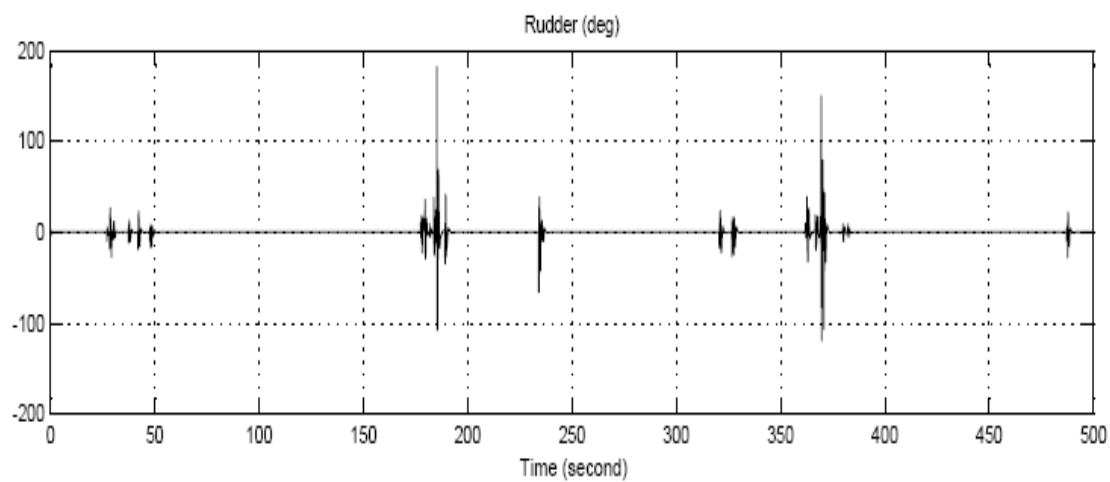
In Fig 6.8 (a), (b) and (c), the five signal inputs are displayed as waves of time response functions. Because the two elevators are controlled simultaneously, the one figure can reflect two control inputs of elevators. In the same way, the control signals of two rudders are figured out in one graph.



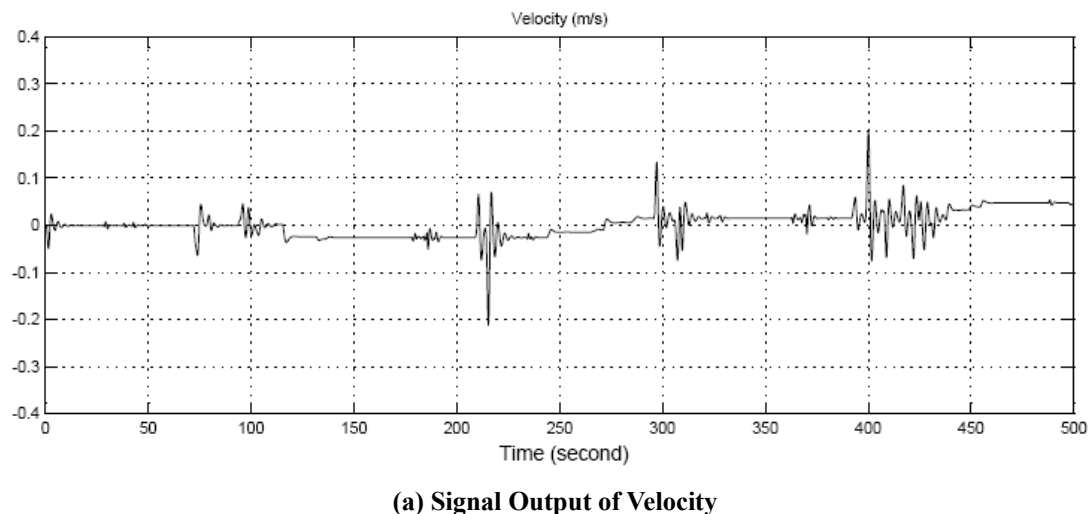
(a) Signal Input of Throttle



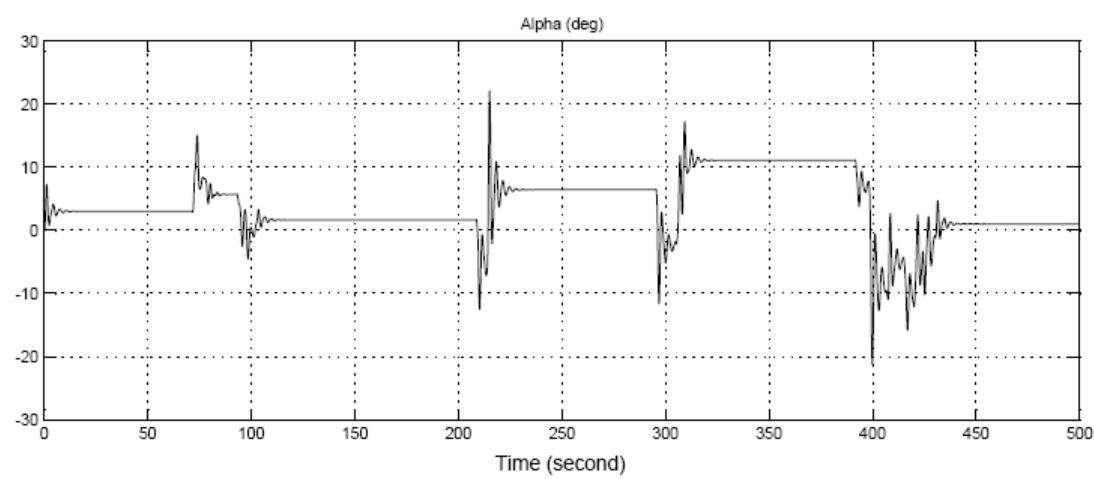
(b) Signal Input of Elevator 1 and Elevator 2



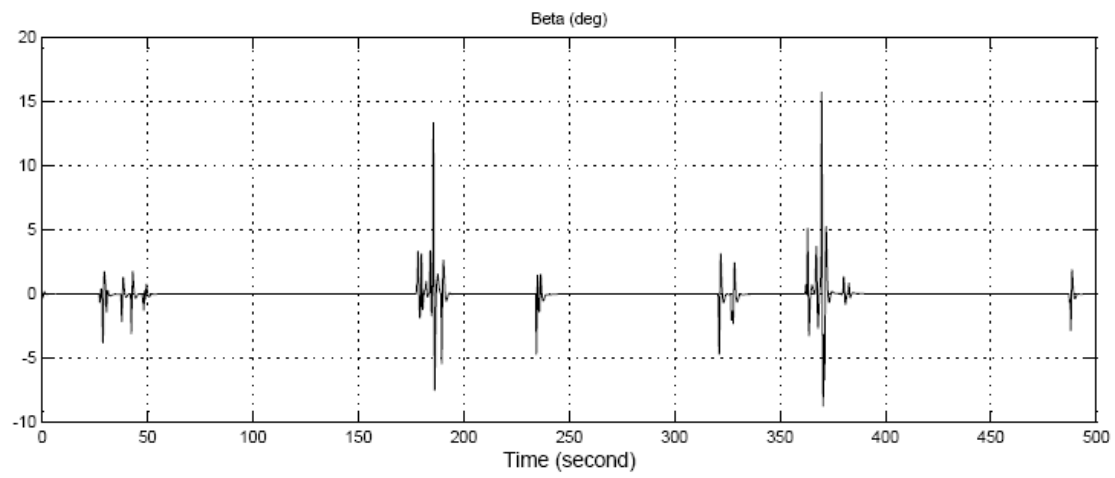
(c) Signal Input of Rudder 1 and Rudder 2
Figure6. 8 Signal Input of UAV Mission



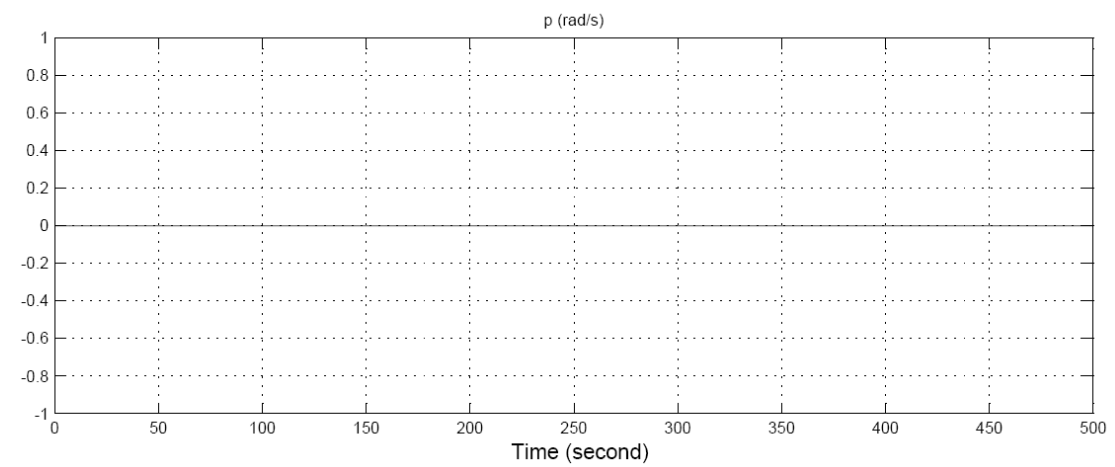
(a) Signal Output of Velocity



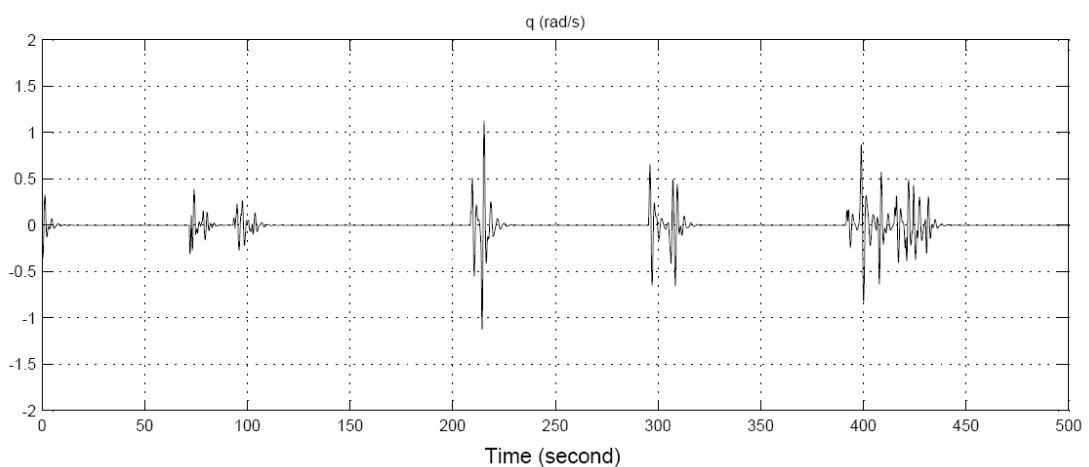
(b) Signal Output of Angle of Attack



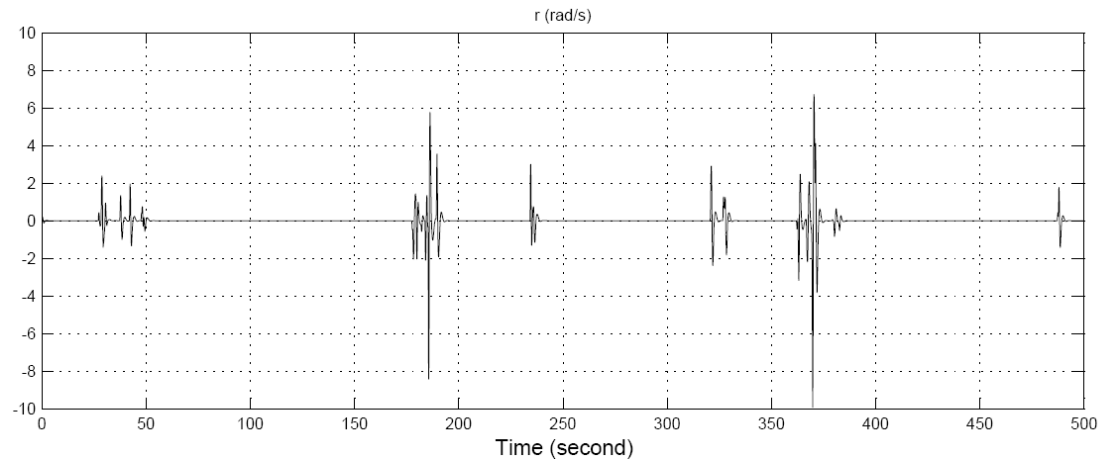
(c) Signal Output of Sideslip Angle



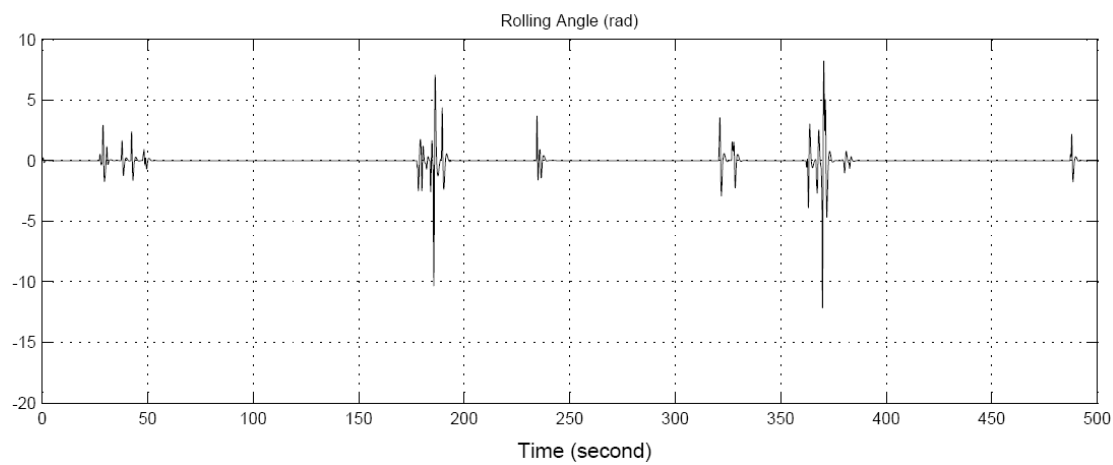
(d) Signal Output of Rolling Rate



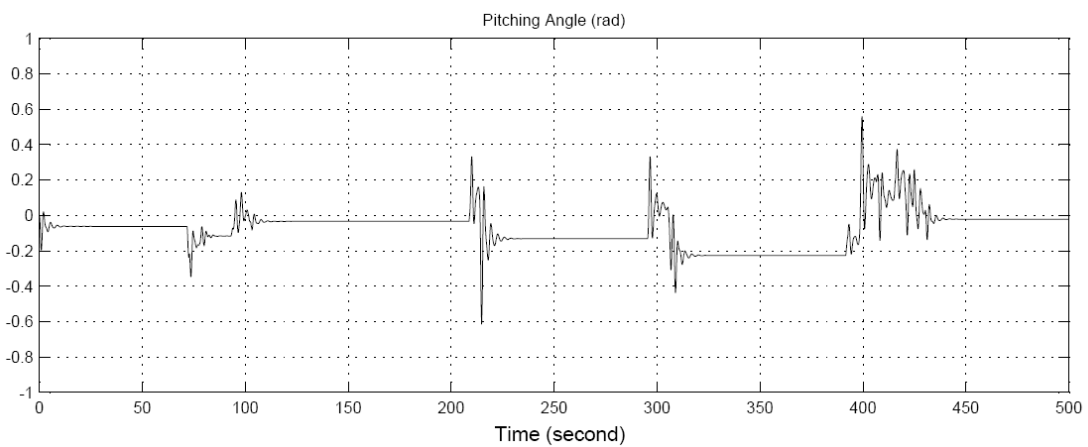
(e) Signal Output of Pitching Rate



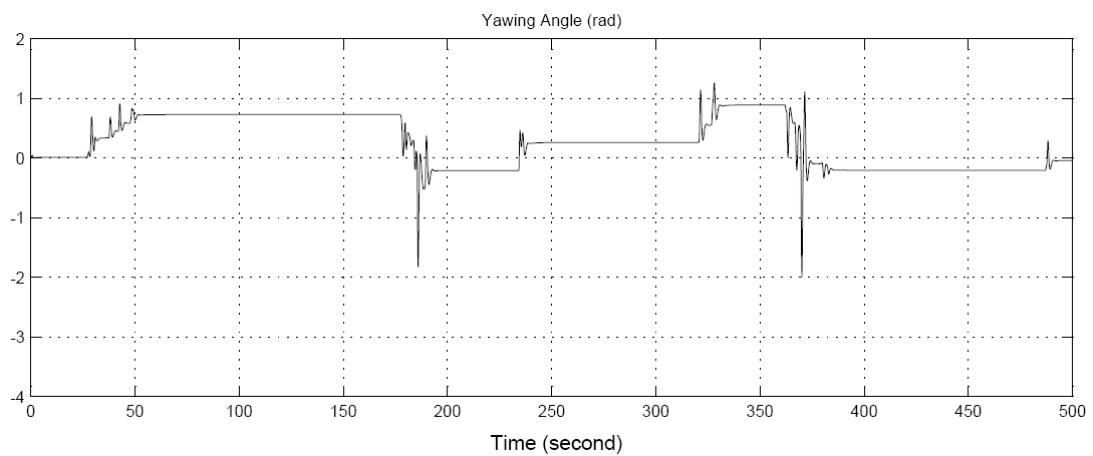
(f) Signal Output of Yawing Rate



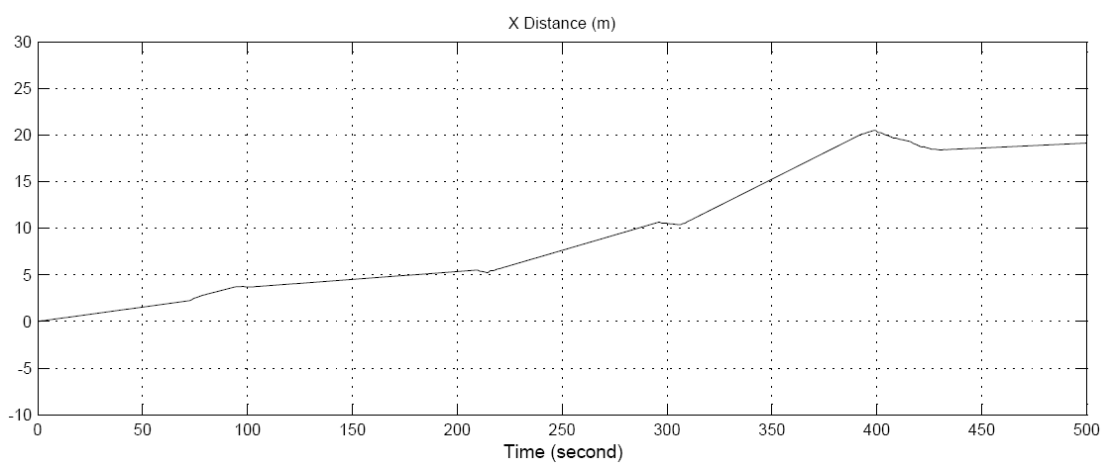
(g) Signal Output of Rolling Angle



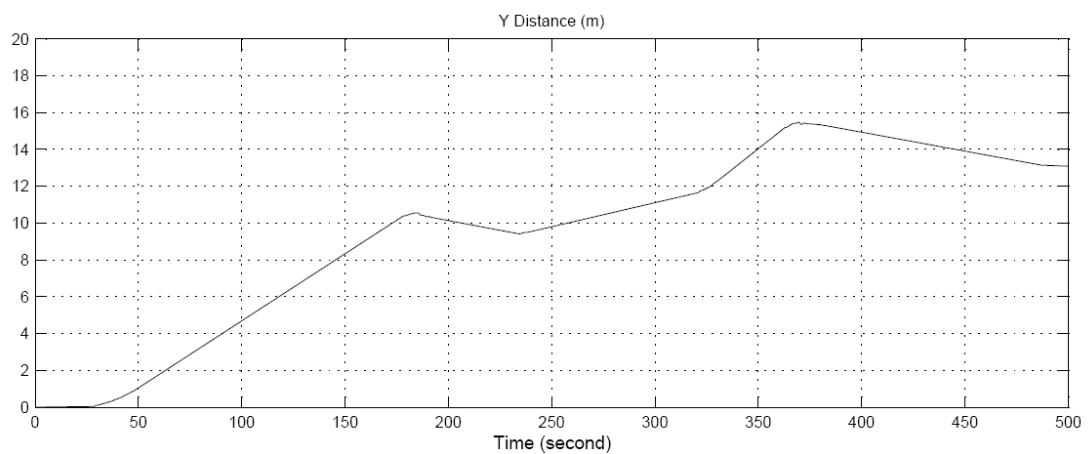
(h) Signal Output of Pitching Angle



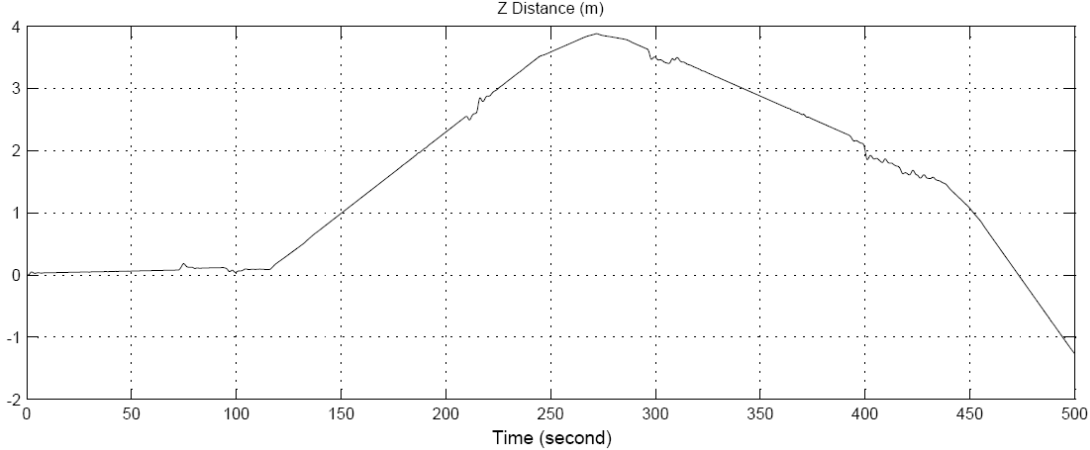
(i) Signal Output of Yawing Angle



(j) Signal Output of X Distance



(k) Signal Output of Y Distance



(L) Signal Output of Z Distance

Figure6. 9 Signal Output of UAV Mission

From Fig 6.9 (a) to (L) we can observe that the attitude and position of UAV change with the variance of time during the past 500 seconds. It proves that our MIMO control laws play a good performance in hovering and low-speed flight control for this ducted fan VTOL UAV. Of course, not only vertical landing is able to be fulfilled, but the vertical take off and climb also can be achieved relying on control laws mentioned in previous sections.

6.2.8 Real-time simulation of UAV Hovering in Crosswind

In this section we will pursue another flight performance of UAV. It has been discussed in chapter 2 of the last section, if a ducted fan UAV is hovering in random crosswind, it is difficult to keep stable without extra control due to the counter pitch moment and ram drag caused by crosswind effect. Following, the real-time simulation of UAV hovering in crosswind is going to be shown and discussed.

We assume the crosswind as an exogenous control input in entire control system so it is convenient for us to build a mathematical model. Therefore, the state space matrix equations are given by,

$$\dot{x} = Ax + Bu + Eu_e \quad (6.35)$$

$$y = x \quad (6.36)$$

According to Eq.(2.48) and Eq.(2.49), we get,

$$D_{Vc} = \rho A_e V_e \quad (6.37)$$

$$M_{Vc} = \rho A_e V_e d \quad (6.38)$$

So matrix E is,

$$E = \begin{bmatrix} \frac{D_{Vc}}{m} \\ 0 \\ \frac{M_{Vc}}{I_y} \\ 0 \\ 0 \\ 0 \\ 0 \\ 0 \\ 0 \end{bmatrix}$$

Substituting matrix A, B and E into Eq.(6.35), the state space of transfer function is given by,

$$\begin{aligned}
& \left[\begin{array}{l} \frac{d\Delta V}{dt} \\ \frac{d\Delta \alpha}{dt} \\ \frac{d\Delta q}{dt} \\ \frac{d\Delta \theta}{dt} \\ \frac{d\Delta H}{dt} \\ \frac{d\Delta \beta}{dt} \\ \frac{d\Delta p}{dt} \\ \frac{d\Delta r}{dt} \\ \frac{d\Delta \phi}{dt} \end{array} \right] = \left[\begin{array}{ccccccccc} \frac{T_V}{m} & -\frac{D_\alpha}{m} & 0 & 0 & 0 & 0 & 0 & 0 & 0 \\ 0 & -\frac{T_* + L_\alpha - mg}{mV_*} & \frac{(mV_* - L_q)}{mV_*} & -\frac{g}{V_*} & 0 & 0 & 0 & 0 & 0 \\ 0 & \frac{M_\alpha}{I_y} & 0 & \frac{M_q}{I_y} & 0 & 0 & 0 & 0 & 0 \\ 0 & 0 & 1 & 0 & 0 & 0 & 0 & 0 & 0 \\ 1 & 0 & 0 & 0 & 0 & 0 & 0 & 0 & 0 \\ 0 & 0 & 0 & 0 & 0 & \frac{Y_\beta - D_*}{mV_*} & 0 & \frac{Y_r - mV_*}{mV_*} & 0 \\ 0 & \frac{l_\alpha}{I_x} & 0 & 0 & 0 & \frac{l_\beta}{I_x} & \frac{l_p}{I_x} & 0 & 0 \\ 0 & 0 & 0 & 0 & 0 & \frac{N_\beta}{I_z} & 0 & \frac{N_r}{I_z} & 0 \\ 0 & 0 & 0 & 0 & 0 & 0 & 1 & \tan\theta_* & 0 \end{array} \right] \begin{bmatrix} \Delta V \\ \Delta \alpha \\ \Delta q \\ \Delta \theta \\ \Delta H \\ \Delta \beta \\ \Delta p \\ \Delta r \\ \Delta \phi \end{bmatrix} \\
& + \left[\begin{array}{ccccc} -\frac{(T_{Ve} - D_{Ve})}{m} & \frac{D_{\delta e}}{m} & \frac{D_{\delta e}}{m} & 0 & \frac{D_{\delta r}}{m} \\ 0 & -\frac{L_{\delta e}}{mV_*} & -\frac{L_{\delta e}}{mV_*} & 0 & 0 \\ 0 & \frac{M_{\delta e}}{I_y} & \frac{M_{\delta e}}{I_y} & 0 & 0 \\ 0 & 0 & 0 & 0 & 0 \\ 0 & 0 & 0 & 0 & 0 \\ 0 & 0 & 0 & \frac{Y_{\delta r}}{mV_*} & \frac{Y_{\delta r}}{mV_*} \\ 0 & \frac{l_{\delta e}}{I_x} & -\frac{l_{\delta e}}{I_x} & 0 & \frac{l_{\delta r}}{I_x} - \frac{l_{\delta r}}{I_x} \\ 0 & 0 & 0 & \frac{N_{\delta r}}{I_z} & \frac{N_{\delta r}}{I_z} \\ 0 & 0 & 0 & 0 & 0 \end{array} \right] \begin{bmatrix} \Delta V_e \\ \Delta \delta_{e1} \\ \Delta \delta_{e2} \\ \Delta \delta_a \\ \Delta \delta_{r1} \\ \Delta \delta_{r2} \end{bmatrix} + \begin{bmatrix} \frac{D_{Vc}}{m} \\ 0 \\ \frac{M_{Vc}}{I_y} \\ 0 \\ 0 \\ 0 \\ 0 \\ 0 \\ 0 \end{bmatrix} [\Delta V_c] \quad (6.3.9)
\end{aligned}$$

ΔV_c is the random crosswind input which is determined by the environment surrounding UAV which belongs to unpredictable variables of natural conditions. This kind of control input is normally called exogenous variable or noise.

Fig 6.10 displays the whole process of UAV hovering with the effect of crosswind by which UAV is difficult to keep a constant attitude in the case of hovering. But relying on extra auto-control to counteract the nose-down moment caused by crosswind the region of hovering can be effectively controlled around a specific point O as shown in Fig 6.11.

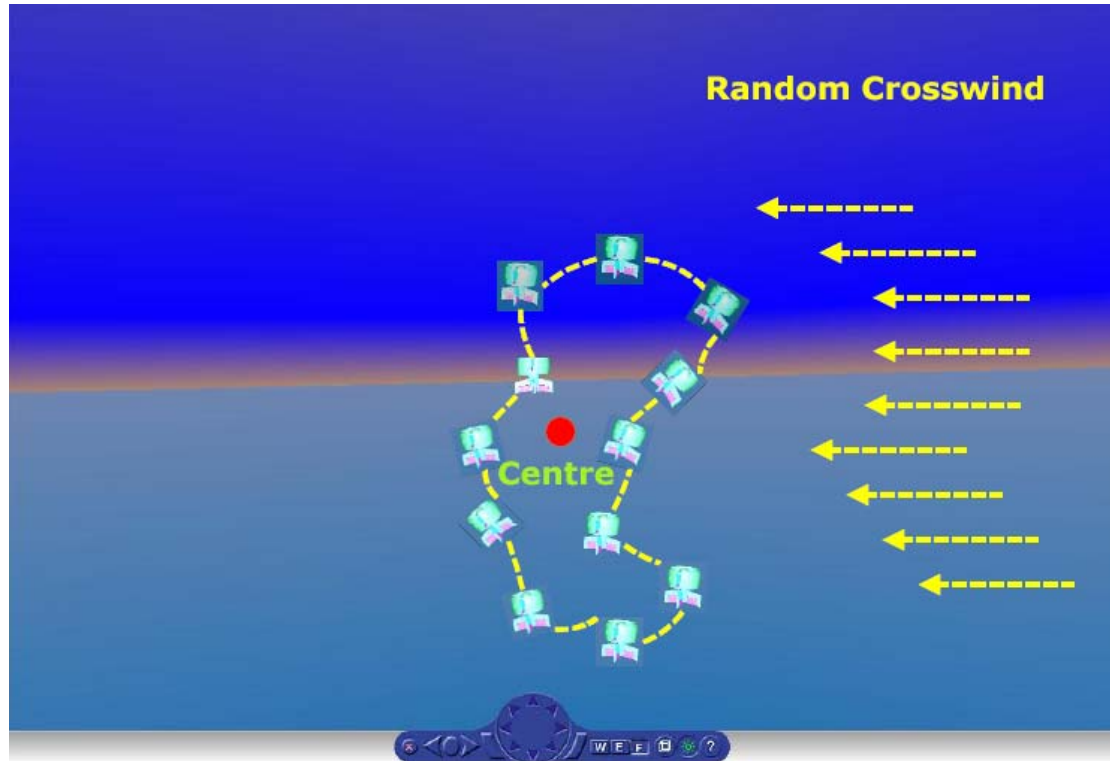


Figure6. 10 Description of UAV Hovering in Crosswind

It is clear that the trajectory of UAV is irregular and fluctuates up and down displayed in Fig 6.11 while the distances between its position and centre O are inter of light blue dash circle whose radius is no more than one meter. Thus, with the help of MIMO control laws the UAV has the capability to keep a state of hovering even if affected by random crosswind. Certainly, the precondition is low speed crosswind of which the range is below 5m/s as pointed out in Fig 6.12 (a). If the speed of crosswind increases, the active area of hovering also rises. And if the sensitivity of control is modified and associated with the external environment, the active area of hovering is able to be optimized.

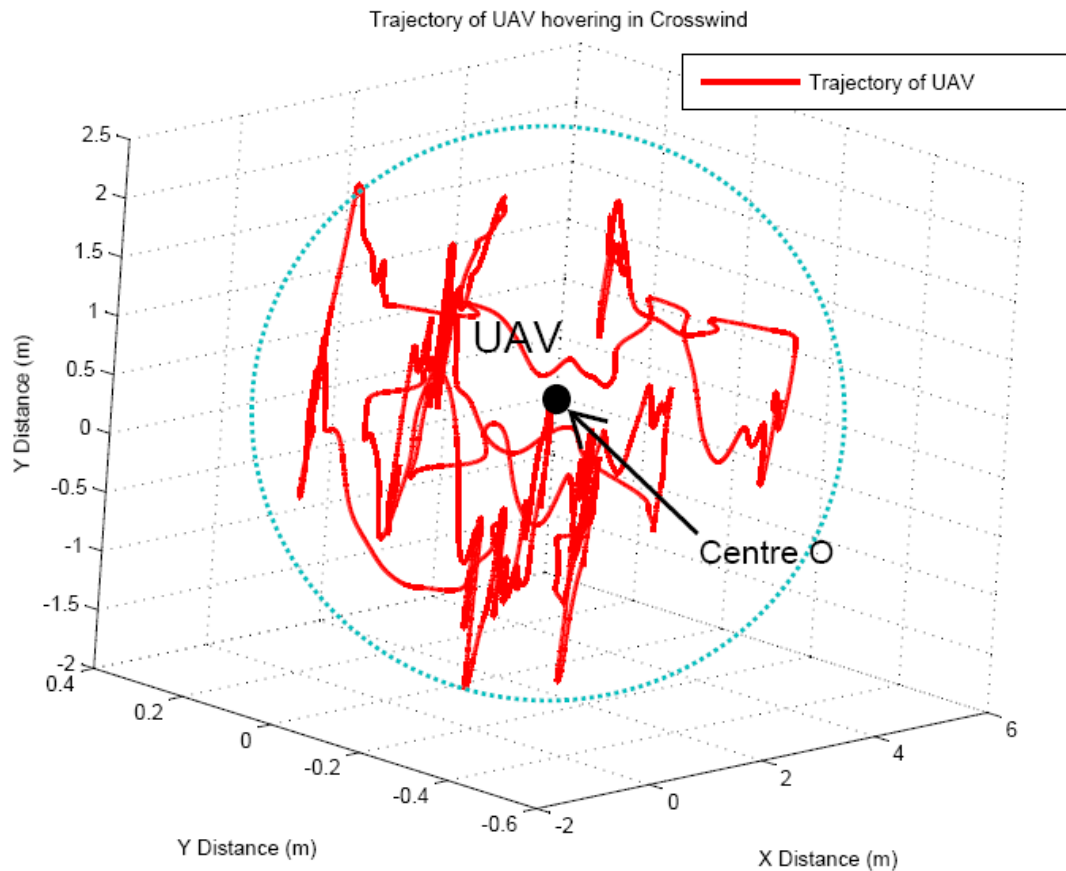
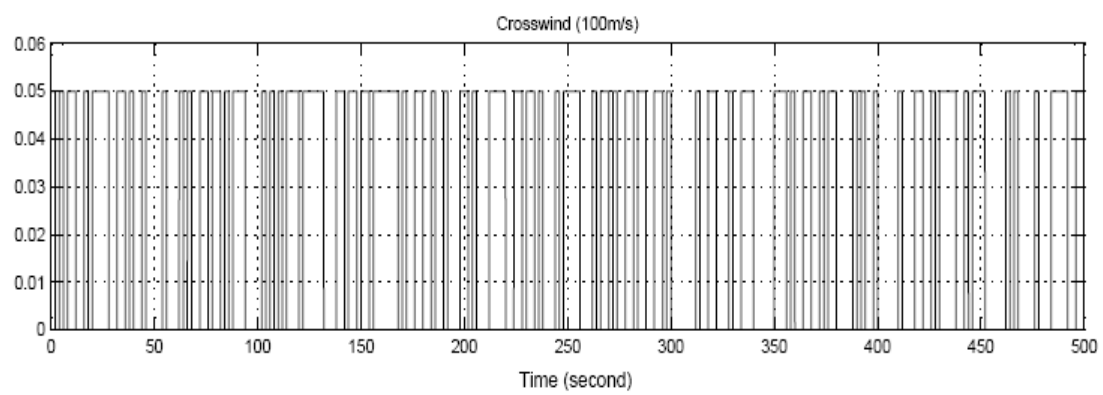
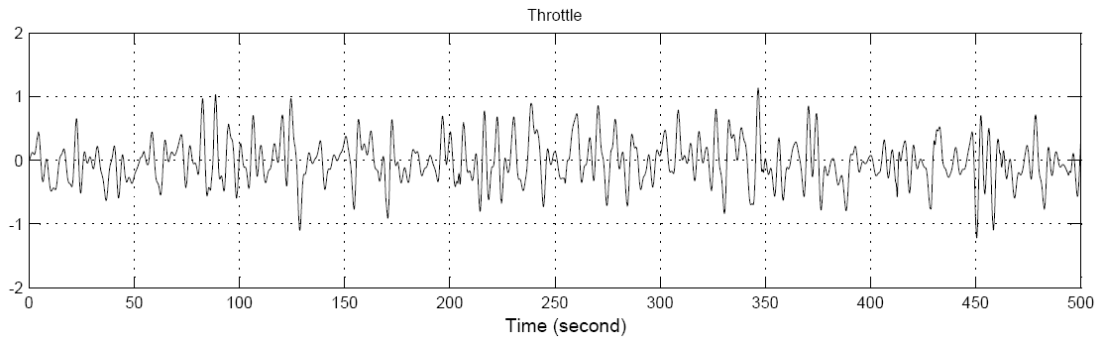


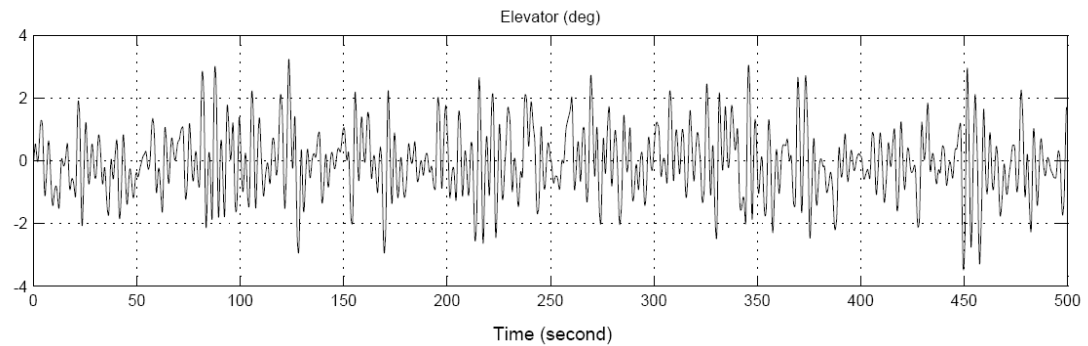
Figure6. 11 Trajectory of UAV Hovering in Crosswind



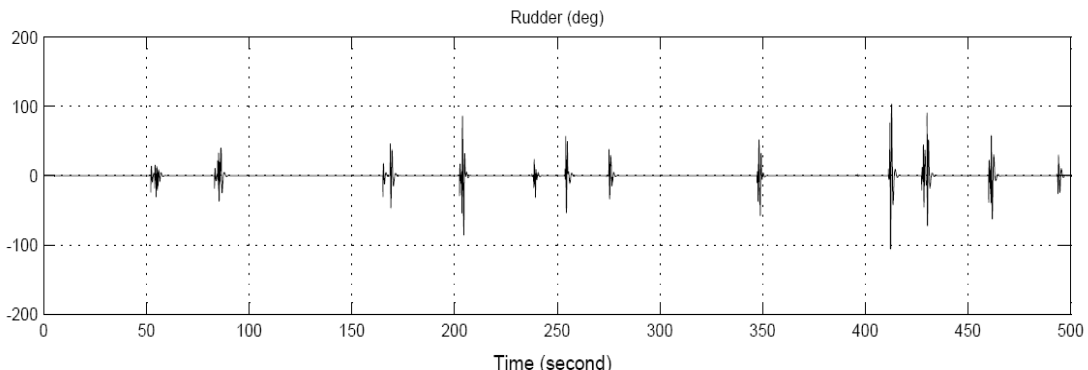
(a) Signal Input of Random Crosswind



(b) Signal Input of Throttle



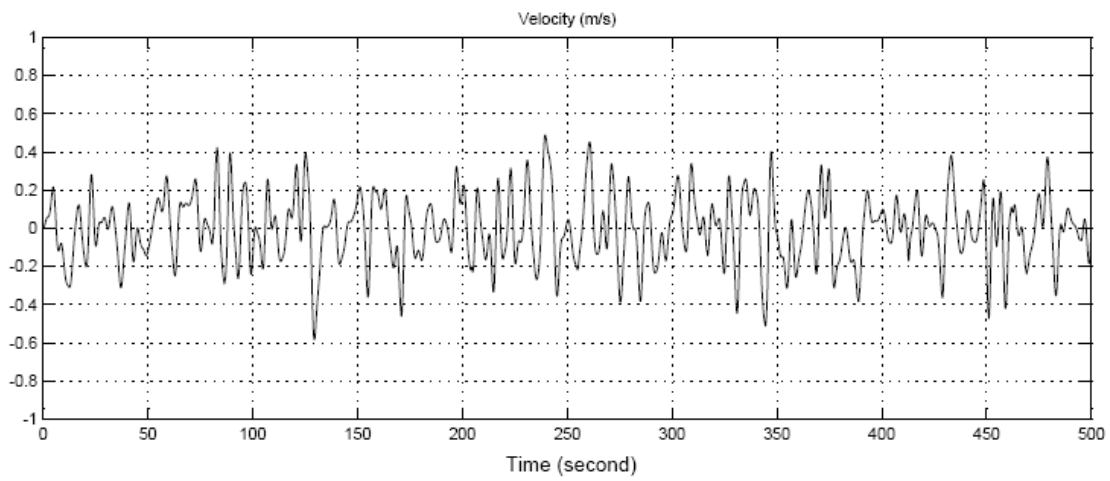
(c) Signal Input of Elevator 1 and Elevator 2



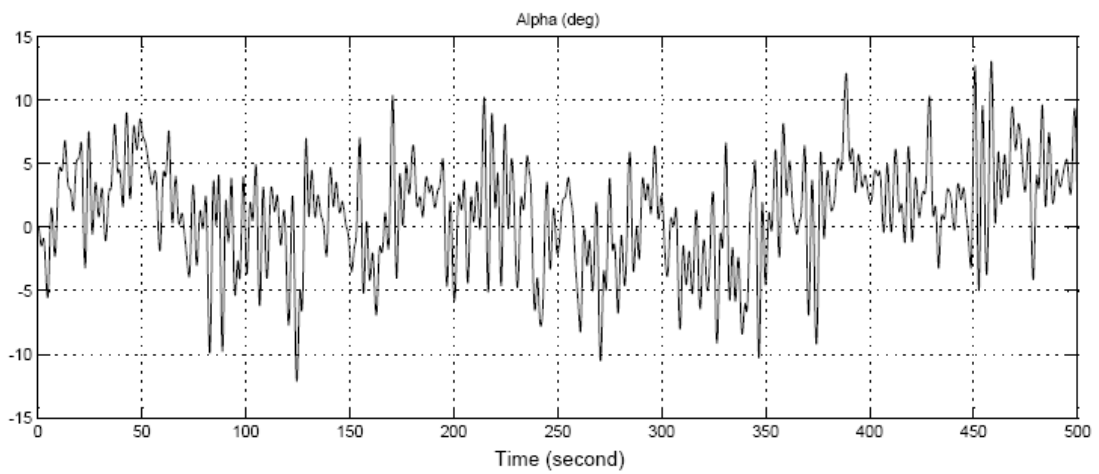
(d) Signal Input of Rudder 1 and Rudder 2

Figure6. 12 Signal Input of UAV Hovering in Crosswind

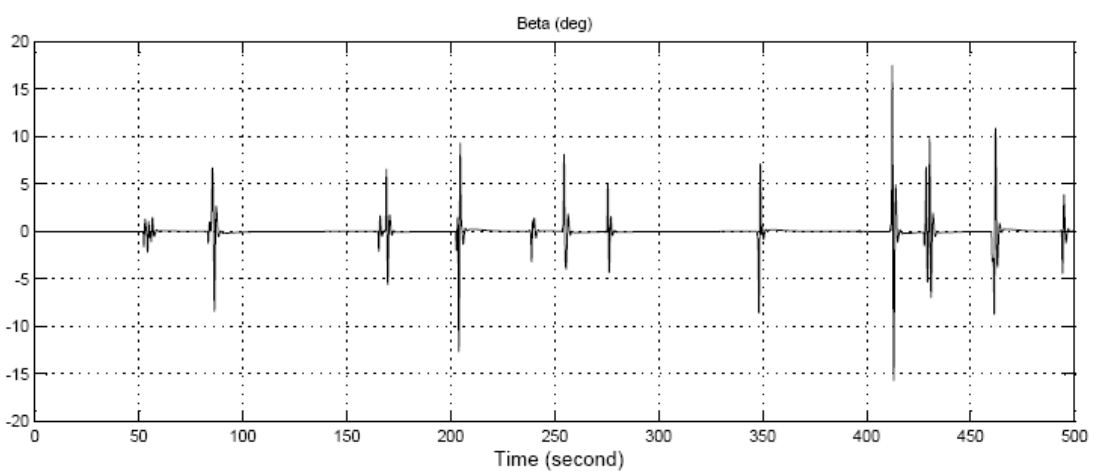
Above Fig 6.12 (b), (c) and (d) represent the signal inputs from throttle, elevator deflection and rudder deflection with simultaneous control. Meanwhile Fig 6.13 from (a) to (L) give the results of signal outputs including attitude (three Euler angles) and position (X, Y and Z) of UAV. They all correspond to trajectory of UAV shown in Fig 6.11.



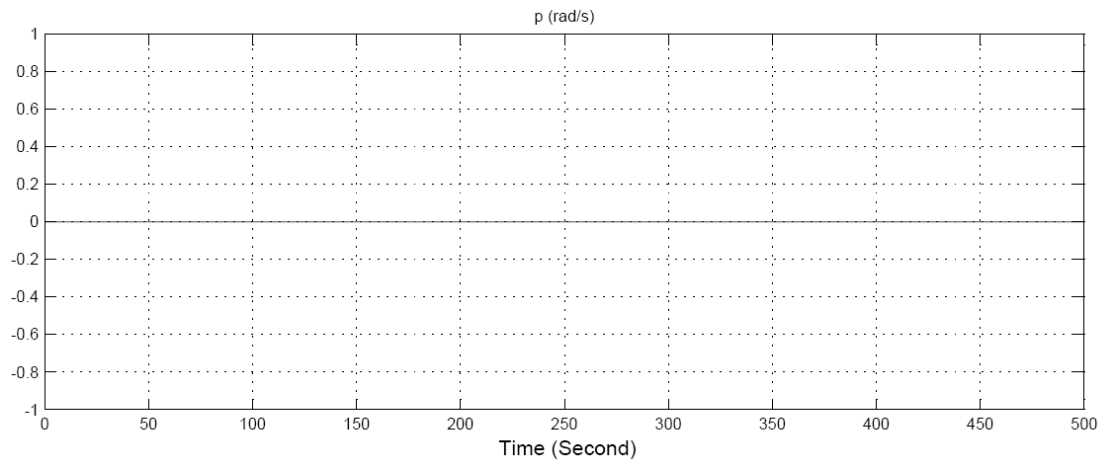
(a) Signal Output of Velocity



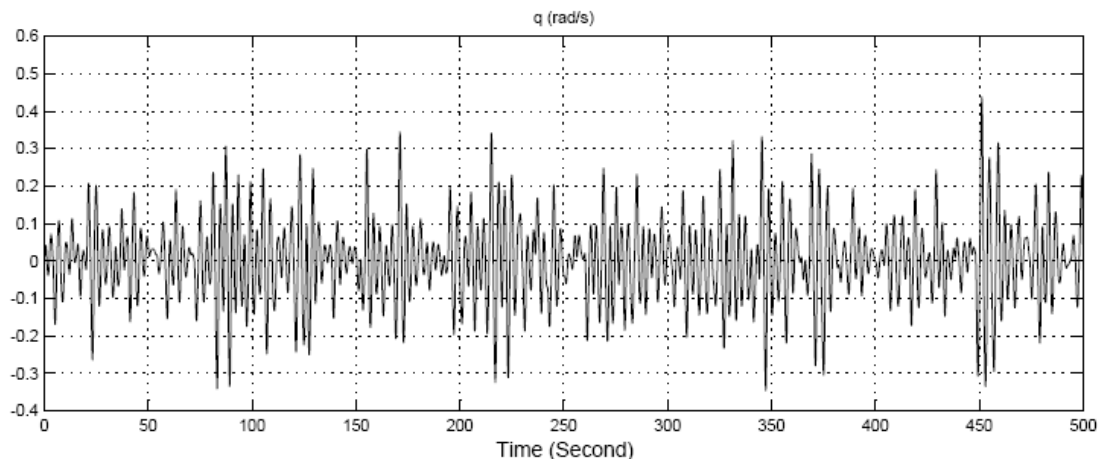
(b) Signal Output of Angle of Attack



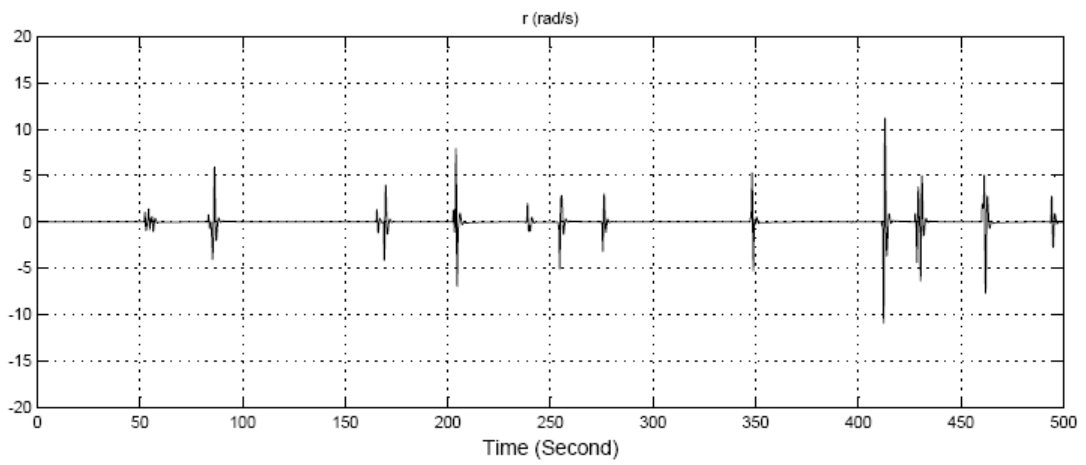
(c) Signal Output of Sideslip Angle



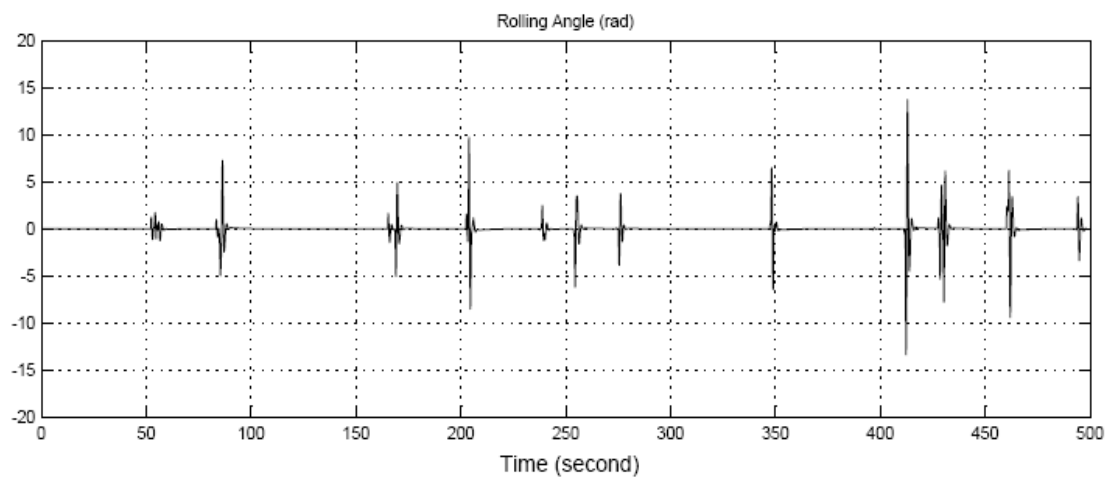
(d) Signal Output of Rolling Rate



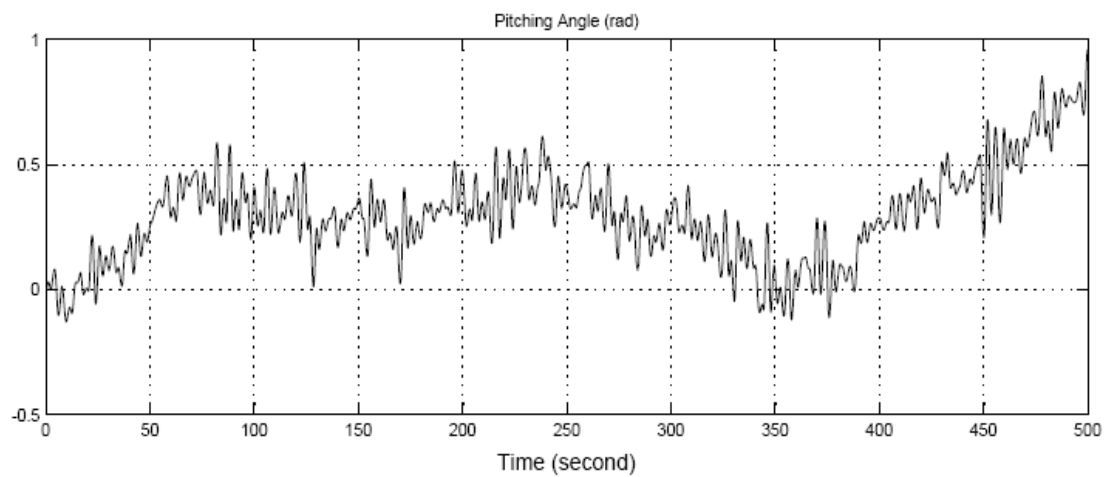
(e) Signal Output of Pitching Rate



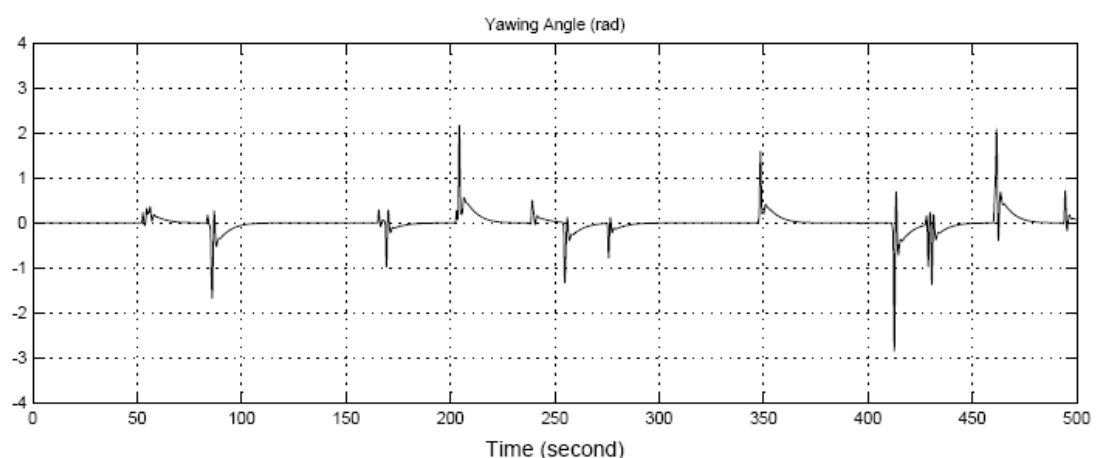
(f) Signal Output of Yawing Rate



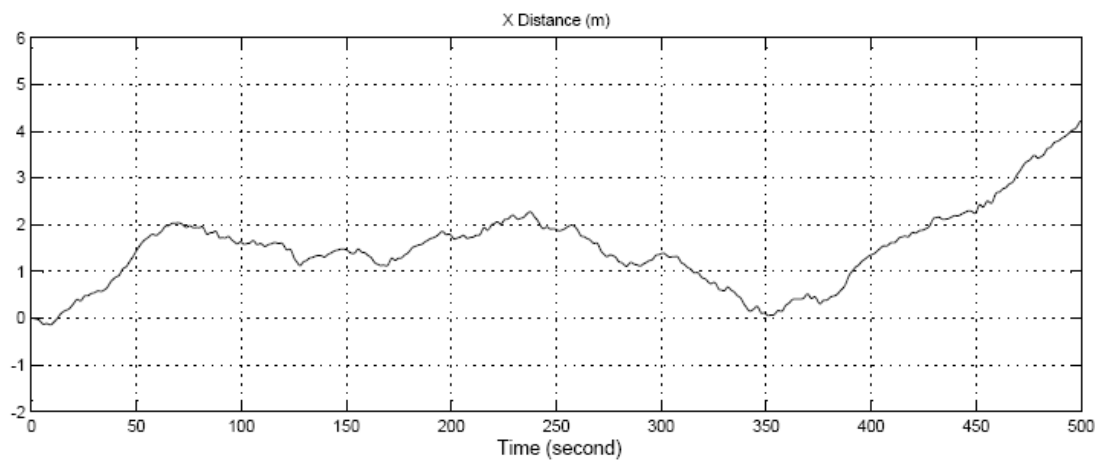
(g) Signal Output of Rolling Angle



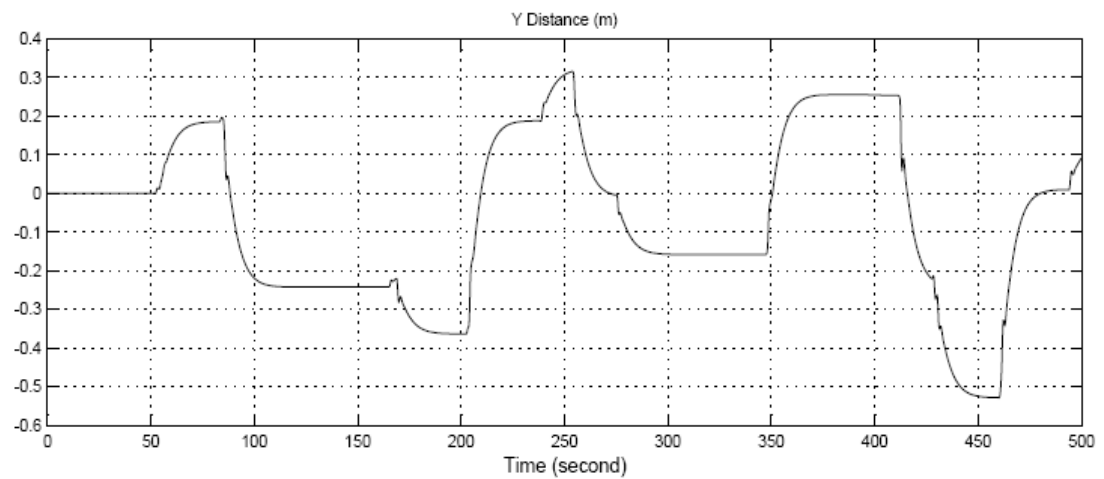
(h) Signal Output of Pitching Angle



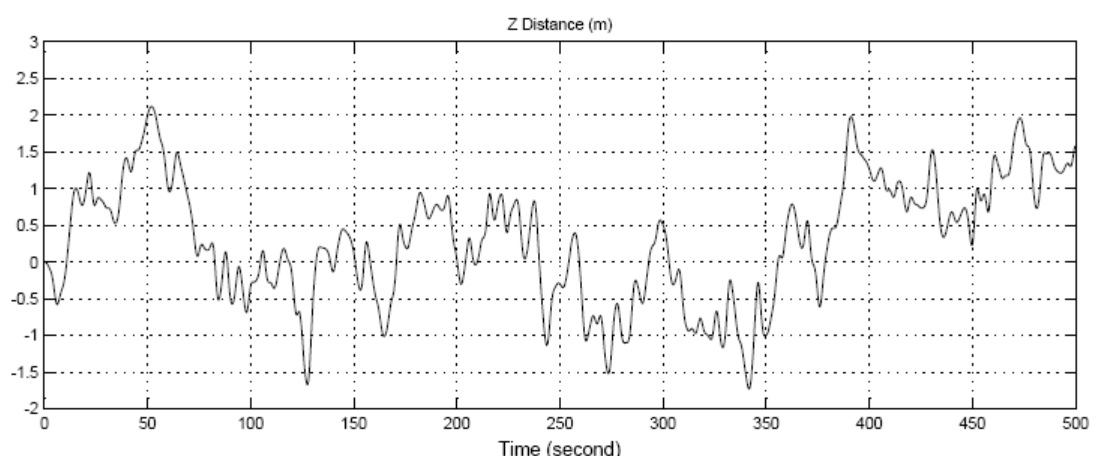
(i) Signal Output of Yawing Angle



(j) Signal Output of X Distance



(k) Signal Output of Y Distance



(l) Signal Output of Z Distance

Figure6. 13 Signal Output of UAV Hovering in Crosswind

6.3 Nonlinear Simulation

As we all know the small disturbance theory is always used to linearize the nonlinear model so as to simplify the mathematical model of aircraft which is in some states of constant. Then it is easier to analyze the flight performance and design the control system. However, the linearization methodology is not suitable for any kinds of flight cases. For instance, large amplitude flight maneuver, including longitudinal and lateral flight transition, isn't able to be analyzed in use of linear model. In this situation, the nonlinear simulation is the only option for us to apply. Indeed, most of the practical problems relative to aircraft flight are nonlinear rather than linear. So nonlinear model and simulation is essential to achieve the analysis of flight performance and control system design.

6.3.1 Six Degree-of-Freedom Dynamic Model in Simulink

The Aerospace Blockset is a tool package of MATLAB which can model aerospace systems in the Simulink environments. It not only provides aerospace subsystems and components in the Simulink block format for aerospace system design and integration, but it also can simulate flight performance from environmental models to equations of motion, from gain scheduling to animation.

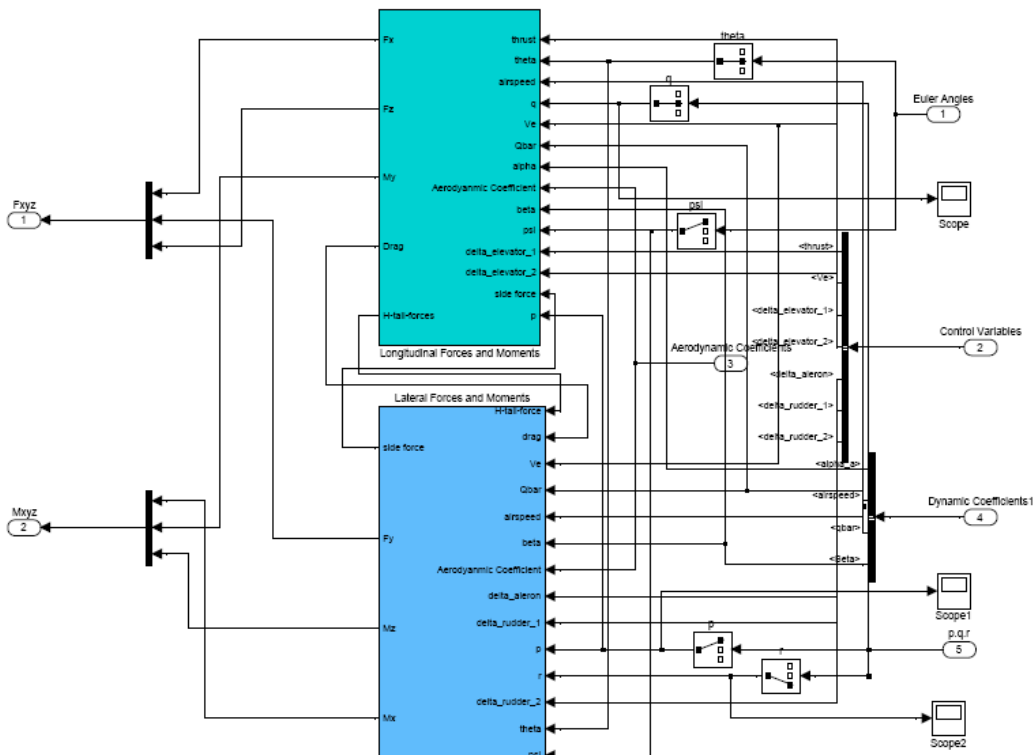


Figure6. 14 Coupled Nonlinear 6 DoF Dynamic Model of Ducted Fan UAV

This figure shows the six degrees of freedom dynamic model of the UAV in Simulink format based on equations in chapter 5. Inputs include aerodynamic coefficients and control input variables which are up to CFD results, Wind Tunnel test and controller. Outputs consists of forces and moments in 3D environment (x, y, z axis). Because the four control surfaces are independent to control the attitude of UAV, the lateral control is coupled with longitudinal control. Obviously, the coupled dynamic control

occurred during hovering, because the UAV keeps stable in a fixed position depended on both lateral and longitudinal control surfaces.

6.3.1.1 Longitudinal Model

In body-axes coordinate of UAV, the longitudinal vectors are composed by forces acting on x axis and z axis, and moment relative to y axis. Thus it is also named 3 degree-of-freedom longitudinal model. The three vectors are formed due to contributions from thrust, drag, lift and gravity which are acting on duct, fuselage, wings and tails, respectively. And the magnitudes of these three vectors are also determined by three Euler angles because of the transform from wind-axes to body-axes. Once the longitudinal external forces on UAV and Euler angles are known, the longitudinal model is built up as figure 6.15 shown.

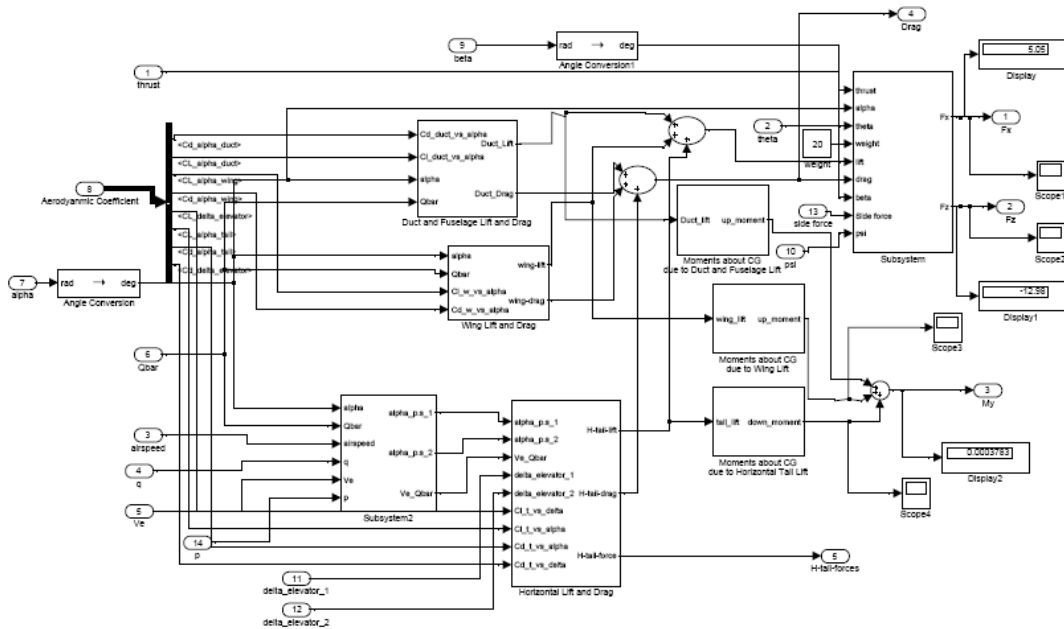


Figure6. 15 Longitudinal Forces and Moments

6.3.1.2 Lateral Model

To build up the 3 degree-of-freedom lateral model, compared with longitudinal model, the only difference is the lateral external forces on UAV should be obtained. Especially the side forces acting on components of UAV should be calculated before getting the expressions of force in y axis and moments in x and z axis. The figure 6.16 shows the lateral model.

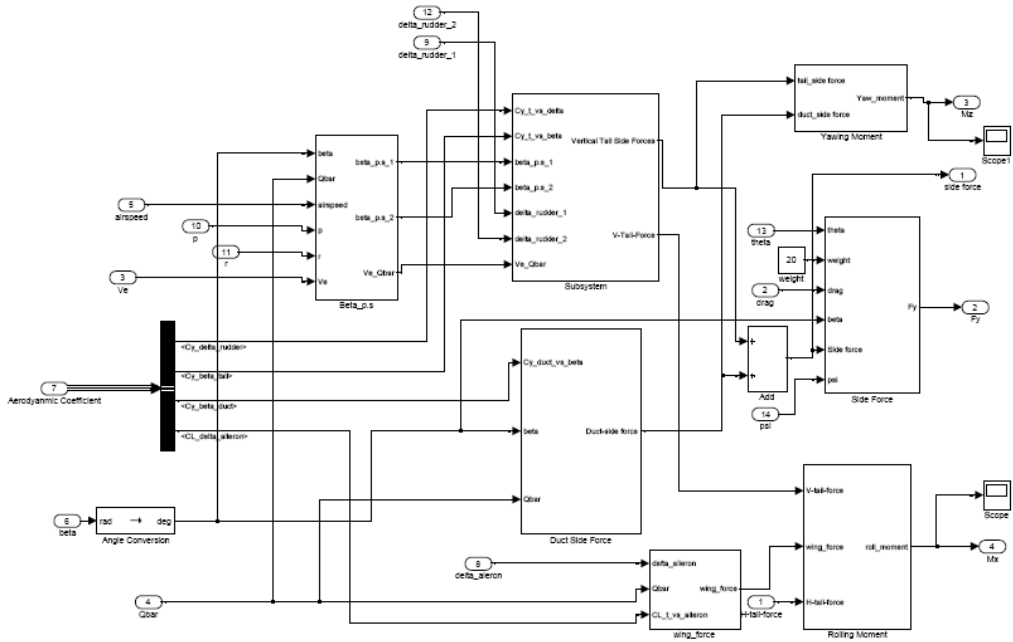


Figure6. 16 Lateral Forces and Moments

6.3.2 Six Degree-of-Freedom Quaternion Model

In Eq.(5.66), Eq.(5.67) Eq.(5.68) and Eq.(5.69) the relationship between Quaternion and Euler angles has been shown. It is easy to use this mathematical relationship to build up the model in simulink environment given by figure 6.17. The advantage of Quaternion model is to avoid the calculation to be broken up because of the singularity appearing in the case of $\theta = \frac{\pi}{2}$.

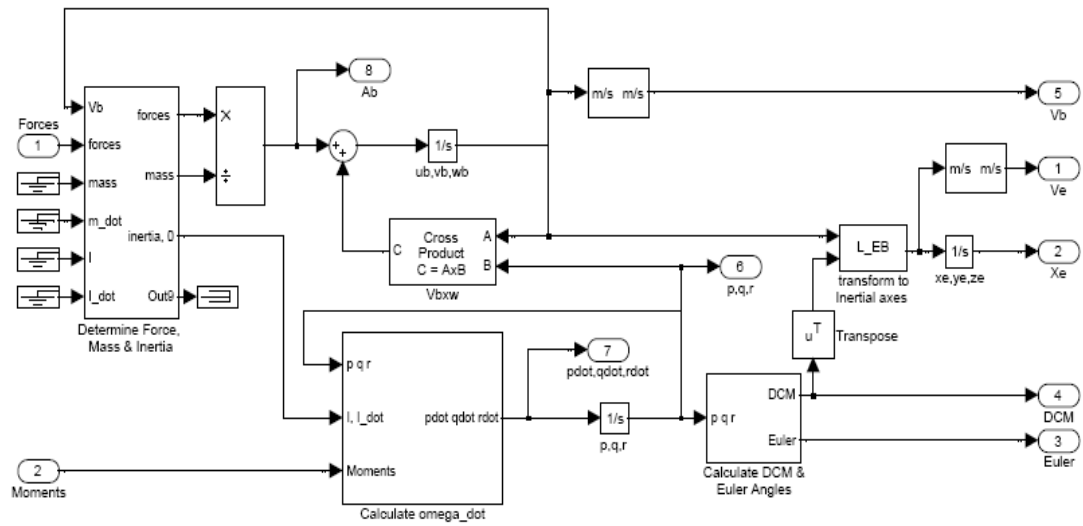


Figure6. 17 From Quaternion to Euler Angles

6.3.3 Flight Environmental Model

To measure airspeed, most light aircraft designs implement pitot-static airspeed indicators based on Bernoulli's principle. Pitot-static airspeed indicators measure airspeed by an expandable capsule that expands and contracts with increasing and decreasing dynamic pressure. Moreover, a pitot-static airspeed sensor contains a restricted volume of air. At high altitudes and high airspeeds, calibrated airspeed is always higher than equivalent airspeed. Because the air density is lower. True airspeed represents the compensation of equivalent airspeed for the density error, the difference in air density at altitude from the air density at sea level, in a standard atmosphere.

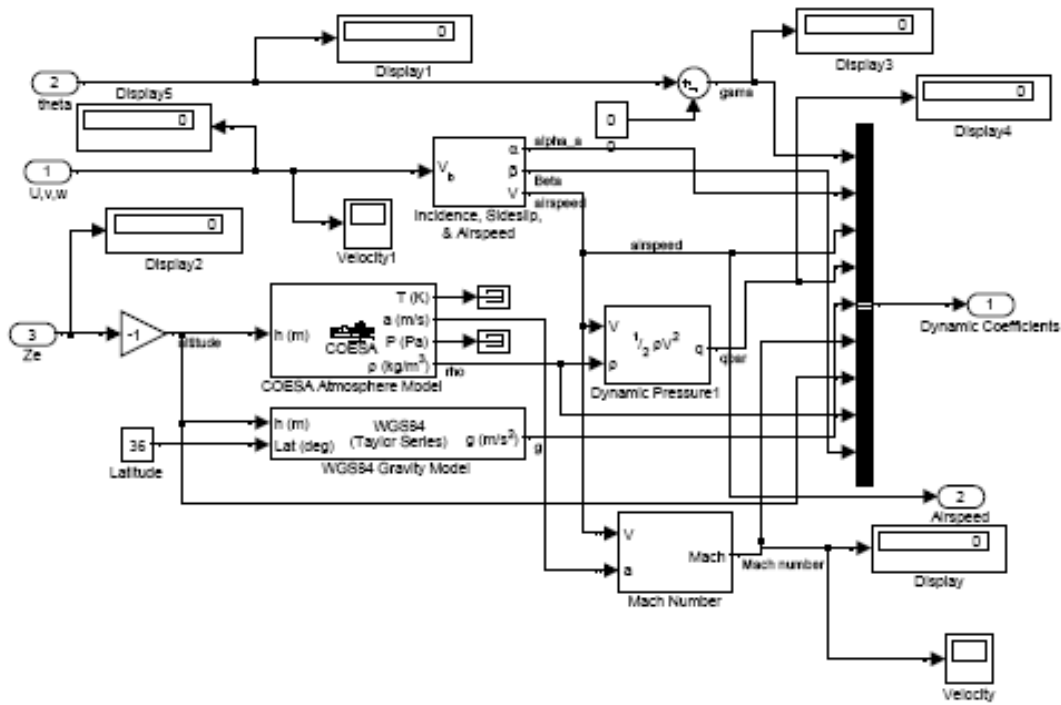


Figure6. 18 Flight Environment of Ducted Fan UAV

(Committee on Extension to the Standard Atmosphere) COESA is a representation of the standard lower atmospheric values for absolute temperature, pressure, density, and speed of sound for input geo-potential altitude. With a decrease or increase in altitude at the standard atmospheric environment, the airspeed of UAV can be measured by setting the parameters in this flight environment.

V-Realm Builder is a kind of powerful three dimensional authoring package for the creation of 3D objects. It is designed not only for expert users but also for novice users. Its point and click capability delivers the same intimate control of the 3D environment that you can get by hand-coding. Yet, in automating VRML development and delivering instant visual feed-back, it dramatically speeds 3D world construction.

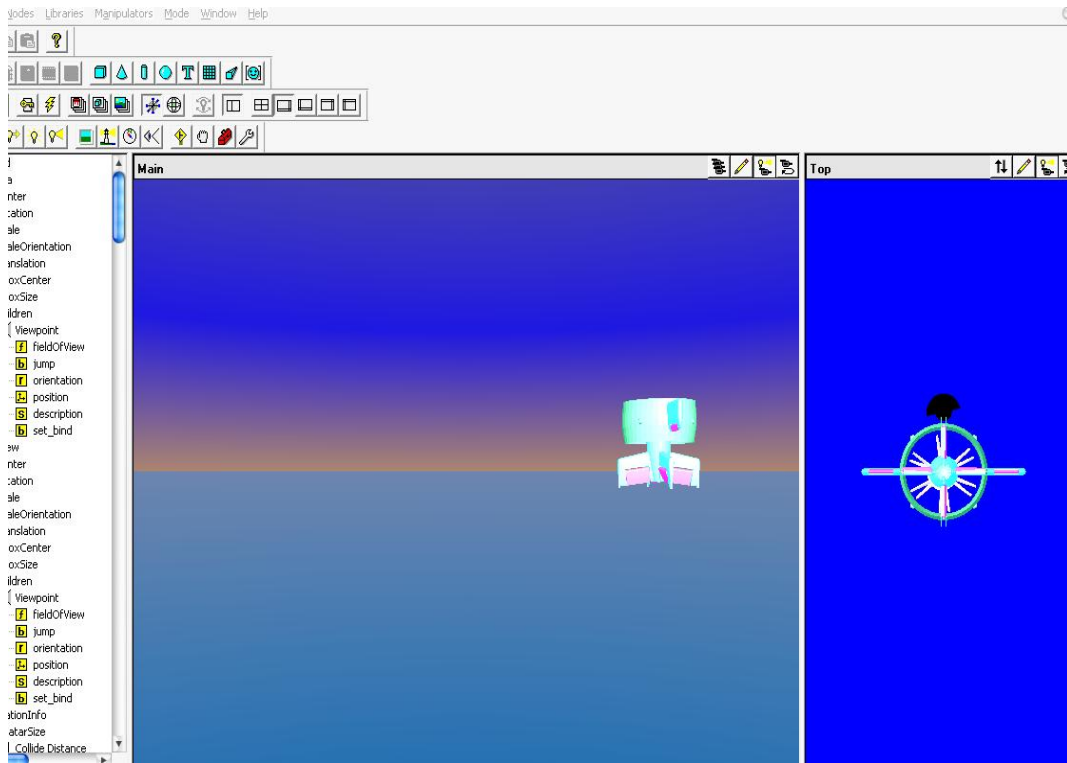


Figure6. 19 UAV Model in V-Realm Builder Environment

Before using MATLAB/Simulink to simulate the flight performance, we have to set up a visual model in 3D environment by V-Realm Builder, see figure.6.19. Once the model is linked with MATLAB/Simulink, as long as we run the simulation in MATLAB, the visual animation of this ducted fan UAV is able to be shown.

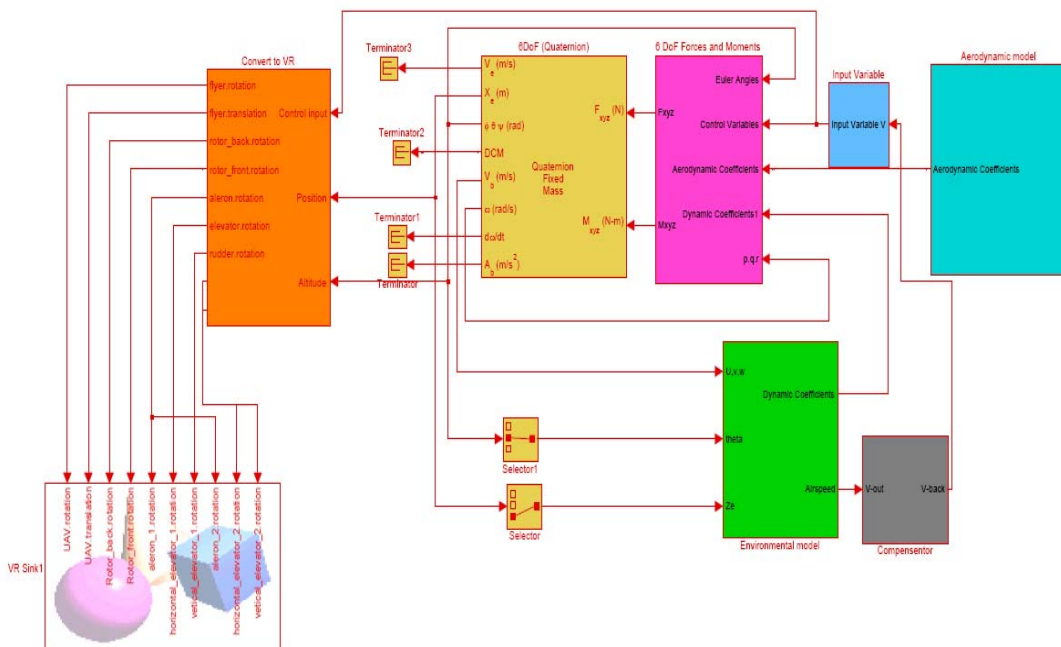


Figure6. 20 Combine V-Realm Builder and MATLAB by Virtual Reality Toolbox

By using Virtual Reality Toolbox to connect the MATLAB model with V-Realm Builder model in the Simulink environment (see figure 6.20), the animated simulation of UAV flight can be achieved visually.

6.3.4 Longitudinal Nonlinear Simulation

In order to fulfill flight transition from vertical climb to horizontal flight as one of the most important performances of this ducted fan UAV, the nonlinear approach should be utilized due to this longitudinal flight maneuver being completed in the big range of pitch angle between 0 to 90 degree as shown in Fig 6.21. Therefore, the small disturbance theory isn't suitable for this situation.

For the control strategy of this nonlinear model, two factors should be considered when including thrust input and velocity hold. To consider this, the modern feedback control law is in use of the case.

Meanwhile, δ_e as the main control input is used to achieve the nose-down or nose-up during UAV flight, in addition, the real-time simulation also has to be considered. Thus δ_e is controlled in real time mode.

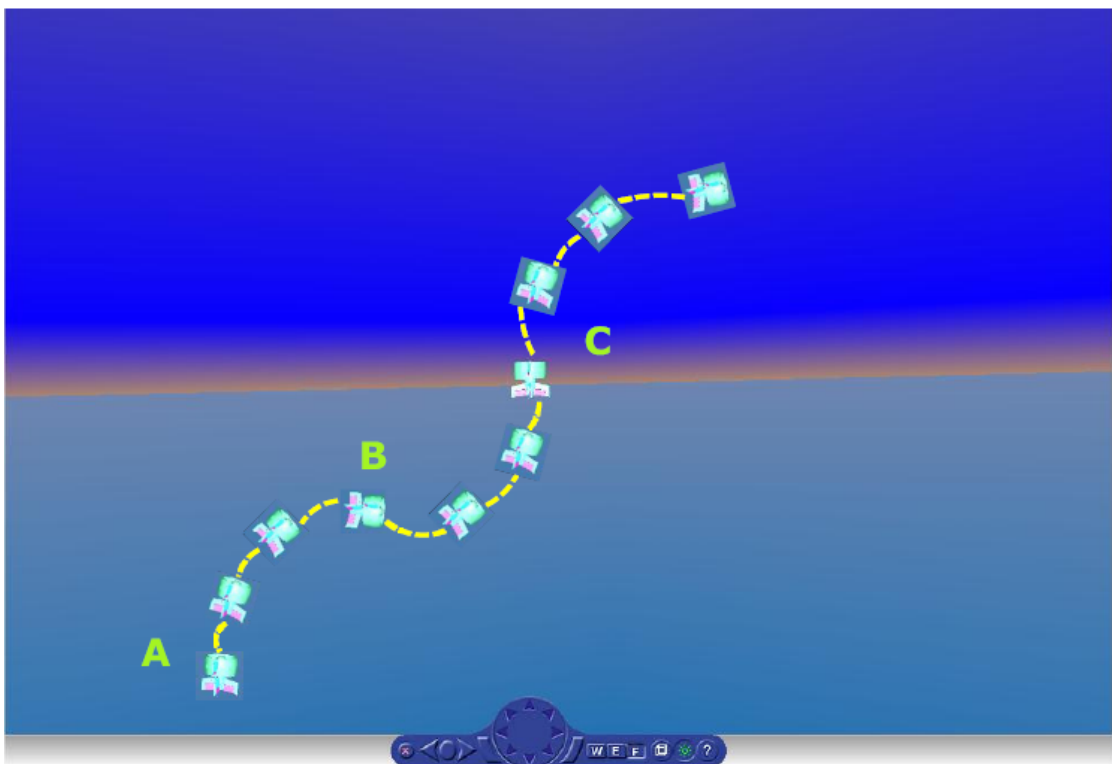


Figure6. 21 Description of Longitudinal Flight Maneuver

To get the trajectory of the UAV, integrate the six-degree-of-freedom using quaternion representation for the orientation of the UAV in space. Compared with Euler angle approach, applying quaternion methodology can avoid the calculation to break off because of the abnormal points at $\theta=90$ degrees.

Setting up the initial position of UAV is (200, 200, 0) m in earth coordinates X, Y, Z respectively. The

initial velocity is $(20, 0, 3.5)$ m/s in body axes, initial angle of attack is 10 degree, angular velocities is $(0, 0, 0)$ rad/s and the initial Euler orientation is $(0, 1.57, 0)$ radians.

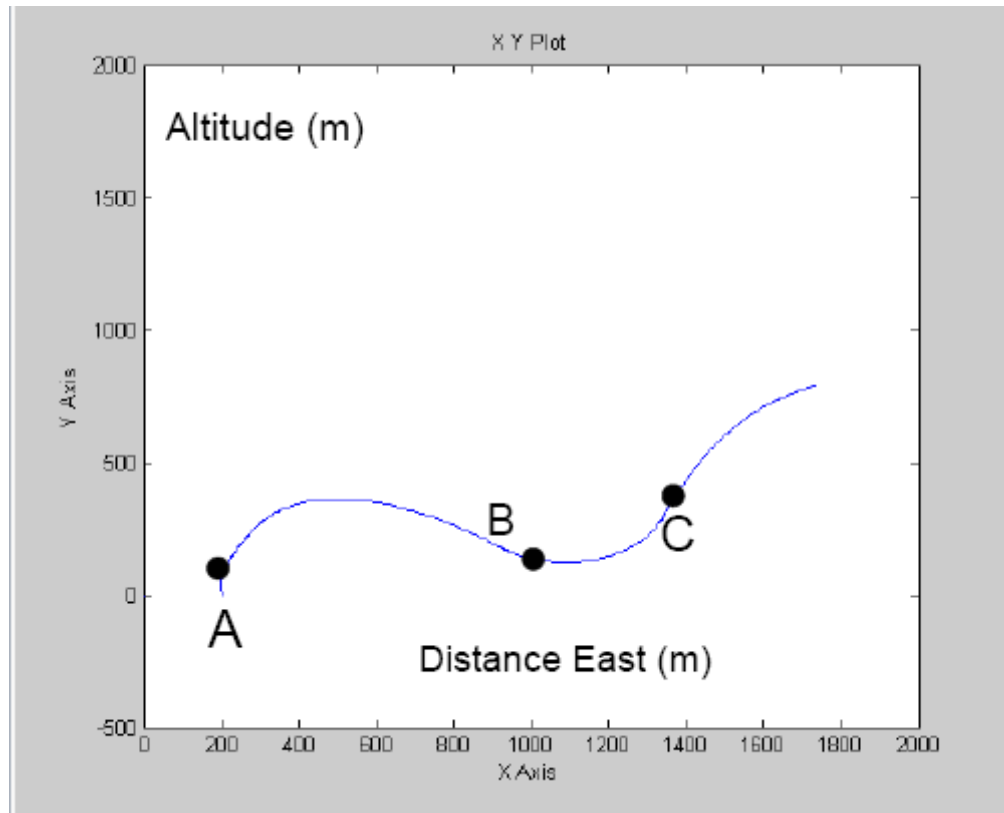


Figure6. 22 Trajectory of Longitudinal Flight Maneuver

To achieve the longitudinal flight transition, the input of two horizontal elevators are controlled simultaneously in real-time mode to avoid lateral motion occurred. For tracking on UAV flight, the trajectory of which is displayed in Fig 6.22. It shows that from point A to point B UAV undergo the maneuver from vertical climb to horizontal flight. Then it transfers again from horizontal flight to vertical climb as the tracks between point B and point C.

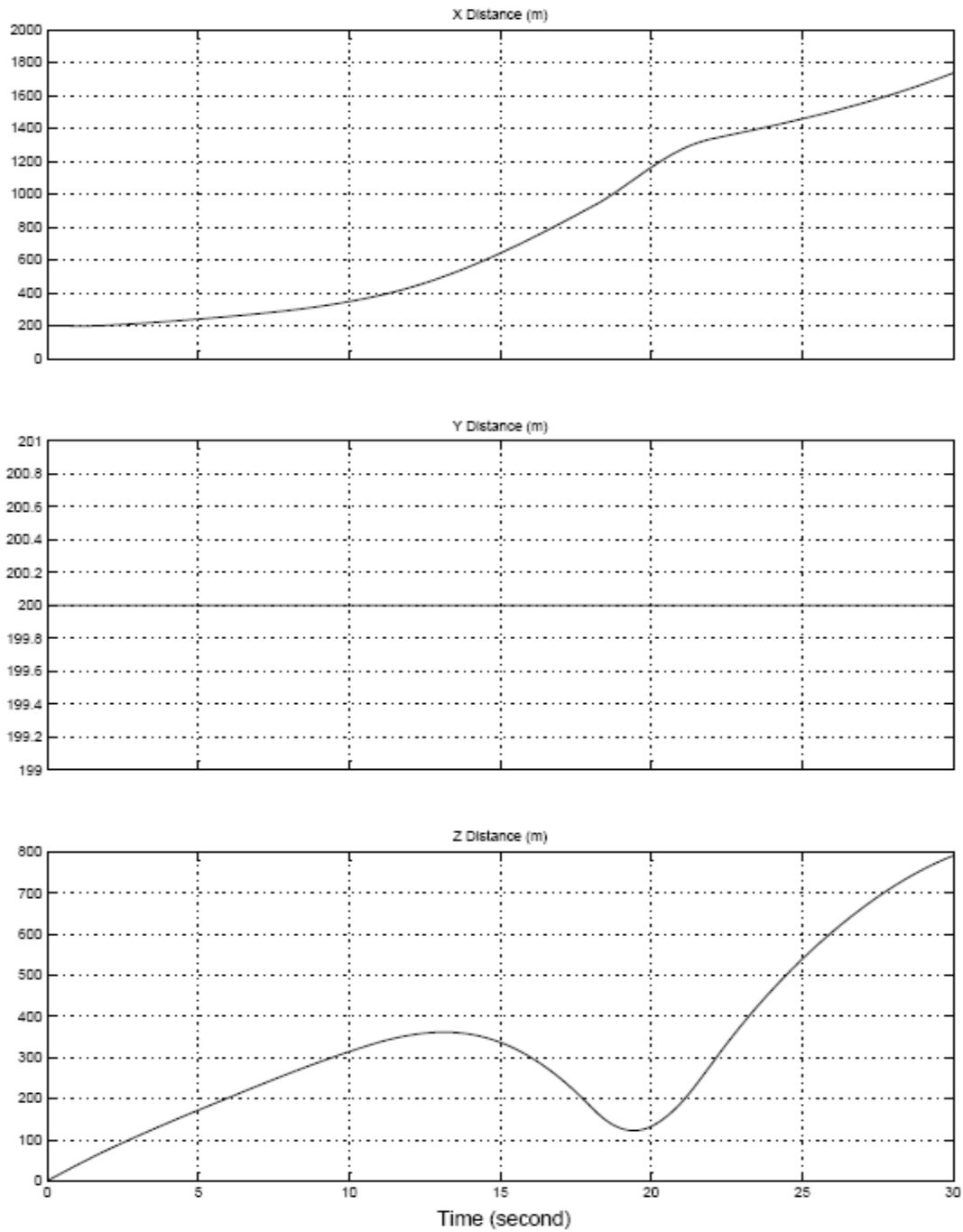


Figure6. 23 Position Tracks of UAV during Flight

Figure 6.23 also shows the trend of position of UAV during flight transition. Both distance of east and distance of altitude are increasing since the model has been running in simulink of MATLAB, whereas the distance of north is no change due to no lateral maneuver happened without lateral control input. These results of Fig 6.23 correspond to the trajectory shown in Fig 6.22.

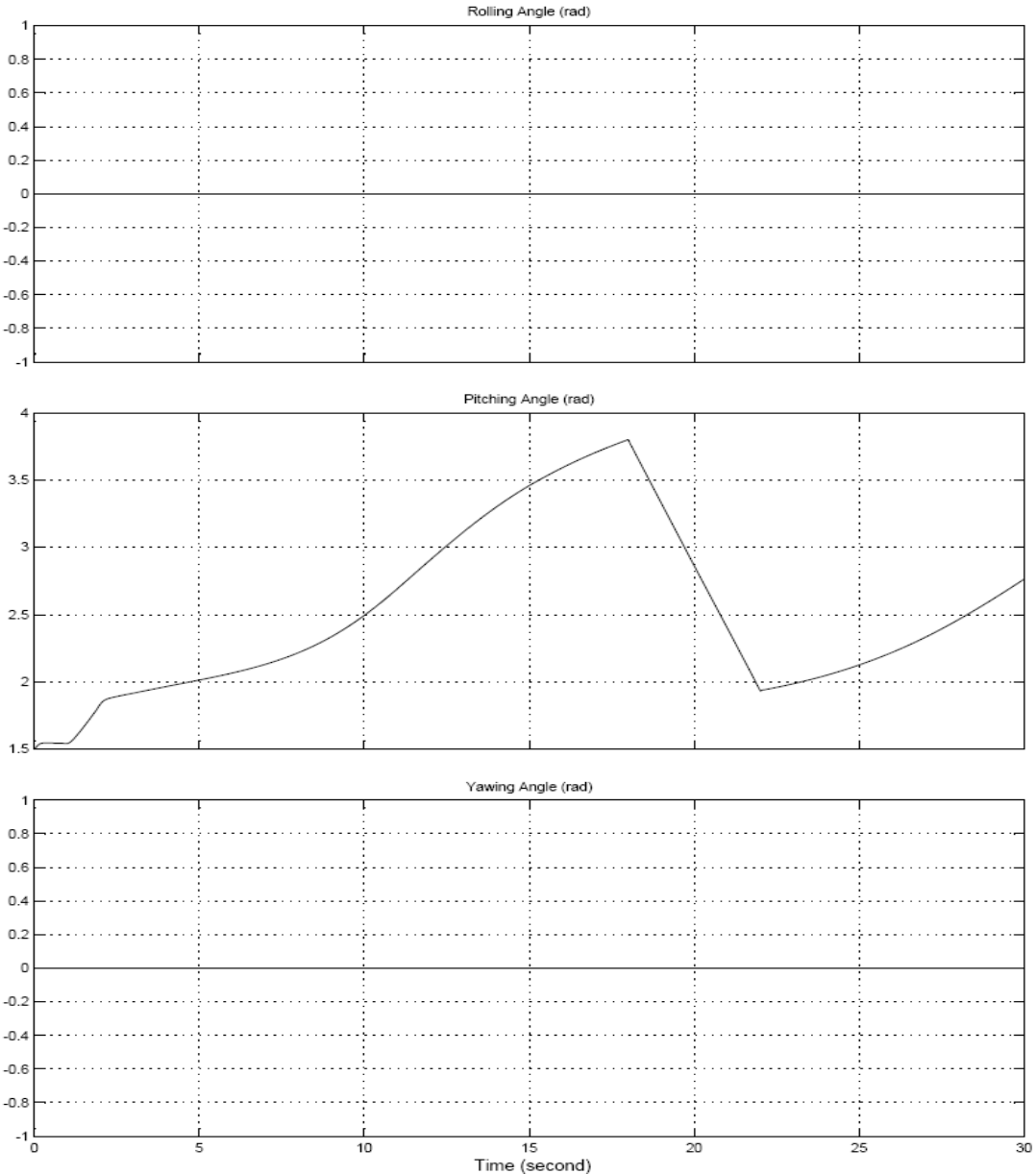


Figure6. 24 Attitude Variation along Trajectory

Above Fig 6.24 represents the attitude of UAV during flight as calculated in Fig 6.22. Only the pitch angle θ is converted significantly twice because of nose-down in point A and nose-up in point B. To fulfill the longitudinal maneuver, elevator control input has to be applied. As double flight transition is achieved, it means that two signals are input. The first signal input happened at 1st second after running simulation, it kept one second as a short pulse signal. The second one is a long pulse signal from 17th second to 22th second. From Fig 6.25 we can see that both pitch rate and angle of attack response to δ_e reflect the signal inputs which are available to achieve the pitch control. The reason why the second signal input is longer than first one is due to the long-period response from first input. This also identifies the sensitivity of elevator control because of high speed propeller slipstream out of ducted fan. Although this control strategy linked with the nonlinear dynamic model is not very effective for pitching control, it does a good job of simulating the flight maneuver of the ducted fan UAV with no complicated control system. By nonlinear simulation we can conclude that the UAV is able to fulfill

longitudinal transition with deflected control and achieve horizontal cruise flight at specific angle of attack and throttle supply.

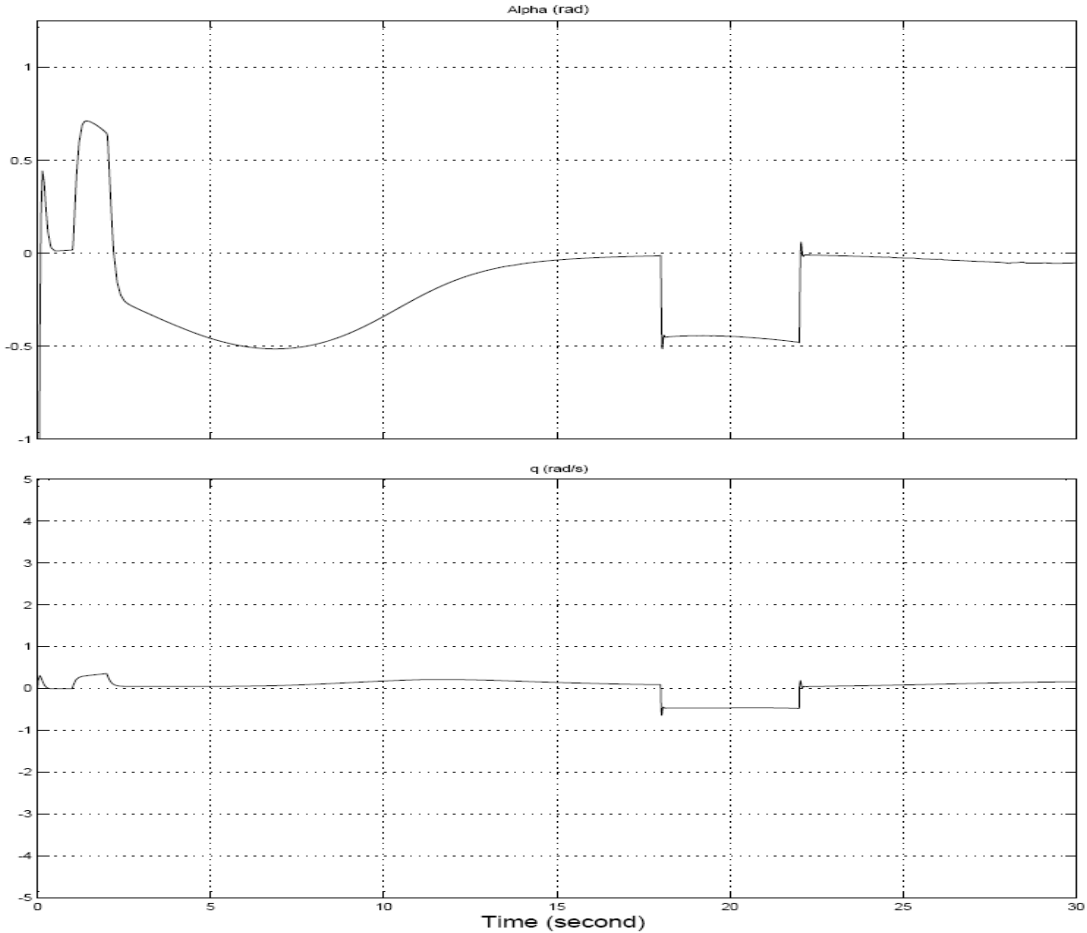


Figure6. 25 Angle of Attack and Pitch Rate in Real-Time Response to Elevator Input

$$\delta_e \text{ deflection of } 1 \text{ deg}$$

6.4 Summary

By designing of MIMO linear control laws for UAV hovering and low-speed slide flight the real-time simulation and modeling in MATLAB combined with Flight-simulator displays several animations and trajectories of UAV missions without or with crosswind effect during fight. From the results of simulation it states that the MIMO control laws playing a good performance in controlling the UAV in case of hovering and low-speed flight within impaction of small disturbance caused by wind. Meanwhile, it proves that our dynamic model of UAV is assembled, according to CFD and wind tunnel testing, is quite accurate to be controlled well with control laws. Although the MIMO nonlinear control laws are still not able to be achieved so far, in terms of the results from section 6.3, which show the control law only for longitudinal control as playing a expectable role in succeeding large angle maneuver. Based on this control strategy and good results, it is convincible that the nonlinear control laws will be done soon.

Chapter 7

7 Conclusion

The ducted fan VTOL UAV, compared with manned aircraft, has the ability of computerizing and autonomous without on-board pilot by using digital, communicating and electronic system. There is no risk of loss of life and it is easier to be maintained than manned aircraft. Even in contrast to existing UAVs, it has the ability of long time hovering and remote controlled or autonomously complete missions, not only in civil roles, but also in military operations. Such as reconnaissance for firefighting and natural disaster, suspect monitoring and strategy attack. To fulfill above roles of UAV, the researcher has been focusing on development of dynamic model since the idea of conceptual design of this UAV came out.

7.1 Discussion of Results

After using CFD technology predicted the complicated longitudinal and lateral characteristics of the preproduction ducted fan VTOL UAV for stability and control at different Mach numbers with no priority wind tunnel data. We can conclude that the innovation of using propeller slipstream effects on control surfaces to achieve attitude control of UAV is identified and available to ensure the UAV low speed flight and hovering. Moreover the investigation of wind tunnel testing provides large quantity of data for estimating derivatives of stability and control. By analyzing the correlation between experimental data and CFD results, it is clear that the results of both are matched with each other very well. It means that the large quantity of data can be employed as important database for aerodynamic model of the UAV airframe. They also identify what we assumed in previous theoretical analysis are available to calculate some parameters of dynamic model. In addition, from wind tunnel data we can clearly see that the flight performance of UAV is improved by assembling two wings which provide sufficient lift for UAV to keep horizontal flight. Indeed, the two wings play a critical role in achieving longitudinal flight transition as we expected before.

Furthermore, by building up mathematical model of flight dynamics in MATLAB, simulation and modeling are completed. Moreover MATLAB model combined with visualize software displays several animations and trajectories of UAV missions without or with crosswind effect during flight. The results of simulation identifies that the dynamic model of UAV is controllable with suitable control law although it is unstable in crosswind. From results we also can find the MIMO linear control laws play a good performance in controlling the UAV in case of hovering and low-speed flight within impact of small disturbance caused by wind. By nonlinear simulation we can conclude that the UAV is able to fulfill longitudinal transition with deflected control and achieve horizontal cruise flight at specific angle of attack and throttle supply. In addition, the flight video provides us a good visual environment to feedback the trajectories of UAV flight in different cases. It is easier for researchers to improve the mathematical model through visual video than only facing to MATLAB scopes.

7.2 Recommended Further work

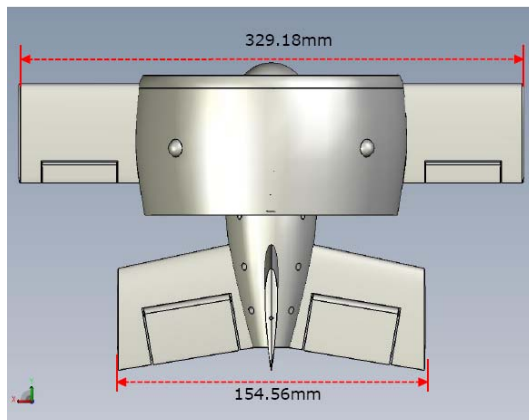
Further work contains dynamic model optimizing, nonlinear control system design and final actual flying. In order to improve the current dynamic model obtained by CFD, wind tunnel testing and theoretical method, the following work is investigating flight testing of ducted fan VTOL UAV. This work is pursued by other students who are focusing on manufacturing flying model of this UAV. Then the flight test will be done by connecting the flying model with actuators and controllers including motor control and control surfaces deflecting at RMIT.

Because our dynamic model of UAV is assembled, according to CFD and wind tunnel testing, to be controlled by using MIMO nonlinear control laws which are still not able to be achieved without flight testing data, some challenges yet to be resolved. For instance, how to measure the flight test parameters is one of the difficulties, which researchers need to consider the use of sensors including gyros and accelerometers. Furthermore, the option of battery is another key technology which should be paid more attention to extend the endurance of flying and reduce the total weight of UAV. In addition, how to overcome the unstable case caused by crosswind or propeller slipstream effects is also a big challenge in future work. After all, the practical situation of flight of UAV is still unknown. Especially, to achieve flight transition of ducted fan UAV, much more research and optimization on this UAV should be pursued. Hopefully, the nonlinear control system can play an effective role in control of both hovering and flight transition.

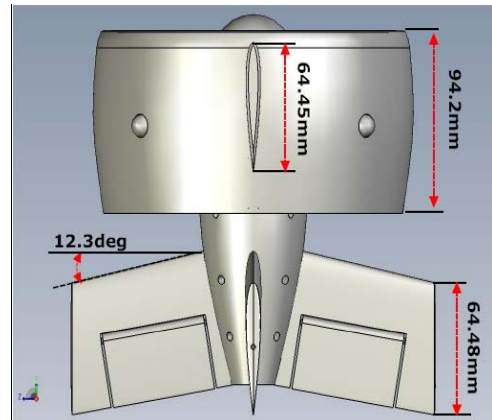
Appendix-A

A Final Design of UAV

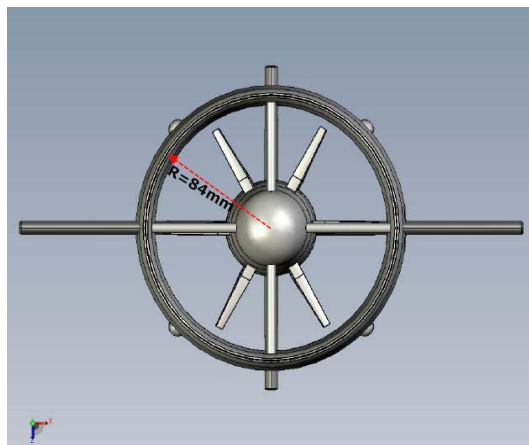
A.1 Three Views of UAV



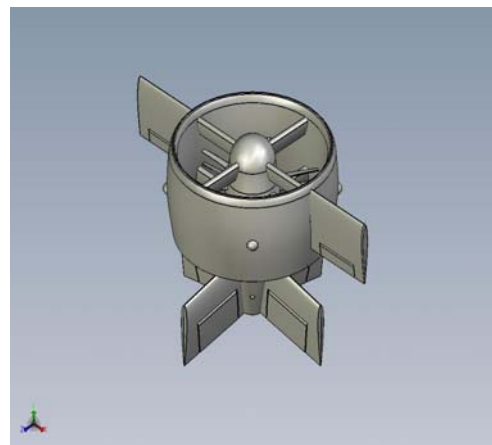
(1) Bottom View



(2) Left View



(3) Front View



(4) Isometric View

The 3D model of Ducted Fan VTOL UAV is modified in Solid-work. The NACA airfoil is used instead of the preliminary design in order to improve the aerodynamic characteristic of whole UAV. In addition, the area of control surfaces and aspect ratio of duct are increasing for higher lift to be generated. Meanwhile, the flow separation is reduced and ratio of lift and drag is promoted as well.

A.2 Geometry Parameters of UAV

Geometry Parameters of Wing	
Chord of wing root	$C_{rw} = 64.45mm$
Chord of wing tip	$C_{tw} = 64.45mm$
Ratio of tip and root	$\lambda_w = 1$
Wing span	$b_w = 161.18mm$
Wing area	$S_w = 10389.6mm^2$
Aspect ratio of wing	$AR_w = 2.5$

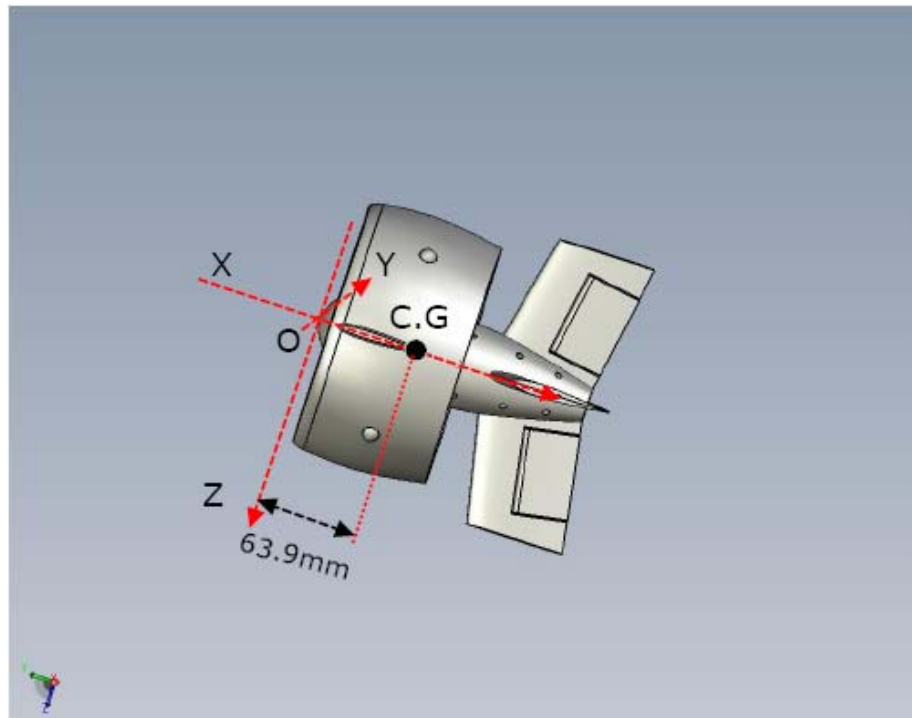
Geometry Parameters of Tail (control surface)	
Chord of tail root	$C_{rT} = 69.77mm$
Chord of tail tip	$C_{tT} = 64.68mm$
Ratio of tip and root	$\lambda_T = 0.927$
Tail span	$b_T = 154.56mm$
Tail area	$S_T = 10497.6mm^2$
Aspect ratio of Tail	$AR_T = 2.3$

Geometry Parameters of Duct	
Radius of duct	$R_d = 84mm$
Chord of duct	$c_d = 94.2mm$
Area of entrance or exit	$A_e = 22140mm^2$
Span area of duct	$S_d = 15825.6mm^2$
Aspect ratio of duct	$AR_d = 1.78$

Appendix-B

B Mass Properties of UAV

B.1 Dimension Measured by Solid-work



Output Coordinate System: X, Y and Z.

Mass = 400.00 grams

Volume = 1111841.357 cubic millimeters

Surface area = 272163.726 millimeters²

Center of mass: (millimeters)

X = 63.9

Y = 0.00

Z = 0.00

Principal axes of inertia and principal moments of inertia: (grams * square millimeters) at the center of mass.

$$I_x = (1.00, -0.00, 0.00) \quad P_x = 16352238.82$$

$$I_y = (0.00, 1.00, 0.00) \quad P_y = 20136155.2$$

$$I_z = (-0.00, 0.00, 1.00) \quad P_z = 22781018.37$$

Moments of inertia: (grams * square millimeters)

Taken at the center of mass and aligned with the output coordinate system.

$$I_{xx} = 16352238.82 \quad I_{xy} = 0 \quad I_{yz} = 0$$

$$I_{yx} = 0 \quad I_{yy} = 20136155.2 \quad I_{xz} = 0$$

$$I_{zy} = 0 \quad I_{zx} = 0 \quad I_{zz} = 22781018.37$$

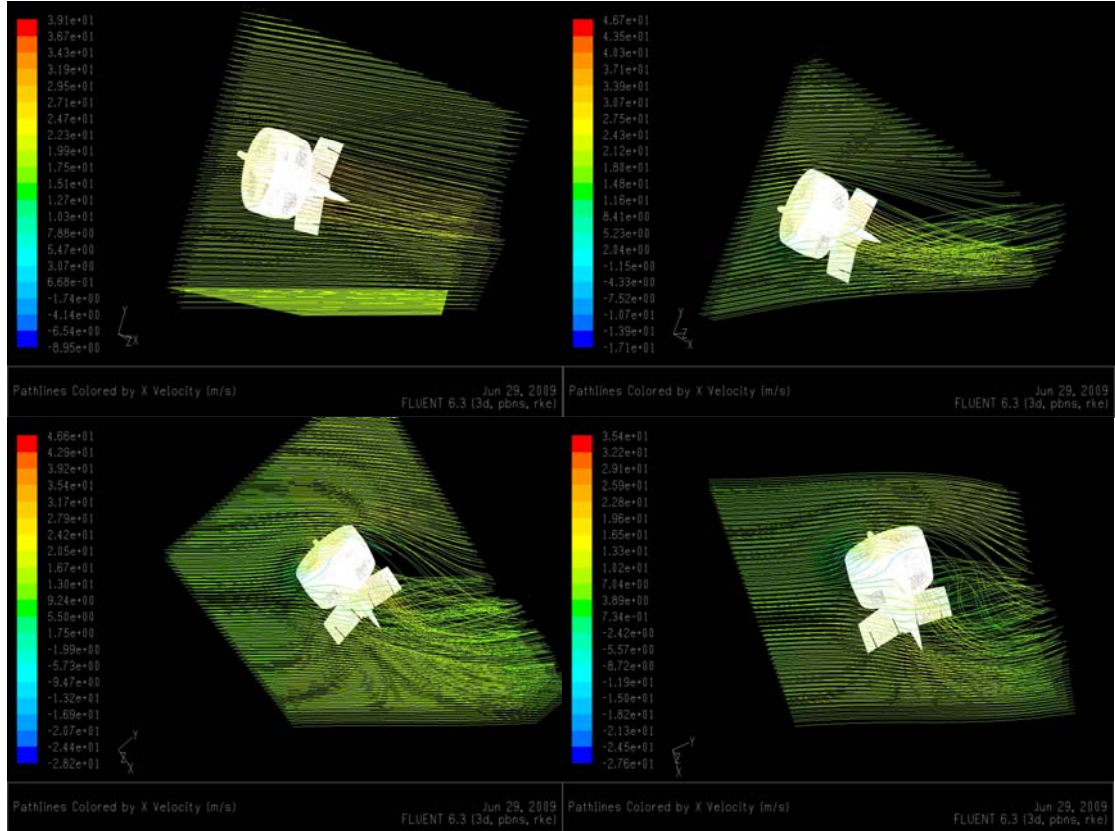
B.2 Aerodynamic Parameters

Aerodynamic Parameters of UAV	
Density of air	$\rho = 1.225 \text{ kg/m}^3$
Pressure of ambient	$P = 1 \text{ atm}$
Mass of UAV	$m = 400 \text{ g}$
Volume of UAV	$Vol = 1111841.36 \text{ mm}^3$
Surface area of UAV	$S_{UAV} = 272163.73 \text{ mm}^2$
Center of gravity	$X_{c.g} = 63.9 \text{ mm}$
Aerodynamic center of wing	$X_{a.c-w} = 16.05 \text{ mm}$ $Y_{a.c-w} = 124.2 \text{ mm}$ $Z_{a.c-w} = 0 \text{ mm}$
Aerodynamic center of horizontal tail	$X_{a.c-t} = 129.06 \text{ mm}$ $Y_{a.c-t} = 38.16 \text{ mm}$ $Z_{a.c-t} = 0 \text{ mm}$
Aerodynamic center of vertical tail	$X_{a.c-t} = 129.06 \text{ mm}$ $Y_{a.c-t} = 0 \text{ mm}$ $Z_{a.c-t} = 38.16 \text{ mm}$
Aerodynamic center of duct	$X_{a.c-d} = 15.12 \text{ mm}$ $Y_{a.c-d} = 0 \text{ mm}$ $Z_{a.c-d} = 0 \text{ mm}$
Moments of inertia	$I_x = 16352000 \text{ g} \times \text{mm}^2$ $I_y = 20136000 \text{ g} \times \text{mm}^2$ $I_z = 22780000 \text{ g} \times \text{mm}^2$

Appendix-C

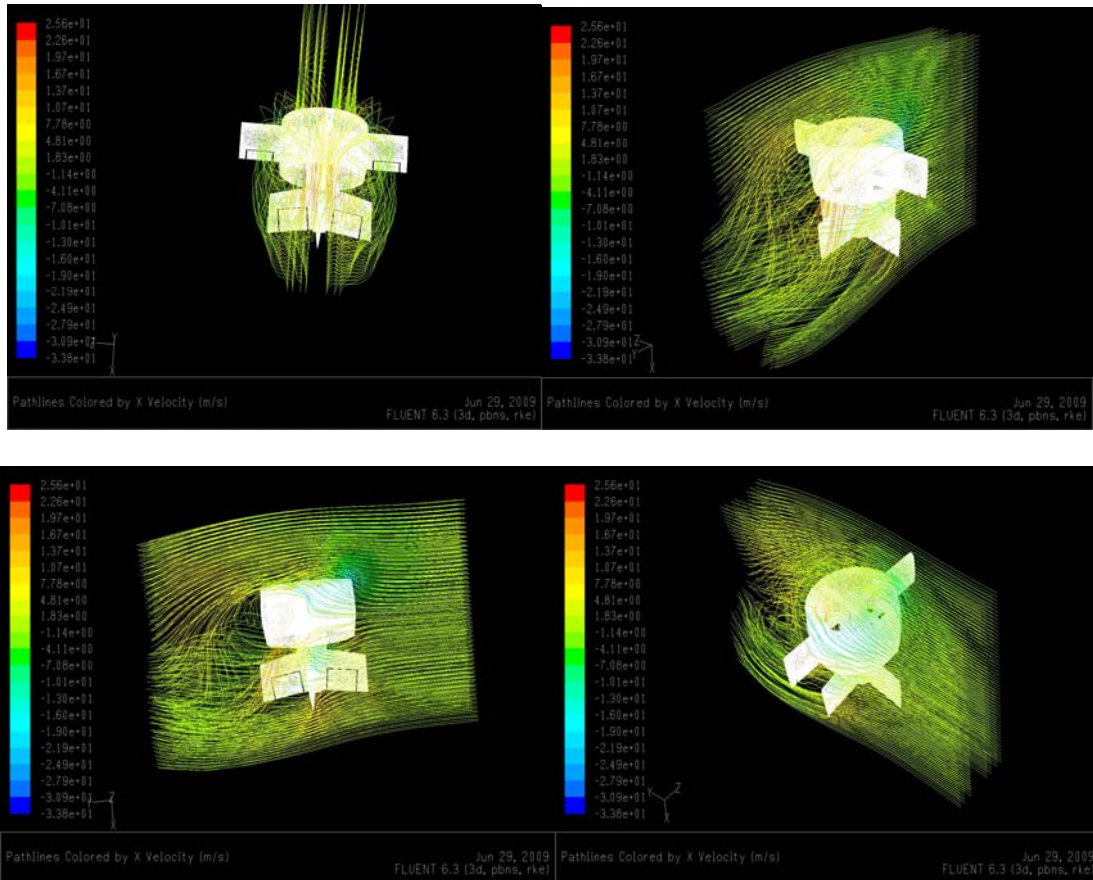
C Flow Visualization in CFD

C.1 Flow Patterns at Different Angle of Attack



These four figures display the flow region around UAV at different angles of attack. They are 10, 30, 50 and 70 degrees, respectively. However, no matter how big the angle of attack is the flow are separated into two types including external flow (free flow or air flow) and internal flow (propeller slipstream flow or exhaust fan flow). The dark color (green) path-line represents the external flow which is passing over the UAV and takes place flow separation behind UAV with the increasing of angle of attack. The light color (yellow) path-line shows the internal flow, compared with external flow, which are almost keeping going through the control surfaces (tails) of UAV with no flow separation. This phenomenon is named propeller slipstream effect used for effective control in the case of hovering or low speed vertical climb of UAV.

C.2 Crosswind Effect on UAV



These figures reflect the flow patterns from four views as the UAV is hovering with crosswind. We can distinguish free flow and propeller slipstream by colors of path-line. The orange color is the slipstream whereas the yellow or green color represents free flow. Obviously, the orange flow is going out from ducted fan and keeping vertical direction. In contrast to slipstream, the yellow flow is going around ducted fan UAV and nearly horizontal. Because of this, the ram drag and nose down moment are caused as explained in previous chapters. Up to here

Appendix-D

D Stability and Control Derivatives

D.1 Case I : Hovering

$T_V = 0.5424$	$l_{\delta e} = -0.0030$	$l_{\delta r} = -0.0045$
$T_{Ve} = 1.0849$	$Y_\beta = 0.3519$	$M_V = 0$
$D_V = 3.1620e-005$	$Y_p = 0$	$M_\alpha = -0.0031$
$D_\alpha = 0.0127$	$Y_r = -0.0011$	$M_q = 1.0098e-005$
$D_{Ve} = 0.0040$	$Y_{Ve} = 0$	$M_p = 0$
$D_{\delta e} = 0.0026$	$Y_{\delta r} = 0.2355$	$M_{Ve} = 0$
$D_{\delta r} = 0.0026$	$l_V = -1.6405e-006$	$M_{\delta e} = -0.0102$
$L_V = 0$	$l_\alpha = 0$	$N_V = 0$
$L_\alpha = 0.0479$	$l_q = 0$	$N_\beta = -0.0229$
$L_q = -1.5511e-004$	$l_r = 0$	$N_{Ve} = 0$
$L_p = 0$	$l_p = -2.8723e-005$	$N_p = 0$
$L_{Ve} = 0$	$l_\beta = 0$	$N_{\delta a} = 0$
$L_{\delta e} = 0.1561$	$l_{Ve} = 0$	$N_r = -0.0014$
$Y_V = 0$	$l_{\delta a} = -8.2026e-008$	$N_{\delta r} = -0.0153$

D.2 Case II : Low-speed Vertical Climb and Slide Flight

$T_V = 0.6780$	$l_{\delta e} = -0.0046$	$l_{\delta r} = -0.0070$
$T_{Ve} = 1.3561$	$Y_\beta = 0.5511$	$M_V = 0$
$D_V = 3.1620e-004$	$Y_p = 0$	$M_\alpha = -0.0048$
$D_\alpha = 0.0199$	$Y_r = -0.0014$	$M_q = 1.2198e-005$
$D_{Ve} = 0.0050$	$Y_{Ve} = 0$	$M_p = 0$
$D_{\delta e} = 0.0041$	$Y_{\delta r} = 0.3680$	$M_{Ve} = 0$
$D_{\delta r} = 0.0041$	$l_V = -1.6405e-005$	$M_{\delta e} = -0.0159$
$L_V = 0$	$l_\alpha = 0$	$N_V = 0$
$L_\alpha = 0.0769$	$l_q = 0$	$N_\beta = -0.0359$
$L_q = -1.8737e-004$	$l_r = 0$	$N_{Ve} = 0$
$L_p = 0$	$l_p = -3.4695e-005$	$N_p = 0$
$L_{Ve} = 0$	$l_\beta = 0$	$N_{\delta a} = 0$
$L_{\delta e} = 0.2439$	$l_{Ve} = 0$	$N_r = -0.0017$
$Y_V = 0$	$l_{\delta a} = -8.2026e-006$	$N_{\delta r} = -0.0240$

D.3 Case III: Horizontal Cruise Flight

$T_V = 1.0849$	$l_{\delta e} = -0.0119$	$l_{\delta r} = -0.0179$
$T_{Ve} = 2.1697$	$Y_\beta = 1.8853$	$M_V = 0.0226$
$D_V = 0.0123$	$Y_p = 0$	$M_\alpha = 0.0270$
$D_\alpha = 0.0538$	$Y_r = -0.0015$	$M_q = 1.6857e-005$
$D_{Ve} = 0.0079$	$Y_{Ve} = 0$	$M_p = 0$
$D_{\delta e} = 0.0106$	$Y_{\delta r} = 0.9420$	$M_{Ve} = -0.0042$
$D_{\delta r} = 0.0106$	$l_V = -3.2810e-004$	$M_{\delta e} = -0.0407$
$L_V = 1.6246$	$l_\alpha = -0.0036$	$N_V = 0$
$L_\alpha = 1.0039$	$l_q = 0$	$N_\beta = -0.1227$
$L_q = -2.5895e-004$	$l_r = 0$	$N_{Ve} = 0.0305$
$L_p = 0$	$l_p = -3.8488e-005$	$N_p = 0$
$L_{Ve} = 0.6280$	$l_\beta = 0$	$N_{\delta a} = 0$
$L_{\delta e} = 0.6245$	$l_{Ve} = 0$	$N_r = -0.0018$
$Y_V = 0$	$l_{\delta a} = -0.0033$	$N_{\delta r} = -0.0613$

Appendix-E

E Dynamic Model Edited in M-file

```
% Aerodynamic Coefficients (based on initial conditions)
rho=1.225;
Ve=();
V=();
alpha=();
beta=();
d_ram=();

% Geometry Parameters
Ae=0.02214;
Sw=0.010389; St=0.010497; Sd=0.015825; Sr=0.054;
Xc_g=0.0639; Xa_c_t=0.129; Xa_c_w=0.016; Xa_c_d=0.015;
Yc_g=0; Ya_c_t=0.038; Ya_c_w=0.124; Ya_c_d=0;
Zc_g=0; Za_c_t=0.038;
bw=0.16118; bt=0.15456;
cw=0.064; ct=0.067;

% Inertia Moment
Ixx=0.016352;
Iyy=0.020136;
Izz=0.02278;
m=0.4;

% Dimensionless Derivatives
Cd_0_w=0.00215; Cd_0_d=0.00263; Cd_0_t=0.003;
Cd_alpha_w=0.000058; Cd_alpha_d=0.000168; Cd_alpha_t=0.00048;
Cl_alpha_w=0.0178; Cl_alpha_d=0.0436; Cl_alpha_t=0.00181;
Cy_beta_d=0.0361; Cy_beta_t=0.0133; Cy_delta_rudder=0.0089;
Cd_delta_rudder=0.0001; Cd_delta_elevator=0.0001;
Cl_delta_aileron=0.002; Cl_delta_elevator=0.0059;

% Dimensional Derivatives for Stability and Control
% Longitudinal Aerodynamic Derivatives
% 1) Thrust Terms
Tv=rho*Ae*Ve
Tve=2*rho*Ae*Ve
% 2) Drag Terms
Dv=rho*V*(Cd_0_w+Cd_alpha_w*alpha)+Sd*(Cd_0_d+Cd_alpha_d*alpha)
D_alpha=1/2*rho*V.^2*(Sw*Cd_alpha_w+Sd*Cd_alpha_d)+rho*Ve.^2*St*Cd_alpha_t
Dve=rho*Ve*St*Cd_0_t
D_delta_elevator=rho*Ve.^2*St*Cd_delta_elevator
D_delta_rudder=rho*Ve.^2*St*Cd_delta_rudder
D0=1/2*rho*Ve.^2*St*Cd_0_t
Dvc=rho*Ae*Ve
% 3) Lift Terms
Lv=rho*V*(Sw*Cl_alpha_w*alpha+Sd*Cl_alpha_d*alpha)
L_alpha=1/2*rho*V.^2*(Sw*Cl_alpha_w+Sd*Cl_alpha_d)+rho*Ve.^2*St*Cl_alpha_t
Lq=-rho*Ve.^2*St*Cl_alpha_t*(Xa_c_t-Xc_g)/(V*cos(alpha)+Ve)
Lp=0
Lve=2*rho*Ve*Sw*Cl_alpha_w*V*alpha/(V+Ve)
L_delta_elevator=rho*Ve.^2*St*Cl_delta_elevator
% 4) Pitching Moment Terms
Mv=rho*V*Sw*Cl_alpha_w*alpha*(Xc_g-Xa_c_w)
M_alpha=1/2*rho*V.^2*[Sw*Cl_alpha_w*(Xc_g-Xa_c_w)+Sd*Cl_alpha_d*(Xc_g-Xa_c_d)]+rho*Ve.^2*St*Cl_alpha_t* ↵
```

```

(Xc. g-Xa. c_t)
Mq=-rho*Ve. ^2*St*Cl_alpha_t*(Xa. c_t-Xc. g)*(Xc. g-Xa. c_t)/(V*cos(alpha)+Ve)
Mp=0
Mve=2*rho*Ve*St*Cl_alpha_t*[V*alpha/(V+Ve)]*(Xc. g-Xa. c_t)
M_delta_elevator=rho*Ve. ^2*St*Cl_delta_elevator*(Xc. g-Xa. c_t)
Mvc=d_ram*rho*Ae*Ve

% Lateral Aerodynamic Derivatives
% 5) Side Force Terms
Yv=rho*V*Sd*Cy_beta_d*beta
Y_beta=1/2*rho*V. ^2*Sd*Cy_beta_d+rho*Ve. ^2*St*Cy_beta_t
Yp=0
Yr=rho*Ve. ^2*St*Cy_beta_t*(Xc. g-Xa. c_t)/(V*cos(beta)+Ve)
Yve=2*rho*Ve*St*Cy_beta_t*V*beta/(V+Ve)
Y_delta_rudder=rho*Ve. ^2*St*Cy_delta_rudder
% 6) Rolling Moment Terms
l_v=rho*V*Ss*Cl_delta_aileron*(Yc. g-Ya. c_w)
l_alpha=1/2*rho*Ve. ^2*St*Cl_alpha_t*(Yc. g-Ya. c_t)
l_q=0
l_r=0
lp=rho*Ve. ^2*St*[Cl_alpha_t*(Ya. c_t-Yc. g)/(V*cos(beta)+Ve)+Cy_beta_t*(Za. c_t-Zc. g)/(V*cos(beta)+Ve)]* ✓
(Yc. g-Ya. c_t)
l_beta=1/2*rho*Ve. ^2*St*Cy_beta_t*(Yc. g-Ya. c_t)
l_ve=0
l_delta_aileron=1/2*rho*V. ^2*Ss*Cl_delta_aileron*(Yc. g-Ya. c_w)
l_delta_elevator=1/2*rho*Ve. ^2*St*Cl_delta_elevator*(Yc. g-Ya. c_t)
l_delta_rudder=1/2*rho*Ve. ^2*St*Cy_delta_rudder*(Zc. g-Za. c_t)
% 7) Yawing Moment Terms
Nv=rho*V*Sd*Cy_beta_d*beta*(Xc. g-Xa. c_d)
N_beta=1/2*rho*V. ^2*Sd*Cy_beta_d*(Xc. g-Xa. c_d)+rho*Ve. ^2*St*Cy_beta_t*(Xc. g-Xa. c_t)
Nve=2*rho*Ve*St*Cy_beta_t*[V*alpha/(V+Ve)]*(Xc. g-Xa. c_t)
Np=0
N_delta_aileron=0
Nr=rho*Ve. ^2*St*Cy_beta_t*[(Xa. c_t-Xc. g)/(V*cos(beta)+Ve)]*(Xc. g-Xa. c_t)
N_delta_rudder=rho*Ve. ^2*St*Cy_delta_rudder*(Xc. g-Xa. c_t)

% State Space in hovering mode
% Initial Values
T0=4.5; g=9.8; V0=0.1; theta0=1.57;

% State Matrix A
a_1_1=Tv/m
a_1_2=D_alpha/m
a_2_2=-(T0+L_alpha-m*g)/(m*V0)
a_2_3=(m*V0-Lq)/(m*V0)
a_2_4=g/V0
a_3_2=M_alpha/Iyy
a_3_4=Mq/Iyy
a_4_3=1
a_5_1=1
a_6_6=(Y_beta-D0)/(m*V0)
a_6_8=(Yr-m*V0)/(m*V0)
a_7_2=l_alpha/Ixx
a_7_6=l_beta/Ixx

```

```

a_7_7=lp/Ixx
a_8_6=N_beta/Izz
a_8_8=Nr/Izz
a_9_7=1
a_9_8=tan(theta0)

% State Matrix B
b_1_1=-(Tve-Dve)/m
b_1_2=D_delta_elevator/m
b_1_3=D_delta_elevator/m
b_1_5=D_delta_rudder/m
b_1_6=D_delta_rudder/m
b_2_2=-L_delta_elevator/(m*V0)
b_2_3=-L_delta_elevator/(m*V0)
b_3_2=M_delta_elevator/Iyy
b_3_3=M_delta_elevator/Iyy
b_6_5=Y_delta_rudder/(m*V0)
b_6_6=Y_delta_rudder/(m*V0)
b_7_2=l_delta_elevator/Ixx
b_7_3=-l_delta_elevator/Ixx
b_7_5=l_delta_rudder/Ixx
b_7_6=-l_delta_rudder/Ixx
b_8_5=N_delta_rudder/Izz
b_8_6=N_delta_rudder/Izz

% State Matrix E
e_1=Dvc/m
e_3=Mvc/Iyy

```

References

- [1]. Ahmed, B., Pota, H. R. and Garratt, M., "Flight Control of a Rotary wing UAV-A Practical Approach," 47th IEEE Conference on Decision and Control Cancun, Mexico, Dec. 9-11, 2008.
- [2]. Akturk, A., Shavalikul, A. and Camci, C., "PIV Measurements and Computational Study of a 5-Inch Ducted Fan for V/STOL UAV Applications," 47th AIAA Aerospace Sciences Meeting and Exhibit, 5-8 January 2009, Orlando, Florida.
- [3]. Anderson, J. D., "Computational Fluid Dynamics: The Basic with Applications," McGill-Hill, New York, 1995.
- [4]. Anderson, J. D., "Fundamentals of Aerodynamics," 4th Edition, McGraw-Hill, New York, 2007.
- [5]. Barlow, J. B., Rae, W. H. and Pope, A., "Low-Speed Wind Tunnel Testing," 3rd Edition, John Wiley & Sons, Inc., New York, NY, 1999.
- [6]. Bradford, E.G. and James, J. C., "Transonic Computational Fluid Dynamics Calculations on Preproduction F/A-18E for Stability and Control," Journal of Aircraft, Vol. 44, No. 2, Mach-April 2007, pp. 420-426.
- [7]. Bernard, F., "Control System Design: An Introduction to State-space Method," McGraw-Hill Book Company, New York, 1986.
- [8]. Bertelsen, W. D. and Bertelsen, W. R., "History of Deflected Slipstream VTOL Aircraft," American Helicopter Society 61st Annual Forum, June 1-3, 2005, USA.
- [9]. Blondeau, J. E., and Pines, D. J., "Wind Tunnel Testing of a Morphing Aspect Ratio Wing Using a Pneumatic Telescopic Spar," AIAA Paper 2003-6659, Sept. 2003.
- [10]. Brian, L. S. and Frank, L. L., "Aircraft Control and Simulation," 2nd Edition, John Wiley & Sons, Inc., Hoboken, New Jersey, 2003.
- [11]. Cook, M.V., "Flight Dynamics Principles," Published by Elsevier Ltd. U.K, 2007.
- [12]. Damodaran, M., "Computational Aerodynamics, Flight Dynamics and Control of Unmanned Aerial Vehicles," Joint Workshop in Mechanical, Aerospace and Industrial Engineering, 10-11 July 2007, Nanyang Technological University, Singapore.
- [13]. Demasi, L., "Investigation on Conditions of Minimum Induced Drag of Closed Wing Systems and C-Wings," Journal of Aircraft, Vol.44, No.1, January-February 2007, pp.81-99.
- [14]. Escare~no, J., Stone, R.H., Sanchez A. and Lozano, R., "Modeling and Control Strategy for the Transition of a Convertible Tail-sitter UAV." Technology University of Compiegne, France. 2006.

- [15]. Escareno, J., Sanchez, A. Garcia, O. and Lozano, R., "Modeling and Global Control of the Longitudinal Dynamics of a Coaxial Convertible Mini-UAV in Hover Mode," *J Intell Robot Syst*, 2008.
- [16]. Fluent Inc, "FLUENT 5 User's Guide Volume 1," Fluent Incorporated, NH, 1998.
- [17]. Fleming, J. , Jones,T., Lusardi , J., Gelhausen, P. and Enns, D., "Improved Control of Ducted Fan VTOL UAVs in Crosswind Turbulence" *AHS 4th Decennial Specialist's Conference on Aeromechanics*, San Francisco, CA, Jan 21-23, 2004
- [18]. Grelaud, N. Bil, C. Gough, M and Chatrenet, N., "Aerodynamic Design of a VTOL Ducted Fan UAV with Surface Flow Control," *Congress Bristol VTOL UAV*, U.K, 2006.
- [19]. Guerrero, I., Londenberg, K., Gelhausen, P. and Myklebust, A., "A Powered Lift Aerodynamic Analysis for the Design of Ducted Fan UAVs," *2nd AIAA "Unmanned Unlimited" Systems, Technologies, and Operations — Aerospace, Land, and Sea Conference and Workshop & Exhibit*, 17-Sep-2003, San Diego, CA
- [20]. Higham, D. J. and Higham, N. J., "MATLAB Guide," 2nd Edition, Society for Industrial and Applied Mathematics, Philadelphia, 2005.
- [21]. Hirschberg, M. J., "An Overview of the History of Vertical and/or Short Take-Off and Landing (V/STOL) Aircraft," *CENTRA Technology, Inc.*, 2000.
- [22]. Hull, D. G., "Fundamentals of Airplane Flight Mechanics," Springer, Berlin, 2007.
- [23]. Hyoung-Jin K, Yoshimichi, T. and Kazuhiro, N., "Error Estimation and Grid Adaptation Using Euler Adjoint Method," *Journal of Aircraft*, Vol. 43, No. 5, September-October 2006, pp. 1317-1323.
- [24]. Jin, L. D., Byoung, M. M., Min, J. T., Hyo, C. B. and Shim, D. H., "Autonomous Flight Control System Design for a Blended Wing Body," *International Conference on Control, Automation and Systems* 2008.
- [25]. John, D.A.., "Fundamentals of Aerodynamics," 4th edition, McGraw-Hill, 2007
- [26]. Johnson, E. N. and Turbe, M. A., "Modeling, Control and Flight Testing of a Small Ducted Fan Aircraft," *AIAA Guidance, Navigation, and Control Conference and Exhibit*, 15-18 August 2005, San Francisco, California.
- [27]. Kallapur, A., Samal, M., Puttige, V., Anavatti, S. and Garratt, M., "A UKF-NN Framework for System Identification of Small Unmanned Aerial Vehicles," *Conference on Intelligent Transportation Systems*, Beijing, China, October 12-15, 2008.
- [28]. Ko, A. and Ohanian, O. J. and Gelhausen, P., "Ducted Fan UAV Modeling and Simulation in Preliminary Design," *AIAA Modeling and Simulation Technologies Conference and Exhibit*, Hilton Head, South Carolina, 20-23 August 2007.
- [29]. Kubo, D. and Suzuki, S., "Tail-Sitter Vertical Takeoff and Landing Unmanned Aerial Vehicle: Transitional Flight Analysis," *Journal of Aircraft*, Vol.45, No.1, January-February 2008, pp.292-297.

- [30]. Lampe, A., "Aerodynamic design of a VTOL UAV," Thesis Report, RMIT Melbourne, 2008.
- [31]. Leishman, J. G., "Principles of helicopter aerodynamics," Combridge University, U.K, 2000.
- [32]. M, J., Soueres, P. and Hamelz, T., "Position control of a ducted fan VTOL UAV in crosswind, International," Journal of Control, Vol. 80, No. 5, May 2007, pp.666–683.
- [33]. Marconi, L. and Naldi, R., "Nonlinear Robust Control of a Reduced-Complexity Ducted MAV for Trajectory Tracking," 45th IEEE Conference on Decision and Control, Vol. 9, 1st January 2006, San Diego, CA
- [34]. Nicola de, D., "Performance and Stability Analysis of a Shrouded-Fan Unmanned Aerial Vehicle," Jounal of Aircraft, Vol. 43, No. 3, May-June 2006, pp. 681-691.
- [35]. Omar, Z., Bil, C. and Hill, R., "The Application of Fuzzy Logic on Transition Maneuver Control of a New Ducted-Fan VTOL UAV Configuration," AIAC12 Congress-2nd Australasian Unmanned Air Vehicles, 2007.
- [36]. Peric, M. and Ferziger, J. H., "Computational Methods for Fluid Dynamics," 2nd Edition, Springer, Berlin, 1999.
- [37]. Rajamani, G. K., "CFD Analysis of Air Flow Interactions in Vehicle Platoons," Master Thesis, School of Aerospace, Mechanical and Manufacturing Engineering, RMIT University, August 2006, Melbourne, Australia.
- [38]. Ramli, M. A., Wei, C. K. and Leng, G, "Design and Development of an Indoor UAV," Aerospace Technology Seminar 2007, 26 February 2007, Singapore
- [39]. Roberts, A. D., "Attitude Estimation and Control of A Ducted Fan VTOL UAV," *Thesis*, Lakehead University, August 2007.
- [40]. Ro, K., Raghu, K. and Barlow, J.B., "Aerodynamic Characteristics of a Free-Wing Tilt-Body Unmanned Aerial Vehicle," Journal of Aircraft, Vol.44, No.5, September-October 2007, pp.1619-1629.
- [41]. Ruban, A.I., "Early Developments of Modern Aerodynamics," University of Manchester, Published 2001.
- [42]. Salazar, S., Romero, H., Lozano, R. and Castillo, P., "Modeling and Real-Time Stabilization of an Aircraft Having Eight Rotors," J Intell Robot Syst, 2008.
- [43]. Salluce, D. N., "Comprehensive System Identification of Ducted Fan UAVs," Master Thesis, California Polytechnic State University, January 2004, San Luis Obispo, USA.
- [44]. Samad, T. and Balas, G, "Software-Enabled Control: Information Technology for Dynamical Systems," Institute of Electrical and Electronics Engineer, John Wiley & Sons, Inc., New Jersey, 2003.
- [45]. Samuel, J. B. and Pines, D., "Design and Testing of a Pneumatic Telescopic Wing for Unmanned Aerial Vehicles," Journal of Aircraft, Vol. 44, No. 4, July–August 2007.

- [46]. Schroijen, M.J.T. and Slingerland, R., "Propeller slipstream effects on directional aircraft control with one engine inoperative," 45th AIAA Aerospace Sciences Meeting, 1st January 2007, Reno, Nev.
- [47]. Solaque, L., Pinzon, Z. and Duque, M., "Nonlinear control of the airship cruise flight phase with dynamical decoupling," Electronics, Robotics and Automotive Mechanics Conference 2008,
- [48]. Srinivas, J., "Control Systems and Mechatronics," Alpha Science International Ltd., Oxford, U.K., 2007
- [49]. Stone, R. H., "Aerodynamic Modeling of the Wing-Propeller Interaction for a Tail-Sitter Unmanned Air Vehicle," Journal of Aircraft, Vol.45, No.1, January-February 2008, pp.198-210.
- [50]. Stone, R. H., "Control Architecture for a Tail-Sitter Unmanned Air Vehicle," 5th Asian Control Conference, 1st January 2004.
- [51]. Tewari, A., "Atmospheric and space flight dynamics: modeling and simulation with MATLAB and Simulink," Boston, Mass, 2007.
- [52]. Versteeg, H. K. and Malalasekera, W., "An Introduction to Computational Fluid Dynamics," 2nd Edition, London, U.K, 2007
- [53]. Walter , D. and Watkins, S., "Force and pitching moment variation of inverted aerofoils at high angles of attack in ground effect," 16th Australasian Fluid Mechanics Conference, Crown Plaza, Gold Coast, Australia 2-7 December 2007
- [54]. Wassim, A. B. and Wahid, S. G., "Drag Prediction in Transitional Flow over Airfoils," Journal of Aircraft, Vol. 44, No. 3, May-June 2007, pp. 824-83
- [55]. Wong, K.C., Peters, H.J.H., and Catarzi, P., "Adapting to Limitations of a Wind Tunnel Test Facility in the Aerodynamic Testing of a new UAV," 9th Australian International Aerospace Congress (AIAC 2001), 5-8 March, 2001, Canberra, Australia.
- [56]. Zhao, H. W. and Bil, C. "Aerodynamic Design and Analysis of a VTOL Ducted-Fan UAV," 26th AIAA Applied Aerodynamics Conference, 18 - 21 August 2008, Honolulu, Hawaii.
- [57]. Zhao, H. W., Bil, C. and Bok, H. Y., "Aerodynamic Analysis of a Ducted Fan VTOL UAV for Transition Maneuver." KSAS-JSASS Joint International Symposium. Korea, December, 2008
- [58]. Zhao, H. W., Bil, C. and Bok, H. Y., "Computational Fluid Dynamics Calculations on Preproduction Ducted Fan VTOL UAV for Stability and Control," 3rd Australasian Unmanned Air Vehicles Conference, 9 - 12 March, 2009